National Library of Canada
Acquisitions and Bibliographic Services Branch
395 Wellington Street
Ottawa, Ontario
K1A 0N4

Bibliothèque nationale du Canada
Direction des acquisitions et des services bibliographiques
395, rue Wellington
Ottawa (Ontario)
K1A 0N4

Your file   Votre référence

Our file   Notre référence

NOTICE

The quality of this microform is heavily dependent upon the quality of the original thesis submitted for microfilming. Every effort has been made to ensure the highest quality of reproduction possible.

If pages are missing, contact the university which granted the degree.

Some pages may have indistinct print especially if the original pages were typed with a poor typewriter ribbon or if the university sent us an inferior photocopy.

Reproduction in full or in part of this microform is governed by the Canadian Copyright Act, R.S.C. 1970, c. C-30, and subsequent amendments.

AVIS

La qualité de cette microforme dépend grandement de la qualité de la thèse soumise au microfilmage. Nous avons tout fait pour assurer une qualité supérieure de reproduction.

S'il manque des pages, veuillez communiquer avec l'université qui a conféré le grade.

La qualité d'impression de certaines pages peut laisser à désirer, surtout si les pages originales ont été dactylographiées à l'aide d'un ruban usé ou si l'université nous a fait parvenir une photocopie de qualité inférieure.

La reproduction, même partielle, de cette microforme est soumise à la Loi canadienne sur le droit d'auteur, SRC 1970, c. C-30, et ses amendements subséquents.

Canada

Numerical Techniques for the Study of HF Coupling Modes on Large Aircraft

Quan Cuong Luu

A Thesis

in

The Department

of

Electrical and Computer Engineering

Presented in Partial Fulfillment of the Requirements
for the Degree of Master of Applied Science at
Concordia University
Montreal, Quebec, Canada

March 1994

National Library of Canada
Acquisitions and Bibliographic Services Branch
395 Wellington Street
Ottawa, Ontario
K1A 0N4

Bibliothèque nationale du Canada
Direction des acquisitions et des services bibliographiques
395, rue Wellington
Ottawa (Ontario)
K1A 0N4

Your file Votre référence

Our file Notre référence

ISBN 0-315-97638-1

Canadä

Abstract

Numerical Techniques for the Study of HF Coupling Modes on Large Aircraft

Quan Cuong Luu

In this thesis, recent increases in computational power are exploited to apply the technique of "high resolution spectral analysis" with the Numerical Electromagnetics Code to obtain a complete diagnosis of HF antenna-to-antenna coupling and antenna-to-airframe coupling on aircraft. The HF antenna installations on two large aircraft, namely, the EC-130/TACAMO and the CL-600/CHALLENGER, are studied. The unusually complex installation of five HF wire antennas on the EC-130 represents a unique challenge. An existing EC-130 wire-grid model is upgraded by removing all modelling errors, and refining the wire-grids representing the wings and stabilizers of the aircraft. The revised model is used to study the inter-antenna coupling and the antenna-to-airframe coupling modes on the EC-130. Results are presented which describe all the coupling modes that have been identified and their impact on radiation patterns and likely operational consequences. Antenna resonant lengths and the loading conditions for passive antennas are found to have significant influence on the inter-antenna coupling modes. The modelling of the notch HF antenna on the CL-600 aircraft reveals the radiation characteristics of this antenna, especially the antenna-to-airframe coupling for the first time. Three current paths are identified on the EC-130's airframe and two on the CL-600's. The information sets provided by this thesis are very difficult, if not impossible to obtain by any scale-model or full-scale measurement programs.

Acknowledgements

I wish to thank Dr. S.J. Kubina and Dr. C.W. Trueman for their guidance and invaluable advice throughout this research project. Their suggestions and corrections in the preparation of this thesis were especially welcome.

I wish to thank National Science and Engineering Research Council of Canada for supporting the work described in this thesis. Dr. S.J. Kubina's enthusiasm about this research work was a constant source of inspiration. A special tribute is owed to Dr. C.W. Trueman for his time devoted in discussing with me the moment methods and some other numerical modelling and electromagnetic theories. Thanks are due also to Dr. R. Paknys for sharing his knowledge of electromagnetics with me in many pleasant and interesting conversations.

I am in debt to Mr. Mike Marak and Mr. David Gaudine for maintaining a ready-to-work computer system, and giving expert advice in text processing and file management. The help of Ms. Pamela Fox with the WordPerfect was also appreciated.

Finally, many thanks to fellow workers Ariel Ramos, who did an excellent job in developing the CL-600 wire-grid model, T.B. Hong Vu, Locson Tonthat, Katayoun Zarrinkoub, and Sameh Wassif, for their occasional help in preparing figures for this thesis.

Table of Contents

Page

List of Figures

Figure Page

List of Tables

Table Page

Glossary of Symbols and Terms

a	Wire Radius
β	Wave Number
ω	Angular Frequency
λ	Wavelength
μ_o	Permeability in Free Space
ε_o	Permittivity in Free Space
ℓ	Wire Length
Δ	Wire Segment Length
γ	Euler's Constant
I	Electric Current
J	Electric Current Density
Φ	Electric Scalar Potential
$\bar{A}$	Magnetic Vector Potential
G	Thin Wire Kernel
G_{EK}	Extended Thin Wire Kernel
Z_{in}	Input Impedance
$C(x)$	Even Fresnel Integral
$S(x)$	Odd Fresnel Integral
NEC	Numerical Electromagnetics Code
EMC	Electromagnetic Compatibility
EMI	Electromagnetic Interference

CHAPTER 1

INTRODUCTION

In the realm of numerical modelling of electromagnetics problems, the immense increase in computational power due to advances in computer technologies has provided the possibility of pursuing comprehensive investigations on certain complicated electromagnetic interactions such as antenna-to-airframe and antenna-to-antenna coupling on aircraft.

Granger [1,2] pioneered the study of aircraft antennas and the airframe coupling problems in the early 1950s. He investigated the radiation characteristics of various types of antennas used on aircraft, and predicted the electromagnetic interaction between the airframe and the exciting antennas depending on the relationship between the airframe dimensions and wavelength. In the HF band, the wavelength is usually comparable with the major dimensions of the aircraft, and aircraft structures have significant influence on the performance of the antenna because of the airframe resonances. Granger's investigations provide knowledge of input impedance and radiation patterns for a variety of aircraft antennas, as well as induced charge and current distributions on aircraft structures. This is extremely useful for aircraft antenna design, especially in the pre-computer era.

Digital computers became widely available in the mid-1960s. Scientists and engineers began to use computers to solve complicated or tedious problems. When a valid technique can be found to simulate or model a complicated problem using computers, it provides an extremely effective and powerful means to predict and analyze the results under different circumstances. Computer simulation of HF antennas in airplanes and helicopters has been under way for more than a decade at the EMC Laboratory and at various institutions around the world. The main objective has been to predict the radiation characteristics of the antennas or to verify scale-model or full-scale measured results. For instance, in the 70s, Forgan [3] studied the performance of a "notch" and a "pod" antenna on a typical aircraft by scale-model measurements and numerical modelling. Kubina and Pavlasek [4] evaluated typical helicopter antennas with the aid of wire-grid modelling. More recent examples include the modelling and measurement of HF antennas for the U.S. coast guard HH-60J helicopter [5].

At the EMC Laboratory, several projects involving studies of aircraft antenna radiation characteristics by numerical modelling had been undertaken by a number of graduate students. Larose [6] simulated the HF antennas on the CP-140/AURORA airframe using a series a models ranging from simple stick models to relatively complex wire-grid models. The performance of each model was evaluated based on the comparisons between the computed and the measured antenna input impedances and radiation patterns. Similarly, Rosenzweig [7] has developed a series of wire-grid models to simulate the five HF antennas on a specialized version of the C-130/HERCULES aircraft called the EC-130/TACAMO, in an effort to resolve the problem of discrepancy between the scale-model and full scale measured radiation patterns. Esfandiari [8] analyzed two types of HF antenna on the Bell CH-135 helicopters by scale-model measurements and computer modelling. Due to the limitations in computational power in the past, these computer experiments were unable to unfold the full detail of antenna coupling phenomena because the simulation was performed only at a limited number of frequencies in the HF band.

This thesis is devoted to the study of two different kinds of HF coupling (antenna-to-airframe and antenna-to-antenna) on two large aircraft in order to evaluate its impact on system performance, using numerical techniques that involve extensive computational and analyzing processes. The two aircraft under investigation are the EC-130/TACAMO and the Canadair CL-600/CHALLENGER executive jet. Computer models of these two aircraft are carefully designed following the known modelling guidelines in order to ensure good results. Computer simulations are performed at extremely fine frequency intervals in the HF band, resulting in high resolution displays of antenna characteristics that reveal the coupling modes in full detail. In addition, the consequences of the coupling on the operations of the antenna systems are assessed since they are of great concern for HF communication system engineers.

1.1 HF Coupling on Large Aircraft

HF antennas are widely used on aircraft for long range communication. HF communication can be established in two major modes, namely, the ground wave and sky wave modes. In the ground wave mode, electromagnetic energy may travel directly from the transmitter to the receiver (direct wave), or may arrive at the receiver after being reflected from the surface of the earth (ground-reflected wave). In addition, the energy may be guided along the earth's surface (surface wave) as an electromagnetic wave guided by a single conducting plate [9]. This is the most common mode for short and medium range communication. By contrast, the sky wave mode relies on the reflection and scattering of electromagnetic waves in the earth's ionosphere and can travel a long distance. Sky wave signals are less stable than the ground wave signals. Their strength depends on the condition of the ionosphere and the operating frequency [9].

For large aircraft, the wavelengths in the HF range are usually comparable with the major dimensions of the airframe such as wingspan and the length of fuselage. This could result in strong parasitic currents being induced on the airframe. This "antenna-to-airframe" coupling results in profound changes in radiation characteristics of the aircraft antennas [1]. Moreover, if more than one antenna is mounted on the aircraft, strong coupling could occur between antennas. Such "antenna-to-antenna" coupling leads to operational interference or even damage to the receivers connected to the antennas. These are serious electromagnetic compatibility problems that must be studied by antenna engineers to assess any antenna system designs. It is for these reasons that the study of HF coupling modes on large aircraft is desirable and should be an important aspect of HF aircraft antenna performance evaluation.

For this kind of study, numerical modelling methods [10, 11] are preferred over scale-model or full-scale measurements because numerical studies are easier to perform and cost less in terms of time and money.

1.2 Numerical Modelling Methods

Thanks to the advance in computer technology, "workstations" and personal computers are now capable of analyzing complicated electromagnetic problems. Computer simulation is based on numerical modelling techniques that have been developed since the mid-1960s. Some well-known examples are: the finite-element method [12], the finite-difference time-domain (FDTD) method [13], the moment method [14], the transmission-line matrix (TLM) method [15], the multipole method [16], and the geometrical theory of diffraction (GTD) method [17, 18, 19]. These techniques have been employed in many applications such as antenna designs and studies of radiation or scattering characteristics of arbitrary structures. Each of these methods has its own features and limitations.

The finite-difference time-domain (FDTD) method divides the region of interest into small cells. Instead of solving the problem involving a partial differential equation with boundary conditions analytically, FDTD solves a discretized version of the partial differential equation in the time domain [11,13]. The frequency response can be obtained by the Fourier transform. When the method is used for an open-region problem, the region must be truncated to a finite size, and an absorbing boundary condition must be enforced on the boundary of the truncated region [20].

Similar to the finite-difference method, the finite-element method divides the region of interest into small cells. Usually these small subregions are polygons such as triangles and rectangles for two-dimensional problems and tetrahedral elements for three-dimensional problems. Functionals are set up and variational expressions are applied to each of the small areas or volumes [11]. The discretization used in this method allows it to be applied to a wide range of structures including the ones with odd shapes. The finite element method, however, has a problem whose exact cause is still to be resolved. The problem is the existence of the so-called spurious zeros [11]. Such zeros correspond to non-physical field structures. Nevertheless, several schemes are available to reduce or eliminate these zeros. They are typically based on the variational expression that involves enforcing $\nabla H = 0$. In addition, like in the case of finite difference, an appropriate absorbing boundary condition is required when the finite element method is applied to an open-region problem.

The TLM method converts the field problem to a three-dimensional equivalent network problem. It is basically a method for simulation of the wave propagation phenomena in the time domain. The frequency response can be obtained by the Fourier transform. In the TLM method, the space is discretized into a three-dimensional lattice with a period equal to a certain length. The introduction of periodic lattice structures result in a typical passband-stopband phenomenon appearing in the frequency-domain data. The useful frequency range is determined by the mesh size. The frequency must be lower than the upper bound of the lowest passband [11].

The moment method transforms a linear equation such as an integral equation in the frequency domain into a system of linear algebraic equations with complex-valued coefficients [12]. It first approximates the solution by a sum of known basis functions with unknown coefficients defined over the region of interest. The resulting equation is then projected on to another set of known functions called weighting functions also defined over the region of interest to form a system of linear algebraic equations. Solving this system will give the coefficients of the basis functions and hence the solution. The moment method is best suited for structures with dimensions equal to several wavelengths. Larger structures will require an increased amount of computer memory and forbiddingly long computational time. The moment method is described in detail in Chapter 2 of this thesis.

Unlike the moment method in which the fields are expressed indirectly through current distributions, the multiple multi-pole method [21] expand the electromagnetic field in a series of easily calculable fields which are solutions of Maxwell's equations in a linear, isotropic and homogeneous medium. The unknown expansion coefficients are determined by enforcing the boundary conditions and/or continuity equations across material boundaries for the field. An overdetermined system of equations is found by imposing the boundary conditions for all the field components at many boundary points. Since the solution is expressed directly in terms of fields, the near field and far field can be readily evaluated. The MMP method is well suited for calculating fields inside waveguides because it can give very accurate results. It can be applied to problems involving dielectric structures as well as conducting structures. However, its applications are limited by the size of the structure.

The Geometrical Theory of Diffraction (GTD) method is preferred for high frequency applications in which the dimensions of the radiating or scattering object are many wavelengths. GTD assumes that energy propagates along ray paths in space, reflects specularly from conducting surfaces and diffracts from edges. Being an extension of the classical geometrical optics (GO), it overcomes some of the limitations of geometrical optics by introducing a diffraction mechanism. This method is simple to apply and can be used to solve complicated problems that do not have exact solutions. Moreover, it provides physical insight into the radiation and scattering mechanisms from the various parts of the structures [19]. Since it is a high frequency asymptotic technique, it cannot be used for low frequency applications.

The main advantages of numerical modelling techniques over full-scale or scale model measurement programs lie in their high flexibility and low cost. For example, effects due to changes in antenna characteristics are more conveniently studied with computer simulations; antenna impedances can be obtained easily using numerical techniques while measured data can only be acquired through full-scale measurement; and computer simulations are not subject to poor weather conditions as are outdoor model ranges. Computers have been much more affordable than modern measurement instrumentation. It should be noted that, however, numerical techniques only give meaningful results when the aircraft are properly modelled and the models validated. In addition, any kind of modelling can only provide an approximation to the real object, and hence the results obtained from modelling are unavoidably subject to certain degree of inaccuracy. Therefore, in the process, effort must be made to ensure that the model is as true a representation of the aircraft surface as possible and is in compliance with the guidelines of the numerical techniques being used to reduce the inaccuracy in the results as much as possible.

1.3 Wire-Grid Modelling

In this thesis, the Numerical Electromagnetics Code (NEC) [22] based on the method of moments is used in conjunction with the wire-grid modelling technique introduced by Richmond [23] to model the antennas and the airframe of the aircraft. The theoretical basis of NEC and its wire-grid modelling guidelines will be reviewed in Chapter 2.

The validity and limitations of wire-grid modelling have been investigated by many researchers and the methodology for optimizing the results has been proposed [23,24,25,26,27]. These limitations will be reviewed in Chapters 2 and 3. Thus in the construction of the aircraft model, measures were taken to minimize the difference between the real object and the model in terms of electromagnetic properties. Trueman and Kubina [26] have proposed principles or "guidelines" for the design of wire-grid models of complex surfaces, which will be presented in Chapter 3. According to Lee et al. [24], best match in self-inductance between a solid surface structure and its wire-grid model is obtained when the radii of the wires in the wire-grid model satisfy the "same surface area" condition. Ludwig [25], Trueman and Kubina [26], and Paknys [27] have verified that the "same surface area" rule indeed gives the best results. Therefore, the "same surface area" rule was employed to calculate the radius for each wire in the aircraft wire-grid models in this thesis. The process of radius-finding will be described in Chapter 3.

Wire-grid modelling is also an art of compromise. Theoretically, the denser the wire-grid (that is, more wires are used to model a fixed area), the better the model. However, when the computing time and computer memory required are taken into account, the number of wires must be limited so that the numerical problem can be handled and solved by the computer in a reasonable period of time. It is for this reason that the wire density on the model is not uniform: high wire density is necessary for regions considered to be critical such as the antenna feed regions and surfaces close to the antennas where strong induced currents are expected. In order to ensure the continuity of current flows on the model, denser wire-grid was used in critical regions such as antenna feed regions, and a smooth transition of wire density was introduced in the regions where the width of the conducting surface is not constant.

A software system has been developed at Concordia's EMC Laboratory [28] for radiation and scattering analysis of complex structures using wire-grid modelling and NEC. The system consists of a variety of software modules for creation, visualization and verification of wire-grid models; display and analysis of current distributions and fields; and preparation of presentation graphics. The computer-aided modelling software facilitates the process of preparing grids representing complex structures such as aircraft and ships which is tedious and prone to error. It also searches a model for violation of NEC's guidelines [29], as explained later in Chapter 3. The process of radius-finding for a wire-grid will be described in Chapter 3. Graphic display software modules are indispensable for effective analysis of the numerical results obtained from running NEC. Currents and fields can be displayed in various formats to help visualize and understand the results.

The first stage of this numerical modelling study is the development of the wire-grid models. The models of the two aircraft under investigation were carefully designed using the EMC Lab's software system.

1.4 The EC-130/TACAMO Model

The EC-130/TACAMO shown in Fig. 1.1 is a U.S. Navy communication platform. It is similar to the well known transport aircraft C-130/HERCULES but uses a different antenna system. The EC-130 is equipped with five external HF wire antennas for long range communication. They include two top mounted antennas that run from either side of the forward fuselage to the vertical stabilizer, two symmetrical "dog-leg" antennas running from mid-fuselage towards the horizontal stabilizer and then to the vertical stabilizer, and one receive antenna, centered on top of the fuselage, aft of the other two longer top mounted antennas, as shown in Fig. 1.1. The EC-130 computer model was originally developed at EMC Laboratory for use with the Numerical Electromagnetics Code to analyze radiation patterns and clarify the discrepancies between the full scale and scale model measured radiation patterns [7]. Due to the enormous increase in computing

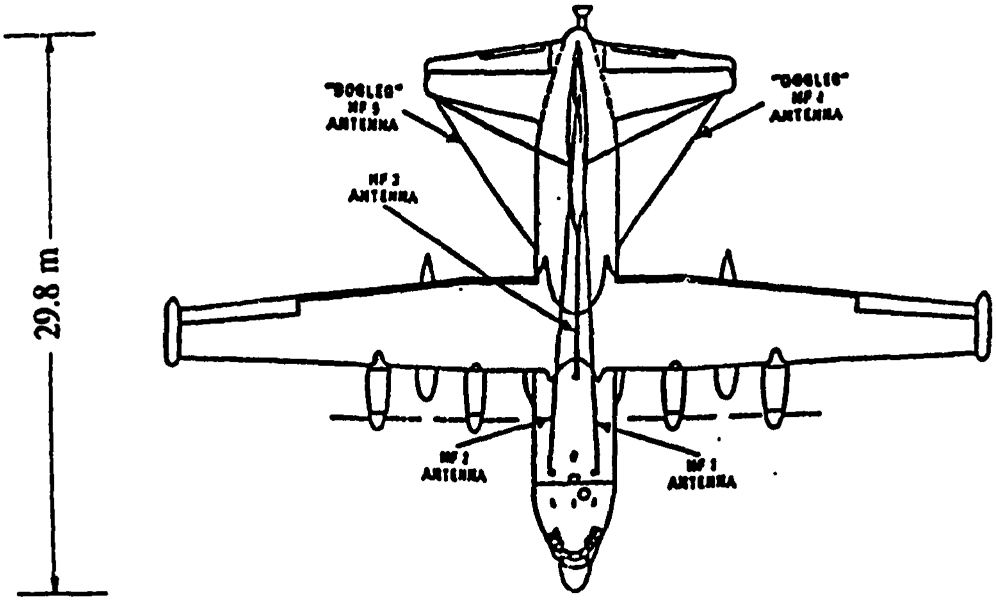

Fig. 1.1 The EC-130/TACAMO HF antenna installation.

power acquired recently, it became possible to study in detail the inter-antenna and antenna-to-airframe coupling for the complex HF antenna installation on this aircraft. In order to take full advantage of the new computing power, the model is further refined in this thesis by adding more wire segments, resulting in a 924 wire segment model. The degree of complexity of the new model is almost doubled compared to the old one (which has 477 wire segments). It takes approximately 30 minutes to analyze the model with NEC at one frequency with our DEC 5000 workstations. This enables us to finish a frequency sweep from 2 - 30 MHz with fine frequency stepping of 0.1 MHz in one week's time. Consequently, high resolution pictures of radiation characteristics can be obtained, showing all detailed variations with respect to frequency. Since strong coupling is usually revealed by rapid changes in input impedance with frequency, frequency sweeps with a fine frequency step provide us with the ability of detecting all possible coupling modes occurring in the HF band. This is the foundation of the study of HF coupling modes in this thesis and is termed "high resolution spectral analysis" [34].

1.5 The CL-600/CHALLENGER Model

The same approach was taken to analyze the characteristics and airframe coupling of an HF "notch" antenna for another aircraft, the Canadair CL-600 Challenger. The CL-600, shown in Fig. 1.2, is a high-speed intercontinental range corporate jet. It is also used for specialized roles in air ambulance or maritime surveillance applications. This aircraft is equipped with an HF "notch" antenna which is formed by insulating the leading edge of the dorsal fin as described in Chapter 6. Modelling the "notch" antenna [30] is a relatively new experiment. Unlike the wire antenna, which can be naturally modelled with a conducting wire, the notch antenna is modelled by using wire segments to outline the shape of the notch and a proper wire-grid to represent the dorsal fin itself as a conducting sheet surrounding the notch. Since a significant amount of current is expected to flow around the notch when the antenna is excited, the wire-grid must be carefully designed to allow currents to flow in all directions as freely as possible.

The CL600 wire-grid model consists of 624 segments. Its elegantly designed wire-grid retains the geometry of the actual aircraft and at the same time fulfils NEC's modelling requirements. Execution of NEC with this model at each frequency takes about 25 minutes on the DEC 5000 workstations.

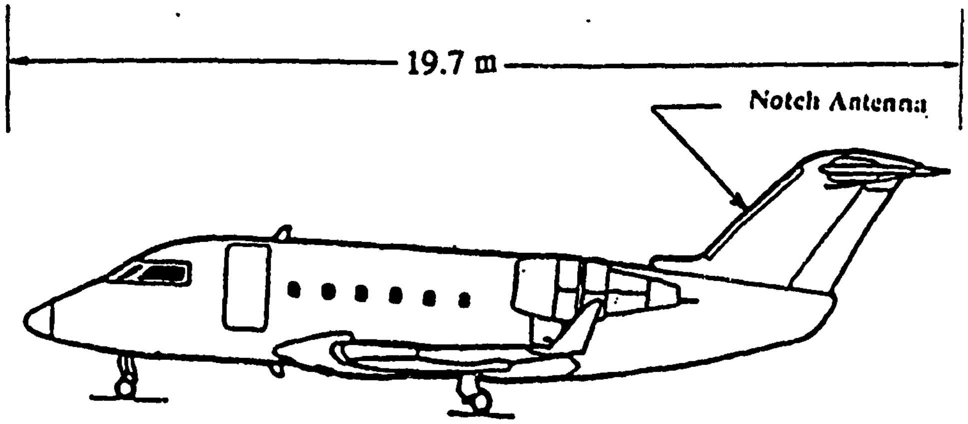

Fig. 1.2 The CL-600/CHALLENGER aircraft with its notch antenna.

1.6 Methodology

A comprehensive study of HF coupling modes requires extensive computational and analyzing processes that involve model creation and verification, execution of NEC, displaying and analyzing the results. Since measured results are not available, the study must be done in a systematic and logical way in order to maximize the credibility of the numerical results.

1.6.1 Creating a Wire-Grid Model

The study begins with the construction of the aircraft wire-grid model. This process involves generating the geometry of the wire-grid representing the aircraft, calculating the radii for each wire segment in the model, and verifying the integrity of the model. Various software modules are used to facilitate the process. The complete procedure will be described in full detail later in Chapters 3 and 4.

1.6.2 High Resolution Spectral Analysis

Upon completion of the model geometry, one proceeds to execute NEC runs as frequency sweeps with fine frequency stepping for different antenna excitations and loading conditions. The output includes antenna input impedances, current magnitudes and phases, and radiation patterns. In Chapters 5 and 6, the input impedances are used to identify coupling, which is revealed as anomalous peaks and valleys in the input impedance curves. The existence of the coupling is then verified by examinations of the current distributions on the aircraft or the induced terminal voltages of the passive antennas at the associated frequencies. It is also desirable to inspect the radiation patterns so that the variations due to strong coupling can be noted and understood.

In the case of the EC-130 presented in Chapter 5, the coupling between the HF antennas and to the airframe gives rise to two main concerns: (1) the magnitude of the induced voltage across the feed points of an antenna could be high enough to cause operational interference or even damage to the receiver connected to the passive antenna; (2) the radiation pattern of each individual antenna could be profoundly altered by the strong currents induced on other antennas and/or on the airframe due to phase additions or cancellations.

As for the CL-600 presented in Chapter 6, the performance of its HF notch antenna had not been studied before. Thus this thesis provides the first comprehensive information on the radiation characteristics of this particular antenna, especially in the relation to its interaction with the airframe, in addition to the coupling modes. Since only one HF antenna is installed, attention will be paid to the antenna-to-airframe coupling, which would define any special features of antenna input impedance and other radiation characteristics changes such as HF radiated power parameter variations. This base frequency study is required for any possible studies of coupling into other higher frequency communication antennas.

The exact frequencies where strong coupling occurs are very difficult if not impossible to identify by direct measurements or simplified calculations. Therefore, the flexibility and economy of numerical techniques make them more attractive for this kind of study. The use of numerical techniques not only allows one to obtain a complete set of critical frequencies associated with strong coupling by fine frequency stepping sweeps, but also to calculate the values of the induced voltages at antenna terminals and the currents on any part of the structure, as well as the radiated field patterns of the antennas. The analysis procedure is explained in Fig. 1.3. It proceeds from generating a valid model with its active antenna excited by a voltage source and its passive antennas under a specific loading condition, analyzing the model with NEC at many frequencies over the HF band, and finally processing and analyzing the numerical results using a variety of software modules. This procedure will be described in detail and used in Chapters 3 to 6.

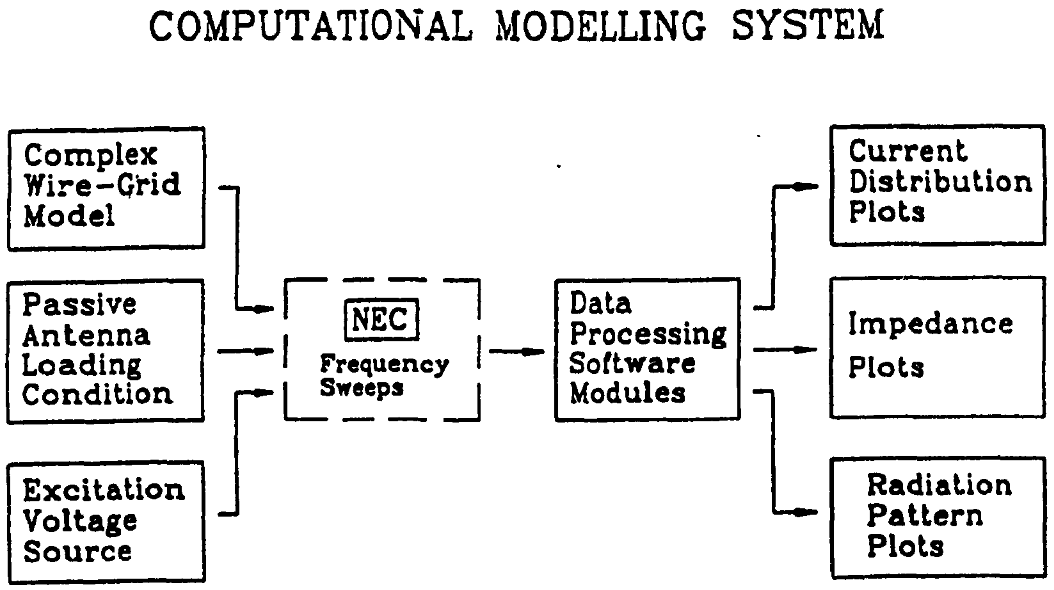

Fig. 1.3 An illustration of the Computational Modelling System.

1.7 Major Achievements

This thesis presents the techniques and the results of the numerical modelling study of HF coupling on two large aircraft with a degree of detail that was impossible to achieve previously. It represents a new plateau in the applications of computer simulations to a complex electromagnetic problem and the understanding of the associated phenomena. The objectives that have been accomplished are summarized as follows.

1.7.1 The EC-130/TACAMO

In Chapter 4, the EC-130 wire-grid model has been upgraded to a complex model of 924 wire segments and the NEC-incompatibility errors existing in the old model have been completely eliminated. Some degree of improvement has been observed in the agreement between the radiation patterns computed with the upgraded model and the ones obtained from scale model measurement, supporting the confidence in the new model. With the execution of NEC runs at extremely fine frequency intervals, high resolution curves of HF antenna input impedances and radiated power parameters have been obtained in Chapter 5. Moreover, complete sets of frequencies where strong coupling occurs for two representative active antennas and for three loading conditions for passive antennas have been identified. In order to observe and analyze the coupling modes and their impact, the current distributions and radiation patterns at frequencies of concern have been plotted and studied. The induced voltages at passive antenna terminals for different loading conditions in the HF range have been calculated and plotted. Thus a complete analysis of performance and a diagnosis of the HF coupling modes has been given by this new technique.

1.7.2 The CL-600/CHALLENGER HF Notch Antenna

With the application of the same modelling techniques to the CL-600 in Chapter 6, high resolution curves of the notch antenna input impedances and radiated power parameters have been obtained and plotted to obtain for the first time the radiation characteristics of the notch antenna on this particular aircraft. Frequencies where strong antenna-to-airframe coupling occurs have been determined and the associated coupled current paths have been identified. The current distributions and radiation patterns at frequencies of concern have been plotted and analyzed. The coupling modes have been thoroughly analyzed and the impact of the coupling on the radiated power and radiation pattern has been assessed. With this understanding, the model is ready for additional EMC coupling studies.

The first part of this thesis, Chapters 1 to 3, is devoted to the theoretical and computational basis of this study and methodology for its application. It consists of a summary of the formulations and assumptions used in the Numerical Electromagnetic Code, plus discussion of the specific process for model creation and verification, NEC execution and output analysis.

The second part presents the results of model development and refinement, as well as the complete numerical results and coupling mode analysis for the two aircraft. Chapter 4 discusses the refinement of the EC-130 model and the development of the CL-600 model. The complete numerical results and the diagnosis of the HF coupling modes for the EC-130 and the CL-600 are presented in Chapter 5 and Chapter 6, respectively. This latter summary also outlines how the coupling affects the HF communication systems in each aircraft.

Finally, the concluding Chapter 7 presents a complete perspective on what has been achieved and discusses the further work that could be done to explore these fascinating and important aspects of such electromagnetic compatibility problems.

CHAPTER 2

THEORETICAL BASIS OF THE NUMERICAL ELECTROMAGNETICS CODE

The Numerical Electromagnetics Code (NEC) [22] is a program for electromagnetic problem analysis in the frequency domain. NEC had its origins in the scattering code BRACT (1967) [35] which was based on the early work of Richmond [36] and Mei [37]. Developed from an antenna modelling version of BRACT, the Antenna Modelling Program (AMP) [38] was the first widely-used program that employs the method of moments. NEC was developed in 1977 from AMP-2 [39], which is a revision of AMP, at Lawrence Livermore National Laboratory. NEC uses the method of moments to analyze the interactions of an electromagnetic field with a structure consisting of wires and surfaces in free space or over a ground plane. The analysis is accomplished by solving the electric field integral equation (EFIE) [19] and/or magnetic field integral equation (MFIE) [19] which impose boundary conditions at the surface of the structure. The excitation can be a voltage source, or an incident plane wave. A structure such as an aircraft is represented by a model that may consist of perfectly or imperfectly conducting wires and smooth surfaces, non-radiating networks, transmission lines, lumped element loading and a ground plane that may be either a perfect or an imperfect conductor [22]. The output may include currents flowing on the structure, near electric and magnetic field strength at locations specified by the user, radiated (far) electric field strength at observation angles specified by the user, and input impedance at the excitation source.

The EFIE is well suited for thin wire structures of small or vanishing volume, while the MFIE is more attractive for structures which enclose a significant volume, especially those having large smooth surfaces. NEC thus uses EFIE for wires and MFIE for surfaces in the structure on which the current is to be determined [22]. However, the implementation of the solution of the MFIE in NEC is not as advanced or highly-developed as NEC's solution of the EFIE. Hence NEC is much more satisfactory for solving structures consisting of interconnections of wires, by solving the EFIE, than for solving for current flowing on patches of surfaces by solving the MFIE. Wire-grid models of aircraft will be used in this thesis, and hence in this chapter the discussion of the theoretical basis of NEC will be restricted to EFIE solution.

Several assumptions are used in NEC to simplify the solution [22,29,40]. These assumptions are valid only if the model is created following the modelling guidelines outlined in the NEC user's manual [22]. These guidelines will be presented and explained later in this chapter. The method of moments [14] is a technique for reducing a linear equation such as an integral equation or an integro-differential equation to a system of linear algebraic equations. In this case, the linear equation is the electric field integral equation. The basic principle of this method will be illustrated in this chapter. In addition, the implementation of the moment method in NEC to solve for the induced current will be discussed in detail.

2.1 Numerical Solution of the Electric Field Integral Equation (EFIE) for Induced Currents

The Numerical Electromagnetics Code employs the Method of Moments to solve the Electric Field Integral Equation (EFIE) for currents induced by sources or incident fields on an arbitrary structure consisting of thin wires in free space or over a ground plane. Once the induced currents are determined, finding near and far fields is a quite straight-forward procedure using integral equations that relate the current distribution to the resulting electromagnetic fields [22].

Pocklington's Equation [41] is an integral equation that expresses the unknown current on a perfectly-conducting wire in terms of the known exciting electric field by enforcing boundary conditions on the surface of the wire.

This section is devoted to the derivation of Pocklington's Equation followed by its numerical solution based on the moment method.

2.1.1 Pocklington's Integral Equation

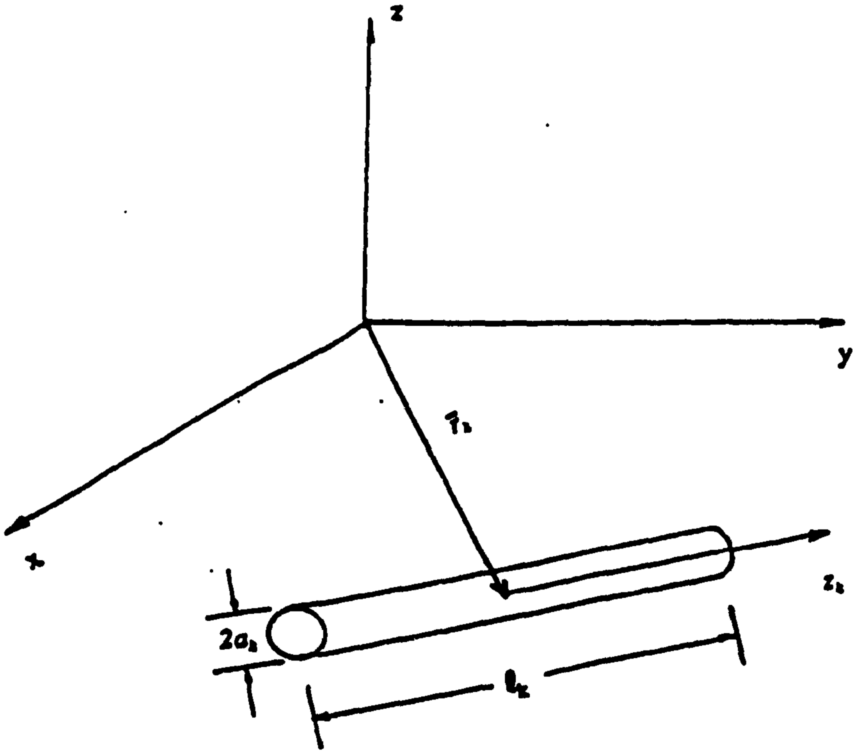

Fig. 2.1 A wire member of a wire-grid structure in the global coordinates.

Fig. 2.1 shows a perfectly-conducting wire which is a member of a wire-grid structure and has a length ℓ_k, and a radius a_k. The vector $\bar{r}_k$ is the position vector of the center of the wire. It is convenient to introduce local cylindrical coordinates for the wire in which z_k is the unit vector in the axial direction of the wire. Assume that the wire is excited by an electric field. Then an electric current is induced on the surface of the wire. This current in turn acts as a radiation source and the electromagnetic field it radiates is called secondary field, to distinguish it from the exciting field which is referred to as primary field $\bar{E}^{pri}$. The secondary field can be expressed as

$$\bar{E}^{sec}(\bar{r}) = -j\omega\bar{A} - \nabla\Phi \tag{2.1}$$

where $\bar{r}$ is the position vector of the field point, $j = (-1)^{1/2}$, ω is the angular frequency, Φ is the electric scalar potential and $\bar{A}$ is the vector potential due to the induced current.

From the Lorentz condition, we have

$$\Phi = -\frac{1}{j\omega\mu_o\varepsilon_o}\nabla\cdot\bar{A} \tag{2.2}$$

where μ_o and ε_o are the permeability and permittivity in free space, respectively. Thus the secondary field $\bar{E}^{sec}(\bar{r})$ can be rewritten as

$$\bar{E}^{sec}(\bar{r}) = -j\omega\bar{A} + \frac{1}{j\omega\mu_o\varepsilon_o}[\nabla(\nabla\cdot\bar{A})] \tag{2.3}$$

In the local coordinates, the vector potential due to the induced current on the kth wire is given by

$$\bar{A}_k(\bar{r}) = \frac{\mu_o}{4\pi}\int_{-\ell_k/2}^{+\ell_k/2}\int_0^{2\pi}\bar{J}_k(z_k',\phi_k')\,\hat{z}_k\frac{e^{-j\beta R}}{R}a_k d\phi_k' dz_k' \tag{2.4}$$

where: $\beta = 2\pi/\lambda$ and λ is the wavelength; $\bar{J}_k(z_k',\phi_k')$ is the density of the induced surface current on the k^{th} wire; a_k is the radius of the k^{th} wire; l_k is the length of the k^{th} wire; R is the distance between the observation point and the current source point. Primed coordinates such as z_k' and ϕ_k' are used to denote the coordinates with respect to the source, whereas unprimed coordinates are reserved for observation points.

Since the wire is assumed to be perfectly conducting, the total tangential electric field on the surface of the wire must be zero,

$$\bar{E}_{\tan}^{total}(\rho_k = a_k) = \bar{E}_{\tan}^{pri}(\rho_k = a_k) + \bar{E}_{\tan}^{sec}(\rho_k = a_k) = 0 \qquad (2.5)$$

where ρ_k is the radial distance from the wire axis, and the subscript "tan" is used to denote the tangential component of the field. It follows from Eq.(2.5) that

$$\bar{E}_{\tan}^{sec}(\rho_k = a_k) = -\bar{E}_{\tan}^{pri}(\rho_k = a_k) \qquad (2.6)$$

Assumptions are made to simplify the analysis. If the radius of the wire is much less than the wavelength ($a \ll \lambda$) and the wire length ($a \ll \ell$), it is reasonable to assume that:

1. the current density $\bar{J}$ has only the axial component and the transverse component can be neglected;
2. the axial current density is not a function of the azimuthal angle ϕ;
3. the current can be represented by a filament on the wire axis; and
4. the boundary condition on the electric field need be enforced in the axial direction only.

These assumptions are known as the "thin-wire assumptions".

The first three assumptions lead to a simple representation of the surface current.

$$2\pi a_k \bar{J}_k(z_k', \phi_k') = I_k(z_k')\,\hat{z}_k \tag{2.7}$$

or

$$\bar{J}_k(z_k', \phi_k') = \frac{1}{2\pi a_k} I_k(z_k')\,\hat{z}_k \tag{2.8}$$

where $I_k(z_k')$ is assumed to be an equivalent filamentary current source on the wire axis.

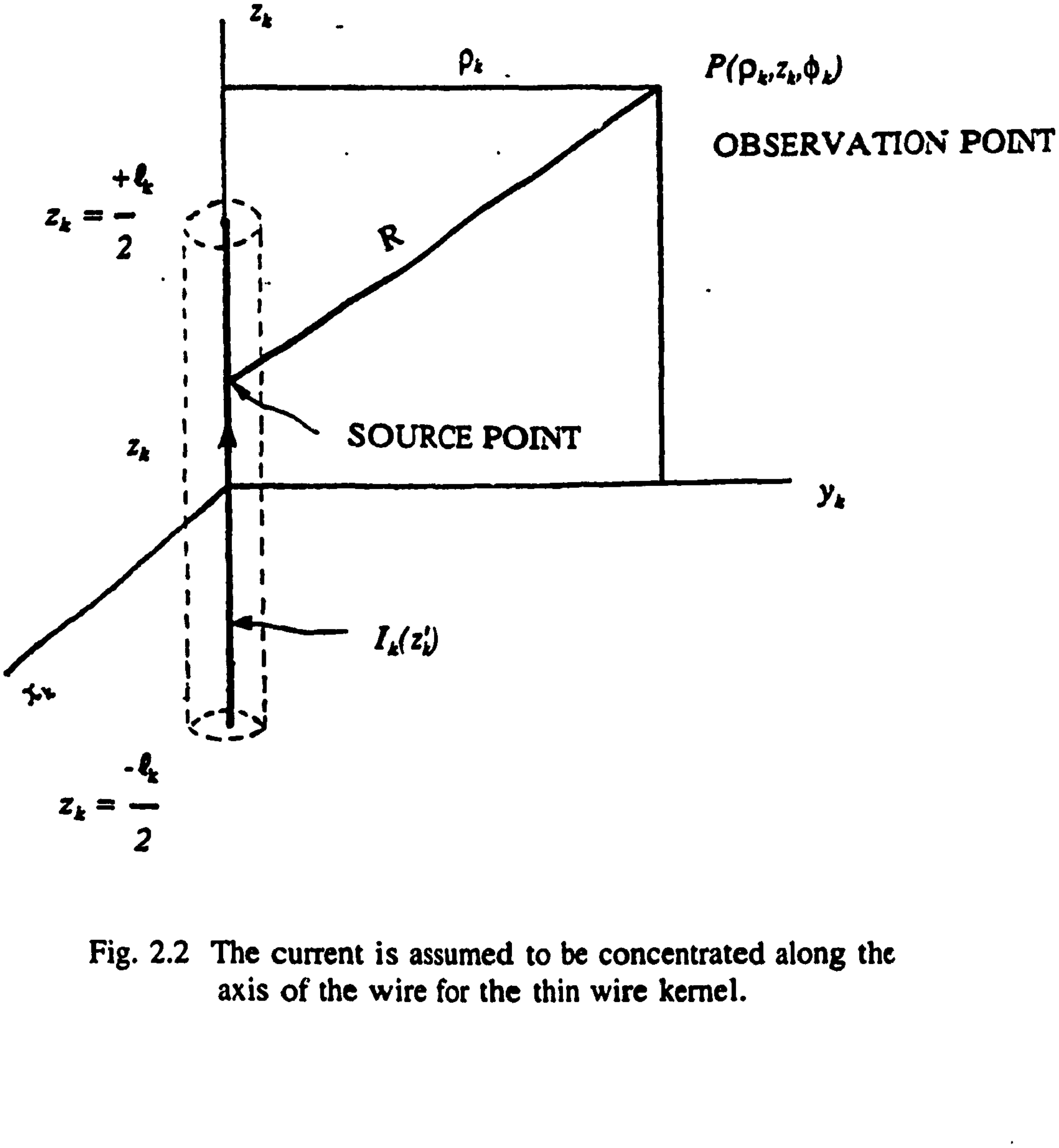

Fig. 2.2 The current is assumed to be concentrated along the axis of the wire for the thin wire kernel.

Thus, the vector potential reduces to

$$\bar{A}_k = A_k\hat{z}_k = \frac{\mu_o}{4\pi}\int_{-\ell_k/2}^{+\ell_k/2}\left[\frac{1}{2\pi a_k}\int_0^{2\pi} I_k(z'_k)\,\frac{e^{-j\beta R}}{R}\,a_k d\phi'_k\right] dz'_k\hat{z}_k \tag{2.9a}$$

$$= \mu_o \int_{-\ell_k/2}^{+\ell_k/2} I_k(z'_k)\, G(\bar{r}, z'_k)\, dz'_k\hat{z}_k \tag{2.9b}$$

In the local cylindrical coordinates, the observation point is defined as (ρ_k, z_k, ϕ_k) and is equal to $(\bar{r} - \bar{r}_k)$. The kernel $G(\bar{r}, z_k')$ in Eq.(2.9 b) is defined as

$$G(\bar{r}, z'_k) = \frac{1}{2\pi}\int_0^{2\pi} \frac{e^{-j\beta R}}{4\pi R}\, d\phi'_k \tag{2.10}$$

in which the distance between the source point and the observation point is given by

$$R = \sqrt{\rho_k^2 + (z_k - z'_k)^2} \tag{2.11}$$

In the local rectangular coordinates of the kth wire, the secondary field in Eq. (2.3) due to current on the kth wire can be expressed as

$$\bar{E}_k^{sec} = -j\omega\mu_o\bar{A}_k + \frac{1}{j\omega\epsilon_o}\left(\hat{x}_k\frac{\partial}{\partial x_k} + \hat{y}_k\frac{\partial}{\partial y_k} + \hat{z}_k\frac{\partial}{\partial z_k}\right)\frac{\partial A_k}{\partial z_k} \tag{2.12}$$

It is desired to obtain the component of the $\bar{E}$ field in certain directions such as the axial directions of the wires because the thin wire assumptions have simplified the boundary condition on the wire surface to that the total electric field needs to be zero in the axial direction only.

Let $\hat{s}$ be an unit vector in an arbitrary direction. The component of the electric field due to the k^th wire in the $\hat{s}$ direction at the observation point is given by

$$
\begin{aligned}
E_{s_k}^{sec} &= \hat{s}\cdot\bar{E}_k^{sec} \\
&= -j\omega\mu_o\hat{s}\cdot\bar{A}_k+\frac{1}{j\omega\epsilon_o}\hat{s}\cdot\left(\hat{x}_k\frac{\partial}{\partial x_k}+\hat{y}_k\frac{\partial}{\partial y_k}+\hat{z}_k\frac{\partial}{\partial z_k}\right)\frac{\partial A_k}{\partial z_k}
\end{aligned}
\tag{2.13}
$$

It is recognized that the second dot product on the right is the directional derivative in direction $\hat{s}$ at the observation point [42], therefore

$$E_{s_k}^{sec} = -j\omega\mu_o\hat{s}\cdot\bar{A}_k+\frac{1}{j\omega\epsilon_o}\frac{d}{ds}\frac{\partial A_k}{\partial z_k} \tag{2.14}$$

Using $\beta=\omega(\mu_o\epsilon_o)^{1/2}$, Eq. (2.14) can be rewritten as

$$E_{s_k}^{sec} = -\frac{j}{\omega\epsilon_o}\left(\beta^2\hat{s}\cdot\bar{A}_k+\frac{d}{ds}\frac{\partial A_k}{\partial z_k}\right) \tag{2.15}$$

Substituting Eq. (2.9 b) into the equation above gives

$$E_{s_k}^{sec} = -\frac{j}{\omega\epsilon_o}\left(\beta^2\hat{s}\cdot\hat{z}_k+\frac{d}{ds}\frac{\partial}{\partial z_k}\right)\int_{-\ell_k/2}^{+\ell_k/2} I_k(z_k')\,G(\bar{r},z_k')\,dz_k' \tag{2.16}$$

Since

$$\frac{\partial G}{\partial z_k} = -\frac{\partial G}{\partial z_k'}\ , \tag{2.17}$$

equation (2.16) is simplified to

$$E_{s_k}^{sec} = \frac{j}{\omega\epsilon_o}\left(-\beta^2\hat{s}\cdot\hat{z}_k+\frac{d}{ds}\frac{\partial}{\partial z_k'}\right)\int_{-\ell_k/2}^{+\ell_k/2} I_k(z_k')\,G(\bar{r},z_k')\,dz_k' \tag{2.18}$$

If the wire-grid structure consists of N wires, then the $\hat{s}$ component of the total secondary field will be

$$E^{sec}_{s_{total}} = \sum_{k=1}^{N} \overline{E}^{sec}_{s_k} \cdot \hat{s} \qquad (2.19)$$

For observations at the surface of the ith wire, the boundary condition of Eq. (2.6) under the fourth assumption of the "thin wire assumptions" requires that sum of the secondary fields due to all the wires plus the primary (source) field has an axial component equal to zero. Since the vector component of interest here is the axial component of the ith wire, the unit vector $\hat{s}$ at the observation point or the "match point" on the surface of the ith wire is equal to $\hat{z}_i$.

$$\overline{E}^{sec}_{total} \cdot \hat{z}_i + \overline{E}^{pri} \cdot \hat{z}_i = 0 \qquad (2.20)$$

or

$$\sum_{k=1}^{N} \overline{E}^{sec}_{k} \cdot \hat{z}_i + \overline{E}^{pri} \cdot \hat{z}_i = 0 \qquad (2.21)$$

Accordingly, *ds* in Eq. (2.18) is replaced by dz_i. It follows that

$$\begin{aligned} \sum_{k=1}^{N} \frac{j}{\omega\epsilon_o} \Big(-\beta^2 \hat{z}_i \cdot \hat{z}_k \int_{-l_k/2}^{+l_k/2} I_k(z_k') G(\overline{r}, z_k') \, dz_k' \\ + \frac{d}{dz_i} \int_{-l_k/2}^{+l_k/2} I_k(z_k') \frac{\partial}{\partial z_k'} G(\overline{r}, z_k') \, dz_k' \Big) \\ = -\overline{E}^{pri} \cdot \hat{z}_i \end{aligned} \qquad (2.22)$$

Equation (2.22) is referred to as Pocklington's integral equation.

2.1.2 Extended Thin Wire Kernel (EK) Option

When the wire radius is too thick to satisfy thin wire condition ($a << \lambda$), the above assumptions may lead to unreliable results. The Numerical Electromagnetics Code offers an option to take into account the thickness of the wire. With the EK option the current is assumed to be uniformly distributed around the circumference of the wire rather than concentrated along the axis of the wire, meaning that condition 3 in the thin wire assumptions is somewhat relaxed.

The extended thin wire kernel is obtained by modifying the expression for the distance between the source point and observation point R in the kernel G.

$$R = \sqrt{\rho_k^2 + a_k^2 - 2a_k\rho_k\cos(\phi_k - \phi_k') + (z - z_k')^2} \tag{2.23}$$

Because of the symmetry of the wire, the electric field due to a current density which is assumed uniform in ϕ does not vary with ϕ_k. For simplicity, let $\phi_k = 0$, then R reduces to

$$R = \sqrt{\rho_k^2 + a_k^2 - 2a_k\rho_k\cos\phi_k' + (z_k - z_k')^2} \tag{2.24}$$

and the full kernel is denoted as G_{EK}.

$$G_{EK}(\bar{r}, \phi_k', z_k') = \frac{1}{2\pi}\int_0^{2\pi} \frac{e^{-j\beta\sqrt{\rho_k^2 + a_k^2 - 2a_k\rho_k\cos\phi_k' + (z_k - z_k')^2}}}{\sqrt{\rho_k^2 + a_k^2 - 2a_k\rho_k\cos\phi_k' - (z_k - z_k')^2}}\, d\phi_k'$$

(2.25)

Since the integral above cannot be evaluated in closed form, a numerical approximation is used by NEC to evaluate the full kernel G_{EK}.

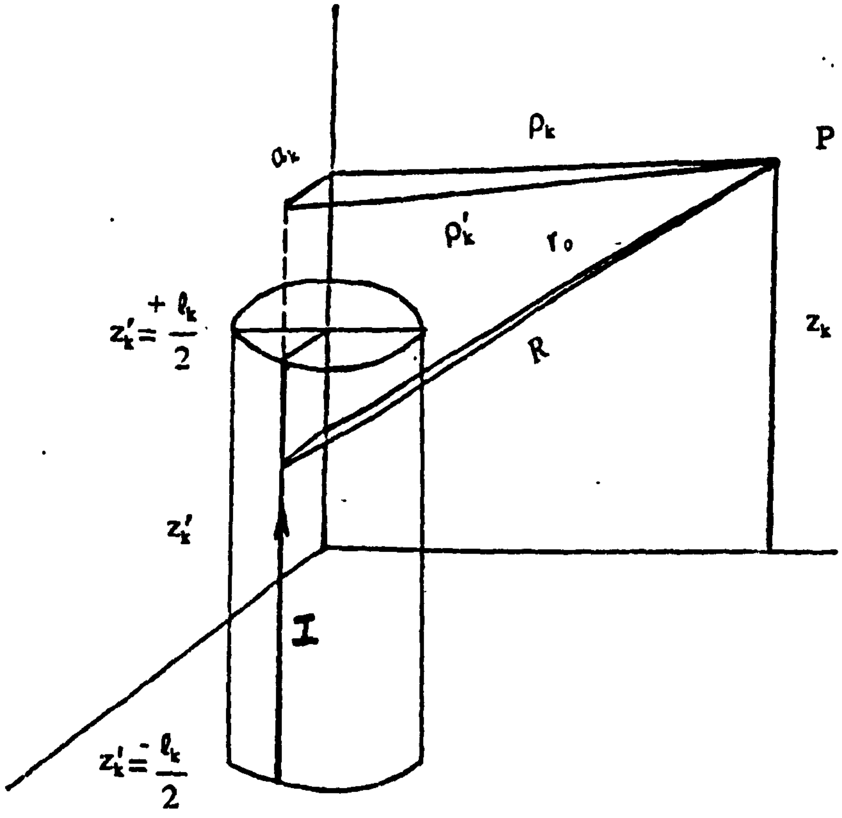

Fig. 2.3 The extended thin wire kernel.

The integrand in the G_{EK} expression is expanded as a MacLaurin series in powers of radius a_k, about $a_k = 0$, with terms of a_k^4 and higher neglected [43]. G_{EK} is evaluated by integrating over ϕ_k' the series representation. This results in

$$G_{EK}(\overline{r},\phi_k',z_k') = \frac{e^{-j\beta D}}{D}\left[1-\frac{a_k^2}{2D^2}(1+j\beta D) + \frac{\rho^2 a_k^2}{4D^4}\left(-\beta^2 D^2+3(1+j\beta D)\right)\right] \tag{2.26}$$

where

$$D = \sqrt{\rho_k^2+(z_k-z_k')^2} \tag{2.27}$$

It is recognized that the first term in the series representation of the full kernel is simply the reduced thin wire kernel G.

With either the thin-wire kernel or the extended kernel, the electric field integral equation (Eq. 2.22) reduces to a one-dimensional integral equation. The integral equation, however, in general is very difficult to solve by calculus and hence further simplification is needed. One way of simplifying the integral equation is to reduce it to a system of linear algebraic equations with complex-valued coefficients using the method of moments, and then solve the system of linear equations with numerical methods, as explained below.

2.2 Numerical Solution Based on the Method of Moments

NEC solves the Pocklington's integral equation numerically by the method of moments. This section deals with the principles of the moment method and the implementation of this technique in NEC to obtain the solution for the current.

2.2.1 Method of Moments

The method of moments is a technique for approximating a linear equation such as an integral equation with a system of linear algebraic equations with unknown complex-valued coefficients. In the case of the Pocklington's integral equation, the unknown function is the current *I*. The moment method replaces the problem of finding *I* by calculus with that of finding a set of unknown complex-valued coefficients. This is accomplished by approximating *I* with a series expansions of basis functions with unknown amplitudes.

A linear equation has a general form

$$\mathfrak{L}\ (A) = \Gamma \tag{2.28}$$

where $\mathfrak{L}$ is a linear operator, A is an unknown response, Γ is the known excitation. If Eq. (2.22) is viewed as a linear equation having the form of Eq. (2.28), then $\mathfrak{L}$ is the integral operator mapping the total current I_{total} into scattered fields, $\mathfrak{L}$(A) is the scattered field due to I_{total} , and Γ is the negative of the source (primary) field on the surface of the wire.

$$\mathfrak{L}\ [I_{total}] = -E^{pri} \tag{2.29}$$

The current I_{total} is approximated by a sum of N linearly independent basis functions b_k defined over the wire structure,

$$I_{total} \approx \sum_{k=1}^{N} I_k b_k \tag{2.30}$$

where I_k are the unknown complex-valued coefficients to be determined.

Substitution of the representation of the current as a sum of basis functions into the linear operator equation gives

$$\mathcal{L}\,[\sum_{k=1}^{N} I_k b_k] \approx -E^{pri} \tag{2.31}$$

Due to linearity, the above equation can be rewritten as

$$\sum_{k=1}^{N} I_k \mathcal{L}[b_k] \approx -E^{pri} \tag{2.32}$$

It is necessary to determine the coefficients $\{I_k\}$ such that the approximate equation is enforced in some way.

Before proceeding to solve for the N current coefficients, we first define the terms "inner product", "orthogonal", and "norm" or "length" for functions. The inner product of 2 functions f and g is defined as

$$\langle f, g\rangle = \int f(z)\, g^{*}(z)\, dz \tag{2.33}$$

where $g^{*}(z)$ is the complex conjugate of $g(z)$. If f and g are orthogonal to each other, then $\langle f,g\rangle = 0$. The norm or length of a function, say f, is given by

$$||f|| = \sqrt{\int |f|^2 dz} \tag{2.34}$$

which is the same as

$$||f|| = \sqrt{\langle f, f\rangle} \tag{2.35}$$

For an approximate equation such as Eq. (2.32), the "residual" is defined as the difference between the left and the right hand side terms. Thus the residual for Eq. (2.32) is given by

$$r(z) = \sum_{k=1}^{N} I_k \mathcal{L}(b_k) + E^{pri} \qquad (2.36)$$

Next we introduce the "projection theorem". If a function *f(z)* is represented in terms of "weight functions" $\{w_k(z)\}$ as

$$f(z) \approx \sum_{k=1}^{N} \alpha_k w_k(z) \qquad (2.37)$$

The "projection theorem" states that choosing $\{ \alpha_k \}$ such that the "norm" of the residual is minimized can be achieved by making the residual

$$r(z) = f(z) - \sum_{k=1}^{N} \alpha_k w_k(z) \qquad (2.38)$$

orthogonal to each of the "weight functions", that is, making

$$\langle r(z), w_j(z) \rangle = 0 \qquad j = 1, \ldots, N \qquad (2.39)$$

It follows that

$$\sum_{k=1}^{N} \langle w_k, w_j \rangle \alpha_k = \langle f, w_j \rangle \qquad j = 1, \ldots, N \qquad (2.40)$$

Applying the "projection theorem" to Eq. (2.32), one can choose the "weight functions" to be the fields produced by the current basis function b_k:

$$w_k(z) = \mathcal{L}(b_k(z)) \qquad (2.41)$$

then find $\{ I_k \}$ to satisfy Eq. (2.32), rewritten as

$$\sum_{k=1}^{N} w_k(z)\, I_k = -E^{pri} \tag{2.42}$$

This is like Eq. (2.37). According to Eq. (2.40), one can write

$$\sum_{k=1}^{N} \langle w_k, w_j \rangle I_k = -\langle E^{pri}, w_j \rangle \qquad j = 1,\ldots,N \tag{2.43}$$

or in full

$$\sum_{k=1}^{N} \langle \mathcal{L}(b_k), \mathcal{L}(b_j) \rangle I_k = -\langle E^{pri}, \mathcal{L}(b_j) \rangle \qquad j = 1,\ldots,N \tag{2.44}$$

Although this procedure will minimize the norm of the residual $\|r(z)\|$, it is not usually done for integral equations because it involves three integrals. Instead, we do the following.

Recall that the residual in our case is given by

$$r(z) = \sum_{k=1}^{N} I_k \mathcal{L}(b_k) + E^{pri} \tag{2.45}$$

we represent $\sum_{k=1}^{N} \mathcal{L}(b_k) I_k$ in terms of the weight functions $\{ w_j \}$ as

$$p(z) = \sum_{j=1}^{N} w_j P_j = \sum_{k=1}^{N} \mathcal{L}(b_k)\, I_k \tag{2.46}$$

we will choose the coefficients to minimize $\|r_p(z)\|$, where

$$r_p(z) = \sum_{j=1}^{N} w_j p_j - \sum_{k=1}^{N} \mathcal{L}(b_k)\, I_k \tag{2.47}$$

Hence we choose

$$\sum_{j=1}^{N} \langle w_j, w_m \rangle p_j = \langle \sum_{k=1}^{N} \mathcal{G}(b_k)\, I_k, w_m \rangle \quad m = 1, \ldots, N \tag{2.48}$$

or in the matrix form

$$[Z_w]\,(p_j) = [Z_{\mathcal{G}}]\,(I_k) \tag{2.49}$$

Then we represent E^{pri} in terms of $\{ w_j \}$ as

$$q(z) = \sum_{j=1}^{N} w_j q_j \approx E^{pri}(z) \tag{2.50}$$

and choose the coefficients to minimize $\| r_q(z) \|$, where

$$r_q(z) = \sum_{j=1}^{N} w_j q_j - E^{pri}(z) \tag{2.51}$$

It follows that

$$\sum_{j=1}^{N} \langle w_j, w_m \rangle q_j = \langle E^{pri}, w_m \rangle \quad m = 1, \ldots, N \tag{2.52}$$

or in the matrix form

$$[Z_w]\,(q_j) = (e^{s}) \tag{2.53}$$

Then Eq. (2.45) is approximated by the space-spanned-by-the-$\{ w_j \}$-weight-functions as

$$\begin{aligned} r(z) \approx r_w(z) &= -\{ \sum_{j=1}^{N} w_j p_j + \sum_{j=1}^{N} w_j q_j \} \\ &= -\{ \sum_{j=1}^{N} w_j (p_j + q_j) \} \end{aligned} \tag{2.54}$$

To minimize $\| r_w(z) \|$ within the space-spanned-by-the-weight-functions we can obviously choose $p_j = -q_j$. It follows from Eq. (2.49) and Eq. (2.53) that

$$[Z_w]\,(p_j) = [Z_g]\,(I_k) \tag{2.55}$$

Since $p_j = -q_j$,

$$-[Z_w]\,(q_j) = [Z_g]\,(I_k) \tag{2.56}$$

From Eq. (2.53), it follows that

$$[Z_g]\,(I_k) = -(e^{s}) \tag{2.57}$$

Note that applying Eq. (2.57) to solve Eq. (2.32) does not minimize $\|r(z)\|$. Instead, it minimizes $\|r_w(z)\|$, that is, the residual in the space-spanned-by-the-weight-functions. If the $\{\, w_j(z) \,\}$ functions are chosen so that they are capable of a high-quality representation of the $\{\, \mathscr{L}(b_k) \,\}$ functions and of the $E^{pri}(z)$ functions, then minimizing $\|r_w(z)\|$ will be close to minimizing $\|r(z)\|$. We must design the basis functions $\{\, b_k \,\}$ so that the fields they give rise to, $\{\, \mathscr{L}(b_k) \,\}$, are "smooth" so that they can be accurately represented by simple weight functions $\{\, w_j \,\}$. It is usually sufficient to ensure that $I(z)$ is continuous and that the charge density - dI/dz is continuous to have "smooth enough" $\{\, \mathscr{L}(b_k) \,\}$ functions. For simplicity, let us use a single conducting wire as an example. The wire is divided into N segments. Choosing

$$w_j(z) = \delta(z_j) \qquad j = 1,\ldots,N \tag{2.58}$$

where z_j are the centers of the wire segments will simplify the evaluation of the matrix elements. This is known as the "point matching" method. In practice, it has been found that "point matching" is sufficient if the functions $\{\, \mathscr{L}(b_k) \,\}$ are smooth functions. Indeed, these functions are smooth if the $\{\, b_k \,\}$ are chosen to make $I(z)$ and dI/dz continuous.

2.2.2 Basis Functions for the Current used in NEC

The basis functions used for the approximation of the current can strongly affect both the solution accuracy and efficiency. In order to simplify the inner product integral and ensure that the interaction matrix Z will be well-conditioned [48], the basis functions I_i in NEC are defined in a localized subsection of the structure rather than the whole structure.

The current on each wire segment is represented by three terms, namely, a constant, a sine and a cosine as

$$I_i(z_i') = A_i + B_i \sin\beta(z_i'-z_{io}') + C_i \cos\beta(z_i'-z_{io}') \qquad |z_i'-z_{io}'| < \frac{\Delta_i}{2} \tag{2.59}$$

where β is the wave number ($2\pi/\lambda$), z_i' is the local coordinate in the axial direction of segment i, z_{io}' is the axial coordinates of the center of segment i, Δ_i is the length of segment i, and A_i, B_i, and C_i are three complex-valued unknown constants. This choice of expansion is justified by the rapid solution convergence [44,45] and the fact that the fields of the sinusoidal currents are easily evaluated in closed form [9].

If a wire is subdivided into *M* segments, there will be *3M* unknowns to be solved in order to obtain the solution for the current on the wire. This calls for *3M* linear equations to be derived. Point-matching method in which electric field boundary condition is forced to be satisfied at the centers of each segment provides *M* equations. Within a wire, continuity of current and charge density is enforced at segment junctions. It follows that if there are M segments in the wire, there are *2(M-1)* such conditions at segment junctions and hence *2(M-1)* equations. The remaining two equations come from the conditions on current and charge at the two wire ends.

For a free end,

$$I_i(z_i')\big|_{z_i' \text{ at end}} = -(\hat{z}_i'\cdot\hat{n}_c)\frac{1}{\beta}\frac{J_1(\beta a_i)}{J_0(\beta a_i)}\frac{\partial}{\partial z_i'}\left[I(z_i')\big|_{z_i' \text{ at end}}\right] \tag{2.60}$$

where a_i is the radius of the wire segment, β is the wave number J_0 and J_1 are Bessel functions of order 0 and 1, $\hat{n}_c$is the unit vector normal to the end cap, $\hat{z}_i$ is the unit vector in the reference direction. This free end condition was derived by Poggio [46] to account for the effect of the current flowing onto the end caps of a wire of finite radius resulting in a non-zero current at the wire end.

On the other hand, if the segment end is part of a junction of two or more wires, then two conditions must be imposed, namely, the King-Wu charge density constraint [47] and the continuity of current (Kirchoff's Current Law or KCL).

T.T. Wu and R.W.P. King had derived a relationship for the charge distribution on the wires adjacent to a junction. The total charge in the vicinity of the junction is assumed to distribute itself on individual wires according to the wire radii, neglecting local coupling effects, according to [47]

$$\frac{\partial I_i(z_i')}{\partial z_i'}\Big|_{z_i' \text{ at junction}} = \frac{Q}{\ln\left(\frac{2}{\beta a_i}\right)-\gamma} \tag{2.61}$$

where Q is related to the charge in the vicinity of the junction and is constant for all wires at the junction, a_i is the radius of the i^{th} wire, and γ is the Euler's constant (γ = 0.5772). Thus for a junction formed by n connected wires, the King-Wu constraint on the junction is given by

$$P_1 \frac{\partial I_1(z_1')}{\partial z_1'} \Big|_{z_1' \text{ at jun.}} = P_2 \frac{\partial I_2(z_2')}{\partial z_2'} \Big|_{z_2' \text{ at jun.}} = \cdots = P_n \frac{\partial I_n(z_n')}{\partial z_n'} \Big|_{z_n' \text{ at jun.}} \tag{2.62}$$

where

$$P_i = \ln\left(\frac{2}{\beta a_i}\right) - \gamma \tag{2.63}$$

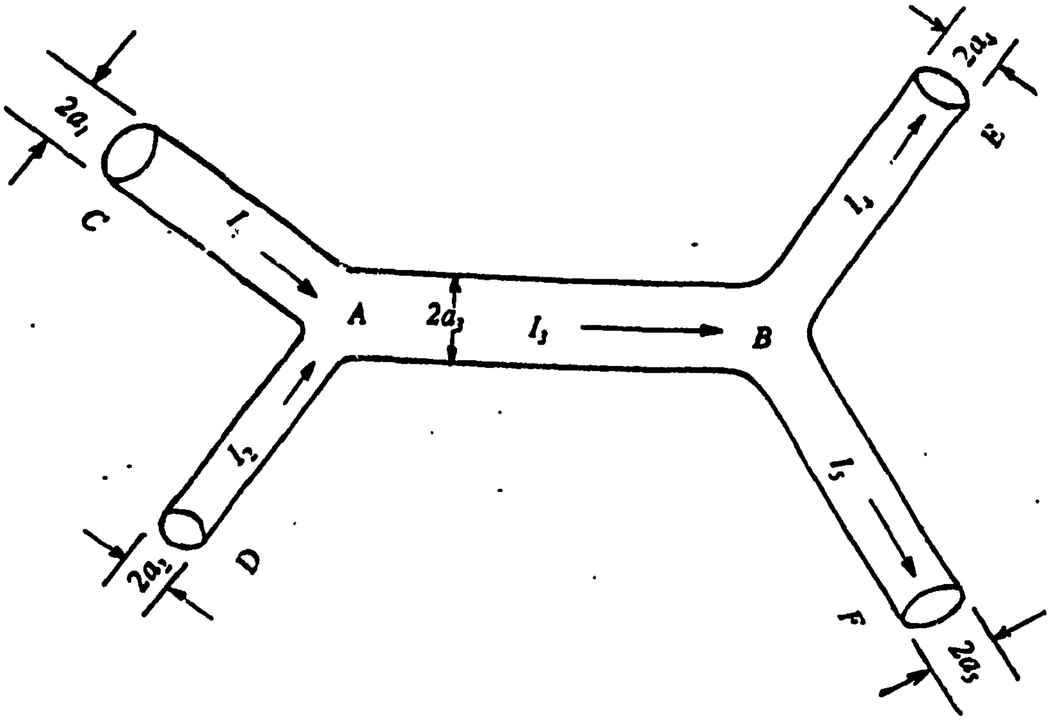

Fig. 2.4 A wire structure consisting of 5 segments and 2 junctions.

As an example, assume there is structure consisting of five wires forming two junctions as shown in Fig. 2.4, with each wire having only one segment. Since the current basis function defined on each wire has 3 unknown coefficients, there are totally 15 coefficients to be determined and hence 15 linear equations are required in this case.

At the two junctions, two equations are obtained from KCL and 6 equations come from King-Wu constraint :

KCL :

$$I_1(z_1')\big|_{z_1' \text{ at junct. } A} + I_2(z_2')\big|_{z_2' \text{ at junct. } A} = I_3(z_3')\big|_{z_3' \text{ at junct. } A} \tag{2.64}$$

$$I_4(z_4')\big|_{z_4' \text{ at junct. } B} + I_5(z_5')\big|_{z_5' \text{ at junct. } B} = I_3(z_3')\big|_{z_3' \text{ at junct. } B} \tag{2.65}$$

King-Wu constraint :

$$P_1 \cdot \frac{\partial I_1(z_1')}{\partial z_1'}\Big|_{z_1' \text{ at junction } A} = P_3 \frac{\partial I_3(z_3')}{\partial z_3'}\Big|_{z_3' \text{ at junction } A} \tag{2.66}$$

$$P_2 \frac{\partial I_2(z_2')}{\partial z_2'}\Big|_{z_2' \text{ at junction } A} = P_3 \frac{\partial I_3(z_3')}{\partial z_3'}\Big|_{z_3' \text{ at junction } A} \tag{2.67}$$

$$P_4 \frac{\partial I_4(z_4')}{\partial z_4'}\Big|_{z_4' \text{ at junction } B} = P_3 \frac{\partial I_3(z_3')}{\partial z_3'}\Big|_{z_3' \text{ at junction } B} \tag{2.68}$$

$$P_5 \frac{\partial I_5(z_5')}{\partial z_5'}\Big|_{z_5' \text{ at junction } B} = P_3 \frac{\partial I_3(z_3')}{\partial z_3'}\Big|_{z_3' \text{ at junction } B} \tag{2.69}$$

$$P_2 \frac{\partial I_2(z_2')}{\partial z_2'}\Big|_{z_2' \text{ at junction } A} = P_3 \frac{\partial I_3(z_3')}{\partial z_3'}\Big|_{z_3' \text{ at junction } A} \tag{2.70}$$

$$P_2 \frac{\partial I_2(z_2')}{\partial z_2'}\Big|_{z_2' \text{ at junction } A} = P_3 \frac{\partial I_3(z_3')}{\partial z_3'}\Big|_{z_3' \text{ at junction } A} \tag{2.71}$$

There are 4 free ends with a free end charge condition for a total of 4 equations:

$$I_1(z_1')\big|_{z_1' \text{ at end } C} = -(\hat{z}_1'\cdot\hat{n}_C)\,\frac{1}{\beta}\,\frac{J_1(\beta a_1)}{J_0(\beta a_1)}\,\frac{\partial}{\partial z_1'}\,[I_1(z_1')\big|_{z_1' \text{ at end } C}] \tag{2.72}$$

$$I_2(z_2')\big|_{z_2' \text{ at end } D} = -(\hat{z}_2'\cdot\hat{n}_C)\,\frac{1}{\beta}\,\frac{J_1(\beta a_2)}{J_0(\beta a_2)}\,\frac{\partial}{\partial z_2'}\,[I_2(z_2')\big|_{z_2' \text{ at end } D}] \tag{2.73}$$

$$I_4(z_4')\big|_{z_4' \text{ at end } E} = -(\hat{z}_4'\cdot\hat{n}_C)\,\frac{1}{\beta}\,\frac{J_1(\beta a_4)}{J_0(\beta a_4)}\,\frac{\partial}{\partial z_4'}\,[I_4(z_4')\big|_{z_4' \text{ at end } E}] \tag{2.74}$$

$$I_5(z_5')\big|_{z_5' \text{ at end } F} = -(\hat{z}_5' \cdot \hat{n}_c)\,\frac{1}{\beta}\,\frac{J_1(\beta a_5)}{J_0(\beta a_5)}\,\frac{\partial}{\partial z_5'}\,[I_5(z_5')\big|_{z_5' \text{ at end } F}] \tag{2.75}$$

The remaining 5 equations are from enforcing boundary condition stated by the Pocklington's integral equation at the "match points" defined at the centers of the segments.

For an *M* segment structure in a general case, the NEC code is formulated in such a way that the KCL and the charge density constraints are implicitly enforced to form an *MxM* moment method matrix rather than a *3Mx3M* matrix.

2.2.3 Computational Procedure for Solving the Matrix Equation for Current

The *N* current-amplitude unknowns for a model consisting of *N* segments are determined by solving for the current matrix [A] in the matrix equation

$$[Z]\ [A] = [E] \tag{2.76}$$

where [Z] is an *NxN* matrix and is referred to as the interaction matrix, [A] is an *Nx1* vector made up of *N* current amplitude unknowns, [E] is an *Nx1* vector with elements representing the negative of the axial component of the exciting electric field at the match points.

Note that the elements in the matrix equation are complex-valued. Element z_{ij} in matrix [Z] corresponds to the axial component of the electric field at the match point of segment i produced by the normalized current basis function associated with segment j. If the exciting source is a voltage source located at segment i, all elements in vector [E] except e_i are zero. The non-zero element e_i is the negative of the applied electric field strength on segment i given by

$$e_i = -\frac{V}{\Delta_i} \tag{2.77}$$

where V is the strength of the voltage source, Δ_i is the length of segment i.

The Gauss-Doolittle method [41] is employed to solve the linear equation system. The matrix [Z] is first decomposed into a product of two matrices [Z] = [L][U], where [L] is a lower triangular matrix and [U] is an upper triangular matrix. This results in [L][U][A] = [E]. NEC then solves [L][F] = [E] by forward substitution. Then [U][A] = [F] and [A] can be readily obtained by backward substitution.

2.3 NEC Modelling Guidelines

Since NEC depends on several basic assumptions involving the wire length, radius, and the interconnections of wire segments, the guidelines are recommended for the need to satisfy these assumptions [22]. In addition, some guidelines are based on the experience gained from the application of NEC to a specific set of problems that has reliable measured data for comparison purposes [26,29]. It is convenient to classify the guidelines into three groups : individual wire guidelines, wire junction guidelines, and wire spacing guidelines.

2.3.1 Individual Wire Guidelines

This group includes guidelines concerning the length and radius of each individual wire segment of the model.

2.3.1.1 Wire Segment Length

Since NEC solves the electric field integral equation with the method of moments, it is required that the lengths of the segments must be small compared to the wavelength in order to obtain accurate results. The length of a segment is restricted to the order of one-tenth of a wavelength. A significant loss of accuracy will happen if segments are allowed to be as long as $\lambda/5$. Segments as long as 0.14λ may be acceptable on long wires or non-critical parts of the a structure, according to Burke [49].

It is stated in the "modelling guidelines" that wire segments shorter than $\lambda/10$ are fully acceptable. A warning is issued for a segment between $\lambda/10$ and $\lambda/5$. Segments longer than $\lambda/5$ are considered to be in error.

2.3.1.2 Wire Radii

The second concern about each individual wire is its radius. As mentioned earlier in this chapter, NEC solutions are based on the "thin wire assumptions". These assumptions are valid only when the wires are electrically thin. It is specified in the NEC User's Guide that the wire radius a must satisfy $2\pi a/\lambda << 1$ or $a << 0.159\ \lambda$. The "modelling guidelines" consider wires thinner than 0.01λ to be fully satisfactory. "Warnings" are given for wires between 0.01λ and 0.0333λ. Wires thicker than 0.0333λ are considered in errors. Thus the error criterion is about 20 percent of the User's Guide's figure.

2.3.1.3 Segment Length to Radius Ratio

In addition to the individual wire length and radius, the ratio of segment length to radius must also be examined. A wire is not thin if its radius is not small compared to its length. It is recommended that the ratio of segment length to radius should be greater than 8 for best results, and should not be less than 2, with the "thin wire kernel" being implemented. If the "extended thin wire kernel" (EK) is used, the restriction is relaxed to 2 for good results, and 0.5 for acceptable results. The guidelines assume that the EK option is employed and hence issues an "error" for a wire with $\Delta/a < 0.5$, where Δ is the segment length. A "warning" is given if $0.5 < \Delta/a < 2$.

2.3.2 Wire Junction Guidelines

The second category of the guidelines is related to wire junctions. Three types of problems fall into this category.

2.3.2.1 Segment Length and Radius at Junctions

Recall that NEC basis functions enforce King-Wu condition at wire junctions. This condition on junction charge, however, is inadequate if the ratio of the largest to the smallest wire radius is too large. The largest acceptable ratio is 10. Ratios less than 5 are recommended.

Besides the radius difference, the segment length difference between the wires forming a particular junction is preferred to be small to ensure no great dissimilarity among those wires both in length and radius. The guidelines specify that the ratio of the longest to the shortest segment length must be less than five.

2.3.2.2 Match Point Errors

One of the most important guidelines not to be violated is that when two wire segments have a common end point and form an angle other than 180°, the match point at the center of either wire must lie outside the volume of the other wire. Violation of this guideline may result in non-physical currents being computed. An example of a match point "error" is shown in Fig. 2.5 . A "warning" is issued if the center of a segment is located within half a radius of another wire's surface.

2.3.2.3 Segment to Radius Ratio at Junctions

Since the "extended thin wire kernel" is not used for segments which are part of junctions, the segment length to radius ratio must be strictly greater than 2 for those segments according to the "thin wire kernel" criteria. Thus segments with $\Delta/a < 2$ are considered in error. The "warning" region is specified as $2 < \Delta/a < 6$.

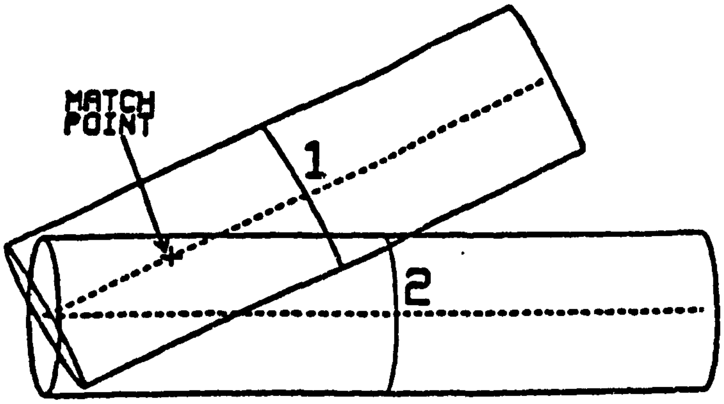

Fig. 2.5 An example of a match point error [40].

2.3.3 Wire Spacing Guidelines

The last category is concerned with the spacing between the wires. This kind of problems arising in a wire-grid model is primarily due to a misleading representation of the model. In the process of designing the wire grid, it is a common practice to represent each wire by its center line regardless of its radius. In fact, every wire has a non-zero radius and it is important to make sure that the spacings between wires are large enough to avoid physical overlap or contact when the wire radii are taken into account. The axial-current-only assumption on a wire segment is not valid if perpendicular wires closely pass one another. The thin wire assumption is not valid either if a wire passes an open-circuited endpoint of another wire in an extremely close distance.

2.3.3.1 Crossed Wires

In NEC, two wires segments are electrically joined only if they have a common segment end-point. It follows that a "crossed wires error" occurs if two wires are physically crossed but the crossing point is not a segment end-point.

2.3.3.2 Overlapping Wires

"Overlap errors" arise when two wires are so closely spaced that they are physically overlapping if viewed as cylinders in space. NEC will give incorrect results if this kind of errors exist. Therefore, wires axes pass closer than the sum of the wire radii will result in "overlap errors".

2.3.3.3 Near Misses

"Near misses" occur when wires that are parallel or nearly-parallel almost touch each other. Although they are not overlapping, the assumption that the current is uniformly spread about the periphery of the wire is not valid and hence constitutes an error. Ideally, wires should be spaced at least several wire diameters apart. In a typical wire-grid model, however, a great number of wires do not meet this requirement. The guidelines issue "warnings" rather than "errors" for this kind of problem to urge the user to modify the wire-grid so that the wires are farther apart. The criterion on which warning issues are based is that wire axes pass closer that 1.5 times the sum of the wire radii.

2.3.3.4 Proximity Errors

Finally, "proximity errors" are referred to the situation that the end-points of wires are too close to one another. Strong capacitive coupling that could exist between the wires may not be correctly computed by NEC in this case. "Errors" will be given when wire end-points are closer than the sum of the wire radii. For wire endpoints closer than 1.5 times the sum of the wire radii, proximity "warnings" will be issued.

Table 2.1 summarizes the above NEC modelling guidelines.

Table 2.1 Summary on NEC Modelling Guidelines [40]

Δ = segment length
a = wire radius
λ = wavelength

INDIVIDUAL SEGMENTS	WARNING	ERROR
segment length	$\lambda/10 < \Delta < \lambda/5$	$\Delta > \lambda/5$
radius	$30 < \lambda/a < 100$	$\lambda/a < 30$
segment to radius ratio	$0.5 < \Delta/a < 2$	$\Delta/a < 0.5$
JUNCTIONS	**WARNING**	**ERROR**
segment length ratio		$\Delta_{big}/\Delta_{small} > 5$
radius ratio	$5 < a_{big}/a_{small} < 10$	$a_{big}/a_{small} > 10$
segment to radius ratio	$2 < \Delta/a < 6$	$\Delta/a < 2$
match point	segment center within half a wire radius of another wire's surface.	segment center lies within the volume of another wire.
WIRE SPACING	**WARNING**	**ERROR**
crossed wires		wire axes cross
overlaps		wire axes pass closer than the sum of the wire radii
near misses	wire axes pass closer than 1.5 times the sum of the wire radii	
proximity	wire endpoints closer than 1.5 times the sum of the wire radii	wire endpoints closer than the sum of the wire radii

2.4 Impedance Loading

A practical structure may contain imperfectly conducting parts. For a wire structure, the effects of finite wire conductivity may become important in the two following ways: 1. the wire does indeed have a finite conductivity or the skin depth is large enough compared to the wire radius that the assumption of vanishing electric field along the wire is no longer strictly valid; 2. there are impedance loads located at discrete points along the wire [10]. The first situation can be treated as a distributed load along the wire, whereas the second case corresponds to lumped loading. Either of these two cases can be modelled using the electric field integral equation for perfectly conducting wires with a suitable modification of the boundary condition enforcing along the wire. The boundary condition is generalized by taking into account the additional effect of the voltage drop in terms of the particular value of impedance located there, by modifying Eq. (2.20) to read

$$\hat{z}_i \cdot [\vec{E}^{sec}_{total} + \vec{E}^{pri}] = Z_w(z_i)\, I(z_i) \ , \qquad (2.78)$$

where $\hat{z}_i$ is the tangent unit vector at z_i on the ith wire and $Z_w(z_i)$ is the impedance per-unit-length at z_i. The matrix equation becomes

$$\sum_{j=1}^{N} g_{ij}\alpha_j = -E_i^{pri} + \frac{Z_{wi}}{\Delta_i} I_i \qquad i=1,\ldots,N \qquad (2.79)$$

where g_{ij} = the interaction matrix elements, α_j = amplitude of basis function j, E_i^{pri} = the primary field on segment i, I_i = current at the center of segment i, Z_{wi} = total impedance of segment i, Δ_i = length of segment i, N = number of segments.

The current is assumed to be essentially constant with value I_i over the length of the segment. This assumption is reasonable for the electrically short segments used in the integral equation solution.

If the load is a lumped element, Z_{wi} is computed from the circuit equations. For a distributed load, Z_{wi} represents the impedance of a length Δ_i of wire. The distributed impedance for a round wire of finite conductivity is given by

$$Z_{wi} = \frac{j\Delta_i}{a_i}\sqrt{\frac{\omega\mu}{2\pi\sigma}}\left[\frac{B_{er}(q)+jB_{ei}(q)}{B'_{er}(q)+jB'_{ei}(q)}\right] \tag{2.80}$$

where $q = (\omega\mu\sigma)^{1/2}\, a_i$, a_i = wire radius, σ = wire conductivity, B_{er}, B_{ei} = Kelvin functions. The above expression allows for the limited penetration of the field into an imperfect conductor [22].

2.5 Conclusion

With the increase in computational power in modern computer systems and the development of the supporting software, the potential power of NEC can be fully exploited to the extent that simulation and analysis of electromagnetic problems may be done with highly complicated wire-grid models with over 1000 wire segments and in a reasonable period of time. In this thesis, NEC was employed for obtaining a complete diagnosis of coupling modes on two large aircraft. In order to do that, complex wire-grid models of the two aircraft were developed using model creation software available at EMC Laboratory, and NEC runs were executed as frequency sweeps with fine frequency stepping. The numerical results were then processed and analyzed with NEC supporting software.

The next chapter introduces the methodology together with the application software modules used for the study of coupling modes in this thesis.

CHAPTER 3

APPLICATION METHODOLOGY

It is important for any engineering work to be done in a logical and systematic way. Good methodology leads to accurate and reliable results. The study of electromagnetic coupling with computer simulation is a complicated task that requires extensive computational and analytical processes and a complete software system to support the creation, visualization, and verification of wire-grid models, ranging from the preparation of NEC input files to the analysis of output data. Over the years, EMC Laboratory has been engaged in developing such a system and a standard procedure has been established for the study of radiation and scattering problems involving large conducting objects such as aircraft and ships [28]. A comprehensive illustration of the software modules used at the EMC Lab is shown in Fig. 3.1. Software modules that were used in the thesis will be discussed in this chapter.

3.1 Model Preparation

The first step of computer simulation is to generate the computer model of the object under study for use with the Numerical Electromagnetic Code. Wire-grid modelling techniques are employed to generate a model in which the solid conducting surface of an object is represented by a conducting wire-grid. The objective is to develop a model such that its electromagnetic properties closely resemble those of the real object. The accuracy of the model is affected by the following factors : the model's shape, the interconnections

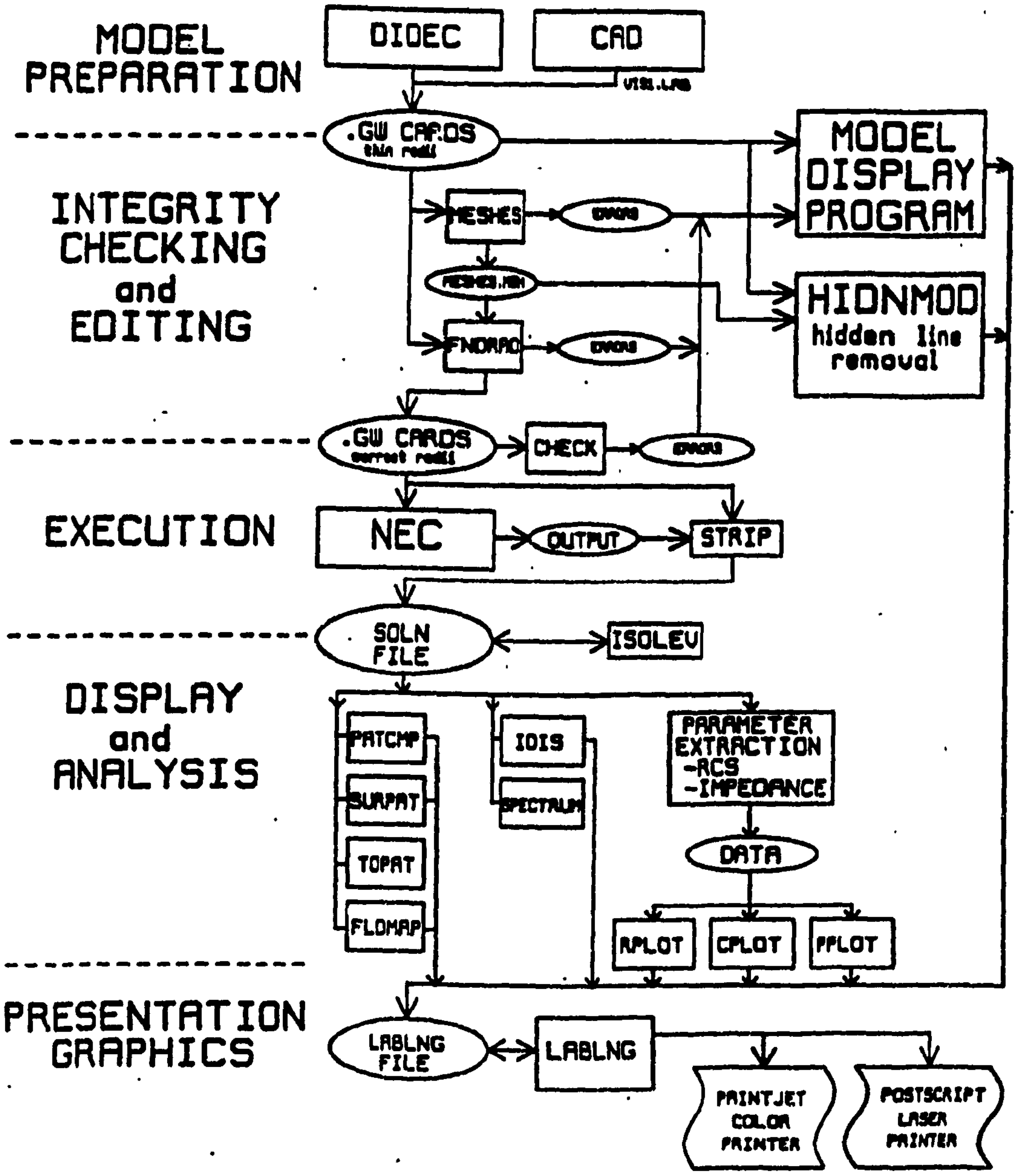

Figure 3.1 The EMC Lab application software modules [28].

of wire segments, the wire radii, and the degree of conformity to the modelling guidelines.

Table 3.1 Wire-Grid Guidelines [26]

1. Use a rectangular grid of wires oriented parallel to edges, with wires along edges.
2. Choose the segment length equal to $\lambda/10$ at the highest frequency of the band. Keep the area of the grid cells comparable to $(\lambda/10)^2$.
3. Keep grid cells square. Keep the cell area constant, hence segment length constant, throughout the grid.
4. Provide elegant transitions.
5. Put wires where current is expected to flow.
6. Avoid wires meeting at very shallow angles.
7. Keep the center of any segment outside the volume of any other segment.
8. Use the "equal-area rule" radius.
9. All meshes in the grid must have peripheries longer than $\lambda/25$.

The starting point of designing a wire-grid model is to obtain the shape of the model. This is usually done by digitizing the three-view drawings of the object being modelled. The next step is to determine a "nominal" segment length based on the modelling guidelines summarized in Table 2.1 such that the model is useful in the desired frequency range. This is because the segment lengths are required to be much shorter than the wavelength at the operating frequency as stated in the modelling guidelines. The surface of the object is then to be covered with square mesh cells of side length equal to the nominal segment length. Since the surfaces of the object in general are not rectangular, it is impossible to have square mesh cells throughout the surfaces. In regions where the surface tapers, triangular cells are to be used to reduce the number of squares and provide a smooth transition of wire density. In some other regions such as regions surrounding the antenna feed points, smaller mesh cells and shorter segments are used, because large currents are expected to flow in these regions and a denser wire-grid can model the current flow more accurately. One should also try to avoid designing wires that meet at very shallow angles, because this kind of wire arrangement can easily result in the center of a wire segment being inside the volume of another wire segment and lead to a "match point" error described in Section 2.3.2.2. All meshes in the grid should have peripheries longer than 1/25 of the wavelength. Electrically small meshes could lead to ill-conditioned interaction matrix in NEC's moment method formulation as explained in [49]. The model is completed after the wire radii are determined according to the "equal area rule" [24] which will be explained shortly. Finally, the resulting model will be verified. If errors are found, it will be modified until a satisfactory model is obtained. Wire-grid designing guidelines are summarized in Table 3.1.

3.1.1 Program DIDEC

Program DIDEC (DIgitize, Display, Edit and Convert) [31] is an interactive program that was written to provide an efficient means of obtaining the (x,y,z) coordinates of wire endpoints on the object surface from three-view drawings while displaying the results. These points, however, are not necessarily the vertices on the wire-grid model. It is not unusual that many points on the object surface are digitized to give a geometrically high fidelity model. The actual vertices are then chosen based on smooth interpolation curves generated by Computer-Aided Drafting (CAD) programs from the digitized points. Once the inter-connections between the wire segments in the grid are completed, the next step is to assign a radius value to each wire segment. The generalized "equal area rule" [24,33] is used to calculate the wire radii. The reason for using the "equal area rule" is as follows.

3.1.2 The Rule for Determining the Wire Radii

Lee, Marin, and Castillo [24] compare the inductance-per-unit-length and the capacitance-per-unit-length of a continuous surface with those corresponding to a wire-grid. They suggest that if the inductance-per-unit-length and the capacitance-per-unit-length of the wire-grid are the same as those of the continuous surface, then the wire-grid would truly represent the continuous surface. The problem is how to choose the radii for the wires forming the grid to satisfy the two conditions. However, their result for the capacitance shows that a wire radius cannot be unambiguously specified. Consequently, we can only choose the wire radius such that the inductance constraint is satisfied. The resulting choice is called the "equal area rule", as explained below.

A surface as in Fig.3.2 (a) is represented by an orthogonal grid of square cells, the "equal area rule" states that the wire radius is chosen so that the total area of the wire surface in one orthogonal direction is equal to the area of the surface that the wire-grid represents. It follows that

$$2\pi a\Delta = \frac{A_1}{2} + \frac{A_2}{2} \tag{3.1}$$

and hence the radius is

$$a = \frac{A_1}{4\pi\Delta} + \frac{A_2}{4\pi\Delta} \tag{3.2}$$

However, in a complex wire-grid model such as the one of an aircraft, many of the grid cells are of irregular shapes, direct application of Eq. (3.2) to this kind of cells will give unsatisfactory results [33]. An improved radius rule is therefore desirable. The "generalized equal area rule" is based not only on the area of the two meshes adjacent to a given wire, but on the distance around the periphery of each mesh as well. Thus in Fig. 3.2 (b), a wire of length Δ is a member of 2 meshes, of areas A_1 and A_2, and peripheral lengths L_1 and L_2. The radius *a* of the wire is calculated using the equation

$$a = \frac{A_1}{4\pi\Delta}\left[\frac{\Delta}{L_1/4}\right] + \frac{A_2}{4\pi\Delta}\left[\frac{\Delta}{L_2/4}\right] = \frac{A_1}{\pi L_1} + \frac{A_2}{\pi L_2} \tag{3.3}$$

Compared to Eq.(3.2), Eq.(3.3) has an additional weight factor for each term in the equation. Note that the weight factors are unity for square mesh cells. The role of the weight factor is to ensure that for three-sided mesh cells, or for irregular four-sided mesh cells, reasonable radius values are obtained.

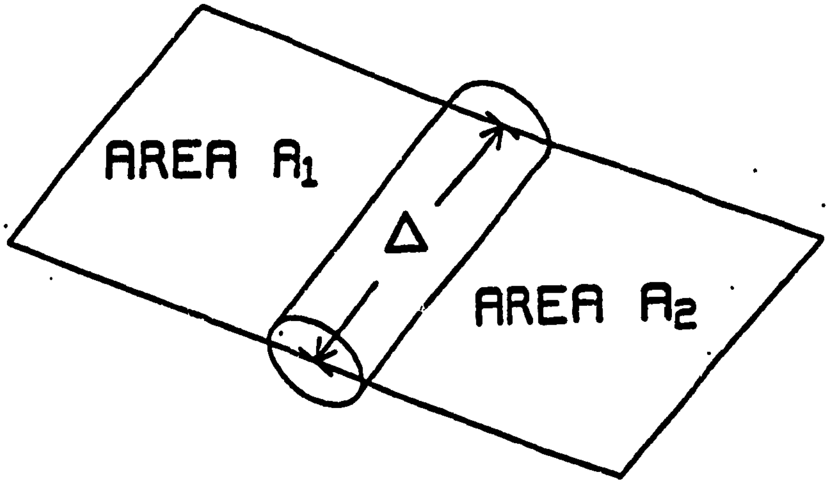

(a) A wire in an orthogonal grid of square cells.

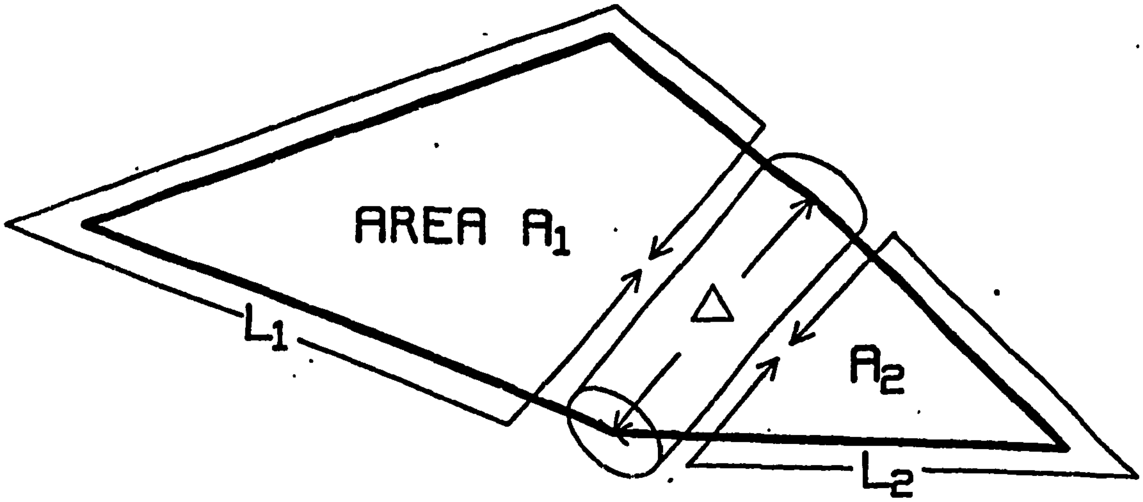

(b) A wire in a general grid.

Figure 3.2 Determination of a wire radius according to the adjoining mesh cells [33].

3.1.3 Radius Calculation Using MESHES and FNDRAD

The process of calculating the wire radii for a complex wire-grid model is tedious and prone to error if done manually. It is for this reason that the rule is implemented in computer programs to facilitate the calculations. As illustrated in Fig. 3.1, the computerized procedure begins with identifying all the meshes existing in the grid using a program called MESHES [33]. MESHES determines for each wire of the grid the wires that form meshes with that wire. The meshes information is then used as the input to the program FNDRAD [33] to compute the radius for each wire according to the generalized "equal area rule" mentioned above. When the wire radii are obtained, a complete model is created. This is, however, by no means the end of the model creation process. Very often, the newly created model contains gross errors such as missing wires, and duplicated wires, or does not perfectly meet the geometry requirements of NEC. Thus the model must be verified and corrected if necessary before it is used to run NEC.

3.2 Model Verification

Modelling errors can be categorized into two kinds: gross errors and NEC-incompatibility errors. Gross errors can usually be identified by visual inspection using a model display program, whereas NEC-incompatibility errors are more difficult to detect and for a complex model one must resort to a computer program to systematically and thoroughly examine the model in order to find out all possible violations of the NEC modelling guidelines. Computer programs such as CHECK and MESHES are also useful for finding certain gross errors.

3.2.1 Gross Error Identification

The first phase of model verification is to check for gross errors. Gross errors in a model can be found by visualization with the help of model display software modules.

In addition to being a model generation program, DIDEC is also a model display program. The model can be viewed from different angles so that the user can inspect his model from a most convenient view angle. Moreover, the user can zoom-in a specific region of the model to get a clearer picture of that region. This is particularly useful when there are complicated wire interconnections in small regions.

Another program specially written for model display is called MODEL. This program works with any files that have a standard NEC input file format. Special features of MODEL include drawing the wires as cylinders with radii corresponding to the values specified in the input file, displaying or highlighting part of the model that is specified by the user with a list of wire tag numbers. Drawing the wires as cylinders with appropriate radii help visualize some problems such as a match point error, where the match point of a wire lies inside the volume of another wire. The feature of highlighting part of the model can help identify errors such as missing wires and missing junctions. For example, program MESHES mentioned above generates group files listing the wires according to the number of meshes to which the wires belong. Displaying the model with the wires belonging to one group highlighted could show us whether the inter-connections of the wires are correct.

There is yet another model display program called HIDNMOD (HIDdeN MODel). This program is particularly useful when MODEL gives a confusing drawing for a complex, three-dimensional wire-grid model because all the wires appear to be on the same plane. HIDNMOD draws the model with the hidden wires removed, resulting in a much simpler and easy to understand wire-grid picture. With the help of this program, the user can inspect his model to see whether it is exactly the design he wants. Fig. 3.3 compares the display of the EC-130 wire-grid model using MODEL with the one using HIDNMOD.

3.2.2 Program CHECK

It is insufficient to verify a model by visual inspection. A sound model must be in compliance with the NEC modelling guidelines. This is very difficult, if not impossible to check manually for complicated models. A computer program called CHECK [21] was therefore written to systematically examine a wire-grid model and identify violations of NEC modelling guidelines. A brief description of NEC modelling guidelines has been given in Chapter 2. The criteria were summarized in Table 2.1.

Program CHECK examines the model in three consecutive phases, each phase deals with one group of guidelines. If a violation is found, the program will issue a warning or an error depending on the severity of the violation. In addition, CHECK does statistics on segment lengths in the model and computes the model's useful frequency range.

After all the errors found by CHECK have been cleared, we are ready to solve the model with the NEC program. The wire segment representing the feed element of the active antenna is excited by a voltage source. In the case of the EC-130, the passive antennas are loaded by impedances to simulate the real termination conditions and to compute the induced voltages.

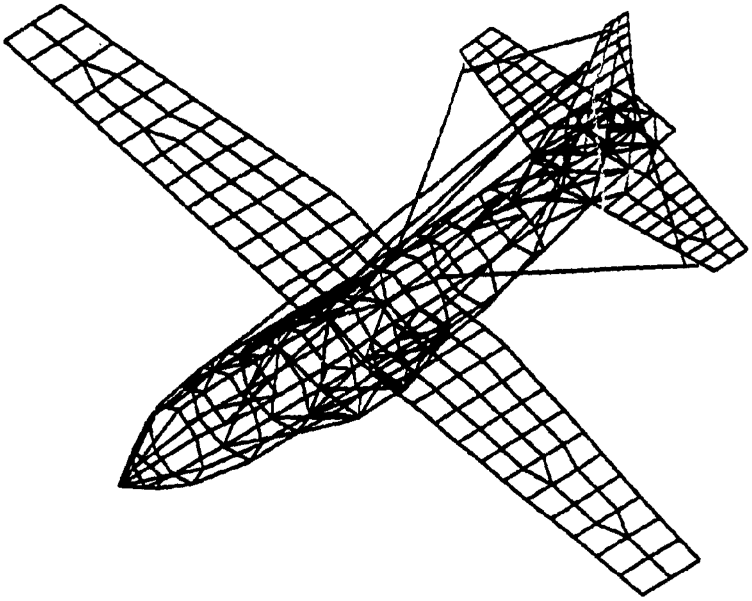

(a) Using MODEL.

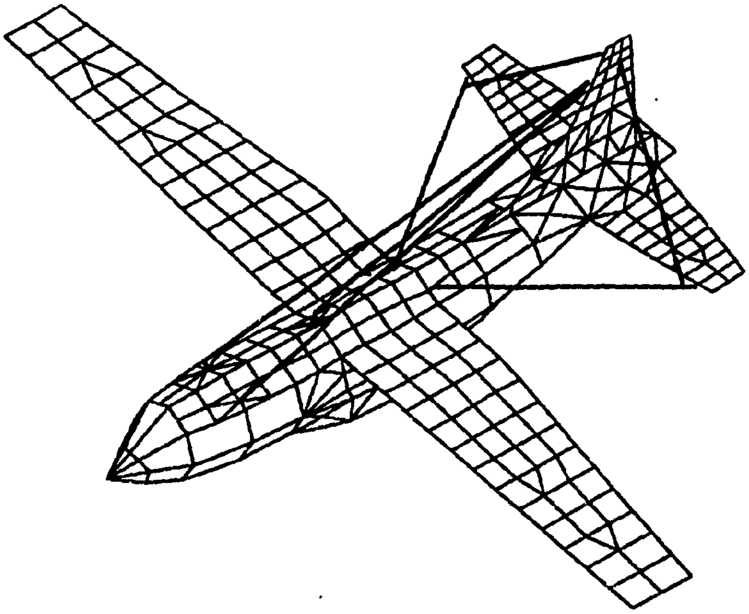

(b) Using HIDNMOD.

Fig. 3.3 Wire-grid models displayed using MODEL and HIDNMOD.

3.3 Loading the Passive Antennas and Calculating the Induced Voltages

An aircraft monopole antenna is usually fed by a coaxial cable penetrating the aircraft's surface. The other end of the coaxial cable is connected to a tuner and a transmitter in the transmitting mode, or to a receiver in the receiving mode, as shown in Figure 3.4. The cable usually has a 50 Ω characteristic impedance, so does the transmitter. The antenna impedance varies with frequency. For signal transmission, in order to have a matched impedance looking from the transmitter toward the antenna, a tuner is required. The function of the tuner is to cancel the reactive part of the antenna-plus-cable impedance and transform the resistive part into 50 Ω. However, the impedance looking from the antenna terminals toward the combination of cable, tuner and transmitter is generally unknown. Its value could be very low or very high. In the receiving mode, the antenna is connected to the receiver via the coaxial cable. When tuned to the designated frequency of the desired signals, the receiver usually has a 50 Ω impedance to match the cable. Its impedance at other frequencies is unknown because specifications for the receivers are not available. Thus we can only consider representative cases: short-circuit, 50 Ω, and open-circuit. These cases represent a low impedance load, a 50 Ω matched load, and a high impedance load, respectively. Simulation of the antenna feed in a wire-grid model for input to NEC is done as follows.

The antenna "terminals" are always connected by a wire "segment". For an exciting antenna, this segment is called the "feed segment". It is excited in series with a 1 V source. For a passive antenna, the segment connecting the terminals models a short-circuit load on the antenna. For a 50 Ω load, a resistance of 50 Ω is placed in series with the segment across the antenna terminals. To model an open-circuit across the antenna terminals, we do not remove the segment across the terminals because NEC does not model the capacitive coupling of the gap between a wire end and the adjacent wire-grid very well. Instead, we load the segment with a series resistance of 1 MΩ. This is illustrated in Fig. 3.5.

On the EC-130 aircraft, there are five external wire antennas. In this thesis, one antenna at a time is chosen to be the active antenna excited by a voltage source. The rest are referred to as passive antennas which are subject to the electromagnetic field radiated from the active antenna. For a passive antenna whose terminal is loaded by an impedance, the induced voltages across its terminals can be calculated by simply multiplying the induced current (computed by NEC) on the wire segment connecting the terminals by the corresponding load impedance.

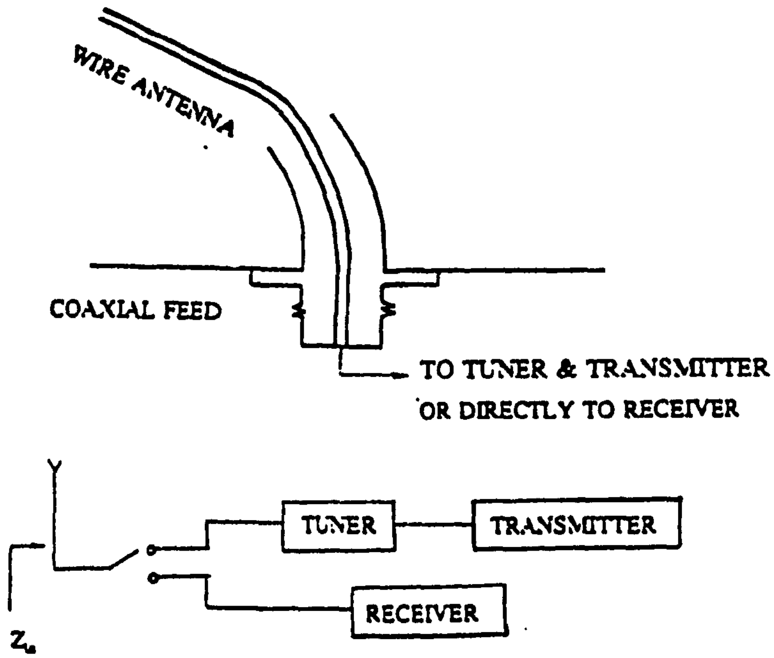

Fig. 3.4 Coaxial feed of a wire antenna on an aircraft.

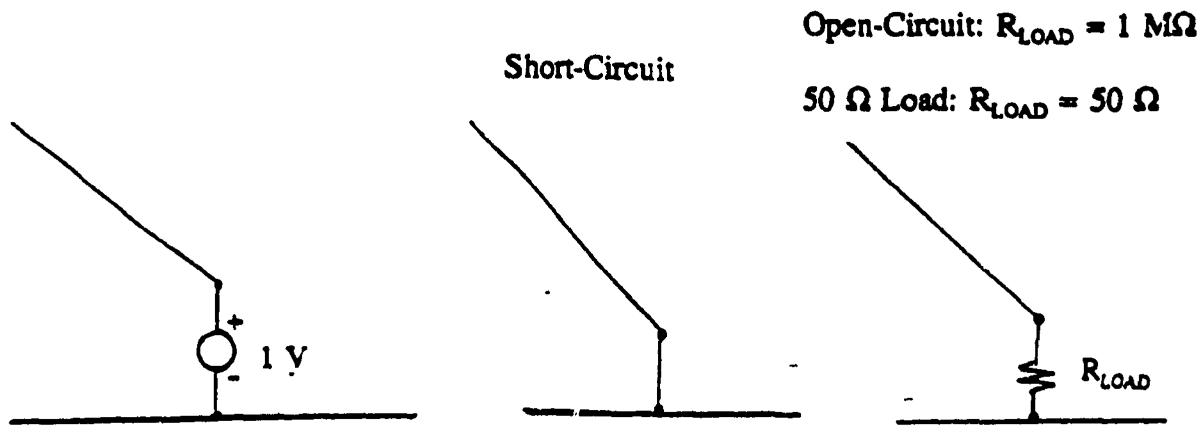

(a) Active Antenna (b) Passive Antenna

Fig. 3.5 Representation of the feed or the base of a wire antenna in a wire-grid model.

3.4 Calculating the Radiation Pattern

The radiated (far) field produced by an active antenna can be calculated in NEC by using the RP command and specifying the desired directions. Calculating the far field in multiple directions enables one to plot a set of radiation patterns characterizing the performance of the antenna.

In this study, the far field is computed to produce radiation patterns for 21 "conical cuts" and 2 "elevation cuts" specified in the military standard MIL-A-9080 (USAF) [43]. $E_\theta(\theta,\phi)$ and $E_\phi(\theta,\phi)$ are evaluated at $\theta = 0°, 25°, 37°, 45°, 53°, 60°, 66°, 72°, 78°, 84°, 90°, 96°, 102°, 108°, 114°, 120°, 127°, 135°, 143°, 150°$ and $180°$, each for $0° \leq \phi \leq 360°$. In addition, two "elevation cuts" are : $\phi = 0°$ and $90°$, each for $-180° \leq \theta \leq 180°$.

Volumetric patterns can be constructed based on the patterns computed at the 21 "conical cuts". A program called TDPAT (Three Dimensional PATtern) is used to plot this kind of pattern which provides a 3D view of the field strength distribution surrounding the radiator. For comprehensive radiation pattern analysis, it is not sufficient to plot the volumetric patterns only. As shown in Fig. 3.1, other pattern display programs are available. They include PATCMP for polar pattern plots and pattern comparisons, FLDMAP for color contour maps of all patterns, and SURPAT for another 3D representation of a pattern. These programs are effective tools for visualizing the distribution of field strength surrounding a radiating antenna, and comparing the radiated fields of different antennas or comparing computed and measured results calibrated to the same power level.

3.5 Output Analysis

Various software modules in Fig. 3.1 have been developed at EMC Laboratory for analysis of the numerical results obtained from running NEC. Without these software tools, the power of the NEC code will be difficult to exploit. For instance, NEC can compute the current on each wire segment of a complex wire-grid model, but it is very difficult for a user to "visualize" the distribution of current on the model by looking at the current magnitude and phase values which are tabulated in a NEC output file, especially if the model consists of hundreds of wire segments.

Major computer programs for processing NEC output data include impedance plotting, radiated power parameters calculation, current distribution plotting, and radiation pattern plotting programs. These programs support files with standard "solution file" format. A "solution file" is the processed version of a NEC output file which contains only the necessary data extracted from the NEC output file. The principles and uses of these application programs are briefly discussed below.

3.5.1 Program ISOLEV

ISOLEV (ISOtropic LEVel) [51] is a program written for computing useful statistical data related to the radiated field and power in a NEC solution. The statistics include maximum field strength, total radiated power, isotropic level, and three aircraft HF antenna assessment parameters, namely, the radiation pattern efficiency (R. P. efficiency), the percentage of power in the E_θ polarization ($\%E_\theta$), and the percentage of useful E_θ power (*Sub-%-*E_θ) [52,58] as described in the following.

The maximum field strength is the maximum value of radiated electric field computed by NEC at the angles specified in the military standard MIL-A-9080 (USAF).

The total radiated power is calculated by integrating power density over the sphere enclosing the aircraft. The time-average power density is given by

$$S(\theta,\phi)=\frac{E_\theta^2(\theta,\phi)+E_\phi^2(\theta,\phi)}{2\eta} \tag{3.4}$$

where E_θ and E_ϕ are the electric far field components which vary as $1/R$ and R is the distance between the radiator and the field point. Note that when the NEC program calculates the far field, the term $e^{-j\beta R}/R$ associated with the far field expression is dropped to give a unique field value for a given direction. Thus the field value can be thought of as being "normalized to the distance R". In effect, the field is being evaluated "at one meter" in volts/meter. From Eq.(3.4), it follows that the total radiated power can be expressed as

$$P = \int_{\theta=0}^{\pi}\int_{\phi=0}^{2\pi} \frac{E_\theta^2(\theta,\phi)+E_\phi^2(\theta,\phi)}{2\eta} R^2 d\phi \sin\theta d\theta \tag{3.5}$$

The total radiated power is independent of the distance R because E_θ and E_ϕ are inversely proportional to R. If the radiated power were distributed isotropically over all of space, the power density in all directions would be

$$S_{iso} = \frac{P}{4\pi(R)^2} = \frac{E_{iso}^2}{2\eta R^2} \tag{3.6}$$

where E_{iso} is the field strength in all directions. Therefore,

$$E_{iso} = \sqrt{\frac{\eta P}{2\pi}}\frac{1}{R} \tag{3.7}$$

E_{iso} is referred to as the isotropic level. When two radiation patterns in two solution files are to be compared, their field strengths are scaled so that their isotropic levels are the same.

The three aircraft HF antenna assessment parameters are defined as follows. The first parameter is the radiation pattern efficiency (R.P. efficiency) which is the percentage of the power radiated in a useful sector (θ=60° to 120°). This sector is defined based on the requirement for long range HF communications via ionospheric reflection within the manoeuvre envelope that aircraft usually encounter [52].

$$R.P.Eff. = \frac{\int_{\phi=0}^{2\pi}\int_{\theta=\pi/3}^{2\pi/3} [E_\theta^2(\theta,\phi)+E_\phi^2(\theta,\phi)]\sin\theta d\theta d\phi}{\int_{\phi=0}^{2\pi}\int_{\theta=0}^{\pi} [E_\theta^2(\theta,\phi)+E_\phi^2(\theta,\phi)]\sin\theta d\theta d\phi} x100\% \qquad (3.8)$$

The percentage of E_θ power is the ratio of the power radiated in the theta polarization to the total radiated power.

$$\%E_\theta = \frac{\int_{\theta=0}^{\pi}\int_{\phi=0}^{2\pi} E_\theta^2(\theta,\phi) d\phi \sin\theta d\theta}{\int_{\theta=0}^{\pi}\int_{\phi=0}^{2\pi} [E_\theta^2(\theta,\phi)+E_\phi^2(\theta,\phi)] d\phi \sin\theta d\theta} x100\% \qquad (3.9)$$

Radiated power in the theta polarization is desirable because in the ground wave propagating mode, the wave is guided by the surface of the earth, and the ϕ-polarized field (which is tangential to the earth surface) cannot be supported.

The last parameter for aircraft HF antenna evaluation is percentage of E_θ power in the useful sector (θ=60° to 120°)

$$SUB\text{-}\%E_\theta = \frac{\int_{\theta=\pi/3}^{2\pi/3}\int_{\phi=0}^{2\pi} E_\theta^2(\theta,\phi) d\phi \sin\theta d\theta}{\int_{\theta=0}^{2\pi}\int_{\phi=0}^{2\pi} [E_\theta^2(\theta,\phi)+E_\phi^2(\theta,\phi)] d\phi \sin\theta d\theta} x100\% \qquad (3.10)$$

3.5.2 Program PATCMP

PATCMP (PATtern CoMParison) is a program written for displaying radiation patterns or plotting two radiation patterns on the same axes for comparison. When two radiation patterns in two files are to be compared , one of the files must be scaled. The scaling is such that the total radiated power is the same in both cases. This scaling adjustment makes comparisons between computed and measured patterns possible even if the measured pattern is obtained for a different level of excitation power.

Patterns are displayed in the form of polar plots. E_θ and E_ϕ patterns for 21 conical cuts and 2 elevation cuts defined in the military specification can be plotted. The user can choose to display one or both polarizations at a time. In order to give a better sense of the orientation of the pattern, the model is drawn in the upper-left corner of the display and oriented according to the cut. Fig. 3.6 shows a pattern displayed with program PATCMP.

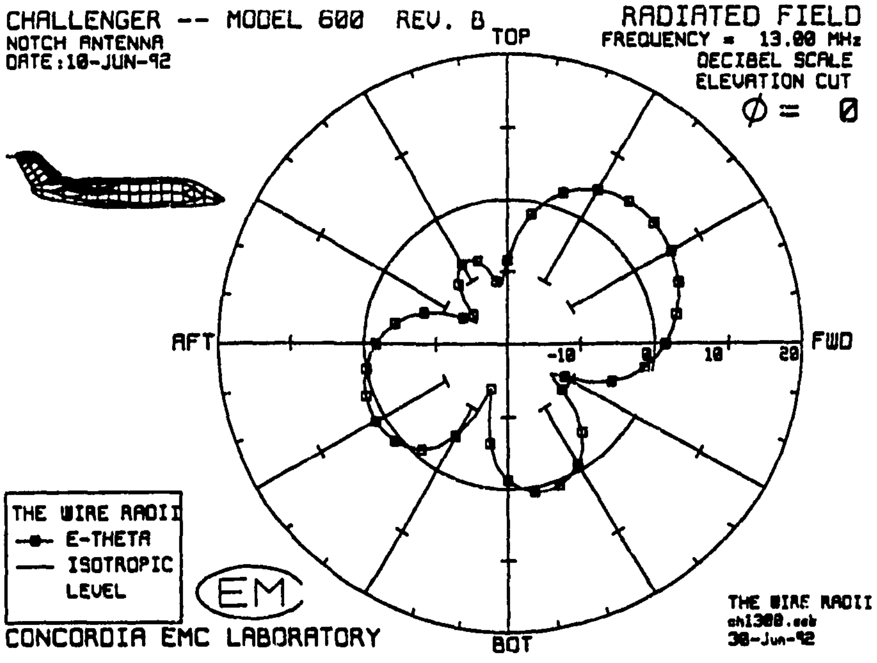

Fig. 3.6 A radiation pattern displayed with PATCMP.

3.5.3 Program TDPAT

Another radiation pattern display program available at EMC Lab is called TDPAT (Three Dimensional PATterns) [6]. This program supports NEC solution files with radiated field computed for the 21 conical cuts specified in MIL SPEC A-9080. Radiation patterns are displayed in a "hidden-surface" three dimensional format through the use of 3-D graphics system MOVIE.BYU [53]. The advantage of using this program is that relative field strength in the free dimensional space surrounding the radiator can be quickly visualized. Similar to PATCMP, a model oriented in the direction associated with the pattern is also displayed. An example of a 3-D pattern displayed with TDPAT is shown in Fig. 3.7.

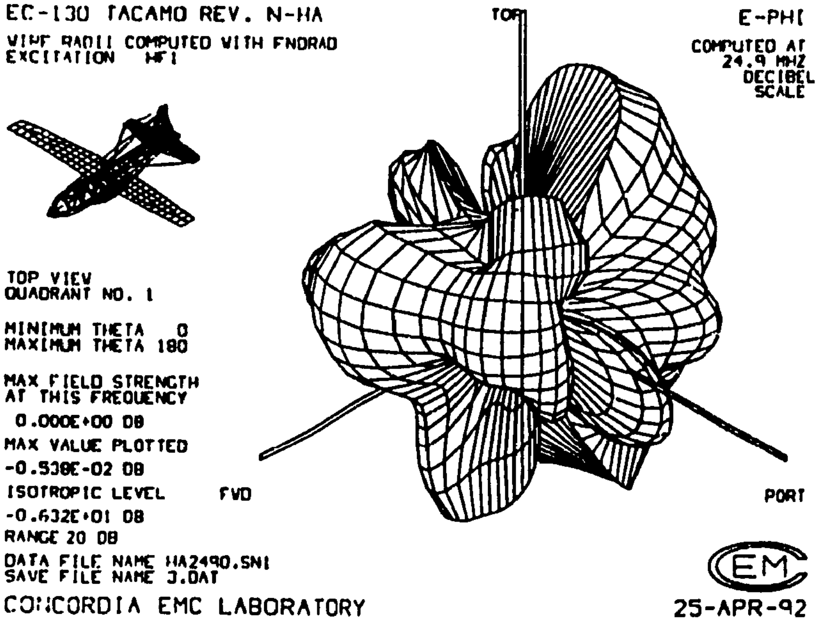

Fig. 3.7 A 3-D radiation pattern displayed with TDPAT.

3.5.4 Program IDIS

Program IDIS (I for current, DIS for display) shows the current distribution on the model. The current magnitude can be displayed in linear or dB scale. The current phase is shown in degrees. Several display modes are available for obtaining comprehensible pictures in different situations. They include "rectangular axis" mode, "perpendicular - lines" mode, "magnitude hot-scale" mode, and "phase color-circle mode". In "rectangular axis" mode, the current magnitude and phase are plotted on rectangular axes as a function of distance along a "current-path", as shown in Fig. 3.8. The wire-grid model is drawn in the three remaining modes. Current magnitude is represented as lines perpendicular to the wire-segments of the model in the "perpendicular-lines model" mode, as illustrated in Fig. 3.9. The "magnitude hot-scale" mode is conveniently used to have an overview of the current distribution on the model in which current magnitude is coded with hot scale color. In order to avoid misleading pictures being displayed, IDIS sorts the current magnitudes to find the largest current magnitude on each wire, then the wires are plotted in ascending order from the wire whose maximum current is smallest to the wire with largest maximum current so that the wires with weak currents will not overwrite the ones with stronger currents. To make the strong currents more prominent, IDIS draws wires with weak currents with thin lines and wires with stronger currents with wider lines. Regions with highest current concentrations can be quickly identified. In the "phase color-circle" mode, segments with the same current phase will have the same color. An arrow head is also shown on each segment to indicate the direction of the current flow. This mode can help identify major current paths on the model which are usually characterized by constant current phases.

When model displaying modes are used, the user must specify the view angles, theta and phi, in a spherical coordinate system. Sometimes, it is more convenient to draw only a specific part of the model such as a set of wires forming a current path. This can be accomplished by inputting a directory file containing the tag numbers of the desired wires.

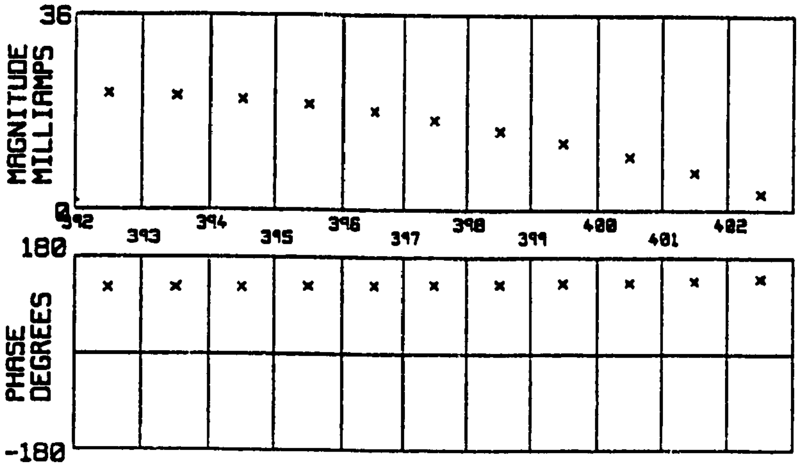

Fig. 3.8 A current path displayed in the "Rectangular Axis" mode of IDIS.

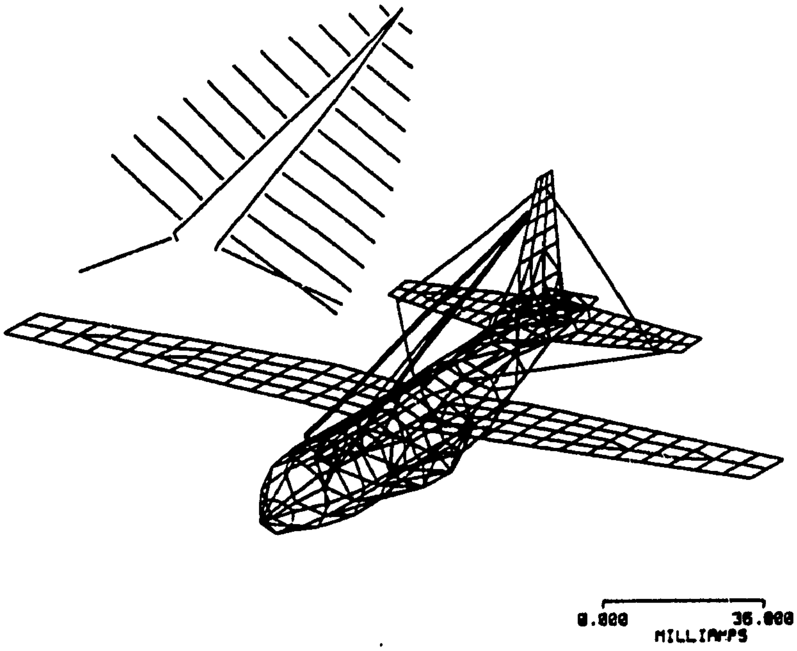

Fig. 3.9 Currents displayed in the "Perpendicular-Lines Model" mode of IDIS.

3.6 High Resolution Spectral Analysis with NEC

This thesis is concerned with the coupling on large aircraft in the HF range from 2 to 30 MHz. The frequency dependency of coupling necessitates multi-frequency calculations. Theoretically, NEC runs should be executed at as many frequencies as possible in order not to miss any possible couplings in the HF band. With advanced computer systems such as the DEC work-stations at the EMC Laboratory, frequency sweeps with very fine frequency stepping can be completed in a reasonable period of time. Plots such as impedance curves that resulted from the NEC output with frequency sweeps are very revealing and make the analysis of coupling modes possible.

A step size of 0.1 MHz was chosen to perform the frequency sweeps, resulting in a total of 281 frequencies at which the solution must be computed. After the sweeps are completed, if it is found that there are drastic changes in radiation characteristics in certain frequency regions, additional calculations will be done at the frequencies in between. As can be seen in the results presented in Chapters 5 and 6, 0.1 MHz stepping is sufficiently fine for observing all the detailed variations in most cases.

In conclusion, this investigation on coupling modes was conducted with numerical simulations using NEC and a system of software modules that support the preparation of models and analysis of the numerical results. The next chapter will describes the two aircraft models being used in this thesis.

CHAPTER 4

MODEL DEVELOPMENT AND REFINEMENT

In this thesis, two large aircraft were modelled numerically to study HF coupling characteristics. The first aircraft is the EC-130/TACAMO which had been modelled at the EMC Laboratory to study its radiation characteristics and to compare the computed radiation patterns with scale-model and full-scale measured patterns, in order to resolve the problem of a discrepancy between the scale-model and full-scale measured patterns [7]. The tremendous increase in computing power acquired at the EMC Lab enables further investigation into other important electromagnetic compatibility problems using a more complex model. The existing model was used as a base line model for further refinement. A substantial number of wires was added to give a finer wire-grid. The geometry of the wire-grid in some regions was modified to eliminate NEC-incompatibility errors found by program "CHECK". Major modifications to the old model and comparisons between the old and new model are presented in the first part of this chapter.

The second aircraft is the CL-600/CHALLENGER. By the time the author finished studying the coupling modes on the first aircraft, the wire-grid model for the CL-600 had been developed by Mr. Ariel Ramos under the supervision of Drs. S.J. Kubina and C.W. Trueman at the EMC Laboratory. It was desired to apply the same computational techniques as the ones used on the first aircraft to the second aircraft as well. There are two major differences, however, between the first and the second aircraft. First of all, the

EC-130 has five HF antennas, whereas the CL-600 has one only. Secondly, the HF antennas on the EC-130 are long thin-wire antennas, but the HF antenna on the CL-600 is a "notch" antenna [30]. The first difference eliminates the need to calculate HF inter-antenna coupling for the CL-600 aircraft, and the second difference results in dissimilarity in radiation characteristics between the two aircraft. The CL-600 wire-grid model is a carefully designed complex model consisting of 624 wire segments. Unlike wire antennas which can be readily represented by thin conducting wires, the notch antenna on this aircraft is much more difficult to model. It is located near the front edge of the aircraft's vertical stabilizer. In order to model it, appropriate wire segments were used to outline the shape of the notch and a fine wire-grid was used to represent the conducting surface surrounding the notch. A brief description of this aircraft model will be given in the second part of this chapter.

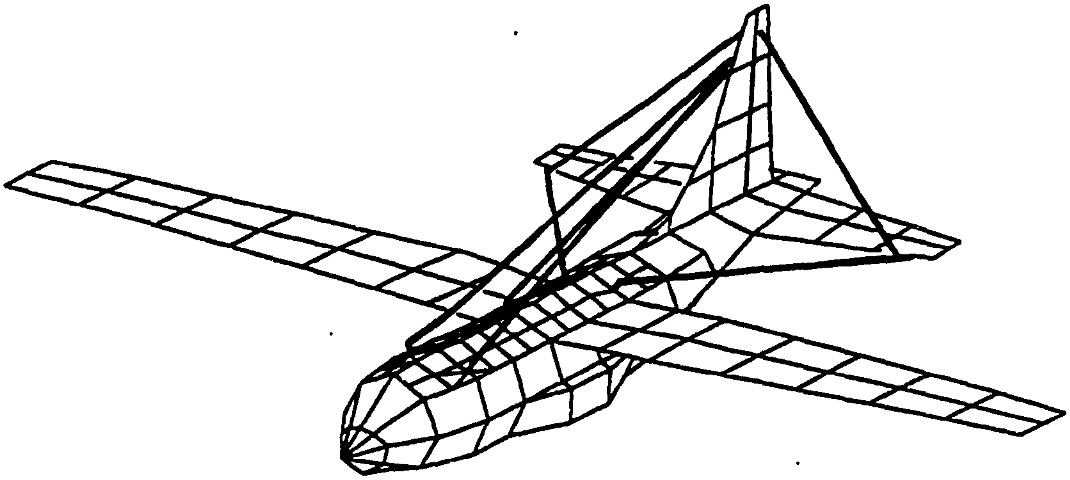

Fig. 4.1 EC-130 "base line" model or model "K".

4.1 Refinement of the EC-130 Model

The wire-grid model for the EC-130 had undergone several modification processes from a primitive model. Major modifications were mainly made to the antenna feed regions. Improvement in the agreement between the scale-model measured patterns and the computed patterns were observed after those modifications were done. A satisfactory model called model "K" was obtained for which good agreement between measured and computed patterns was observed at selected frequencies for three representative HF antennas on the aircraft [7]. Fig. 4.1 shows the design of model "K". It is a complex model with a total of 477 wire segments. We will use the term "base line model" to refer to model "K". Note that this wire-grid model violates the guideline of "square mesh cells" as can be seen in Fig. 4.1.

NEC-incompatibility errors were found when the author used the program "CHECK" to verify the integrity of the base line model at 15 MHz. Errors related to the ratio of segment length to wavelength were observed on the wings and stabilizers. Spacing errors such as proximity errors and overlap errors were found in the tail, the nose and near the landing gear compartments of the aircraft. Some of the errors are related to the geometrical design of the wire-grid, others are due to the thick wires representing the wings and stabilizers [7]. These unusually thick wires are the results of doubling the wire radii calculated by same-surface-area rule to represent double-sided surfaces of the wings and stabilizers. Match point warnings were also issued by CHECK for various locations in the model. It is desired to eliminate these kinds of warnings as well, because match points are critical for obtaining correct solutions. Fig. 4.2 shows the locations of the problem wires in this model. A "revised" model will be developed by refining the base line model to eliminate CHECK errors.

The first step in the refinement process is to remove all "CHECK errors" and as many "CHECK warnings" as possible. Then, the next step is to refine the wire-grid in order to take advantage of the increased computational power acquired by the EMC Laboratory at the time the author started his project.

4.1.1 Removal of NEC-Incompatibility Errors

The removal of the errors and warnings shown as "highlighted" segments in Fig. 4.2 requires modifications of the wire-grid geometry and/or recalculations of wire radii.

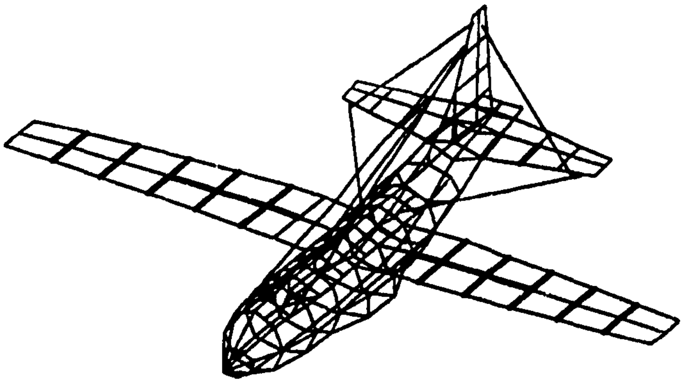
Ratio of Segment Length to Wavelength Errors

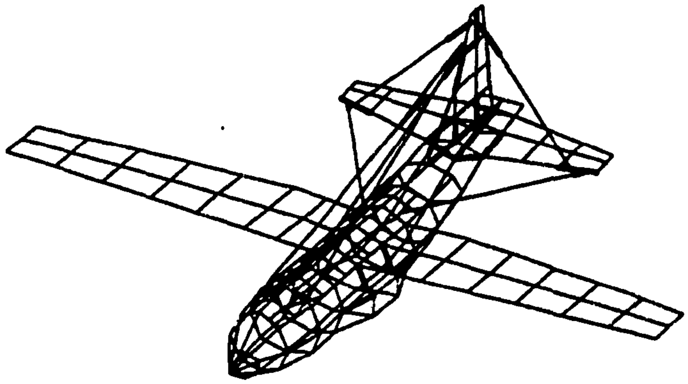
Overlap Errors

Fig. 4.2 Locations of problem wires in the base line model of the EC-130.

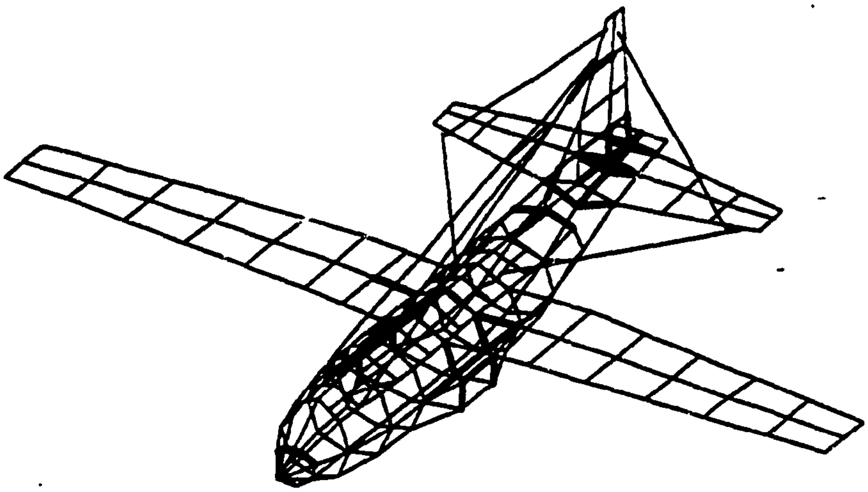

Proximity Errors

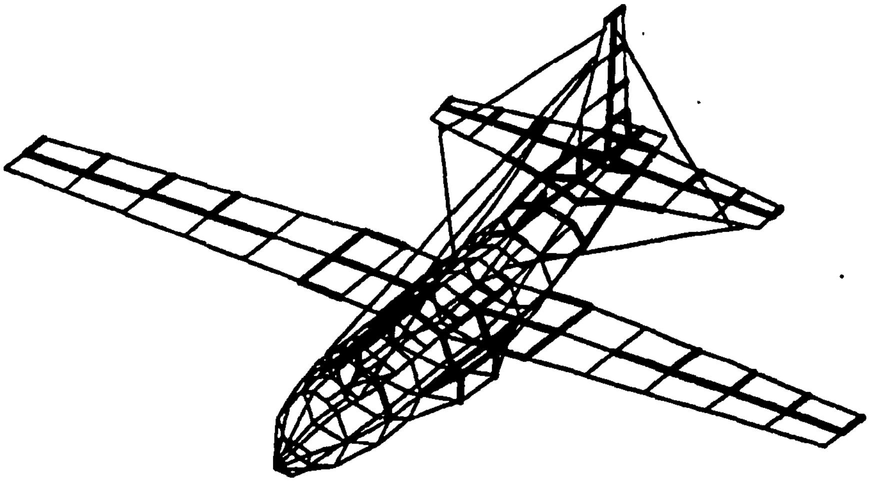

Match Point Warnings

Fig. 4.2 (Cont'd)

As can be seen in Fig. 4.2, wire segments with spacing errors are mainly distributed in the tail region and the bulge regions of the fuselage where the landing gear is stored. It is the particular geometry of these regions that makes the modelling difficult to achieve without violating the modelling guidelines and at the same time fully following the "same-surface-area" rule. In the tail region, the top and bottom surfaces of the fuselage form a very shallow angle. Consequently, the wire segments used to model the top and bottom surfaces are in very close proximity. In order to avoid spacing errors the radii of the wires must be small. One way of reducing the radii is to make the areas of the mesh cells smaller by using more wire segments to model the surfaces. This strategy is not a bad choice since increased computing power has been acquired at the EMC Lab. Similarly, on the top surface of the bulge regions on either side of the fuselage, wire segments are closely spaced. These regions are surrounded by large mesh cells with thick wires. These thick wires and the closely spaced wires cause spacing errors and match point warnings. The same strategy was used to eliminate these errors and warnings. However, how and where to add more wire segments to the existing grid to achieve our goal is not a straight-forward task and requires trial and error in most cases.

The resulting wire-grids for the tail and fuselage bulge regions are shown in Fig. 4.3. The modified wire-grids have some non-square cells but they pass the integrity test.

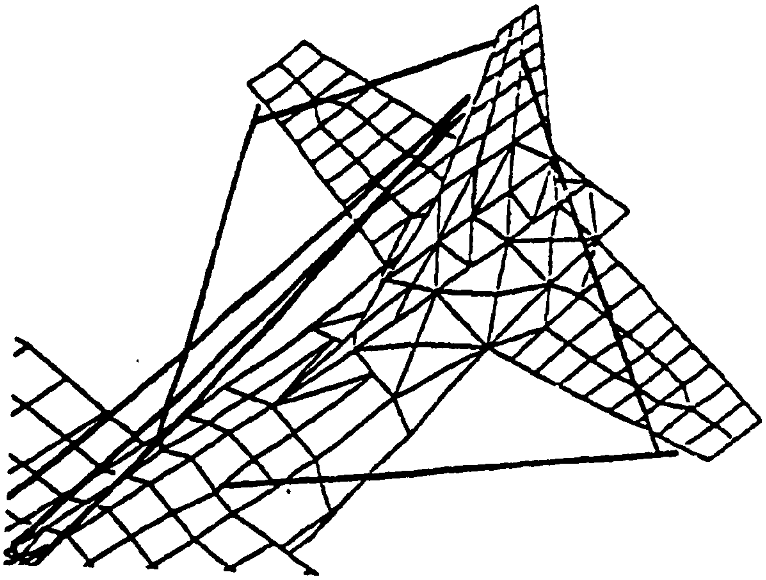

(a) Tail region.

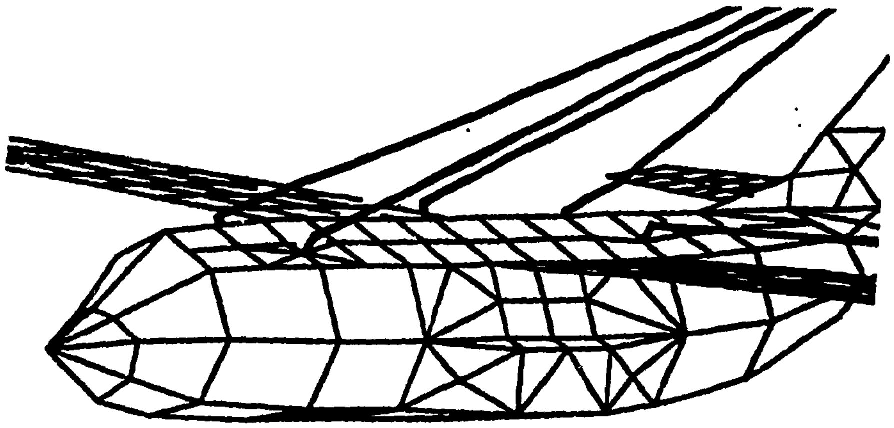

(b) Fuselage bulge region.

Fig. 4.3 Modified wire-grid in the tail and fuselage bulge regions.

There are also some spacing errors such as overlap and proximity errors in the vertical and horizontal stabilizers, as can be seen in Fig. 4.2. The cause of these errors are obvious. The ends of all five HF antennas are extremely close to either the vertical or horizontal stabilizers and the radii of the wires representing the surfaces of the stabilizers are too large. Removal of these errors calls for a finer wire-grid with much thinner wires. Thus much smaller mesh cells were used to redesign the wire-grid and triangular cells were employed where the number of cells along the width of the stabilizers change. The resulting wire-grid can be seen in Fig. 4.3 (a).

4.1.2 Refinement of the Wings

In the base line model, the mesh cells on the wings are quite large compared to those on the top of the fuselage. This non-uniformity is due to the requirement of keeping the total number of segments as small as possible to cope with the limitation in computing power of computer systems used at the EMC Lab in recent years. As the limitation was considerably pushed back with the new computer systems replacing the old ones, it was desired to further reduce the cell sizes on the wings and so that the current paths on them can be better modelled. Moreover, "CHECK errors" due to large ratios of segment length to wavelength can be removed by the reduction of cell sizes. Fig. 4.4 shows the complete wire-grid for the new model. It can be seen that the cell sizes on the wings are made comparable to the ones on the top of the fuselage. In addition, triangular cells were used in the regions where the width of the wings tapers to smooth the transition of cell sizes. The number of wire segments has been increased to 924 in this

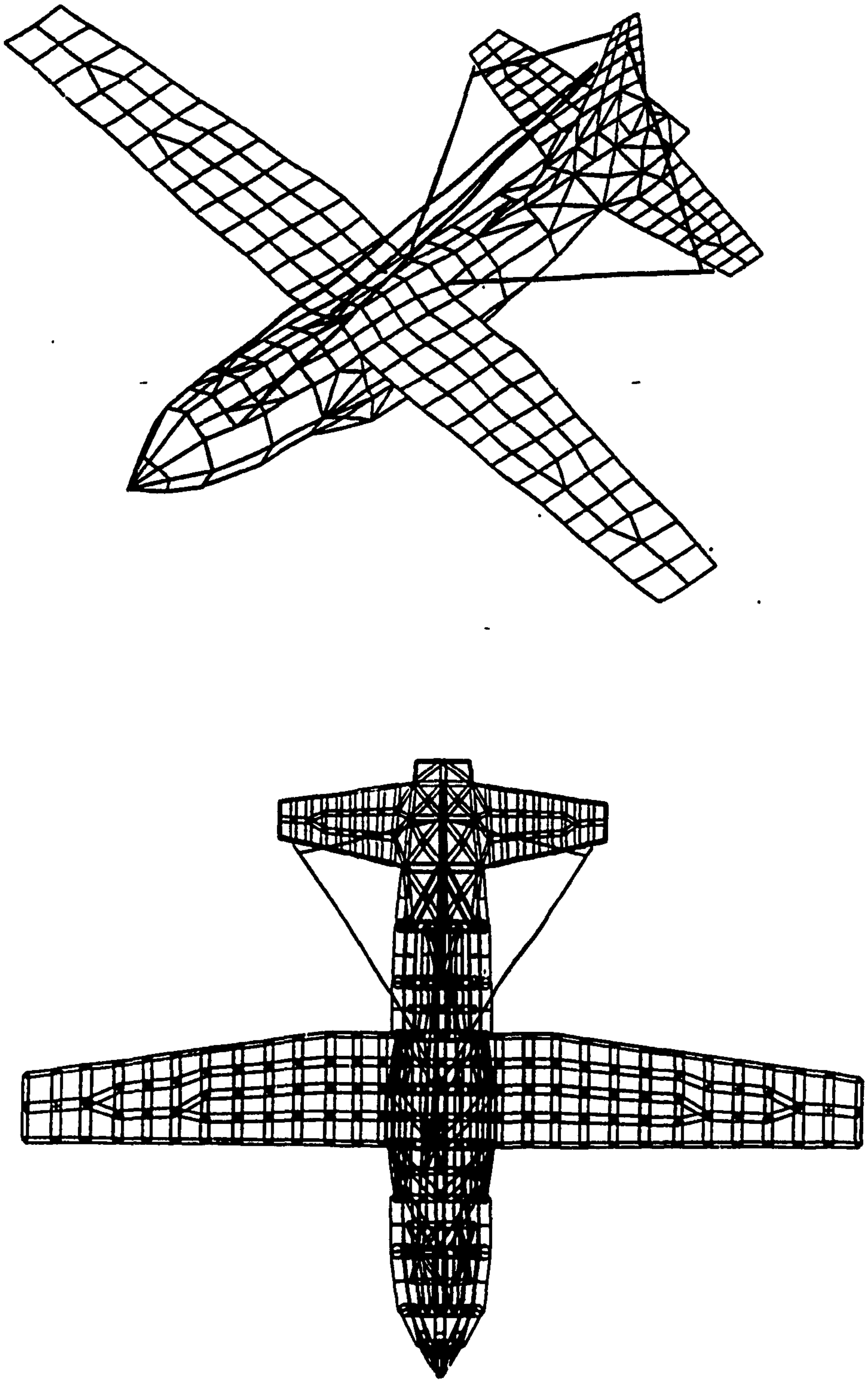

Fig. 4.4 The revised EC-130 wire-grid model.

revised model. Note that in the revised model, there are still some large cells in the fuselage. This is because these cells are not located in critical regions and we do not want the number of segments to be too large.

4.1.3 Removal of the EK Card

The numerical results shown by Rosenzweig [7] were obtained from running NEC with the EK card included. When smaller mesh cells are used to redesign the wire-grid, however, using the EK option at lower frequencies (typically from 2 to 6 MHz) can cause non-physical currents circulating around small meshes in the NEC solutions. This is because when the peripheral length of a mesh is very small compared to the wavelength, an ill-conditioned interaction matrix in the moment method matrix equation will result and hence lead to incorrect numerical solutions [49]. It was discovered that removing the EK card can greatly reduce the problem and provide more reliable results. Fig. 4.5 shows the computed E_θ patterns compared to the measured patterns for the revised model with and without the EK card at 2.13 MHz when HF1 is excited and passive antennas are short-circuited to the airframe. In this figure, the measured E_θ pattern is a circle (dashed-line-with-crosses) at about the same field strength as the isotropic level (solid line). With EK, in Fig. 4.5 (a), the calculated E_θ (solid-line-with-squares) is at less than half the isotropic level and has a null at about 260°. But when EK is removed, Fig. 4.5(b), the E_θ pattern coincides with the measured pattern. It is clear that the agreement in radiation pattern for the model without EK is much better than the one with EK.

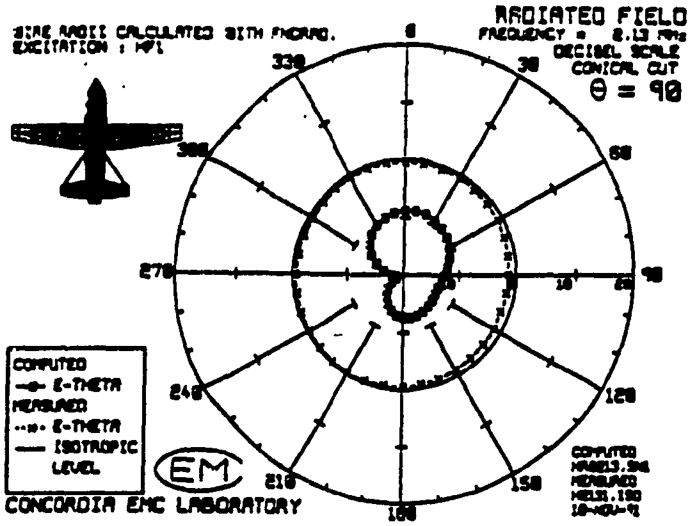

(a) With EK.

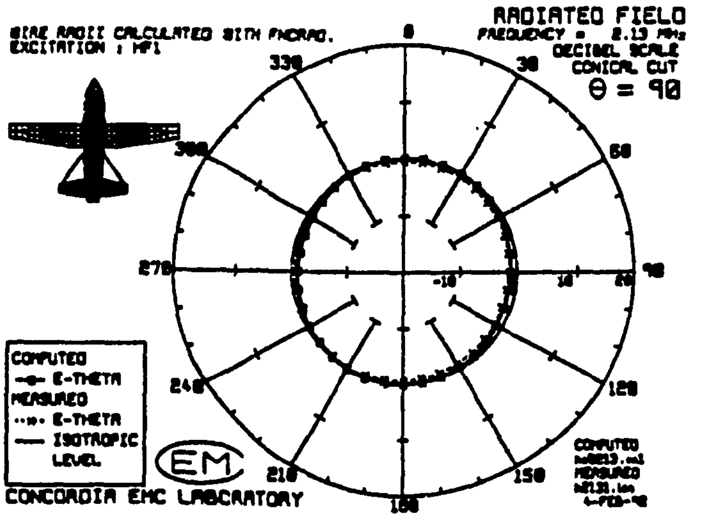

(b) Without EK.

Fig. 4.5 A comparison between radiation patterns computed with and without the EK card on the revised EC-130 model.

4.1.4 Comparisons between the Base Line and Revised Models

As an assessment of the revised wire-grid model, designated as model "N", it is compared with the base line model from three aspects: conformity to NEC guidelines, agreement between measured and computed radiation patterns, and statistics on the models.

4.1.4.1 Improvement in Conformity to NEC

As mentioned earlier, the base line model was found to violate certain modelling guidelines in some parts of the model when examined by program CHECK. All of the errors had been eliminated in the process of developing the revised model. The revised model is error-free in the whole HF band from 2 to 30 MHz, as verified by program CHECK. This greatly increases the credibility of the model. Comparisons of measured and computed patterns support this confidence.

4.1.4.2 Improvement in the Agreement between the Computed and Scale-Model Measured Radiation Patterns

Although the radiation patterns computed using the base line model agree fairly well with the measured patterns, there is still room for improvement at certain angles and frequencies.

For instance, the E_θ pattern for HF1 computed using the base line model and the measured pattern did not match very well at f = 2.13 MHz, $\theta = 155°$ when the passive antennas are short-circuited to the airframe, as shown in Fig. 4.6(a). Significant improvement was observed when the same pattern was computed using the revised model, as illustrated in Fig. 4.6(b). The alignment on the right hand side is much better and the

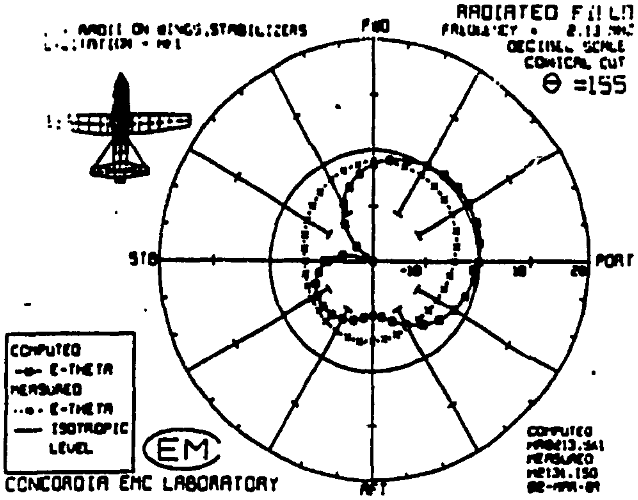

(a) Base line model.

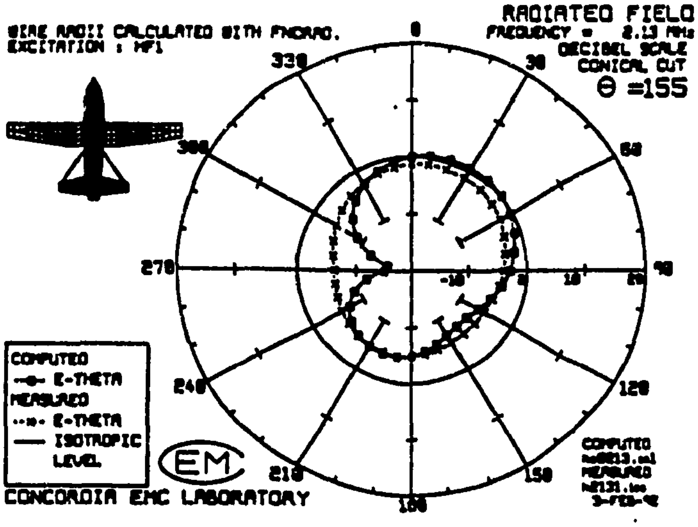

(b) Revised model.

Fig. 4.6 A comparison between E_θ patterns of HF1 computed with the base line and revised models of the EC-130 at 2.13 MHz, $\theta=155°$.

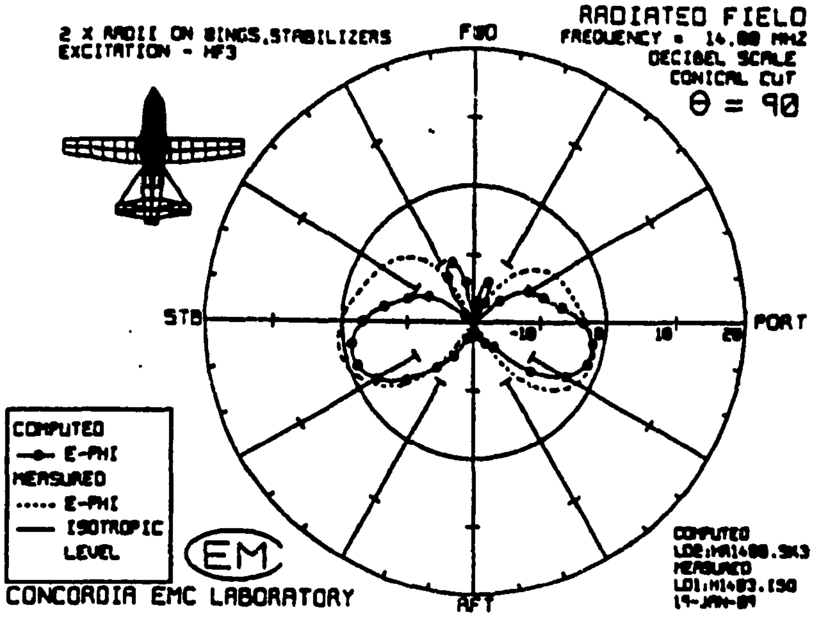

(a) Base line model.

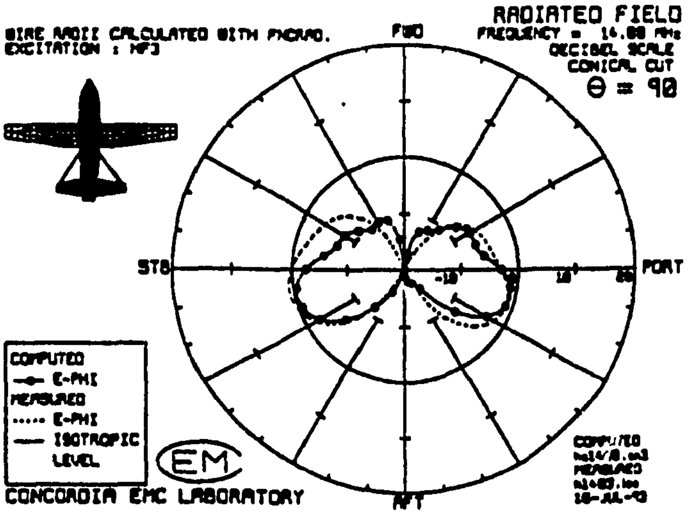

(b) Revised model.

Fig. 4.7 A comparison between E_ϕ patterns of HF3 computed with the base line and revised models of the EC-130 at 14 MHz, θ=90°.

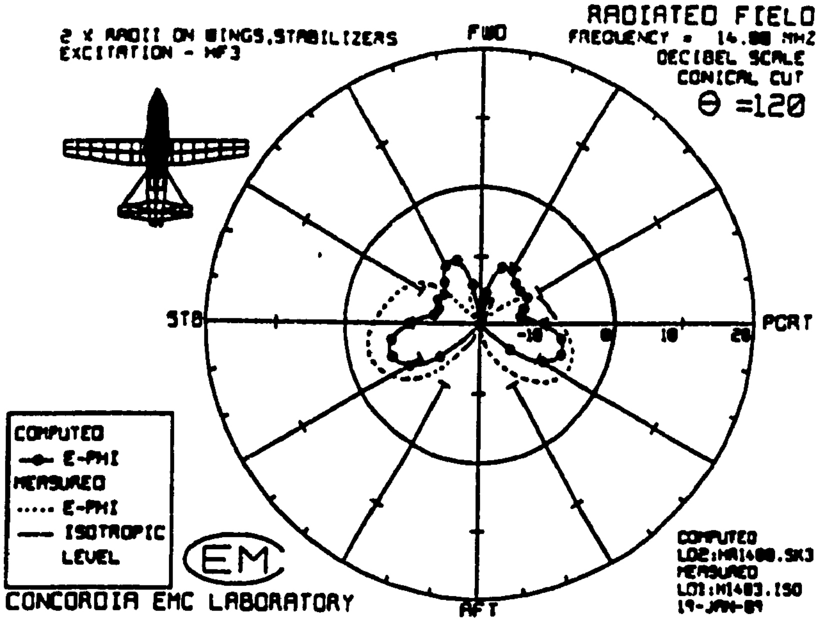

(a) Base line model.

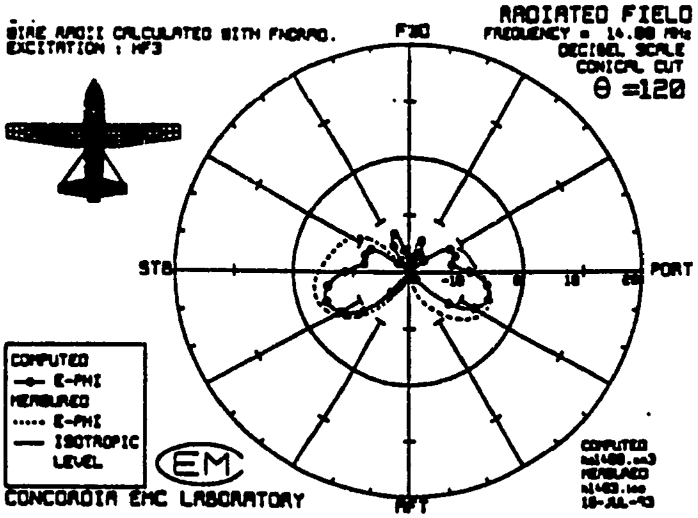

(b) Revised model.

Fig. 4.8 A comparison between E_ϕ patterns of HF3 computed with the base line and revised models of the EC-130 at 14 MHz, $\theta=120°$.

dissimilarity on the left hand side is less severe.

As another example, the agreement between the computed and measured E_ϕ patterns for HF3 degrades at 14 MHz with passive antennas short-circuited to the airframe. The numbers of lobes in the computed patterns were different from those in the scale-model measured patterns. Fig. 4.7(a) shows the comparison between the measured pattern and the pattern computed with the base line model at $\theta = 90°$. The computed pattern is seen to have 4 lobes, whereas the measured pattern has only 2. However, when the same pattern is computed using the revised model, the extra lobes disappear and the level of E_ϕ is better in the upper half of the graph, as can be seen in Fig. 4.7(b). Similarly, in Fig. 4.8(a), the measured pattern for $\theta = 120°$, has two large lobes aft on the port and starboard sides and two very small lobes in the forward direction which are very difficult to see in the figure. The pattern computed with the base line model has 2 large lobes in the forward direction in Fig. 4.8(a). This problem was resolved when the revised model was used to calculate the same pattern, as shown in Fig. 4.8(b), where the size of the small lobes in the forward direction is greatly reduced.

4.1.4.3 Statistics on Segment Lengths

In addition to verifying a wire-grid model against NEC modelling guidelines, program CHECK provides statistics on segment lengths in the model. CHECK calculates the mean segment length and the distribution of segment lengths normalized to the mean segment length. The segment length distributions for the base line and revised model are shown in Fig. 4.9(a) and 4.9(b), respectively. It is noted that the revised model has a much shorter mean segment length than the base line model (1.26 m compared to 1.67

m). There are four major "blocks" in Fig. 4.9(a) corresponding to four groups of wire segment length in the base line model. The number of long segments in the base line model represented by the "rectangular block" on the far right of Fig. 4.9(a) has been greatly reduced in the revised model, Fig. 4.9(b). This is the result of refining the wire-grids for the wing and stabilizers. The remaining long segments in the revised model mainly distribute on the sides of the forward- and aft-fuselage where large cells are seen. The presence of these long segments is reflected by the narrow vertical "bar" on the right-hand side of Fig. 4.9(b). These segments were kept because they are located in the regions that are relatively non-critical. It may be worthwhile to eliminate these long segments completely in the future. The deviation from the mean segment length in the revised model is smaller compared to the base line one. This means the wires are generally shorter and more evenly divided in the revised model and hence a more accurate moment method solution is expected.

In summary, refinement of the EC-130 wire-grid model has improved the credibility of the model and thus increased the reliability of the numerical results.

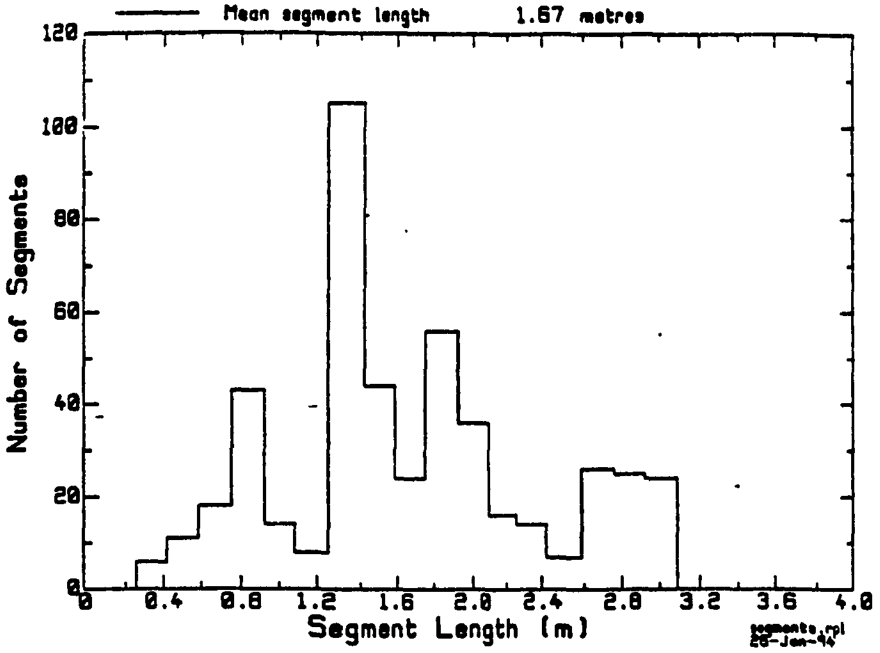

(a) Base line model.

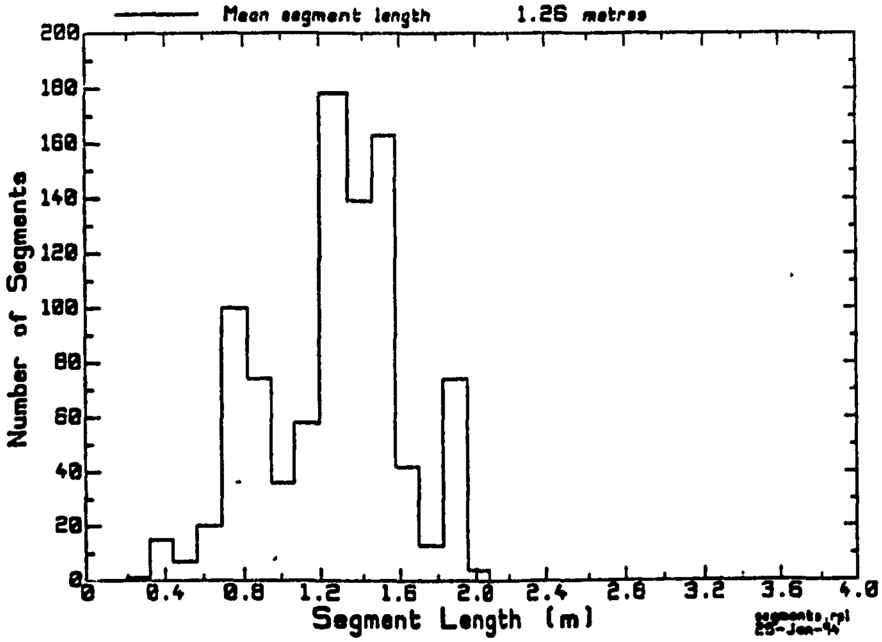

(b) Revised model.

Fig. 4.9 A comparison of segment length distribution in the base line and revised model of the EC-130.

4.2 Development of the CL-600 Model

The CL-600 consists of a cylindrical fuselage, a one-piece wing attached to the bottom, two engines mounted on either side of aft-fuselage, and one vertical stabilizer attached to the top of aft-fuselage with two horizontal stabilizers on its top. The aircraft's only HF antenna is located near the front edge of the vertical stabilizer, as can be seen in Fig. 1.2 in Chapter 1.

4.2.1 Model Creation

Program DIDEC was used to obtain the topology of this aircraft model by digitizing the top, side, and front view scale drawings supplied by the manufacturer CANADAIR. These drawings provide accurate geometrical description of the aircraft's shape and hence are ideal for the development of the model.The resulting digitized sketches are then converted to Autocad [32] files for further processing. In order to generate the wire-grid model, the digitized sketches must be segmented to form wires with appropriate lengths that are best suited for running NEC in the HF range from 2 to 30 MHz. Detailed segmentation of the sketches based on the digitized points to form the wire-grid was done with Autocad.

The CL-600 model is shown in Fig. 4.10, it was designed as follows. A "nominal" segment length, $\Delta_{NOM} = \lambda/10$ (1 m) at the nominal frequency $f_{NOM} = 30$ MHz was chosen. The nominal frequency is the highest frequency of the HF band. Then the fuselage was divided axially into cross-sections spaced Δ_{NOM} apart. Each cross section periphery was subdivided into segment of length approximately equal to Δ_{NOM}. In the original digitized sketches, the fuselage cross sections were elliptical. The large elliptical cross sections of the mid-fuselage were transformed into octagons with eight wire segments. Other smaller cross sections corresponding to the forward- and aft-fuselage were modelled with regular polygons of six or four sides. This measure ensures that the side lengths of the polygons are approximately the same for all cross sections. The resulting model had square mesh cells of uniform size.

The wings and stabilizers are tapering flat surfaces. Squared mesh-cells were used to model most part of these surfaces, with triangular mesh-cells being employed in the transitional regions where the number of cells along the width changes.

The two cylindrical shaped engines were modelled using techniques similar to the ones used for the fuselage. Regular polygons of six sides were used to model the cross sections of the engines. In order to account for the fact the two engines are not hollow, a vertical wire segment is added across the front opening of each engine.

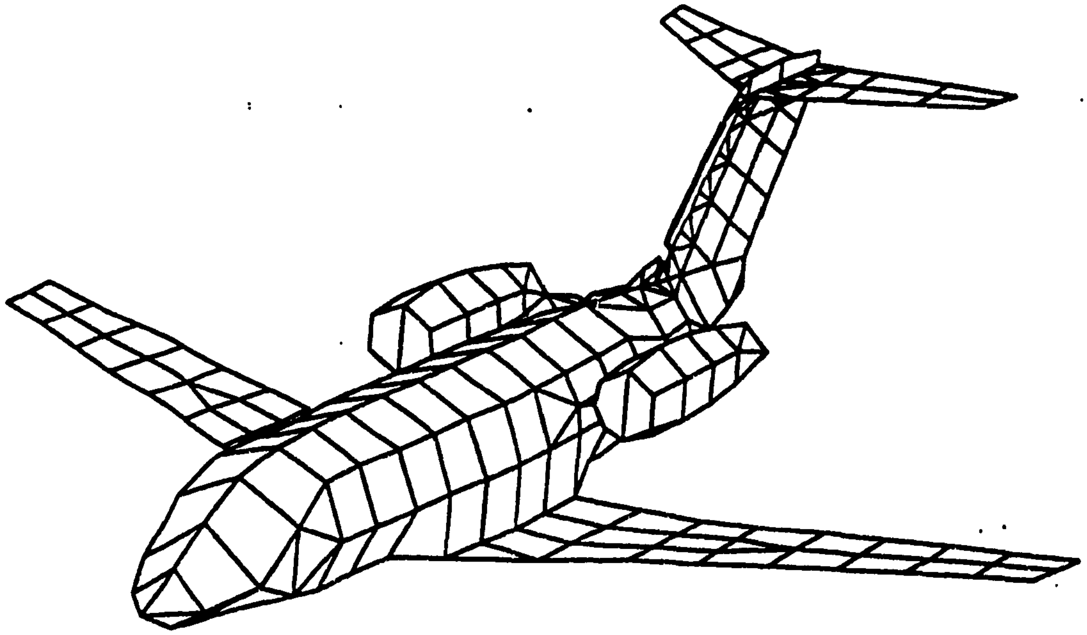

Fig. 4.10 The CL-600 wire-grid model.

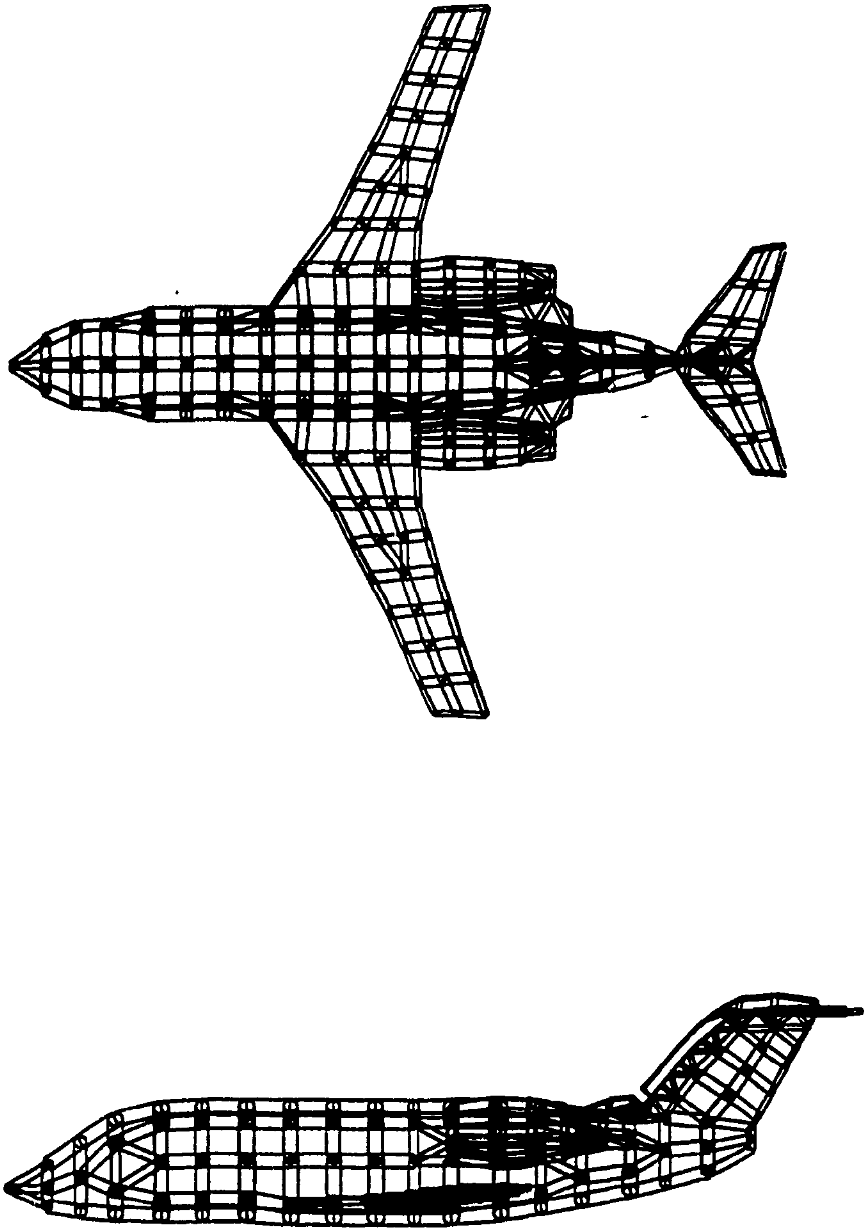

Fig. 4.10 (Cont'd)

Unlike the EC-130 model, the CL-600 model maintains a much more uniform square cell size throughout. This can be easily seen by comparing the EC-130 model in Fig. 4.4 and the CL-600 model in Fig. 4.10.

The only HF antenna on this aircraft is a "notch" antenna located near the front edge of the dorsal. Modelling the notch antenna is not as straight-forward as modelling the thin wire antenna since the latter can be readily represented by a thin conducting wire. For the notch antenna on this particular aircraft, the most difficult thing is to decide how to model as a wire-grid the very narrow conducting strip bordered by the front edge of the dorsal fin and the notch. The simplest way is to outline the border of the strip with a single mesh. The radii of the wire segments forming the mesh will be determined by the "same surface area" rule. It seemed more natural to add some wires connecting the dorsal edge and the edge of the notch. However, the additional wires will form small meshes whose peripheral lengths may be much shorter than the wavelength and result in inaccurate NEC solutions. Initially, two models with different designs of wire-grid in the notch antenna region shown in Fig. 4.11 were generated and tested by executing NEC. The results showed that the simpler design seemed to gives more reasonable results in terms of input impedance. In addition, the high currents circulating around the small meshes in the narrow conducting strip region mentioned above further favours the simpler design.

Finally, the Autocad file that contains the complete wire-grid geometry was converted to a standard NEC input file. Then programs MESHES and FNDRAD were used to compute the radii for each wire in the model.

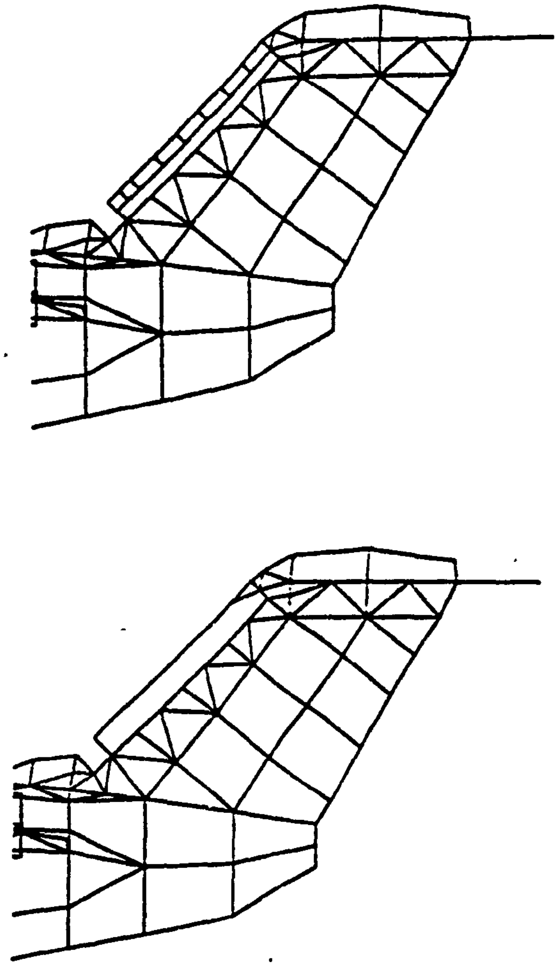

Fig. 4.11 Two wire-grid designs for modelling the notch antenna on the CL-600.

4.2.2 Model Verification

This model was verified in the HF band (from 2 to 30 MHz) by program CHECK, no errors were found and the model was considered a sound model.

As can be seen from the segment length distribution chart in Fig. 4.12, there are two groups of wires represented by two distinctive blocks. The block on the left represents shorter wire segments. Most of these shorter segments are associated with the critical feed region and its neighbors such as the tail and the engines. Longer segments associated with the rest of the airframe correspond to the narrow block on the right. The lengths of these longer segments are in between 1.0 to 1.4 times the mean segment length or 0.847 λ to 1.18 λ. This is the larger group of wires and the segment lengths for this group are quite uniform because the deviation is shown to be relatively small.

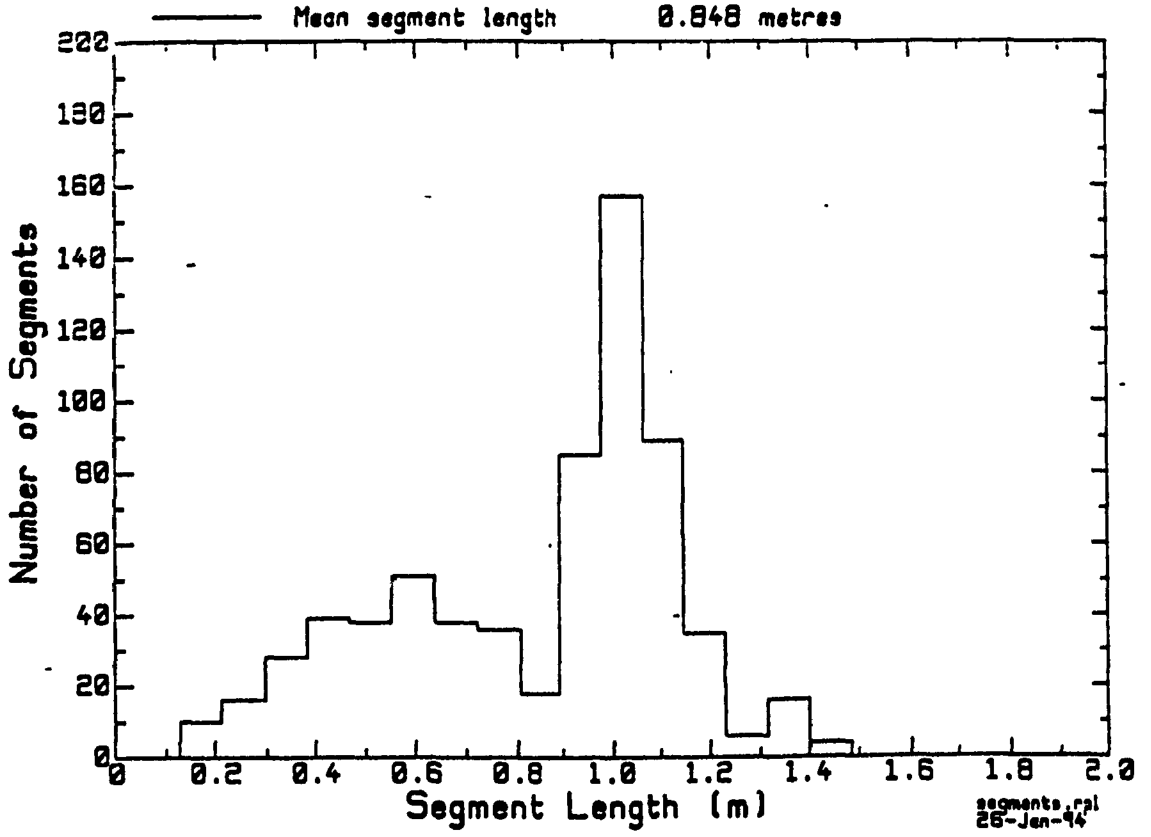

Fig. 4.12 Segment length distribution in the CL-600 model.

4.3 Concluding Comments

The refinement of the EC-130 model has removed all violations of NEC modelling guidelines in the base line model. The resulting revised model consisting of 924 segments has a more elegant wire-grid design and was shown to be more reliable compared to the base line model by the better agreement between the measured and computed patterns.

The highly sophisticated CL-600 wire-grid model has a total of 624 wire segments. It was delicately designed to meet all NEC modelling requirements and at the same time preserve the aircraft's actual geometry as much as possible.

It required approximately four weeks of full-time work to refine the EC-130 model and about eight weeks or more of full-time work to construct the brand-new CL-600 model. A great amount of time was spent on designing the wire-grid for some special regions by trial and error to avoid violating the modelling guidelines.

With care in the refinement and development of complex wire-grid models, it is possible to take advantage of increased computational power to apply the high resolution spectral analysis technique for complete diagnosis of HF coupling modes on the two aircraft. The results for the EC-130 and the CL-600 are presented in Chapter 5 and Chapter 6, respectively.

CHAPTER 5

HF COUPLING MODES ON THE EC-130

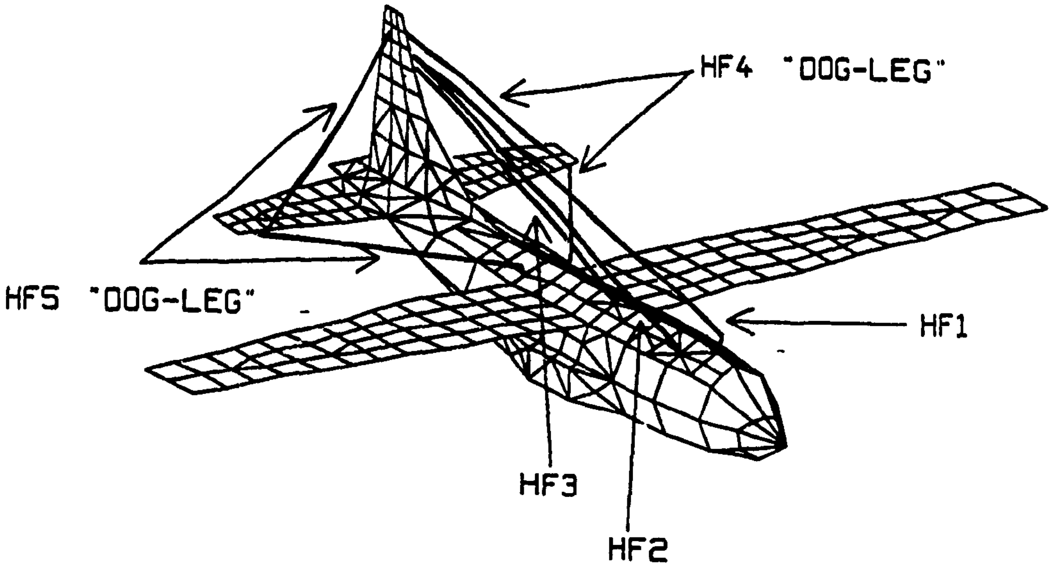

Fig. 5.1 The EC-130 aircraft and its HF antennas.

The HF antenna system on the EC-130 is unusually complex as can be seen from Fig. 5.1. It consists of five wire antennas: HF1 and HF2, both of length 20.38 m, symmetrically located on either side of the fuselage; HF3 of length 14.94 m, located close to the plane of symmetry of the aircraft; and HF4 and HF5, of length 20.72 m, which are "dog-leg" antennas to the horizontal stabilizers and dorsal. This complexity provides an extraordinary opportunity for the investigation of inter-antenna and antenna-to-airframe electromagnetic coupling modes. The HF coupling modes on this aircraft were analyzed based on the numerical results obtained from running NEC at very small intervals of frequency using the refined EC-130 aircraft wire-grid model described in Chapter 4. This chapter presents antenna input impedance, induced currents on the aircraft, and induced voltages at the terminals of the passive antennas due to coupling from an excited antenna. It will be shown in this chapter that strong coupling exists among the various HF antennas. Sharp peaks in the input impedance of each antenna fall near resonant and anti-resonant frequencies of the passive antennas. It will be shown that when a passive antenna is open-circuited to the aircraft, large induced voltages are formed when strong inter-coupling exists. The HF reference parameters defined in Chapter 4 will be shown to change rapidly with frequency when strong coupling between antennas exists.

Strong antenna-to-antenna coupling might constitute a threat to the normal functioning of the communication systems. The induced voltage could be high enough to damage a receiver connected to the antenna terminals or to cause operational interference in the case of simultaneous operations. The induced current on the passive antennas and on the airframe could profoundly change the radiation pattern of an active antenna. These are major electromagnetic compatibility issues that aircraft antenna system engineers must deal with.

The first objective here is to identify all the coupling frequencies from the impedance or induced voltage curves. Then through explorations of the induced current distributions at the critical frequencies, the coupling modes are deduced. Finally, the impact is assessed by an examination of the induced voltage magnitude, aircraft HF antenna assessment parameters and the radiation patterns.

In the antenna-to-antenna coupling study, one antenna is excited with a voltage generator, and the four other antennas are terminated in a load impedance. As described in Chapter 4, three terminating impedances are of interest: short-circuit to the aircraft skin; matched load or 50 Ω load simulating the input impedance of a matched receiver; and high-impedance or "open-circuit" condition, modelled with a 1 MΩ load impedance. The open-circuit case obtains the worst-case induced voltages across a poorly-matched receiver input.

From Fig. 5.1, it is seen that antennas HF1 and HF2 have the same length (20.38 m) and are symmetric about the axial center line of the fuselage; HF3 (14.94 m) is only 0.25 m off the center line; and HF4 and HF5 also have the same length (20.72 m) and are symmetric about the center line. Four of the antennas (HF1, HF2, HF3, HF4) on this aircraft are used for both transmitting and receiving, whereas HF3 is a receive only antenna. Based on the considerations of geometrical symmetry and the actual functions of the antennas, it is sufficient to chose only two of the five antennas, HF1 and HF4, as active antennas and excite them in turn. The results for HF2 and HF5 are expected to be the same as those for HF1 and HF4, respectively. HF3 is a receive antenna and hence it is always a passive antenna.

A frequency sweep in the HF band from 2 to 30 MHz in steps of 0.1 MHz results in 281 impedance values corresponding to 281 frequencies. These values are plotted versus frequency to give a high resolution curve that reveals detailed variations in the impedance with respect to frequency. Most antenna-to-antenna coupling gives rise to rapid changes in input impedance and the frequencies where coupling occurs can be identified from the frequencies of the sharp peaks in the impedance curve. To obtain a complete diagnosis of coupling modes requires executing NEC at 281 frequencies for HF1 active and HF4 active and for three different loading conditions for the passive antennas: short-circuit, 50 Ω matched load and 1 MΩ open-circuit load.

The computational results for this thesis are too extensive to present in full detail. In the following a complete diagnosis of HF coupling modes is given, with representative numerical results to illustrate specific coupling modes.

5.1 Input Impedance as Coupling Indicators

The wire antennas mounted on the aircraft can be considered as monopole antennas with the metallic airframe simulating the ground plane, although the antennas are not vertically erected due to aerodynamic considerations. The computed input impedances of these antennas will be shown to have the same pattern as the monopole or dipole antenna.

In the following the input impedance of the 20.38 m HF1 antenna, and of the 20.32 m HF4 antenna are presented as a function of frequency for three loading conditions for the passive antennas. Each of the exciting antennas behaves roughly as a monopole on a perfect ground plane, namely the aircraft itself. As an aid to understanding the input impedance curves to be presented, the impedance of a 40 m dipole in free space was computed and is shown in Fig. 5.2. The format of the graph is customary in aircraft antenna impedance studies. The magnitude of the resistance is plotted in a log scale from 1 to 10000 ohms in the upper half. The reactance can be positive or negative: positive reactance appears in a log scale in the upper half, and negative reactance in the lower half. Values in the range from -1 to +1 are omitted.

Fig. 5.2 clearly demonstrates the "resonances" and "anti-resonances" of the monopole antenna. "Resonances" occur when the reactance has a zero, going from negative values to positive values. The resistance is low near a resonance. "Anti-resonances" fall where the reactance has a negative-going zero and the resistance is high in value. The 40 m dipole has 4 resonances and 4 anti-resonances in our frequency range.

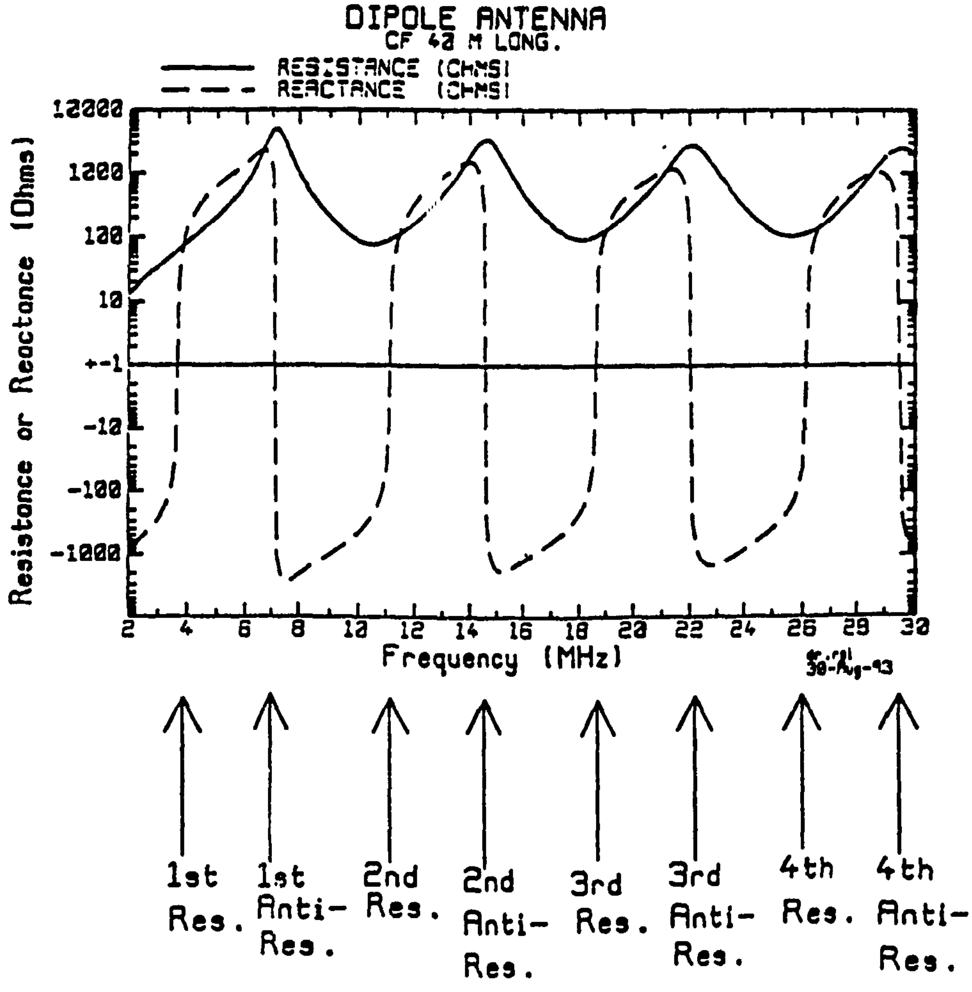

Fig. 5.2 Input impedance of a dipole antenna.

5.1.1 Resonant Length of the Monopole Antenna

If a dipole antenna is considered as an open-circuited parallel-wire transmission line with the wires separated as shown in Fig. 5.3, then the current distribution on the dipole can be assumed to be the same as that on the transmission line. It is known from the transmission line theory that the phasor current will be distributed sinusoidally with the position along the wire for an open-circuited transmission line. The current distribution in Fig. 5.3(a) can be described by the equation

$$\begin{aligned} I(z) &= Ae^{-j\beta L}[e^{j\beta z}-e^{-j\beta z}] \\ &= Ae^{-j\beta L}[2j\sin\beta z] \end{aligned} \qquad (5.1)$$

where L is the length of the line, A is an amplitude constant, and β is the wave number. Due to the open-circuit load, the current must go to zero at the endpoints as implied in Eq. (5.1): $I(z=0) = 0$. At resonance, the input current is a maximum and has zero phase. An open-circuited transmission line resonates at frequencies where the wire length is equal to the odd integral multiple of $\lambda/4$. It is at anti-resonance when the wire length is equal to the even integral of $\lambda/4$. Ideally, these frequencies should apply to a center-driven dipole antenna with its half length equal to the length of the transmission line.

Since a monopole on a ground plane can be thought of as a dipole divided in half at its center feed point and fed against a ground plane as shown in Fig. 5.4, the current distribution along the upper arm of a dipole is the same as the one on the monopole. Fig. 5.5 shows the current distribution along the monopole when it is at resonance and anti-resonance. The input impedance for a monopole is half that of its dipole counter part [55], but the resonant and anti-resonant frequencies are the same for both.

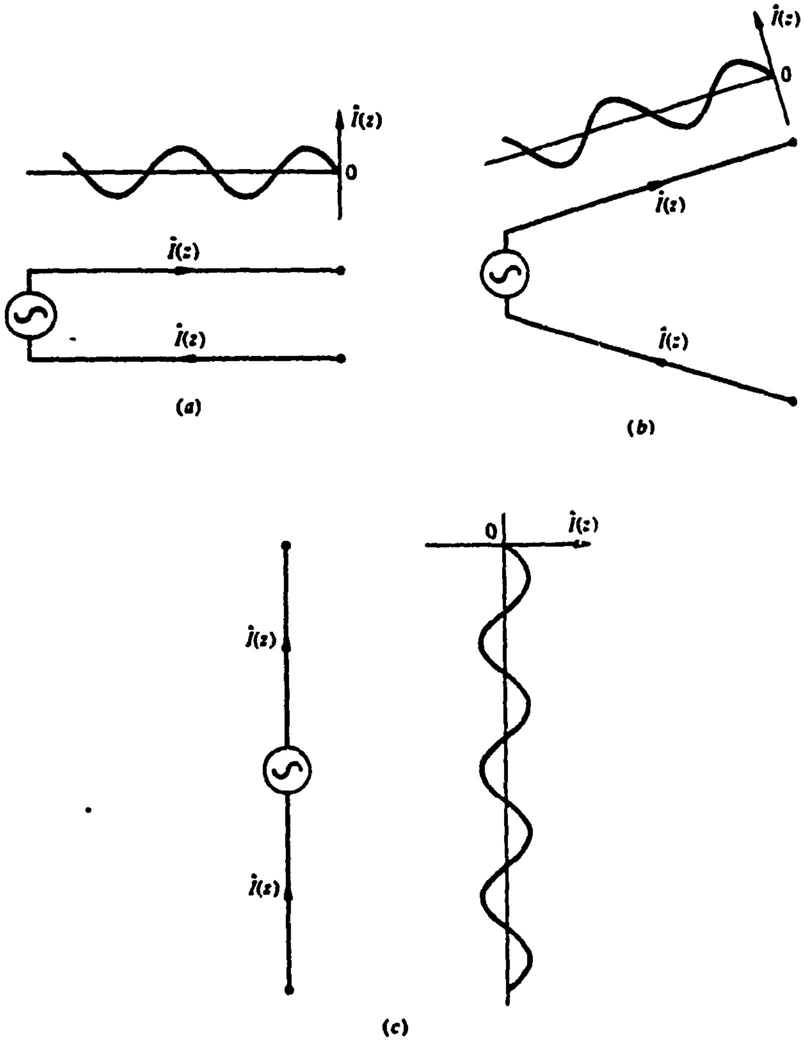

Fig. 5.3 Assumption of current distribution on the dipole antenna using the transmission line approach [54].

(a) The dipole antenna, and (b) the monopole antenna

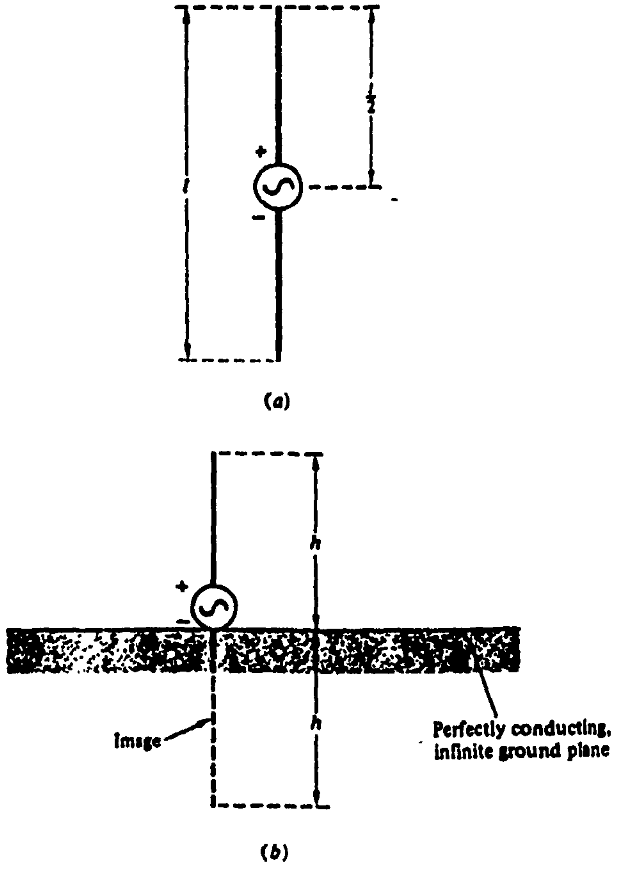

Fig. 5.4 Comparison between a monopole antenna and a dipole antenna [54].

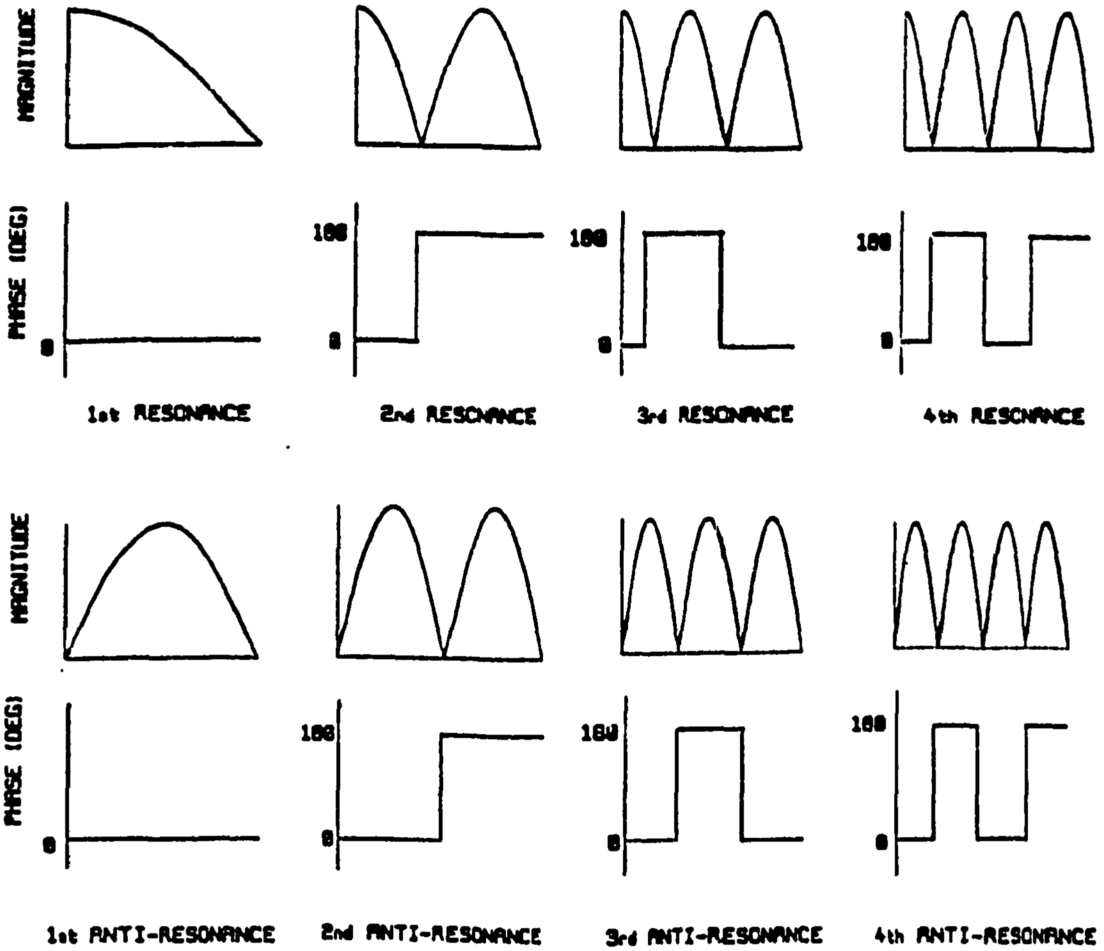

$$f_n = n \frac{c}{4L}$$

RESONANCES: n odd.

ANTI-RESONANCES: n even.

Fig. 5.5 Ideal current distributions along a monopole at resonances and anti-resonances.

5.1.2 Resonant Frequency Estimates for the EC-130 Antennas

Based on the lengths of the antennas, one can calculate the "ideal" resonant and anti-resonant frequencies for the five monopole HF antennas on the EC-130 aircraft. The results are listed in Table 5.1. Note that HF1 and HF2 have the same resonant and anti-resonant frequencies because these two antennas are of the same length. Similarly, the resonant and anti-resonant frequencies for HF4 and for HF5 are the same since HF4 and HF5 are equal in length.

Table 5.1 Ideal Resonant and Anti-Resonant Frequencies for the HF Antennas on the EC-130 Aircraft.

Ant.	Frequency (MHz)							
	1st order		2nd order		3rd order		4th order	
	Res.	Anti-Res.	Res.	Anti-Res.	Res.	Anti-Res.	Res.	Anti-Res.
HF1	3.7	7.4	11.0	14.8	18.4	22.1	25.8	29.4
HF2	3.7	7.4	11.0	14.8	18.4	22.1	25.8	29.4
HF3	5.0	10.0	15.1	20.1	25.1	30.1	35.1	40.1
HF4	3.6	7.2	10.9	14.5	18.1	21.7	25.3	29.0
HF5	3.6	7.2	10.9	14.5	18.1	21.7	25.3	29.0

5.1.3 HF1 as the Active Antenna

The input impedances of HF1 for short-circuit, open-circuit, and 50 Ω loading are shown in Figures 5.6(a), 5.6(b), and 5.6(c), respectively. Compared with the input impedance curve of the dipole in free space, the input impedance for the short-circuit and open-circuit conditions exhibit high degree of anomaly at certain frequencies. Conversely, the input impedance for the 50 Ω loading condition follows the impedance pattern of a dipole antenna in free space, with some small differences near 3 MHz and elsewhere. In this section, we will first identify all the frequencies where strong antenna-to-antenna coupling could exist from the impedance curves and then verify that it does exist by examining the current distributions on the antennas and aircraft.

In the short-circuit case shown in Fig. 5.6(a), there is an oscillation of input reactance at frequencies near 3.6 MHz, the "ideal" resonant frequency of HF4 and HF5 shown in Table 5.1. In addition, the reactance goes from negative to positive near 3.2, 10.4, 17.6 and 25.0 MHz, indicating that HF1 is at resonance at these frequencies. Note that these frequencies are somewhat different from those tabulated in Table 5.1. There will be a separate section to discuss this discrepancy later in this chapter. Associated with these frequencies are the rapid changes in the resistance, which shows that strong coupling to the other antennas could exist. Note that these frequencies are also the resonant frequencies of the passive antenna HF2 because HF1 and HF2 are of the same length. Other rapid changes in resistance occur near 4.7 and 14.2 MHz. These frequencies are close to the "ideal" resonant frequencies of HF3 shown in Table 5.1. From these observations, a clue to the inter-antenna coupling modes has emerged: the coupling modes are related to the resonant lengths of the active or passive antennas. Further observations of the input impedance curves for other loading conditions and for other exciting antennas are required before we can draw a conclusion.

In the open-circuit case shown in Fig. 5.6(b), it was surprising to find that the input resistance and reactance of the active antenna are quite different from those in the short-circuit case. First of all, no oscillation of input reactance is found near 3.6 MHz, instead, the oscillation occurs at frequencies near 29.0 MHz, which is close to an "ideal" anti-resonant frequency of HF1, HF2, HF4 and HF5. Moreover, unlike the short-circuit case, the most drastic changes in input resistance do not occur at the resonant frequencies of the antennas. In the resistance curve, sharp resistance peaks are observed at 6.4, 13.8, 21.0, and 28.8 MHz. These frequencies are near the anti-resonant frequencies of HF1 where HF1's reactance changes from positive to negative. It is important to note that these frequencies are also anti-resonant frequencies of HF2. In addition, there is a "spike" followed by a "notch" near 9 MHz; a "shallow notch" near 19 MHz; and another "spike" at 29.2 MHz. These frequencies are associated with the anti-resonances of HF3 rather than its resonances, judged from the "ideal" resonant and anti-resonant frequencies tabulated in Table 5.1.

With the passive antennas terminated in 50 Ω resistances, the magnitude of coupling is reduced throughout the HF range. The only strong coupling indication visible in the input resistance curve shown in Fig. 5.6(c) occurs near 3.2 MHz. Other much weaker indications are seen near 10.4, 17.6, and 25.0 MHz which are close to the resonant frequencies of the active antenna HF1 and of the passive antenna HF2. In the

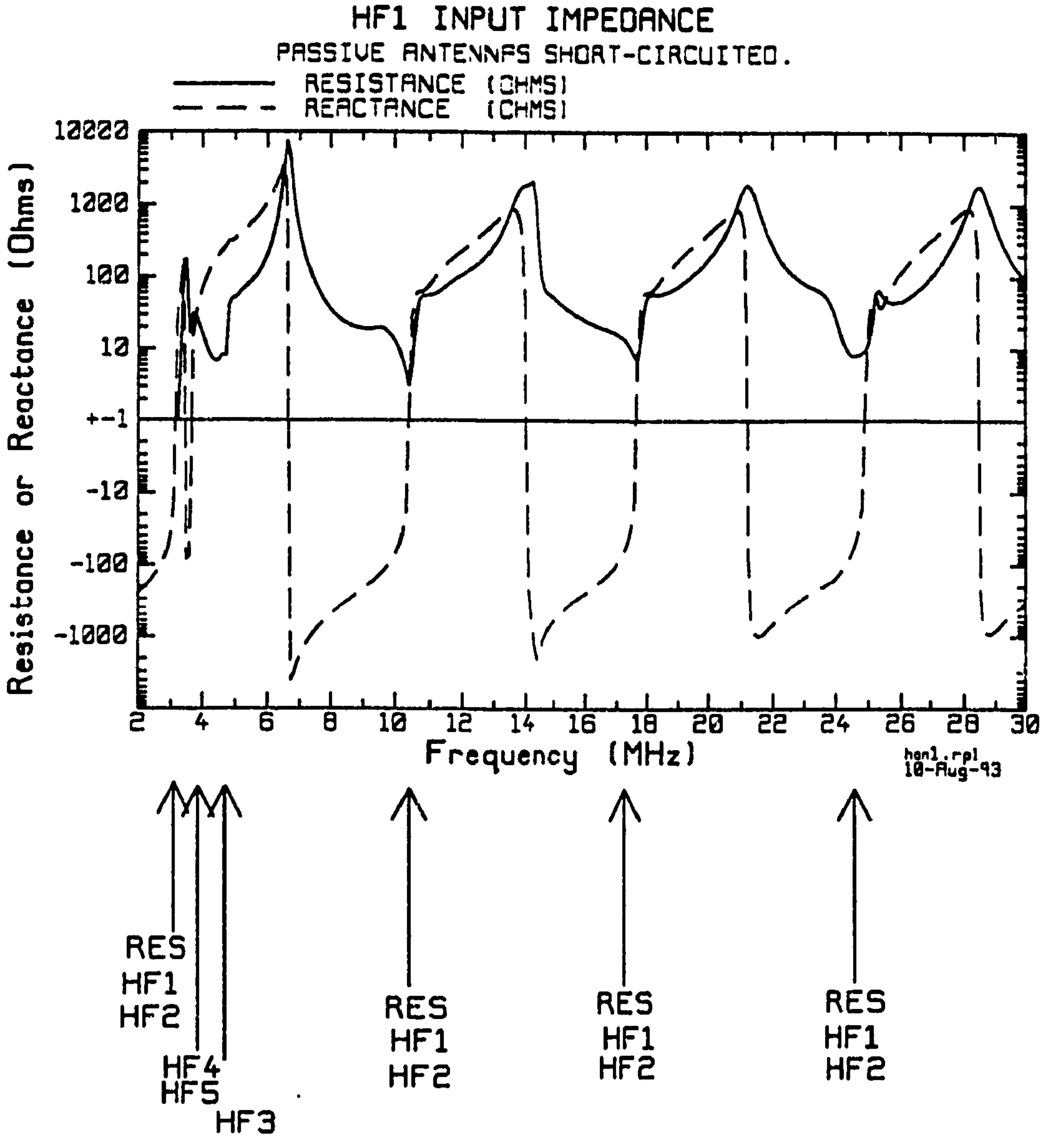

(a) Passive antennas short-circuited

Fig. 5.6 Input impedance of antenna HF1 for three loading conditions for passive antennas.

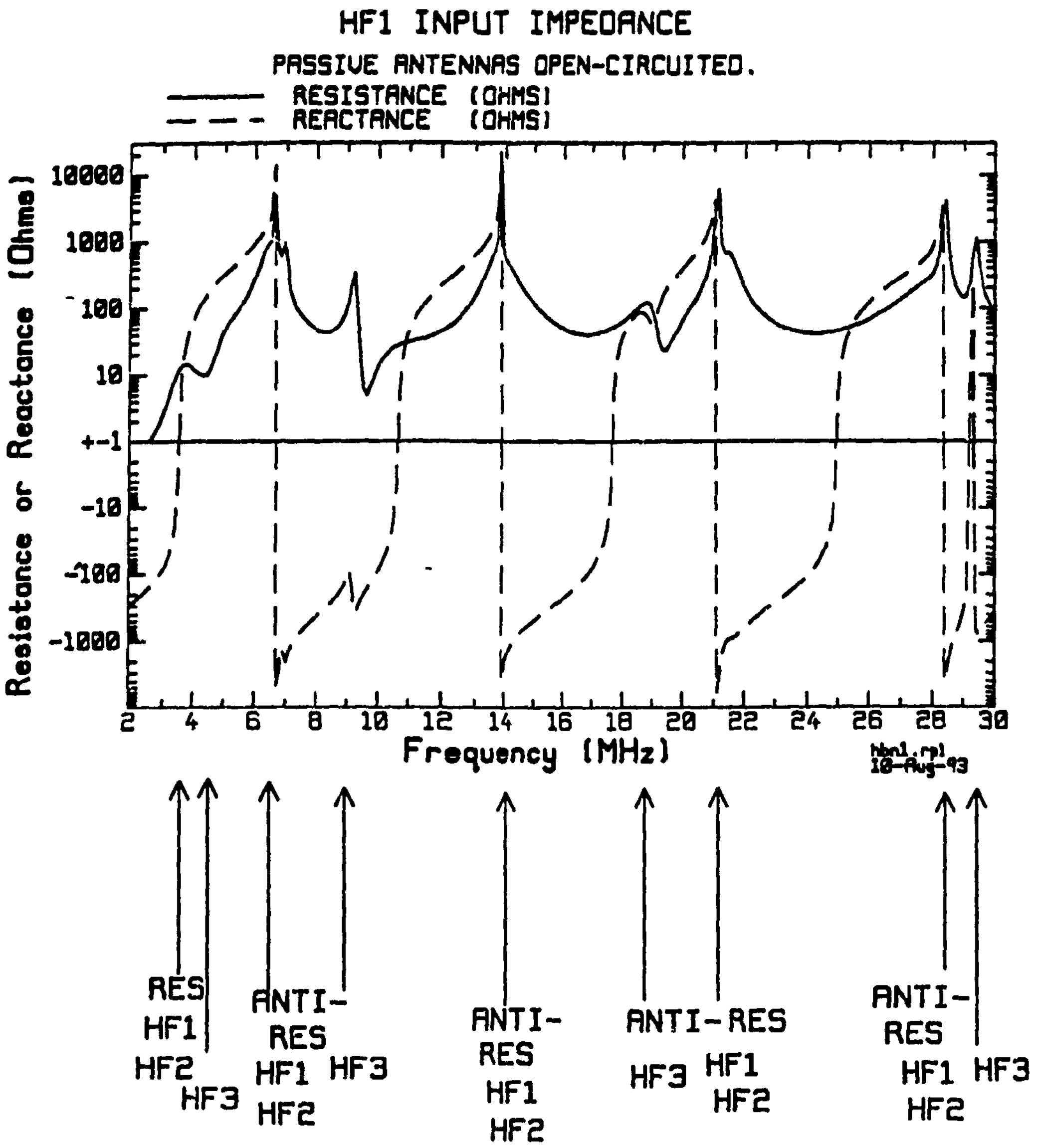

(b) Passive antennas open-circuited

Fig. 5.6 (Cont'd)

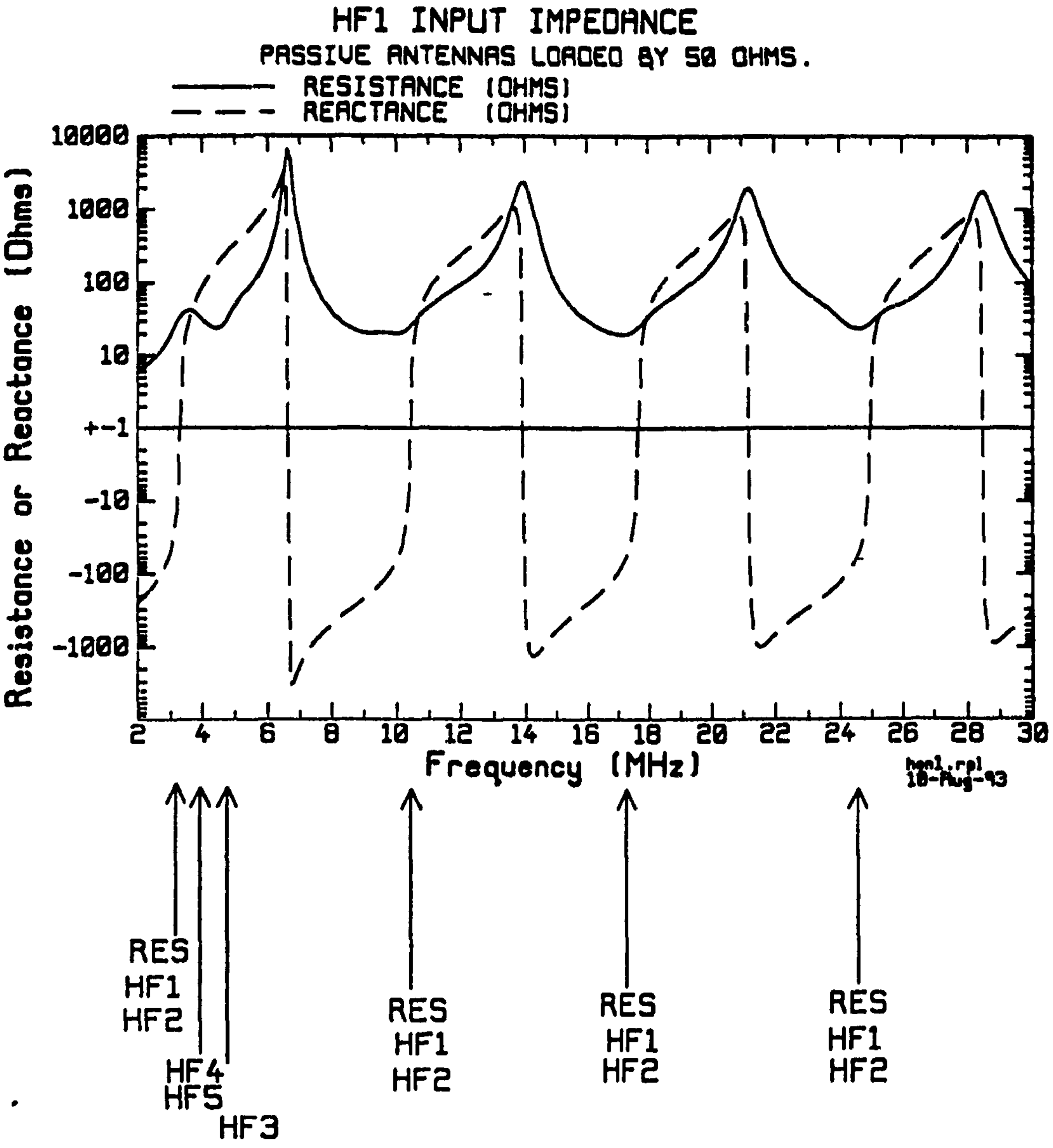

(c) Passive antennas loaded by 50Ω

Fig. 5.6 (Cont'd)

following, the current distributions at selected frequencies associated with various peaks and minima in Fig. 5.6 will be examined to identify resonance modes.

5.1.3.1 Current Distributions with the Passive Antennas Short-Circuited

Fig. 5.7 shows current distributions in color obtained by running program IDIS described in Sec. 3.5.4 of Chapter 3. The current magnitude is shown in a "hot-scale" with blue representing the smallest or "coldest" currents, through cyan, green, yellow, and orange to red representing the large or "hottest" currents. The phase is shown in a color-circle with complementary colors (red-cyan, green-violet, yellow-blue) representing currents 180° apart in phase. The arrowheads in the current segments show the direction of flow of current with zero phase angle.

In the short-circuit case, it was observed that there is a "spike" near 3.15 MHz and three other "notches" in the input resistance curve near 10.4, 17.6, and 24.9 MHz. These are resonant frequencies of the active antenna HF1, which incidentally are also the resonant frequencies of the passive antenna HF2 (HF1 and HF2 are of the same length). Figures 5.7(a) through 5.7(d) show the current distributions at 3.15, 10.6, 17.65, and 24.9 MHz, where strong coupling between HF1 and HF2 occurs. In Fig. 5.7(a), the magnitude of the induced current on HF2 is as large as the exciting current on HF1. The current gradually decreases from its maximum value at the base of the antenna to near zero at the open-circuited end segment. The current phase is constant along HF2 and along HF1. This resembles the current and phase plots for a monopole antenna at the first resonance in Fig. 5.5, showing that HF1 and HF2 are at resonance. In Fig. 5.7(b), the current distribution on HF1 and HF2 at 10.6 MHz reveals that HF1 and HF2 are at their second resonance. The current distribution on HF1 and HF2 is similar to that in Fig. 5.5 for a monopole antenna at its second resonance. There is a maximum current at the base of the antenna, and a second maximum at 2/3 of the distance to the tip. The phase is constant-with-distance, with an abrupt 180° change at the null in the current magnitude. Note that the induced current on the passive antenna HF2 has even larger peak values than the current on the driven antenna HF1. The current distribution in Fig. 5.7(c) indicates that HF1 and HF2, with three current peaks in magnitude and three regions of constant phase, are at their third resonance at 17.65 MHz. Similarly, the coupling between HF1 and HF2 associated with the fourth and last resonance for HF1 and HF2 in the HF band is shown in Fig. 5.7(d). Like the current plots for the fourth resonance in Fig. 5.5, the current on HF1 and HF2 at this frequency has four peaks and four regions of constant phase. The "notch" in the input resistance curve near 4.7 MHz is due to coupling between HF1 and HF3, as shown in Fig. 5.7(e). Here the magnitude of the induced current on the passive antenna HF3 has a peak value larger than that of the exciting current on the active antenna HF1. The one-peak, constant phase current on HF3 shows that HF3 is at its first resonance. The current distribution at 14.2 MHz (not shown) where a rapid change in resistance was seen, indicates strong coupling between HF1 and HF3, with HF3 at its second resonance. The oscillation of reactance around 3.6 MHz was found to be due to strong coupling between the active antenna (HF1) and all the four passive antennas (HF2, HF3, HF4, and HF5) by an examination of the current distribution at the associated frequencies. As shown in Fig. 5.7(f), the magnitudes of the induced currents on the passive antennas are comparable to that on the active antenna HF1 at 3.65 MHz. The

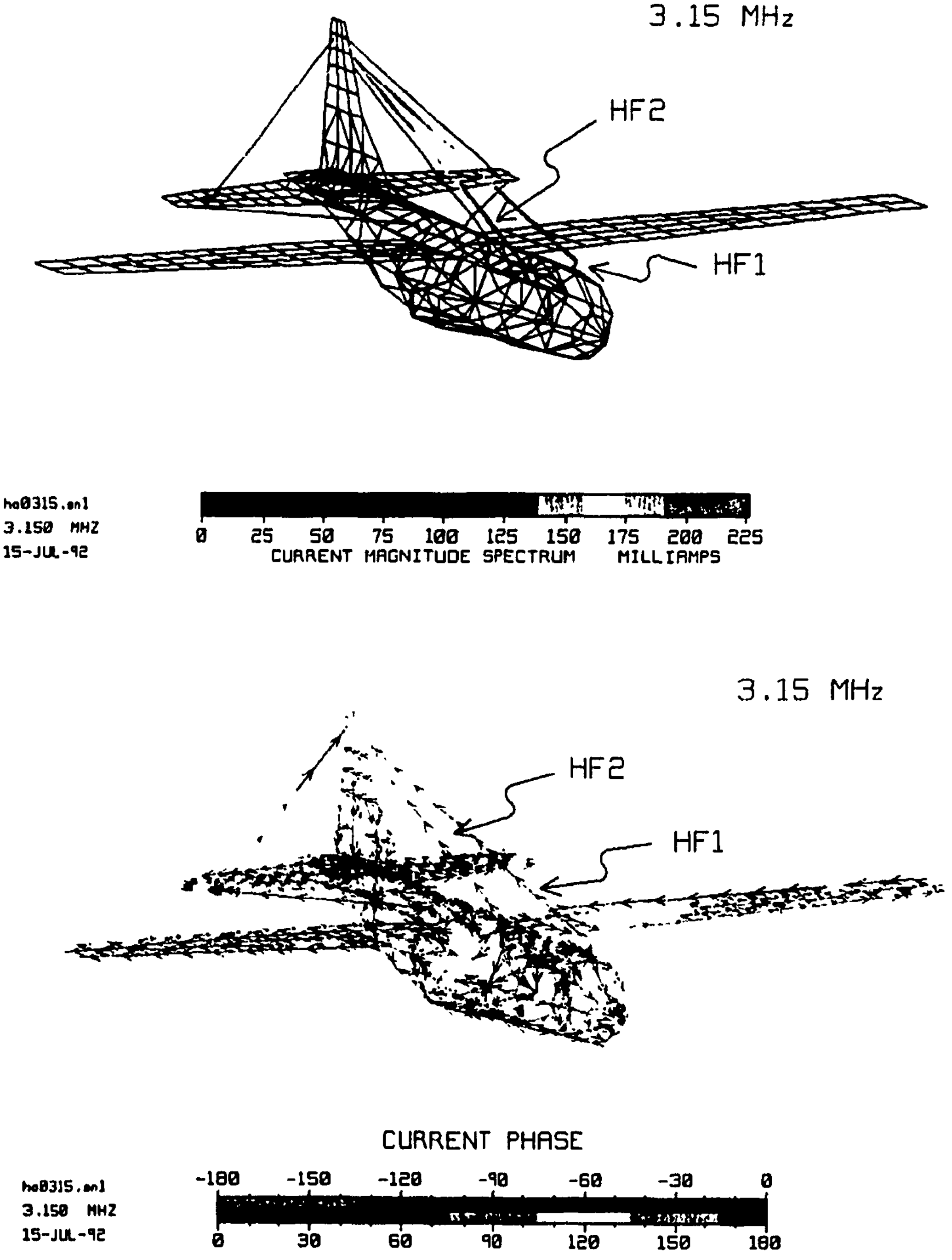

(a) 3.15 MHz

Fig. 5.7 Current distribution plots at selected frequencies for HF1 excited, passive antennas short-circuited.

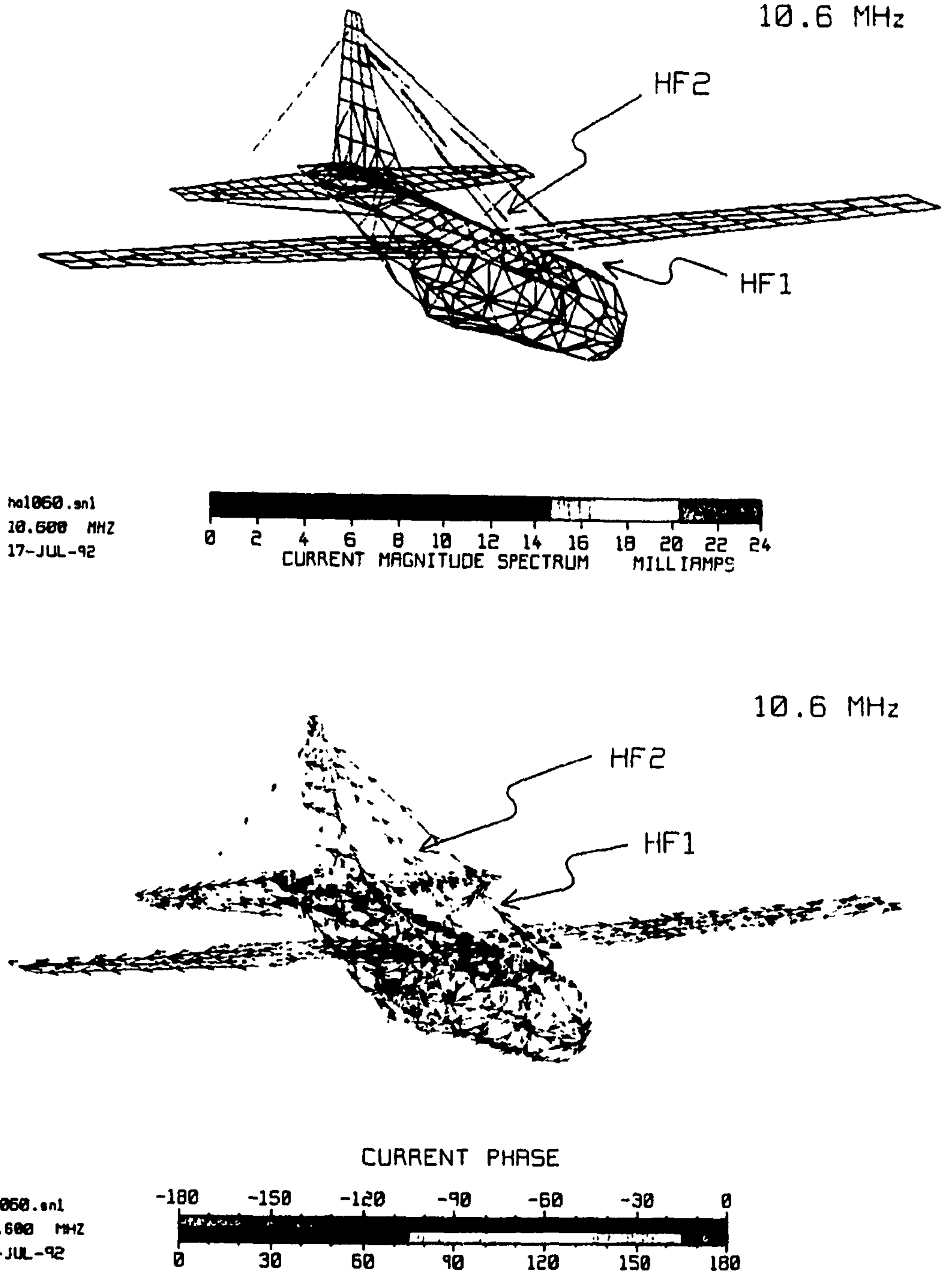

(b) 10.6 MHz

Fig. 5.7 (Cont'd)

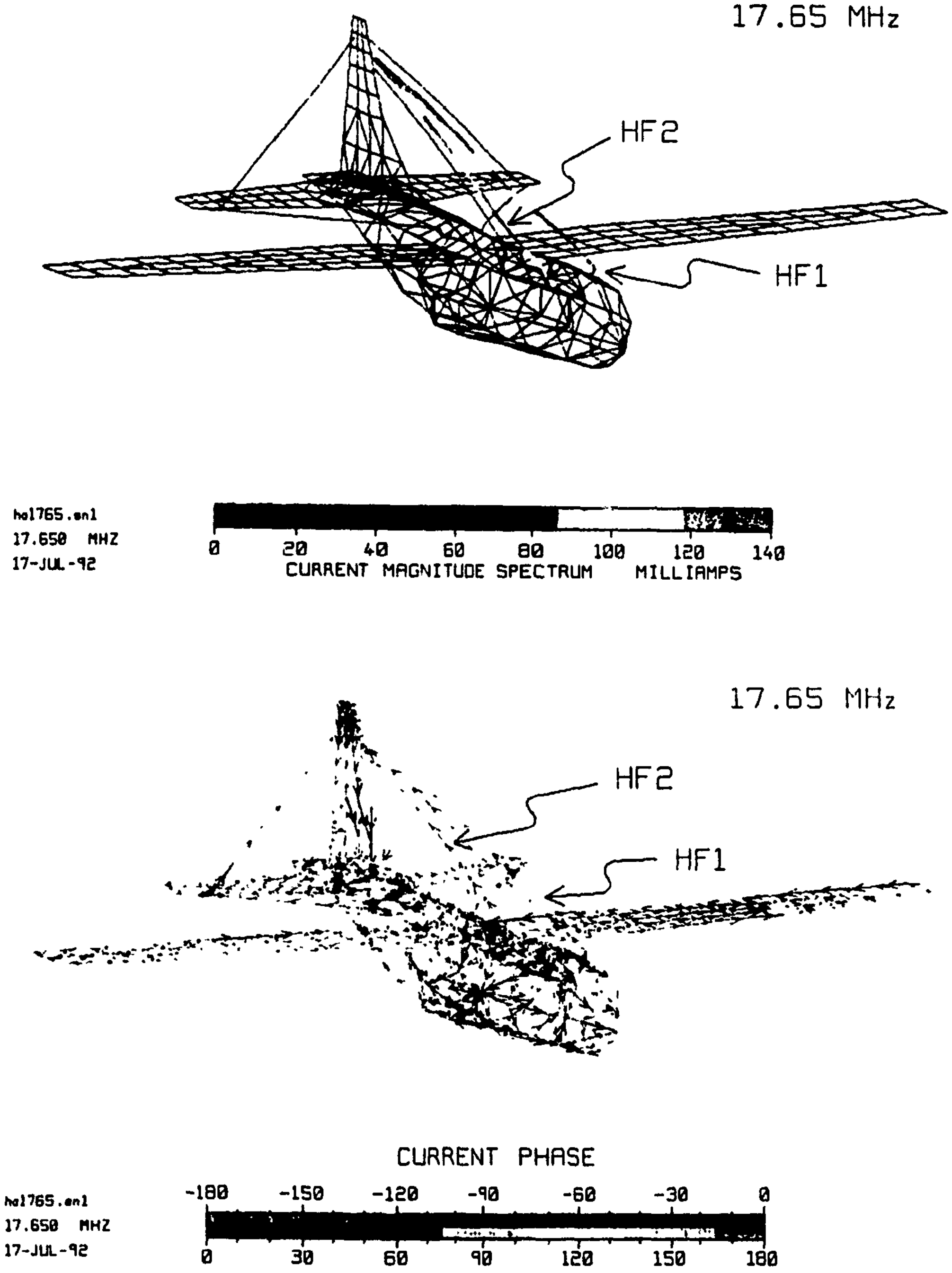

(c) 17.65 MHz

Fig. 5.7 (Cont'd)

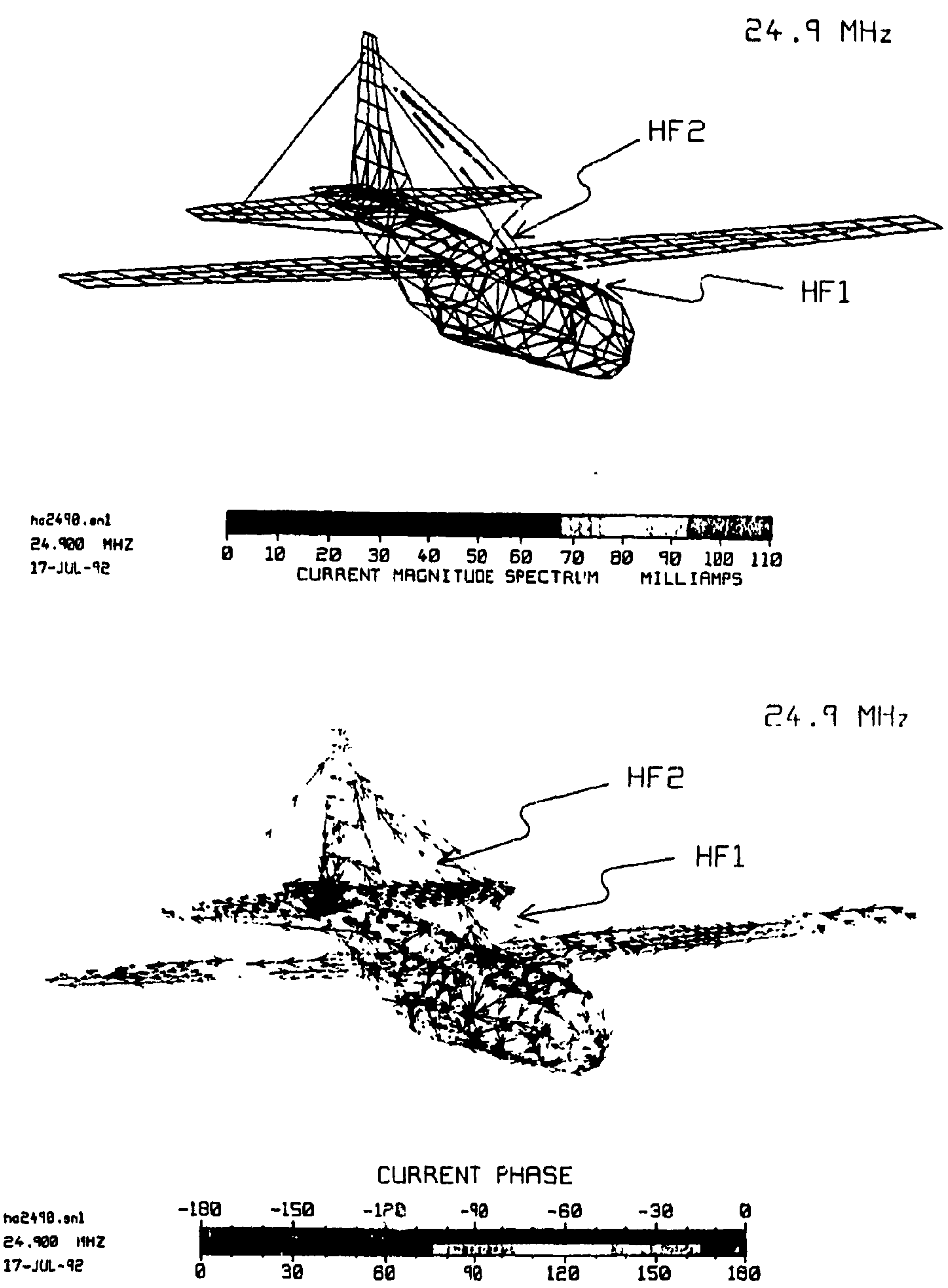

(d) 24.9 MHz

Fig. 5.7 (Cont'd)

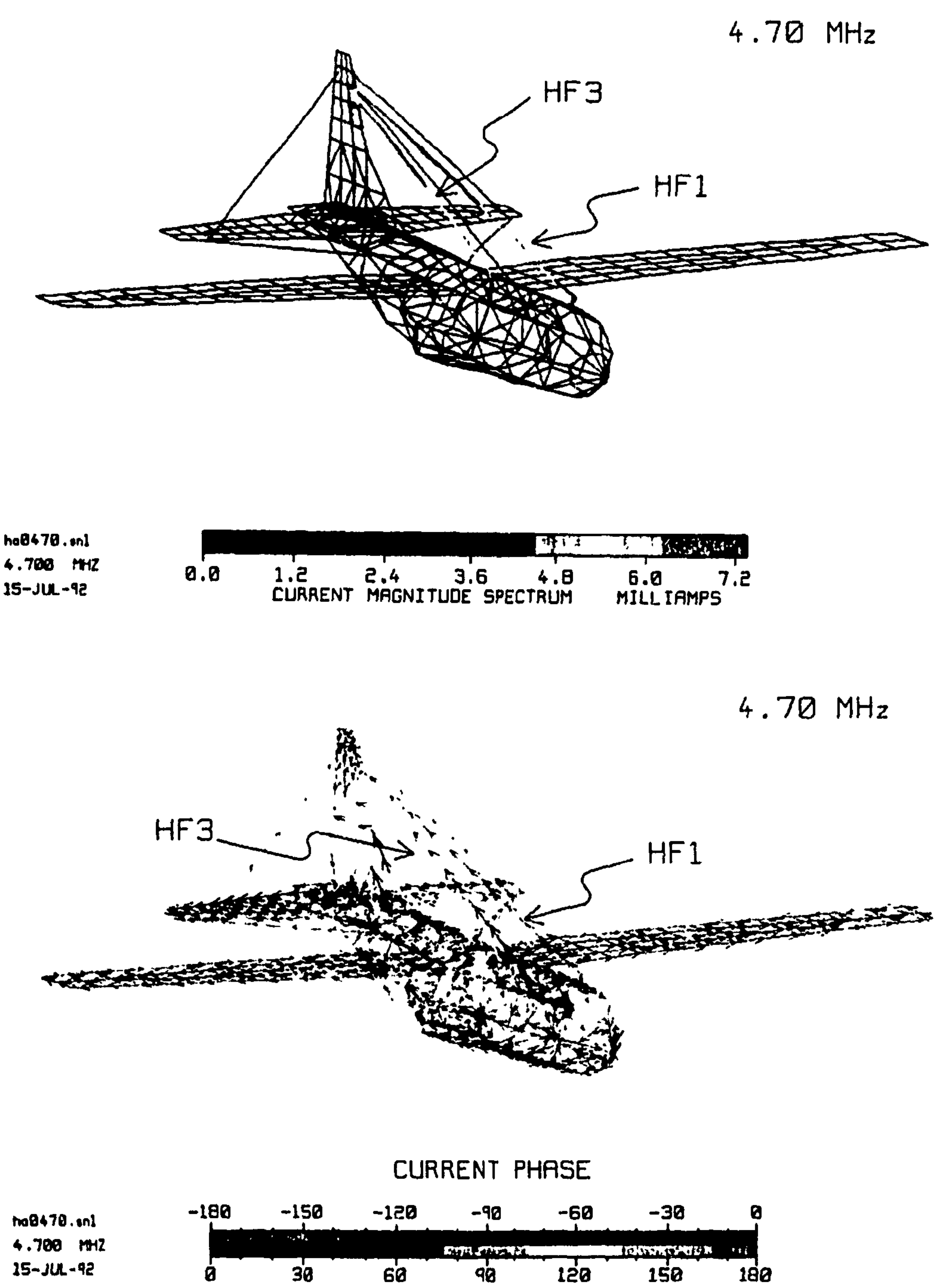

(e) 4.7 MHz

Fig. 5.7 (Cont'd)

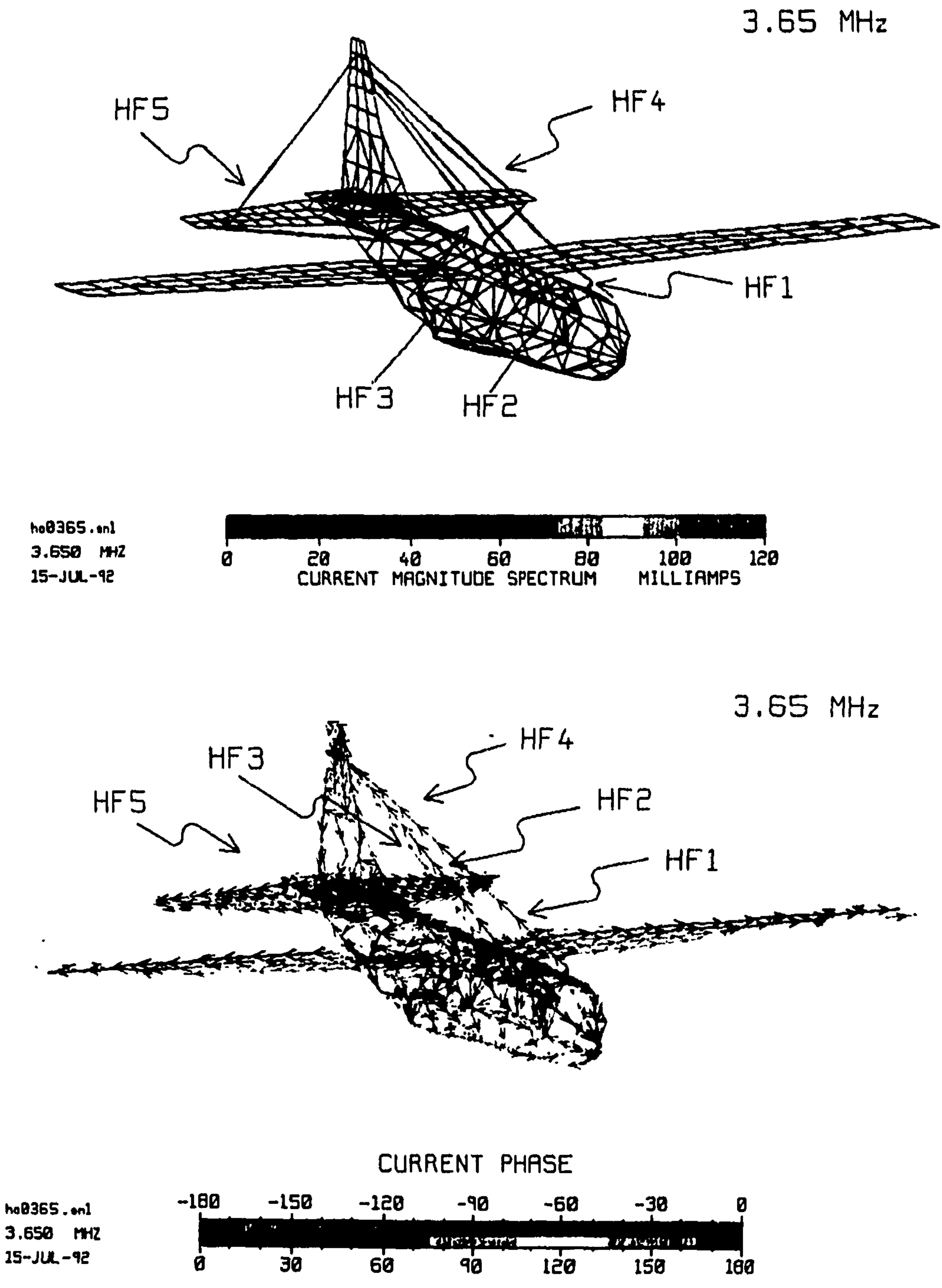

(f) 3.65 MHz

Fig. 5.7 (Cont'd)

current magnitude and phase on all the antennas (active and passive) exhibit the first resonant behavior with one magnitude peaks at each antenna feed point and one constant phase along each antenna. Note that the currents on HF1 and HF2 are in the same phase, as are the currents on HF4 and HF5. The phase of the currents on HF1 and HF2 is about 120° different from that on HF4 and HF5.

5.1.3.2 Current Distributions with the Passive Antennas Open-Circuited

Figures 5.8(a) through 5.8(c) show the current distributions at 9, 19.4, and 29.2 MHz, with HF1 active and with the passive antennas (HF2, HF3, HF4 and HF5) open-circuited to the airframe. The current distribution on HF3 shows that HF3 is at anti-resonance at all of these three frequencies. At these frequencies rapid changes in input resistance of HF1 were seen in Fig. 5.6(b). At 9 MHz, Fig. 5.8(a), the current on HF3 has a peak at the center of the antenna and gradually decreases to zero toward the open end and toward the base of the antenna, with a constant phase throughout the antenna. This is the first anti-resonance illustrated in Figure 5.5. HF2 also has a noticeable induced current but the magnitude is much smaller compared to HF3. In Fig. 5.8(b), HF3 is shown to be at the second anti-resonance at 19.4 MHz with two peaks and two constant-phase regions. At 29.2 MHz, where the oscillation of reactance takes place, large induced currents are seen on HF2 and HF3 in Fig. 5.8(c). Both HF2 and HF3 are shown to be at the third anti-resonance with three peaks in magnitude and three constant-phase regions. The current distributions at 6.4 and 14 MHz (not shown), where rapid changes in resistance were also seen, indicate that HF2 has large induced currents at these two frequencies and is at its first anti-resonance at 6.4 MHz and second anti-resonance at 14

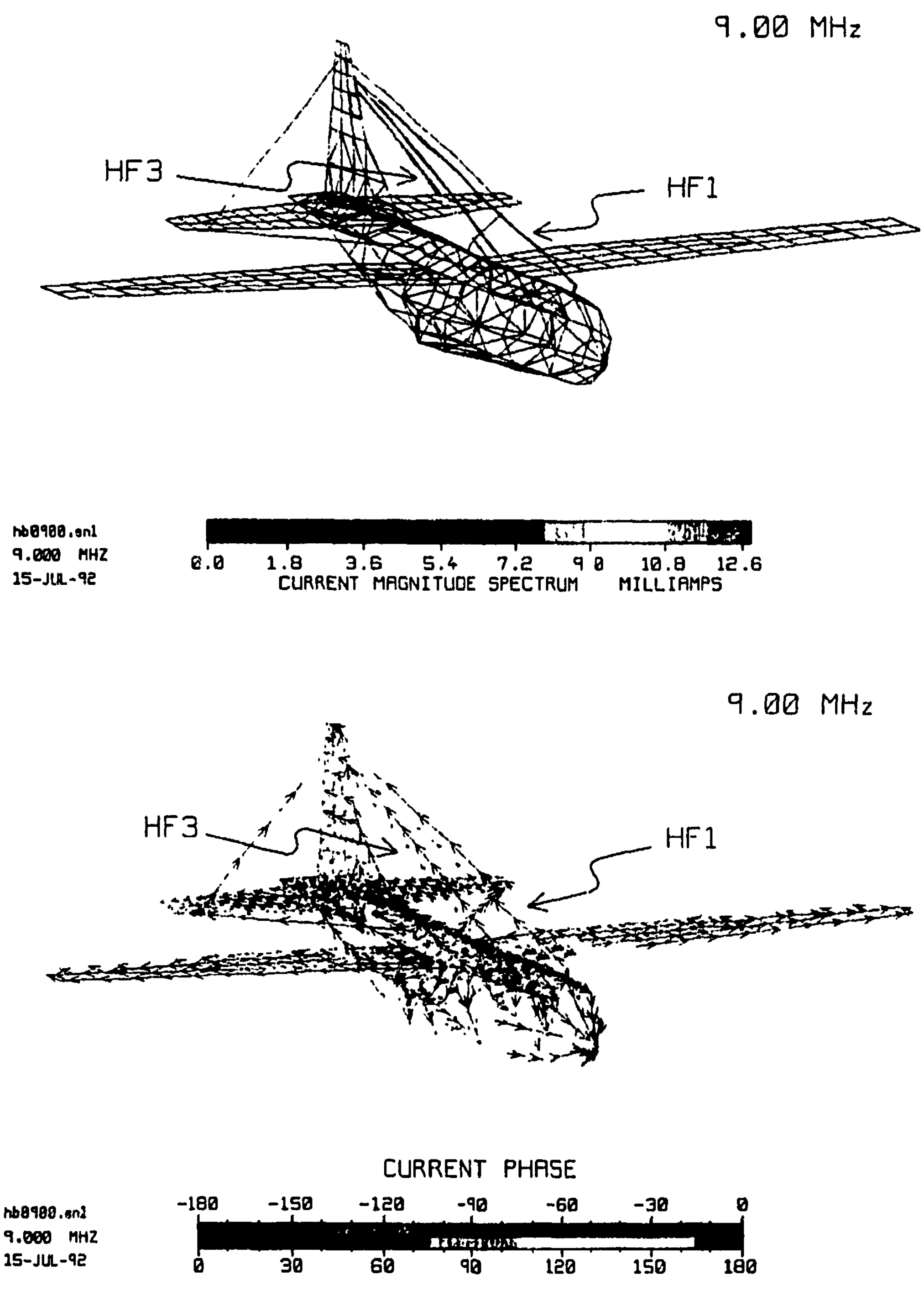

(a) 9.0 MHz

Fig. 5.8 Current distribution plots at selected frequencies for HF1 excited, passive antennas open-circuited.

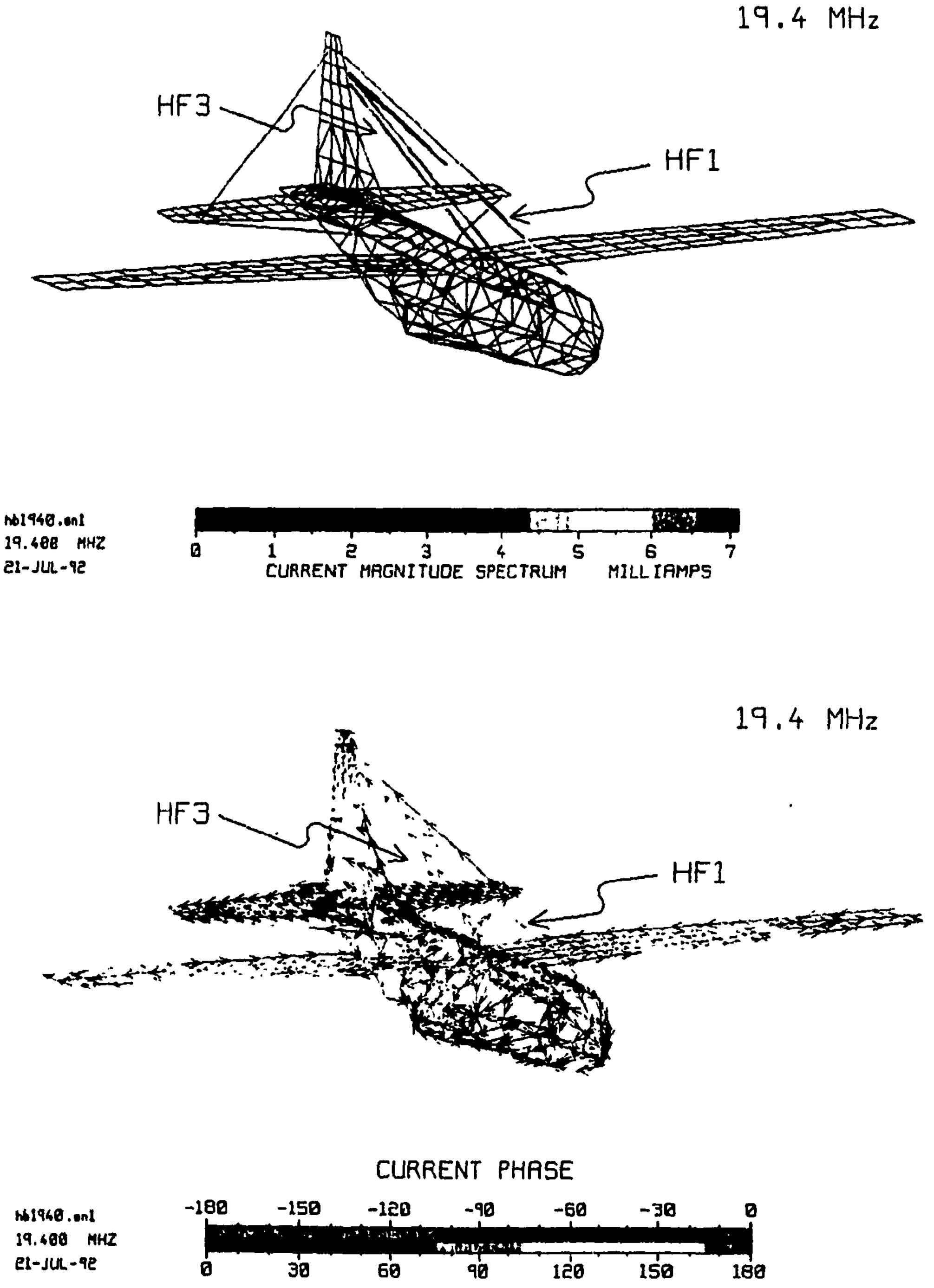

(b) 19.4 MHz

Fig. 5.8 (Cont'd)

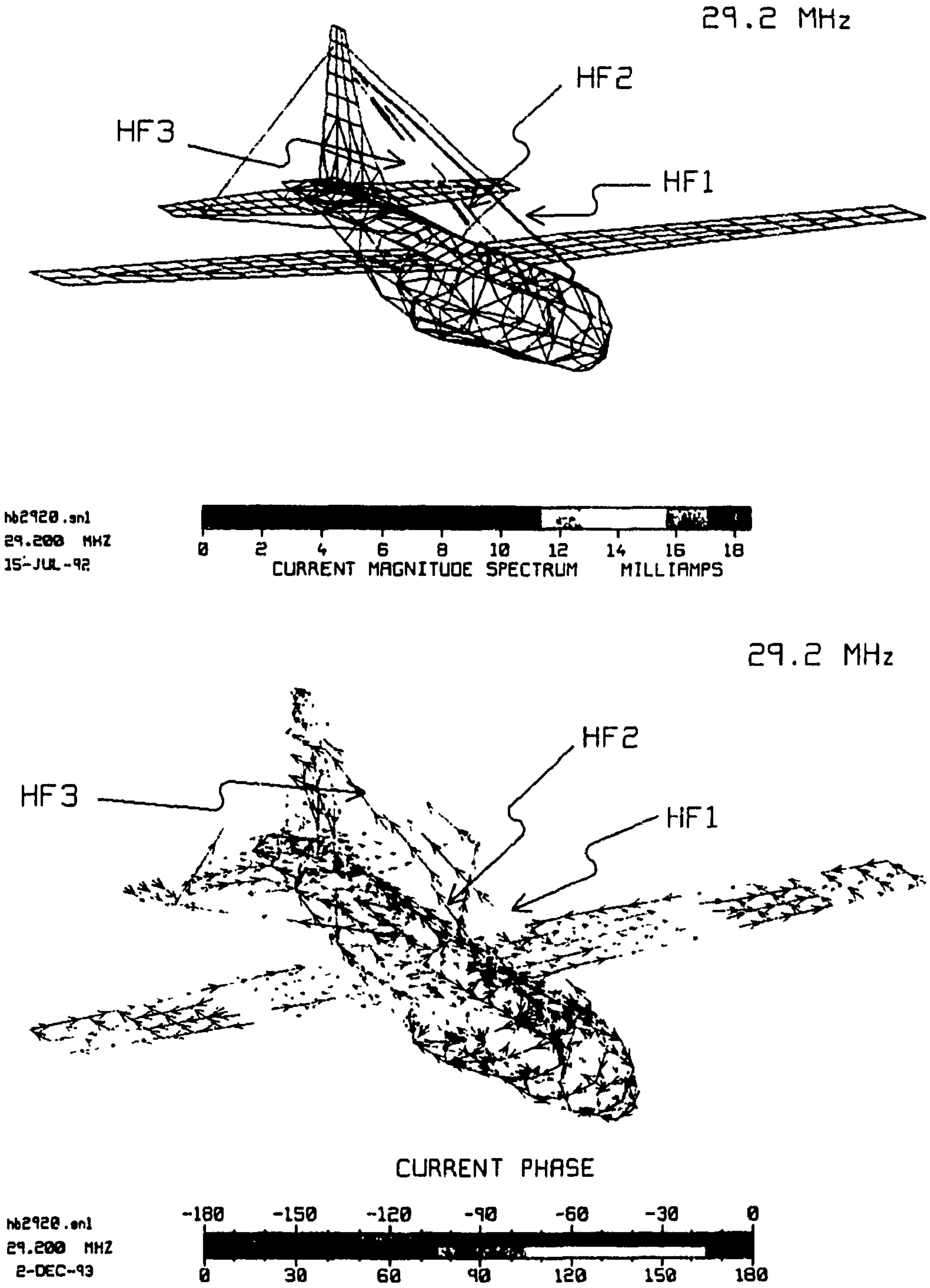

(c) 29.2 MHz

Fig. 5.8 (Cont'd)

MHz.

5.1.3.3 Current Distribution with 50 Ω Loading

Figure 5.9 shows the current distributions at 3.3 and 10.4 MHz, with HF1 active and with each passive antenna terminated in a 50 Ω resistance. HF2 is seen to have a relatively large induced current at these two frequencies. In Fig. 5.9(a), HF2 is seen to exhibit a first resonance phenomenon, although the magnitude of the induced current is much smaller compared to the short-circuit case in Fig. 5.7(a). A even smaller induced current is seen on HF3. When the frequency is increased to 10.4 MHz, where a very weak coupling indication is seen in the impedance curve, the small induced current on HF2 exhibits a second resonance phenomenon. The current distributions at 17.6 and 25 MHz not shown), where weaker coupling indications were observed in the resistance curve, reveal that small currents are induced on HF2 and these currents exhibit resonant behavior.

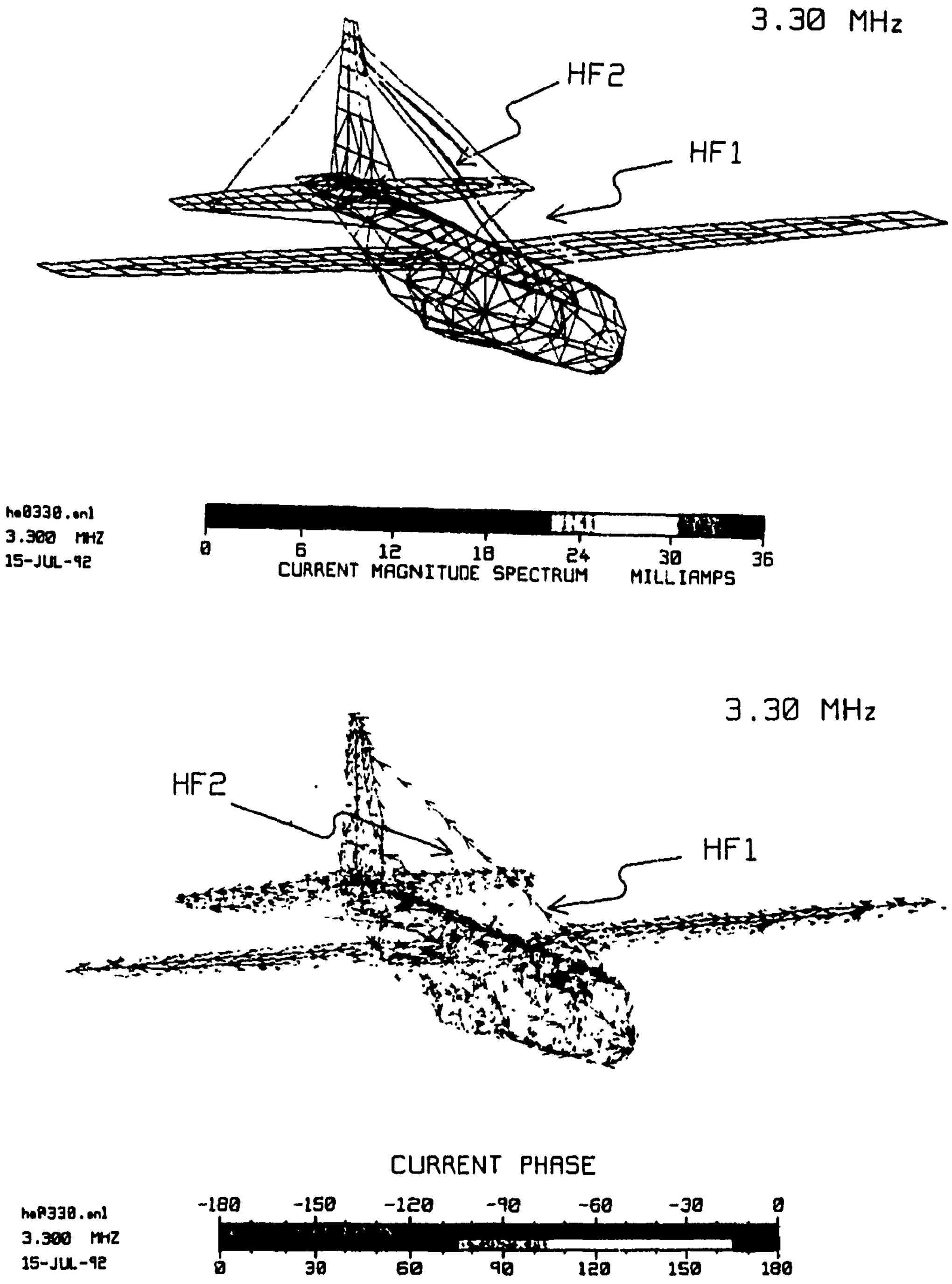

(a) 3.3 MHz

Fig. 5.9 Current distribution plots at selected frequencies for HF1 excited, passive antennas loaded by 50Ω.

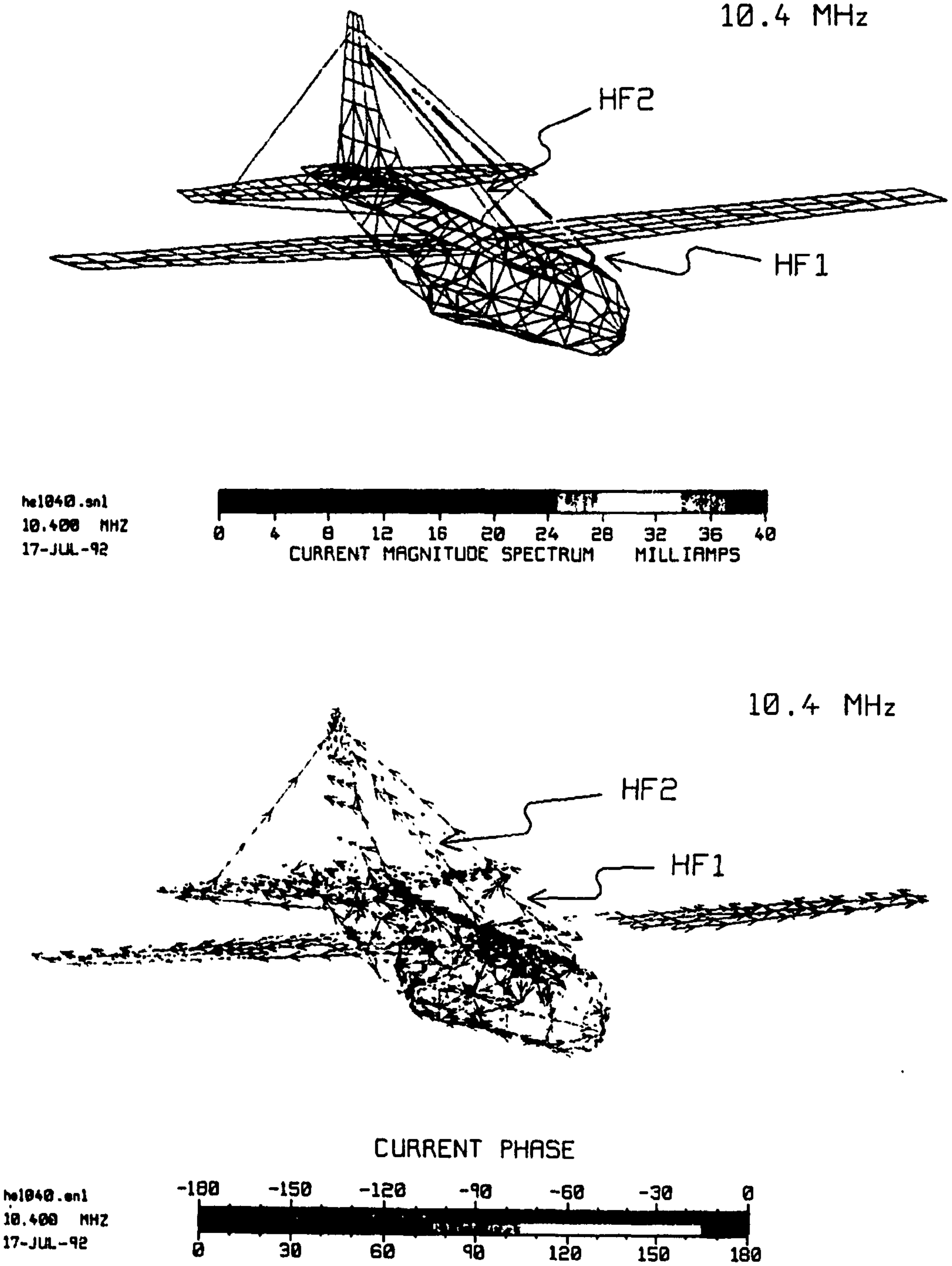

(b) 10.4 MHz

Fig. 5.9 (Cont'd)

5.1.4 HF4 as the Active Antenna

Although HF4 is a "dog-leg" shaped bent wire antenna, its input impedance pattern is still comparable to that of a dipole in free space. As shown in Fig. 5.10, the input impedances for all three loading conditions for passive antennas are very similar, indicating that for the most part, HF4 does not strongly couple to the other antennas. However, the input resistance changes quite abruptly near 3.6 and 4.7 MHz for the short-circuit case but not for the other two cases. The rapid changes will be shown to be related to strong inter-antenna coupling at these frequencies by inspection of current distributions at associated frequencies, which is shown in Fig. 5.11.

Fig. 5.10(a) shows the input impedance of HF4 for passive antennas short-circuited to the airframe. Compared to the impedance curves of HF1 shown in Fig. 5.6, the impedance curves of HF4 are less "periodical". The input resistance does not change periodically with frequency. One can see that it has a relatively "flat" region between 9 and 17 MHz. On the other hand, the reactance has uneven frequency periods. Although the reactance can be seen to go through four complete cycles, it changes from negative to positive and then changes back to negative "faster" in the second and fourth cycles than in the first and third cycles.

When the passive antennas are open-circuited to the airframe, no significant changes are observed in reactance compared to the short-circuited case, as shown in Fig. 5.10(b). The most obvious changes take place in the resistance curve near 3.6 and 4.7 MHz, where the resistance has abrupt changes with frequency in the short-circuit case and is smooth in the open-circuit case.

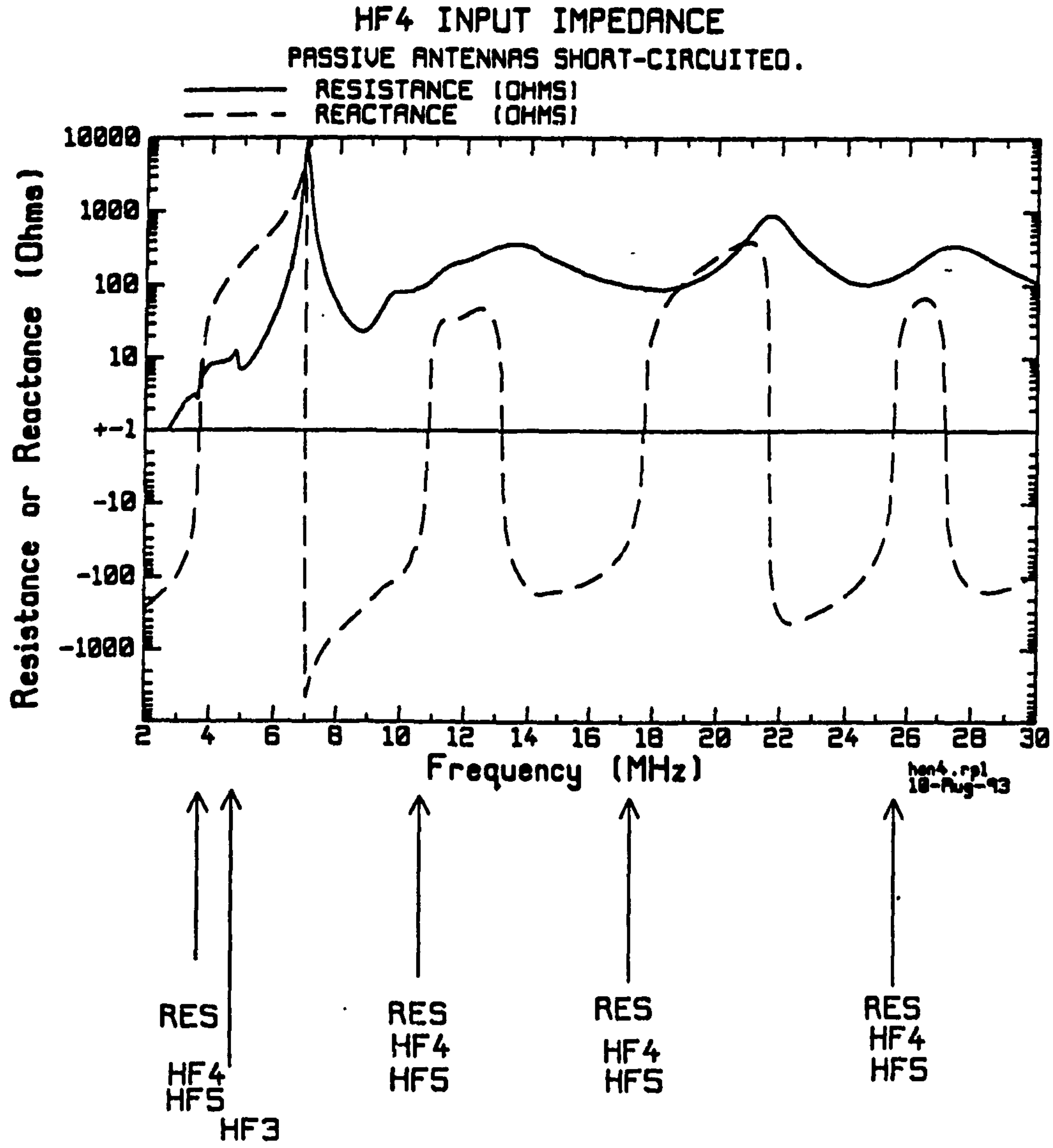

(a) Passive antennas short-circuited

Fig. 5.10 Input impedance of antenna HF4 for three loading conditions for passive antennas.

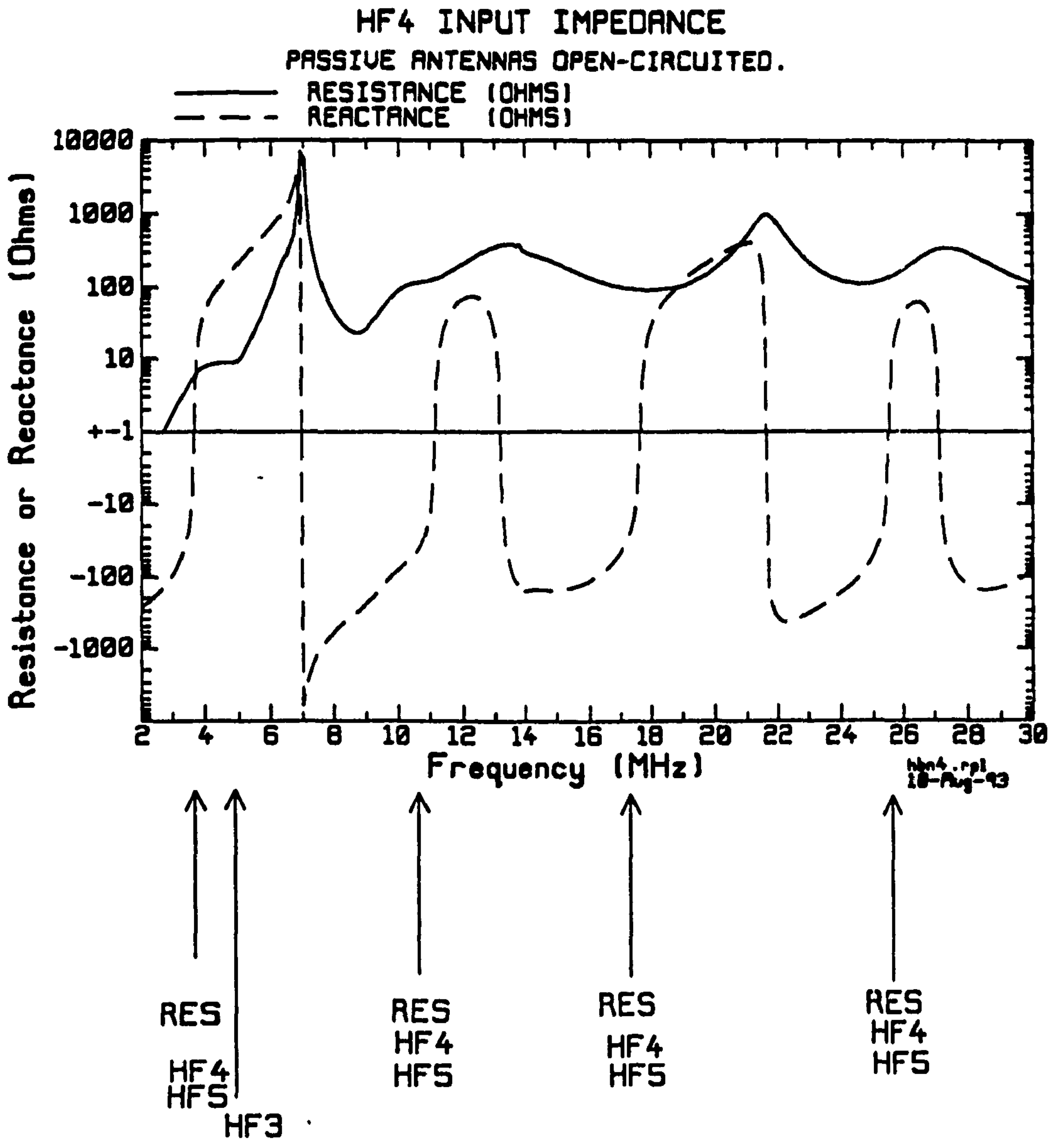

(b) Passive antennas open-circuited

Fig. 5.10 (Cont'd)

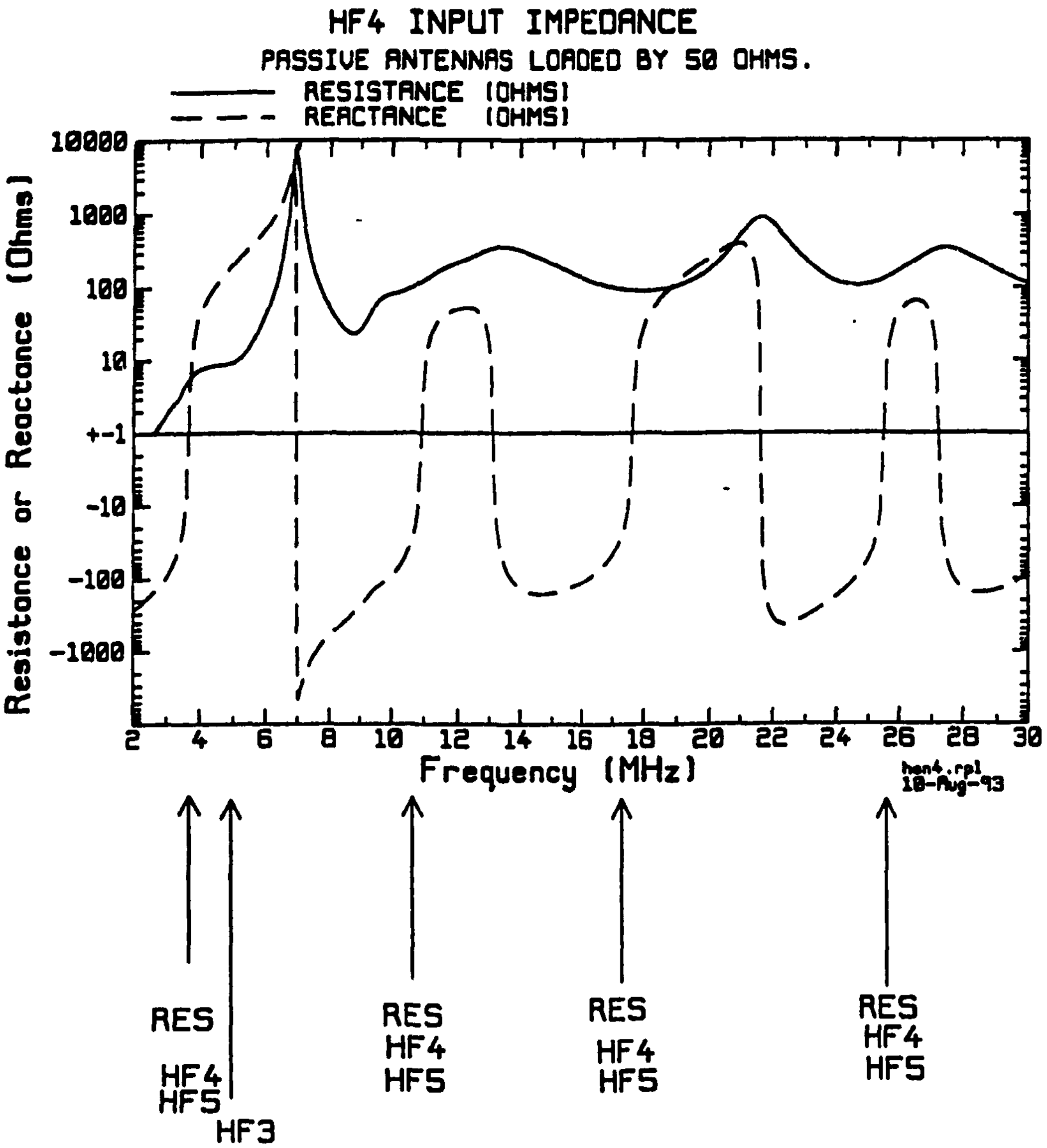

(c) Passive antennas loaded by 50Ω

Fig. 5.10 (Cont'd)

In Fig. 5.10(c), the input impedance of HF4 with passive antennas terminated in 50 Ω loads is shown to be nearly identical to the impedance for the open-circuit case in Fig. 5.10(b). This is very different from the results for HF1 active where substantial differences are observed between the results for open-circuit and 50 Ω termination.

5.1.4.1 Inter-Antenna Coupling

The magnitude of inter-antenna coupling due to this active antenna is much smaller than that in the case of HF1 as the active antenna. This can be seen from the magnitude of the induced current and the magnitude of the induced voltages at the terminals of passive antennas which will be presented shortly. We have seen that for HF1 active, coupling indications such as rapid changes in impedance with frequency fall near the resonant frequencies of the passive antennas when they are short-circuited to the airframe. However, for HF4 active, such indications only appear at the lower end of the HF band. Figures 5.11(a) and 5.11(b) show the distributions of current at 3.6 and 4.7 MHz, respectively, for HF4 active and passive antennas short-circuited. At 3.65 MHz, Fig. 5.11(a), all the passive antennas are shown to have relatively large induced currents, especially HF1, HF2, and HF5 whose first resonant frequencies are closer to this frequency than HF3. The induced current on the passive antenna HF5 is even larger than the exciting current on the active antenna HF4. In Fig. 5.11(b), HF3 is shown to have large induced current at its resonant frequency of 4.7 MHz, as in the case of HF1 active. This suggests that we should examine the current distributions at higher order resonant frequencies of the passive antennas although no obvious coupling indications are seen in the impedance curve. The results show that coupling indeed occurs at those frequencies

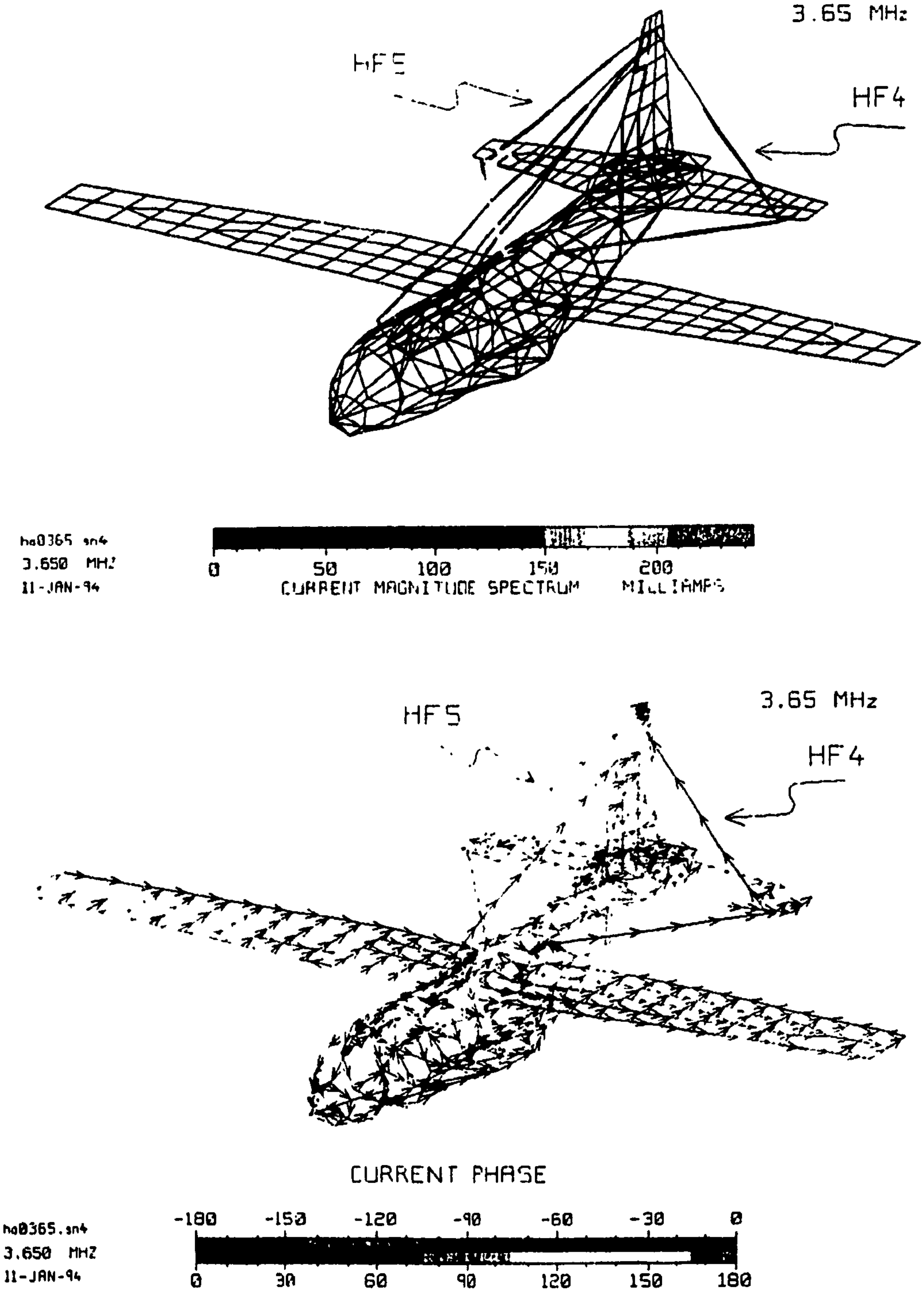

(a) 3.65 MHz

Fig. 5.11 Examples of inter-antenna coupling for HF4 active and passive antennas short-circuited.

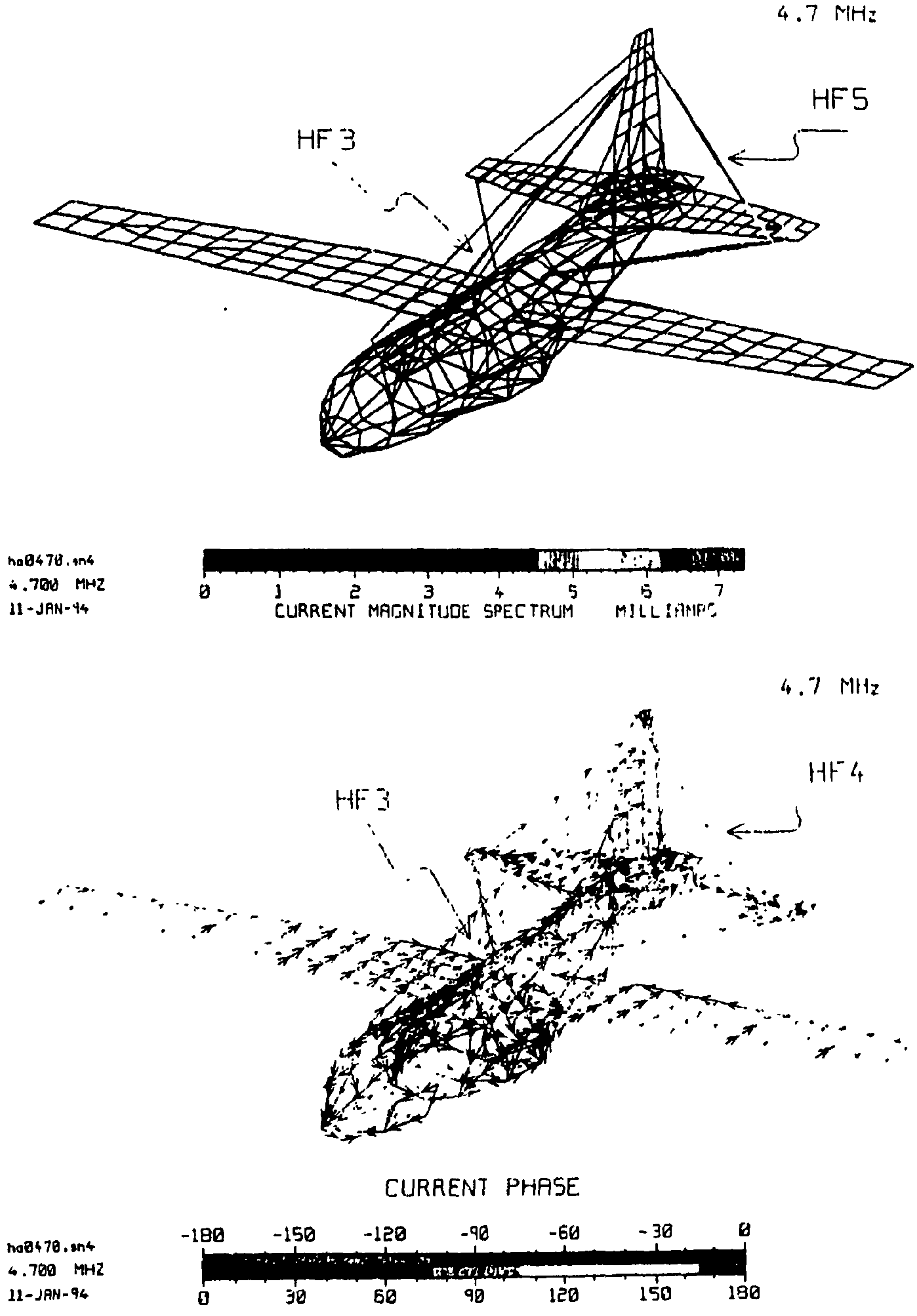

(b) 4.7 MHz

Fig. 5.11 (cont'd)

as in the case of HF1 active, although the magnitude of coupling is somewhat lower.

5.1.4.2 Antenna-to-Airframe Coupling

Strong antenna-to-airframe coupling co-exists with the inter-antenna coupling throughout the HF band. The antenna-to-airframe coupling on this aircraft has a broad-band nature, that is, strong coupling can exists over a wide frequency band. This can "smooth out" the "peaks" due to inter-antenna coupling in the impedance curve, especially if these "peaks" are small. Three major induced current paths due to antenna-to-airframe coupling are identified on this EC-130 airframe: (1) the path along antenna HF4, port side of the fuselage and the port horizontal stabilizer shown in Fig. 5.12(a); (2) the path along antenna HF4 and the port (left) wing of the aircraft shown in Fig. 5.12(b); and (3) the path along the vertical stabilizer and the left horizontal stabilizer, as shown in Fig. 5.12(c). The currents along the first two paths are found to be large near the following frequencies: 4, 12, 20, and 27 MHz, whereas the current along the third path is largest near 9 MHz.

Fig. 5.13(a) shows the current distribution at 4 MHz for HF4 active and the passive antennas short-circuited to the airframe. The current magnitude is plotted in a dB scale with a reference value of 1 A. It is recognized that there are two current paths: the path consisting of HF4, part of the fuselage and left horizontal stabilizer as outlined in Fig. 5.12(a) and the path consisting of HF4 and the left wing as outlined in Fig. 5.12(b). An examination of the induced current path lengths shows that they are approximately equal to $\lambda/2$ at 4 MHz. The phase along the path outlined in Fig. 5.12(a) is seen to be constant (note that the arrowheads for half of the path are reversed and complementary

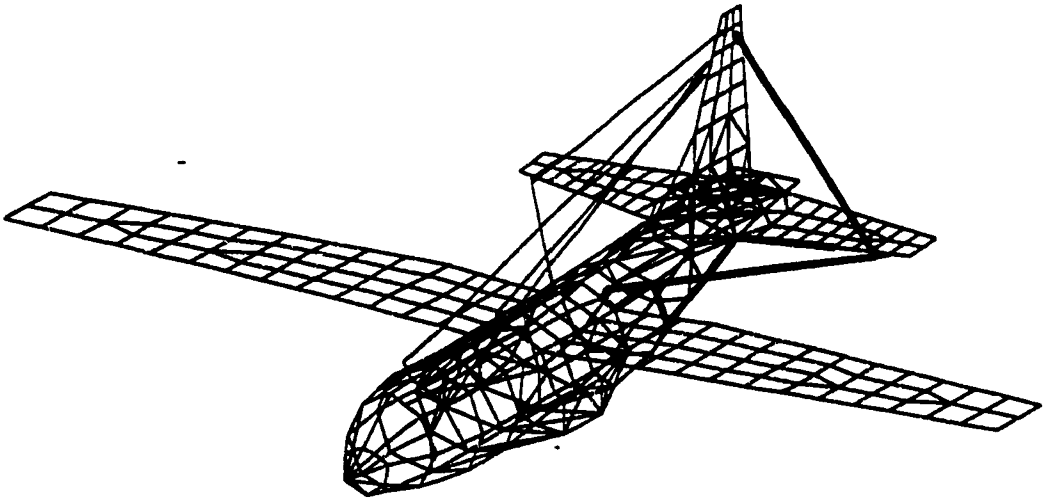

(a) HF4, fuselage, and port horizontal stabilizers.

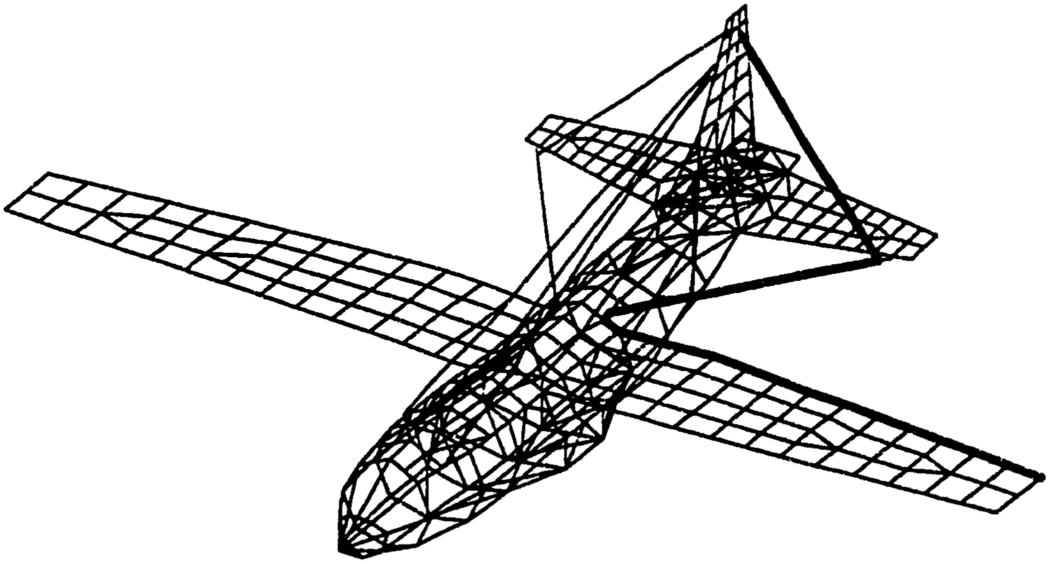

(b) HF4 and port wing.

Fig. 5.12 Current paths on the EC-130 airframe due to Excitation of HF4.

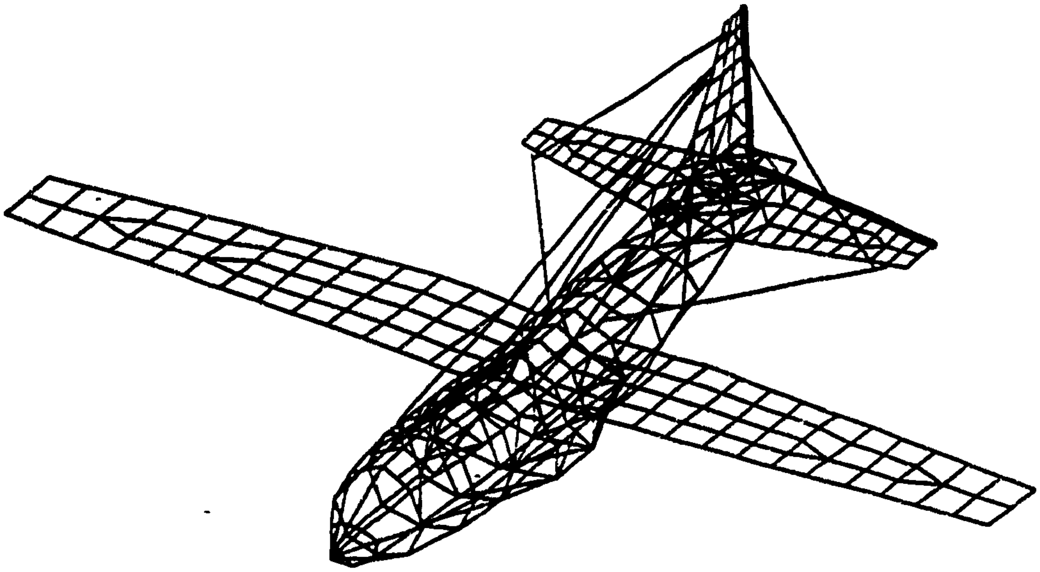

(c) Vertical and port horizontal stabilizers.

Fig. 5.12 (Cont'd)

colors (green and violet) are seen). For the path outlined in Fig. 5.12(b), however, there is a 45° shift in phase between the wing and the antenna (HF4). In order to see the current distributions along these two current paths more clearly, the rectangular axis mode is to unfold the path used in Fig. 5.13(b) to display the current magnitude and phase. We can see that the current on each path is roughly like the current on a half-wavelength resonant dipole with a magnitude peak at the center and one constant phase throughout the path.

At 9 MHz, relatively high induced currents are found on the vertical and the port horizontal stabilizer, as can be seen in Fig. 5.14. This is another $\lambda/2$ resonant path which goes along the vertical and horizontal stabilizers as illustrated in Fig. 5.12(c). The phase plot in Fig. 5.14 clearly shows that this path has a constant phase by the violet arrows along the trailing edge of both the dorsal and the horizontal stabilizers. An examination of the path length reveals that this is a half-wavelength resonant path. The strong vertically directed currents on the vertical stabilizer can significantly enhance the E_θ field near this frequency and result in high $\%E_\theta$ power.

Fig. 5.15 shows the current distribution at 12 MHz (passive antennas short-circuited to the airframe). Some induced currents can be seen on the port wing and the stabilizers. The phase plot shows that the phase along the vertical and port horizontal stabilizers is still constant, although the length of this path is longer than the half-wave resonant length at this frequency.

When the frequency is increased to 20 MHz, the only noticeable induced current on the airframe is along the aft-fuselage and port stabilizer, as shown in Fig. 5.16. The

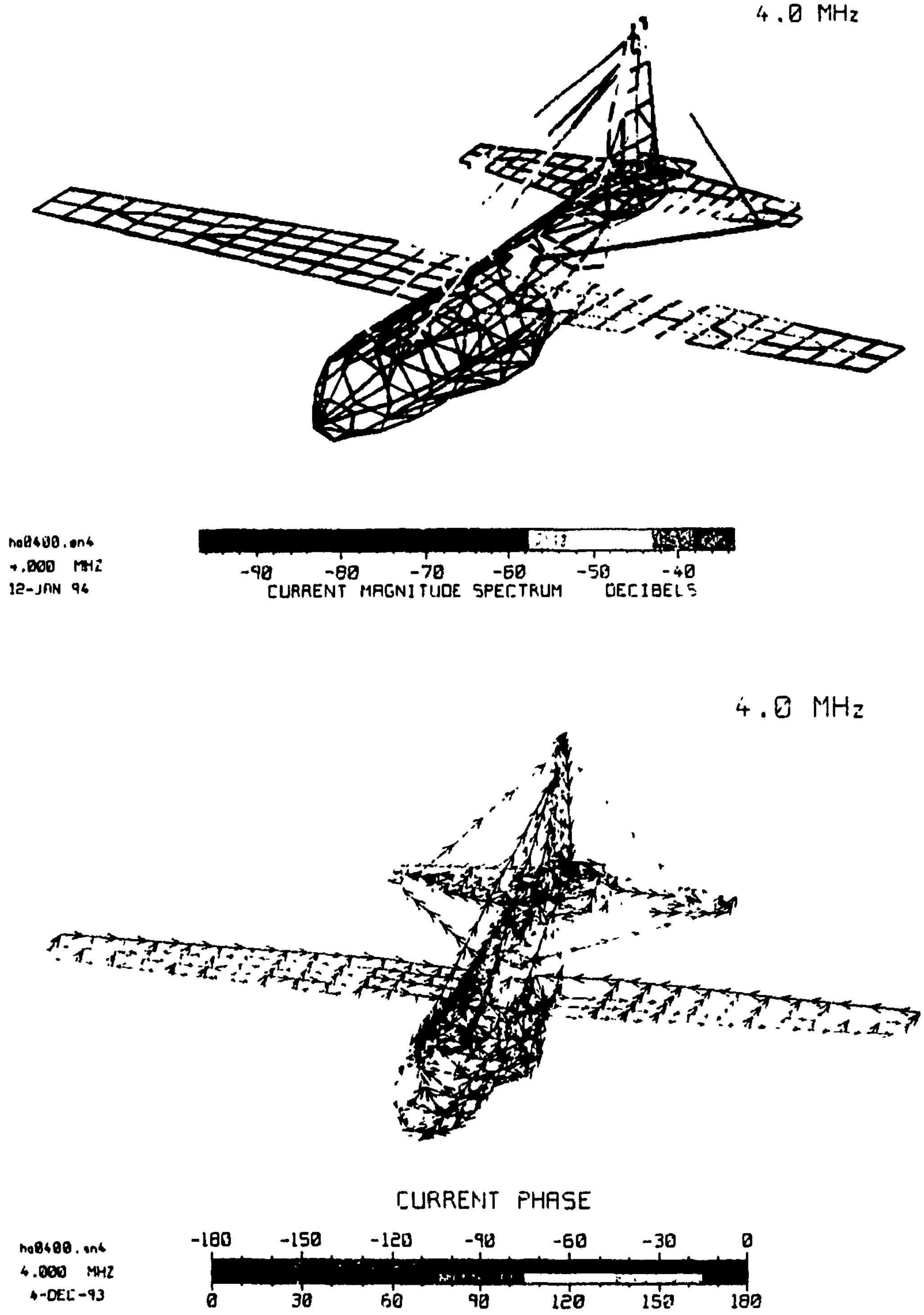

(a) Current magnitude and phase shown in color

Fig. 5.13 Induced currents on the airframe at 4 MHz for HF4 excited, passive antennas short-circuited.

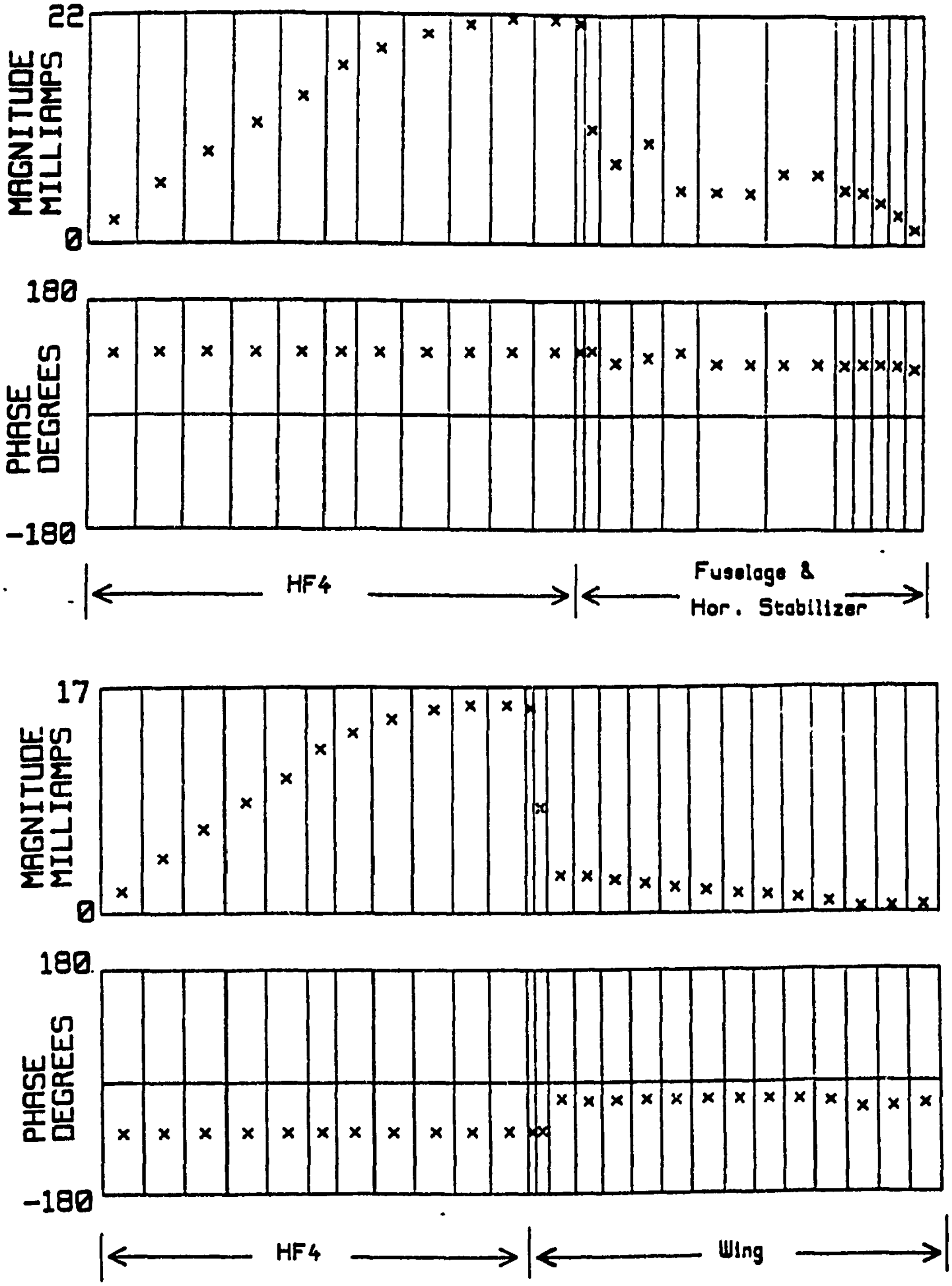

(b) Currents along the paths at 4 MHz displayed in the rectangular axis mode

Fig. 5.13 (cont'd)

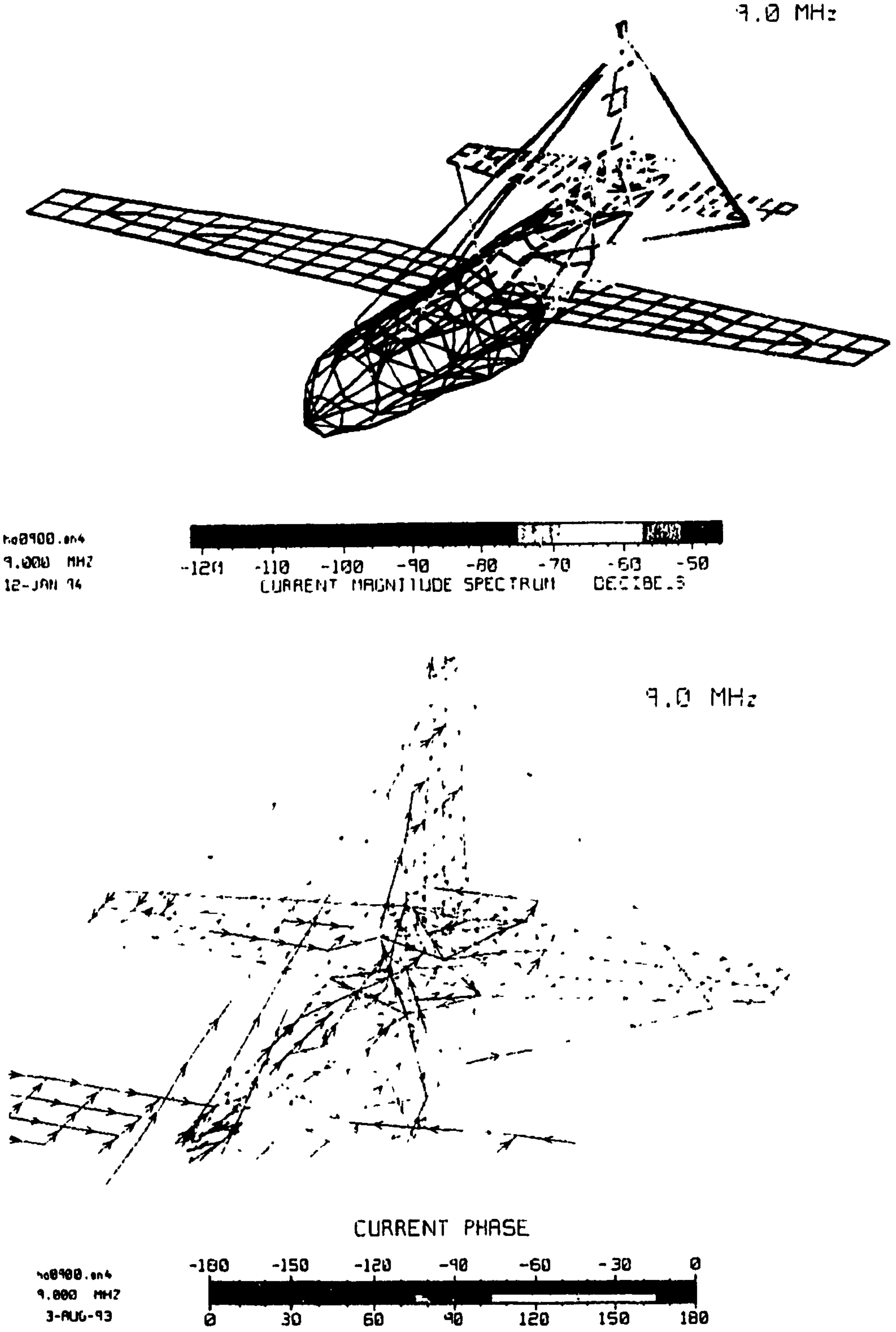

Fig. 5.14 Induced currents on the airframe at 9 MHz for HF4 and passive antennas short-circuited.

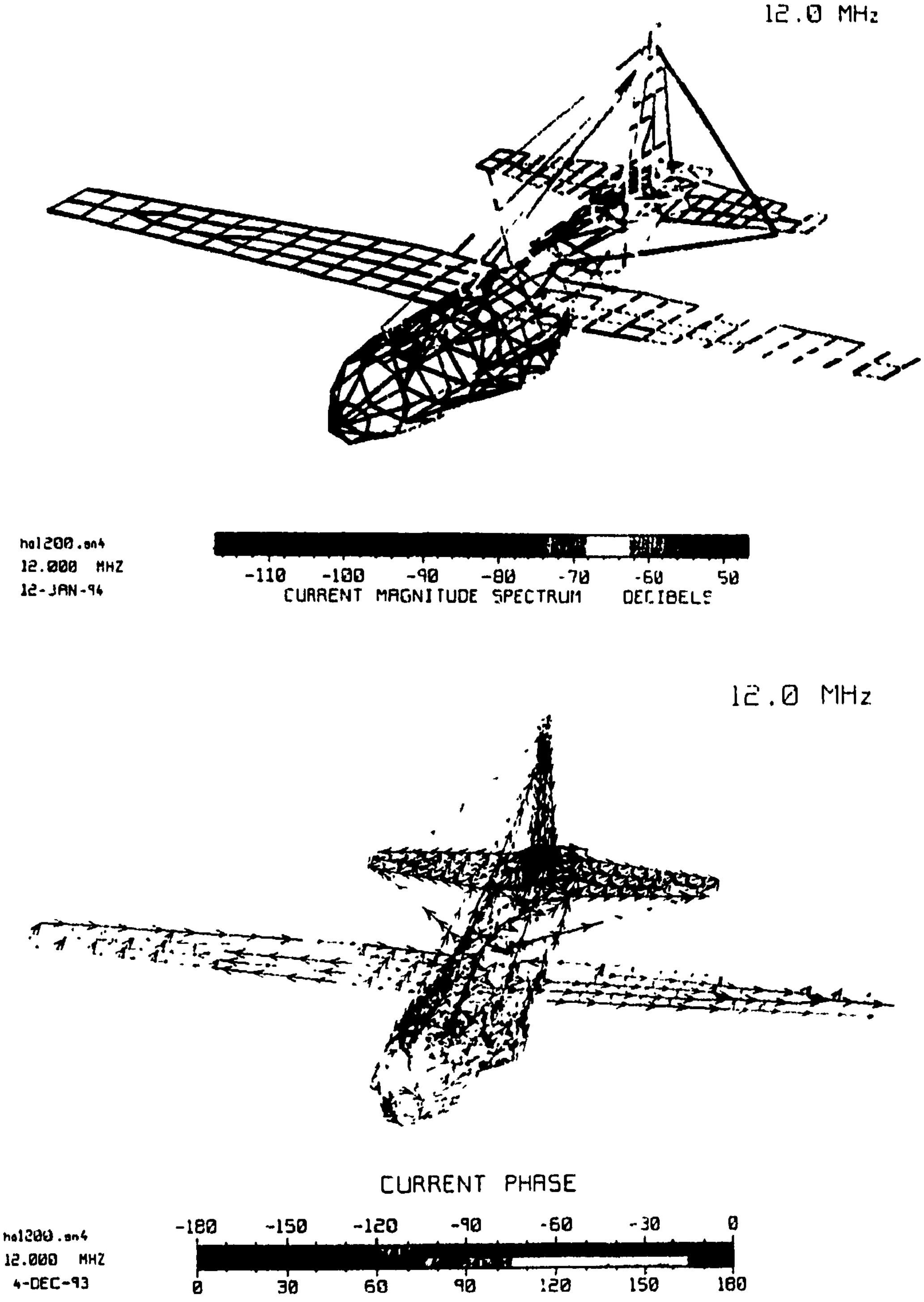

Fig. 5.15 Induced currents on the airframe at 12 MHz for HF4 active and passive antennas short-circuited.

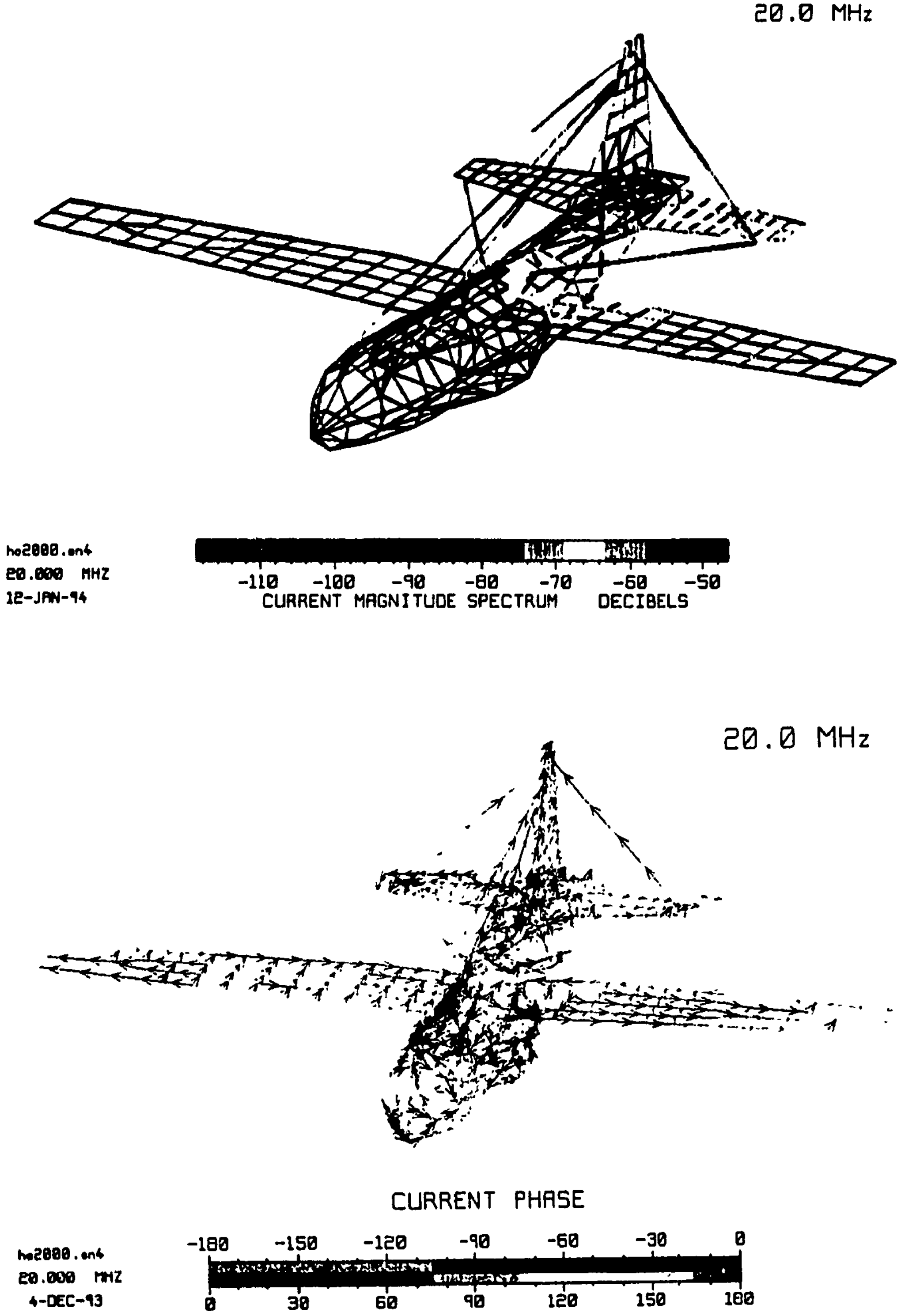

Fig. 5.16 Induced currents on the airframe at 20 MHz for HF4 active and passive antennas short-circuited.

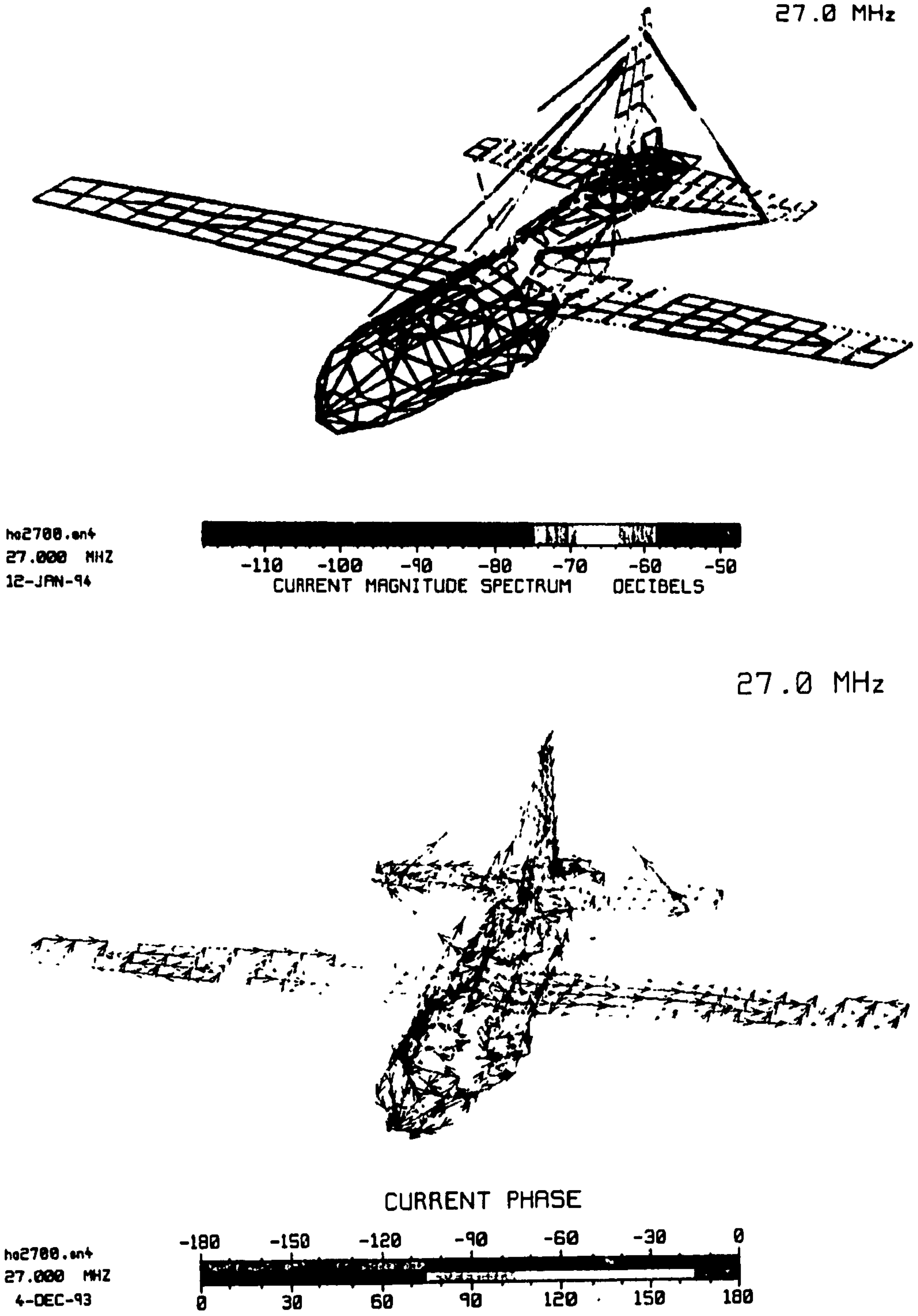

Fig. 5.17 Induced currents on the airframe at 27 MHz for HF4 active and passive antennas short-circuited.

phase plot does not show that this is a resonant path because the distribution of current phase cannot be associated with any resonant phase patterns.

Finally at 27 MHz, the small induced currents are found along the forward-edge and of the port horizontal stabilizer and the aft-edge of the port wing, as shown in Fig. 5.17. An examination of the phase plot does not lead to any identification of resonances.

5.1.4.3 Coupling in the Cases of Open-Circuit and 50 Ω Loading

As mentioned earlier, the impedance curve with the passive antennas open-circuited to the airframe is very similar to the one for 50Ω termination. Both curve do not have obvious coupling indications. However, examinations of current distributions at small intervals show that inter-antenna and antenna-to-airframe coupling do exist for these two loading conditions for passive antennas. The antenna-to-airframe coupling modes are the same as in case of short-circuit, that is, there are three major current paths and the coupling is strongest near the frequencies mentioned above. For inter-antenna coupling, the coupling modes found in the case of HF1 also applies here. In the open-circuit case, strong induced current is found on a passive antenna near the anti-resonant frequencies of this passive antenna. In the case of 50Ω termination, strong induced currents are observed on passive antennas near the resonant frequencies of the active antenna (HF4). The induced voltages at the terminals of the passive antennas will be presented shortly. These voltages curves will help us further analyze the coupling modes when the passive antennas are loaded. Before going to this, we will first reexamine the resonant and anti-resonant frequencies of HF antennas on this aircraft from the computed results and compare them with the "estimated" or "ideal" frequencies shown in Table 5.1.

5.1.5 Computed Resonant Lengths of the HF antennas on the EC-130

It was pointed out in Sec. 5.1.1 that the resonant and anti-resonant frequencies of a monopole antenna can be calculated based on its length. The similarity in input impedance between the HF antennas mounted on the EC-130 and the monopole antenna enables us to identify the resonant and anti-resonant frequencies using the monopole model. The zero-crossing points in the computed reactance curves shown in Fig. 5.6 and Fig. 5.8 correspond to the resonant or anti-resonant frequencies of HF1 and HF4, respectively. As demonstrated in the two previous sections, the inter-antenna coupling phenomena are found to have a relationship with the resonances and anti-resonances of the antennas by examinations of the current distributions. The reasons for identifying these resonant and anti-resonant frequencies from the reactance curves are to verify that the current distributions at these frequencies follow the patterns shown in Fig. 5.5 and to compare with the "ideal" frequencies listed in Table 5.1. Recall that we calculated the input impedance of HF1 and HF4 for three loading conditions for the passive antennas. As mentioned in the two previous sections, the loading conditions have great influence on the input impedance in the case of HF1 but have much smaller influence in the case of HF4. As far as the zero-crossing points in the reactance curves (the ones which are due to resonant lengths and not to coupling) are concerned, however, the locations of these points are not much changed for all three loading conditions. We will use the curves for 50 Ω terminations, which have weakest coupling indications, as our reference curves to derive the resonant and anti-resonant frequencies for the HF antennas.

As shown in Fig. 5.6(c), the reactance curve going from negative to positive crosses the zero level (+-1 in the plot) at 3.2, 10.4, 17.6, and 25.0 MHz. These points correspond to the resonant frequencies of HF1. The anti-resonant frequencies correspond to the zero-crossing points where the reactance curve is going from positive to negative: 6.4, 13.8, 21.0, and 28.8 MHz. Since HFl and HF2 have the same length and they are symmetrically mounted on the aircraft, we assume HF2 has the same resonant and anti-resonant frequencies as HF1.

Fig. 5.8(c) shows the input impedance of HF4 for passive antennas terminated in 50 Ω loads. Again, we identify the resonant frequencies of HF4 by examining the frequencies of the positive-going zero-crossing points in the reactance curve. The resonant frequencies are: 3.6, 10.8, 17.8, and 25.2 MHz. Similarly, an examination of the negative-going zero-crossing points in the reactance curve gives the anti-resonant frequencies: 7.0, 13.0, 22.0, and 27.0 MHz. These resonant and anti-resonant frequencies also applies for HF5 because HF4 and HF5 are identical in length and shape and are symmetrically mounted on the airframe.

Although HF3 is not used for transmitting, in order to find out its resonant and anti-resonant frequencies in the HF band, we computed the input impedance across the HF band for HF3 active with passive antennas terminated in 50 Ω loads. The reactance curve obtained from the results is used to identify the frequencies of interest using the method described above. The resonant frequencies are found to be: 4.7, 14.1, and 25.0 MHz. The anti-resonant frequencies are 9.0, 19.0 and 29.2 MHz. Note that the fourth resonant and anti-resonant frequencies of HF3 are outside the HF band. Table 5.2 summarize the resonant and anti-resonant frequencies for all five HF antennas on the EC-

Table 5.2 Resonant and Anti-Resonant Frequencies for the HF Antennas on the EC-130 Based on the Computed Antenna Input Impedances.

Ant.	Frequency (MHz)							
	1st order		2nd order		3rd order		4th order	
	Res.	Anti-Res.	Res.	Anti-Res.	Res.	Anti-Res.	Res.	Anti-Res.
HF1	3.2	6.4	10.4	13.8	17.6	21.0	25.0	28.8
HF2	3.2	6.4	10.4	13.8	17.6	21.0	25.0	28.8
HF3	4.7	9.0	14.1	19.0	25.0	29.2	–	–
HF4	3.6	7.0	10.8	13.0	17.8	22.0	25.2	27.0
HF5	3.6	7.0	10.8	13.0	17.8	22.0	25.2	27.0

These resonant and anti-resonant frequencies, however, are somewhat different from the values calculated based on the lengths of the antennas and the transmission line theory [54] tabulated in Table 5.1.

There are several reasons that may cause the discrepancy in resonant and anti-resonant frequencies between the computed and the ideal values. The first thing one should note is that these aircraft antennas are not vertical monopoles and the ground plane (which is the airframe in this case) is not flat and infinite in size. The second reason is that the antennas have finite radii and hence the current path along an antenna is longer than the antenna length because the current can flow onto the "end caps". The third reason is the capacitance present between the open-circuited antenna ends and the nearby vertical and horizontal stabilizers which NEC may not model precisely.

A relatively simple formula for computing the impedance of a cylindrical antenna can be derived based on a sinusoidal current distribution using the induced emf method explained in [9]. This formula, which is given below, is valid when the half length of the dipole antenna is not much longer than a quarter wavelength [30].

$$Z_{in} = R(\beta\ell) - j\,[120(\ln\frac{2\ell}{a} - 1)\cot\beta\ell \; - \; X(\beta\ell)] \qquad (5.2)$$

where Z_{in} = input impedance in ohms of a center-driven cylindrical antenna of total length 2ℓ and of radius a, $\beta\ell = 2\pi(\ell/\lambda)$ = electrical length, corresponding to ℓ, measured in radians.

The functions $R(\beta\ell)$ and $X(\beta\ell)$ are tabulated in Table 5.2 for the range $\beta\ell \le \pi/2$. An examination of the above equation shows that the antenna does not resonate when the half length of the antenna is exactly equal to $\lambda/4$. Instead, it will resonate when the half length is a little less than $\lambda/4$. The antenna is at resonance when the reactance is zero

$$120(\ln\frac{2\ell}{a} - 1)\cot\beta\ell \; - \; X(\beta\ell) = 0 \qquad (5.3)$$

or

$$\cot\beta\ell = \frac{X(\beta\ell)}{120(\ln\frac{2\ell}{a}-1)} \qquad (5.4)$$

If the length is much larger than the radius, the right hand side of Eq. 5.4 must be equal to a positive small value because $X(\beta\ell)$ is positive as shown in Table 5.3. This implies that $\cot k\ell$ is not equal to zero at resonance but has a small positive value. In order to satisfy this condition, ℓ must be a little less than $\lambda/4$. This is consistent with the computed results shown in Table 5.2. One can also explain the resonant frequency shift from a physical point of view. Since the current can flow onto the "end caps" of an antenna with a finite radius, the actual length of the current path may longer than the length of the antenna and hence lower the resonant frequency.

Table 5.3 Values of $R(\beta\ell)$ and $X(\beta\ell)$ in Equation 5.2 for the Range $\beta\ell \leq \pi/2$ [30]

$\beta\ell$	$R(\beta\ell)$	$X(\beta\ell)$	$\beta\ell$	$R(\beta\ell)$	$X(\beta\ell)$
0	0	0	0.9	18.16	15.01
0.1	0.1506	1.010	1.0	23.07	17.59
0.2	0.7980	2.302	1.1	28.83	20.54
0.3	1.821	3.818	1.2	35.60	23.93
0.4	3.264	5.584	1.3	43.55	27.88
0.5	5.171	7.141	1.4	52.92	32.20
0.6	7.563	8.829	1.5	64.01	38.00
0.7	10.48	10.68	$\pi/2$	73.12	42.46
0.8	13.99	12.73			

Examinations of the currents on the antennas at the frequencies listed in Table 5.2 reveal that the currents do distribute in accordance with the resonant or anti-resonant patterns shown in Fig. 5.5. This means that the frequencies listed in Table 5.2 are indeed the resonant or anti-resonant frequencies of the antennas. Also, the identification of resonance modes based on examinations of current distributions in Sections 5.1.3 and 5.1.4 is valid.

5.2 Induced Voltages at the Terminals of the Passive Antennas

In Section 5.1, we explored the coupling phenomena through examinations of impedance curves and current distributions. This is an indirect way to identify the existent of coupling but it is useful if the passive antennas are short-circuited to the aircraft. If the passive antennas are loaded, strong coupling can be identified directly as high induced voltages across the load of a passive antenna. Investigations presented in this section on how the magnitude of the induced voltage changes with frequency will help us obtain a complete picture of the coupling modes in this case. For a loaded passive antenna in our computer models, the induced voltage at the terminals was calculated by multiplying the induced current at the feed element of the passive antenna by the load impedance. Since an open-circuit was simulated by a 1 MΩ resistive load at the "feed point" of the antenna, the induced voltage (in volts) is the induced current (in amperes) at the feed point times 1 MΩ. As for the 50 Ω termination, the induced voltage is simply the induced current times 50 Ω. The results were plotted versus frequency to complement the input impedance curves as coupling indicators. Intriguing induced voltage curves are presented in the following for two cases: HF1 active; and HF4 active.

5.2.1 HF1 as the Active Antenna

Fig. 5.18(a) shows the induced voltages versus frequency at the terminals of the passive antennas for "open-circuit" (1 MΩ) loads, with HF1 excited with 1 volt. These plots give even clearer pictures regarding the bandwidth as well as the magnitude of each coupling. Evidently, HF2 and HF3 have much higher induced voltages than HF4 and HF5. This is a sensible result because these two antennas are farther away from HF1 than the other two passive antennas. The highest induced voltage is found at HF3 near 19.0 MHz which is 5 times the excitation voltage at HF1. For clarity, each curve in Fig. 5.18(a) is plotted separately in Figures 5.18(b) through 5.18(e).

For HF2, Fig. 5.18(b), voltage peaks are found near 3.5, 6.5, 9.0, 10.5, 14.0, 17.5, 19.0, 21.0, 25.0, and 29.0 MHz. The highest peak (4.5 v) is near 3.5 MHz and the second highest (3.25 v) is near 29 MHz. It is noted that 3.5, 10.5, 17.5, and 25.0 MHz are close to the resonant frequencies of HF1 and HF2, whereas 6.5, 14.0, 21.0, and 29.0 MHz are close to the anti-resonant frequencies of HF1 and HF2. The remaining two frequencies (9.0 and 19.0 MHz) correspond to the anti-resonant frequencies of HF3. It is also noted that 29.0 MHz is a frequency close to the anti-resonant frequency of both HF3 (29.2 MHz) and HF2 (28.8 MHz). For HF3, Fig. 5.18(c), the induced voltage surges near 3.5, 9.0, 10.6, 17.5, 19.0, 25.0, and 29.0 MHz with the highest peak (5.0 v) located near 19.0 MHz. These frequencies can be categorized into two groups. The first group consists of 3.5, 10.6, 17.5, and 25.0 MHz. This group corresponds to the resonant frequencies of HF1 (and HF2). The second group consists of 9.0, 19.0, and 29.0. This second group

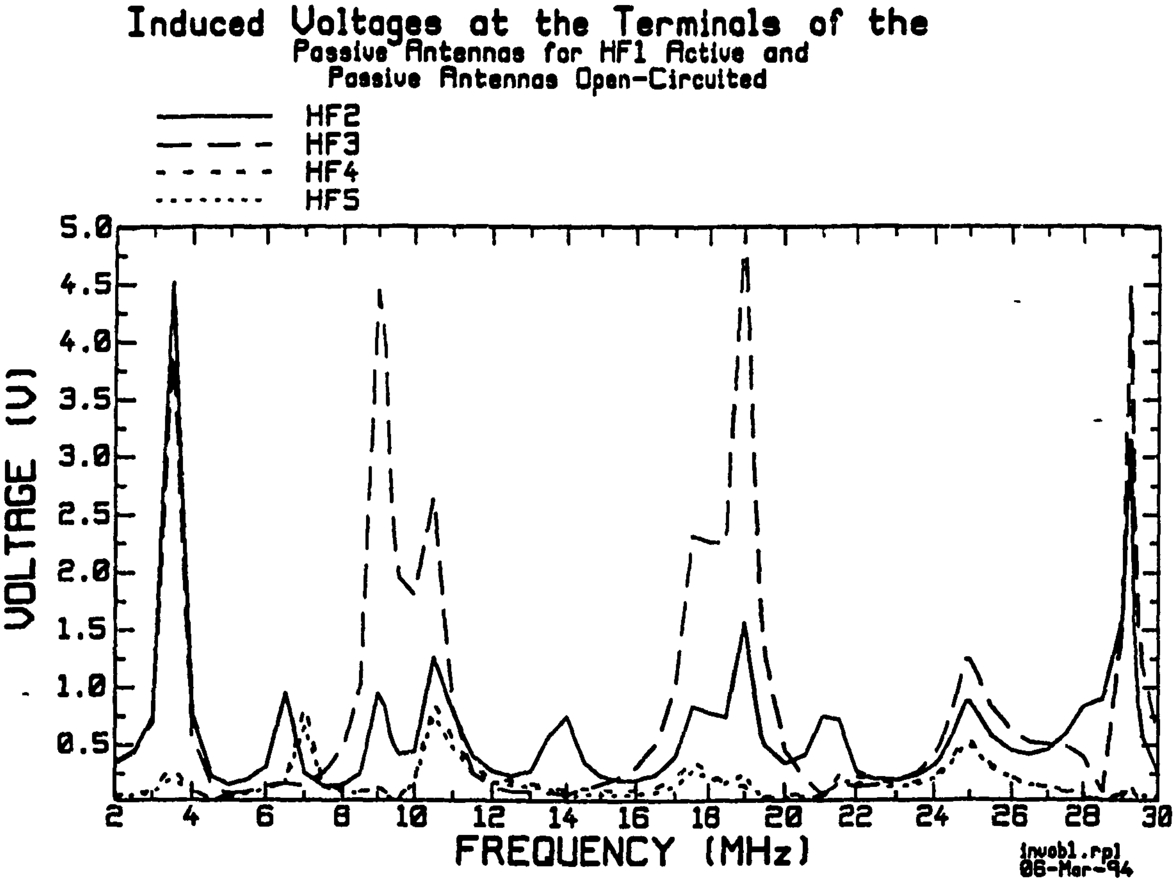

(a) Comparison of induced voltages at the terminals of the open-circuited passive antennas with HF1 active

Fig. 5.18 Induced voltages at the terminals of the open-circuited passive antennas with HF1 active.

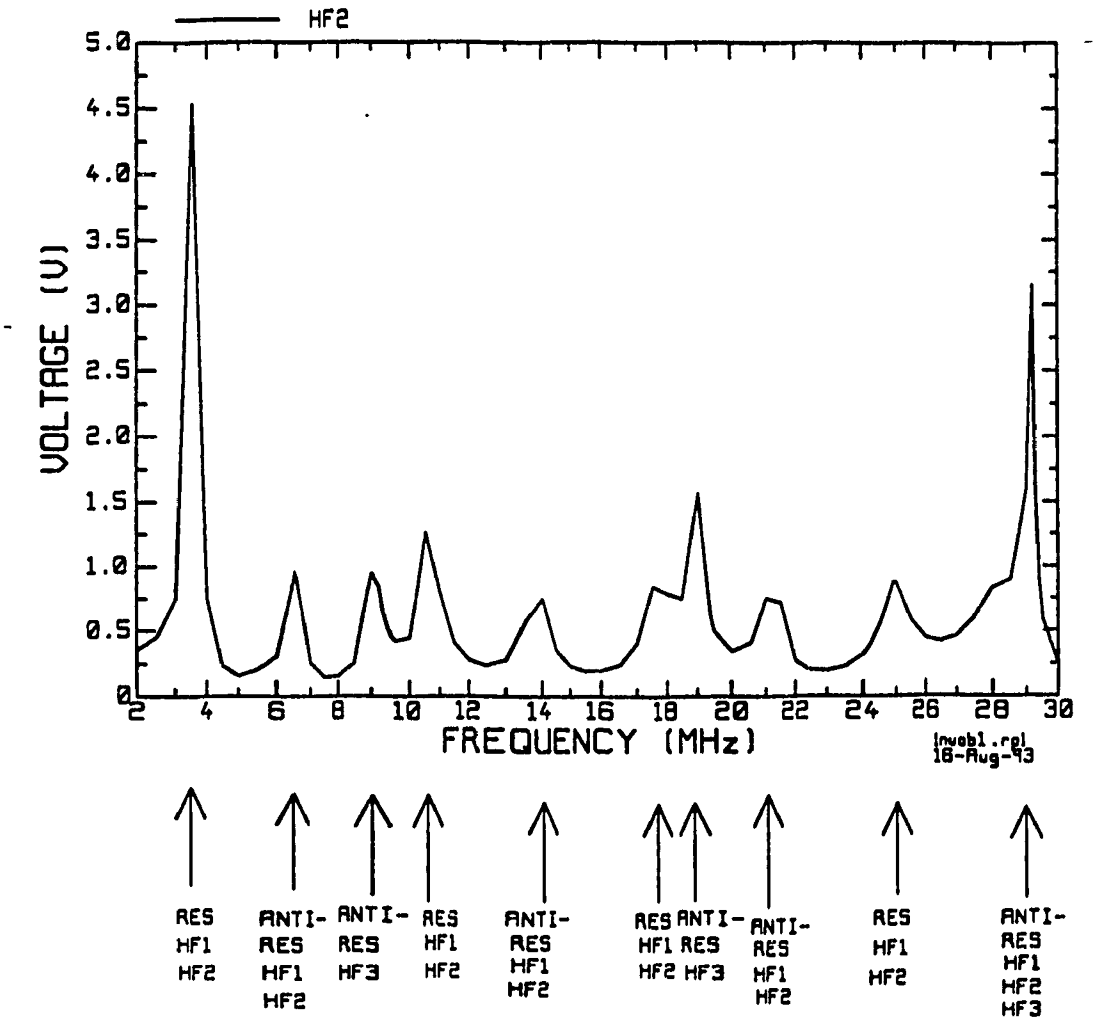

(b) Induced voltage at HF2's terminals when open-circuited

Fig. 5.18 (Cont'd)

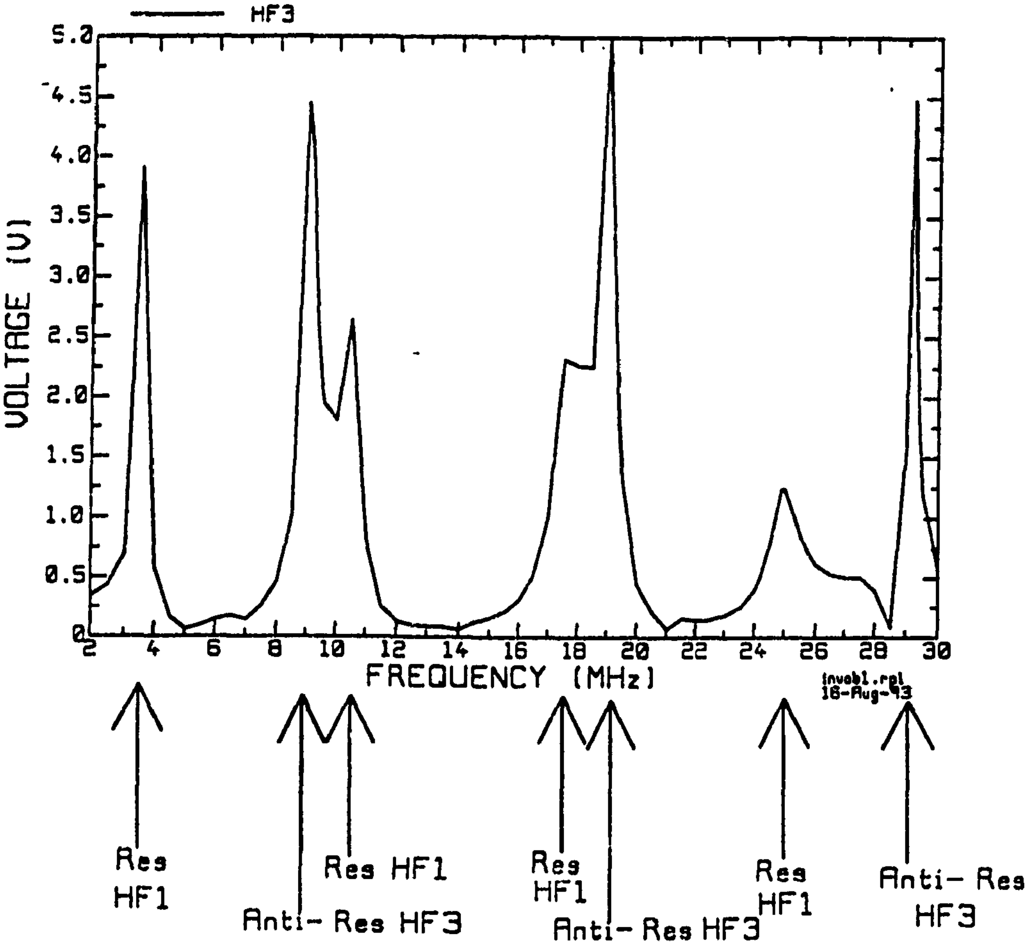

(c) Induced voltage at HF3's terminals when open-circuited

Fig. 5.18 (Cont'd)

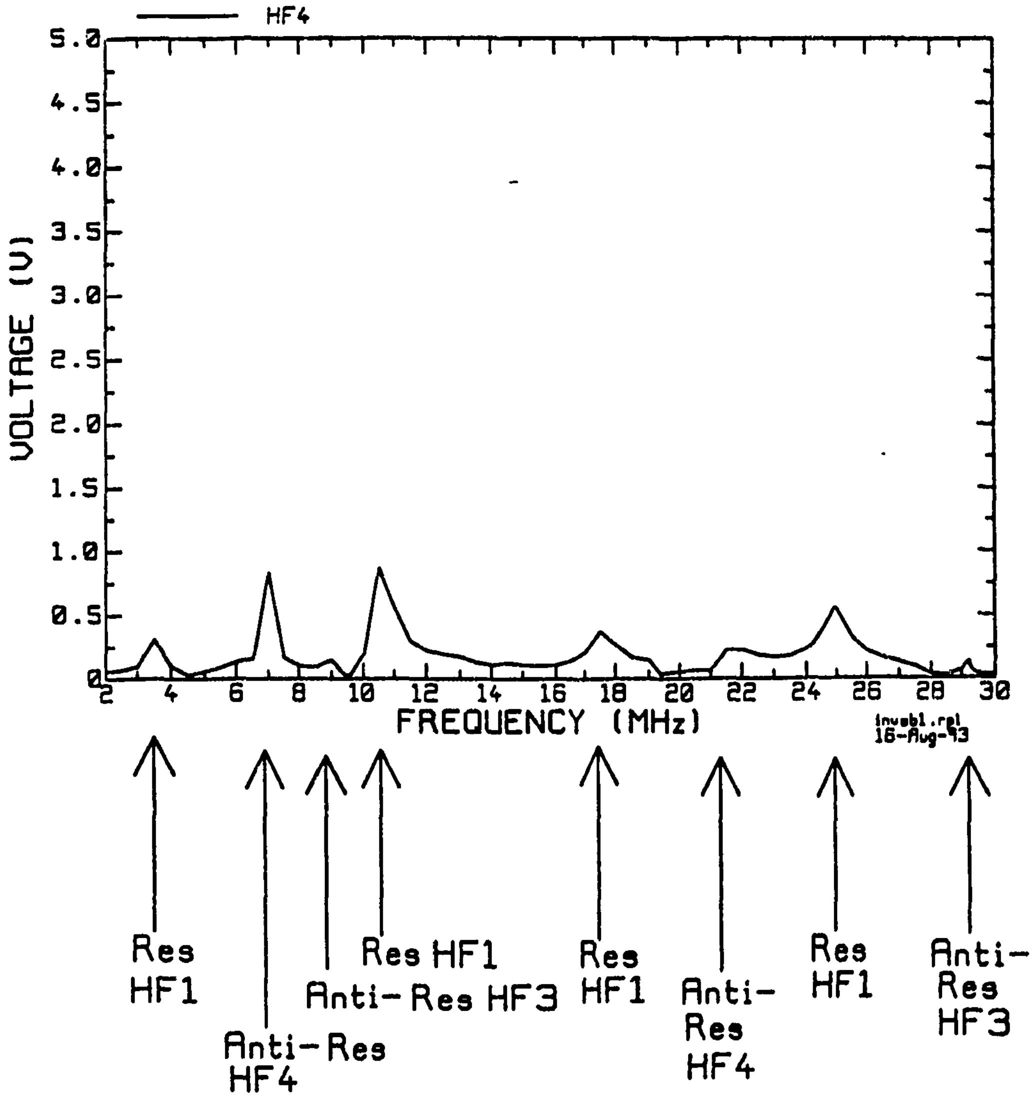

(d) Induced voltage at HF4's terminals when open-circuited

Fig. 5.18 (cont'd)

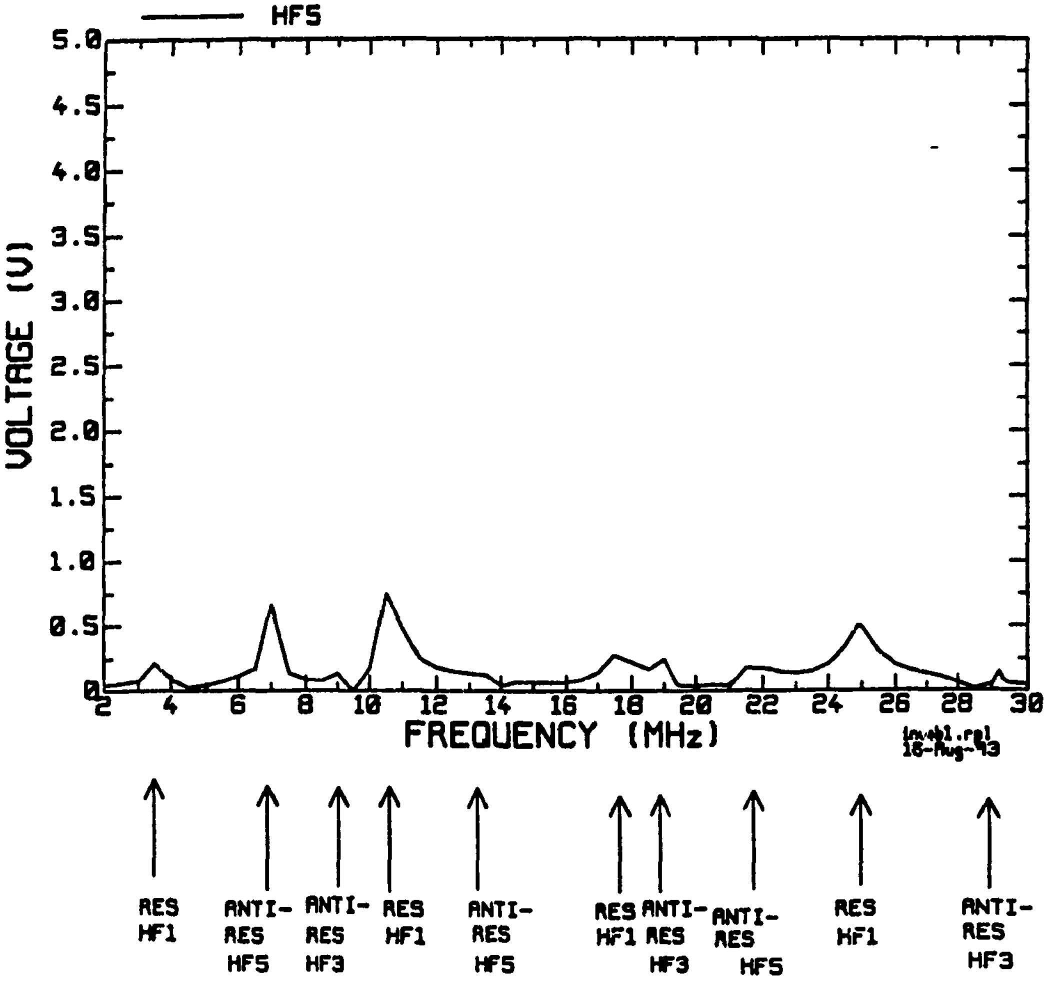

(e) Induced voltage at HF5's terminals when open-circuited

Fig. 5.18 (Cont'd)

corresponds to the anti-resonant frequencies of HF3. The magnitudes of all three peaks at the anti-resonant frequencies of HF3 are high, whereas the magnitudes of the peaks corresponding to the resonant frequencies of HF1 decrease as the frequency is increased. In the case of HF4 and HF5, parts (d) and (e), peaks are located near 3.5, 7.0, 9.0, 10.5, 17.5, 19.0, 22.0, 25.0, and 29.2 MHz. Again, these frequencies can be divided into three groups. The first group corresponds to the resonant frequencies of HF1 (and HF2): 3.5, 10.5, 17.5, and 25.0 MHz. The second group corresponds to the anti-resonant frequencies of HF3: 9.0, 19.0, and 29.2 MHz. Finally, the third group corresponds to the resonant frequencies of HF4 (and HF5): 6.5, and 22.0 MHz. The induced voltages on HF4 and HF5 are considerably low compared to the cases of HF2 and HF3.

In summary, for open-circuit loading, strong coupling between the active antenna and a passive antenna occurs near the anti-resonant frequencies of this passive antenna, as identified from the impedance curve. In addition, strong coupling between the active antenna and a passive antenna also occurs near the resonant frequencies of the active antenna. This cannot be easily seen from the impedance curve.

For 50 Ω loading, the induced voltages plotted versus frequency are shown in Fig. 5.19(a). It is noted that the highest induced voltage in this case occurs at HF2 near 3.5 MHz and is 1.1 times the excitation voltage at HF1. It is also observed that the magnitude of coupling decreases as the relative distance between the active and passive antennas increases. HF2 is closest to HF1, thus it experiences strongest coupling. Being the farthest passive antenna from HF1, HF5 has lowest coupled voltages among the four. Again, for clarity, each curve in Fig. 5.19(a) is plotted separately in Figures 5.19(b) through

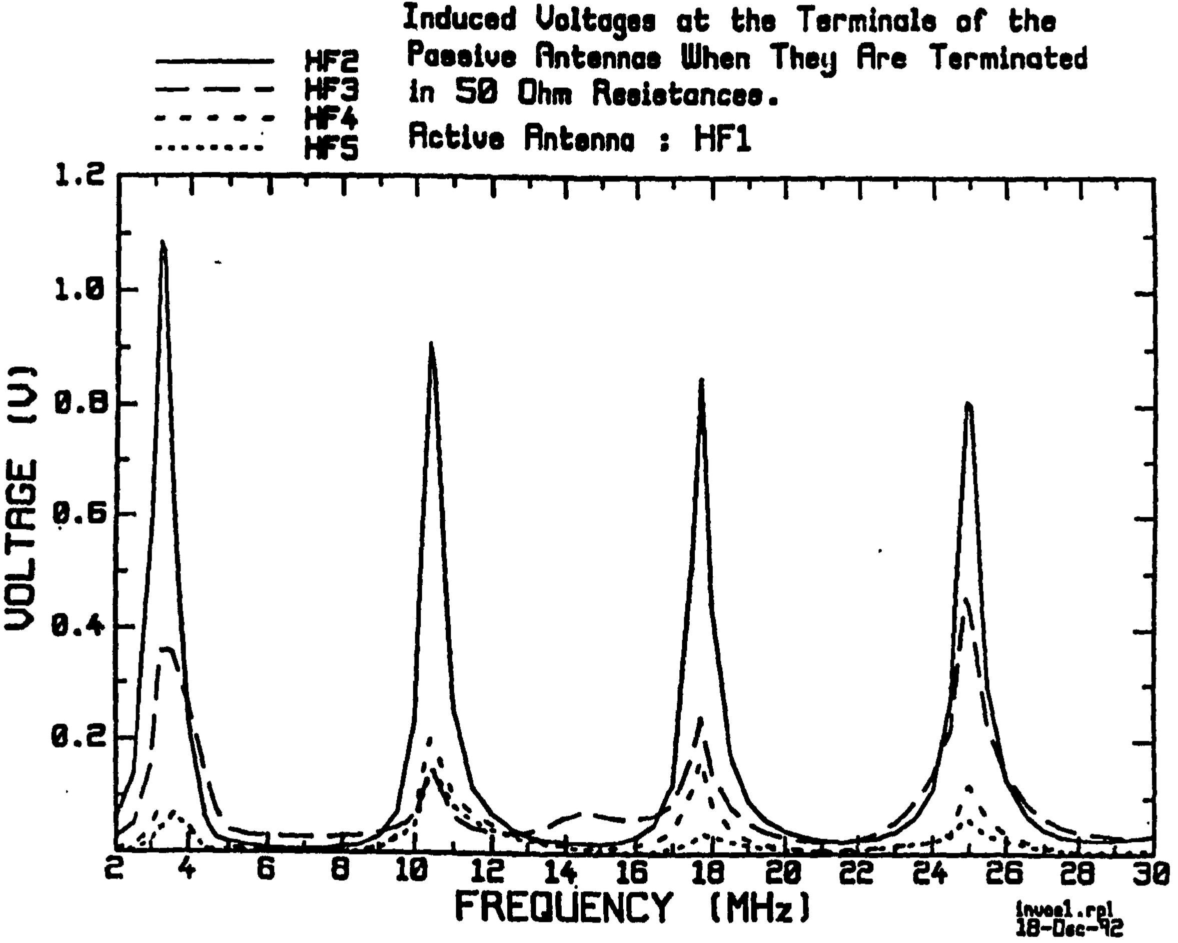

(a) Comparison of induced voltages at the terminals of the 50Ω terminated passive antennas with HF1 active

Fig. 5.19 Induced voltages at the terminals of the 50Ω terminated passive antennas with HF1 active.

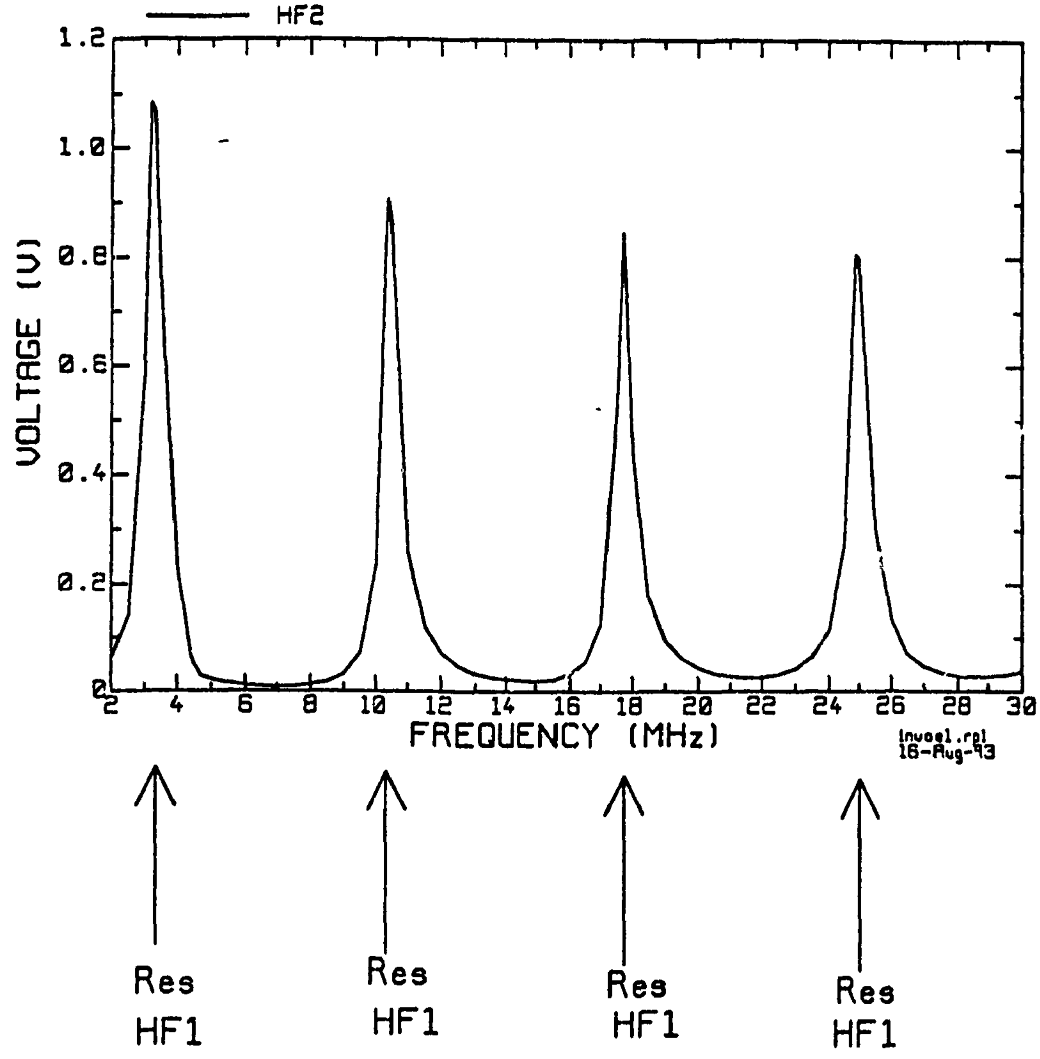

(b) Induced voltage at HF2's terminals when loaded by 50Ω

Fig. 5.19 (Cont'd)

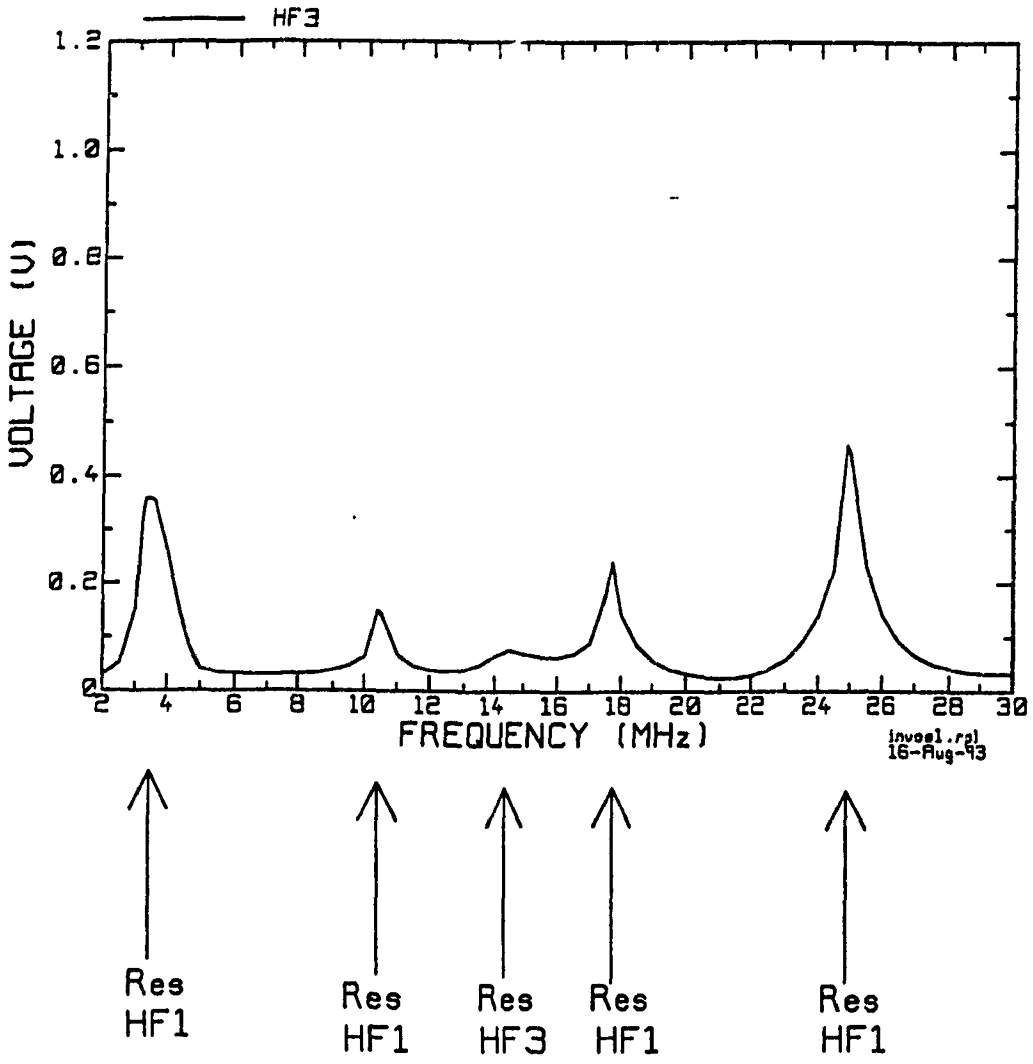

(c) Induced voltage at HF3's terminals when loaded by 50Ω

Fig. 5.19 (Cont'd)

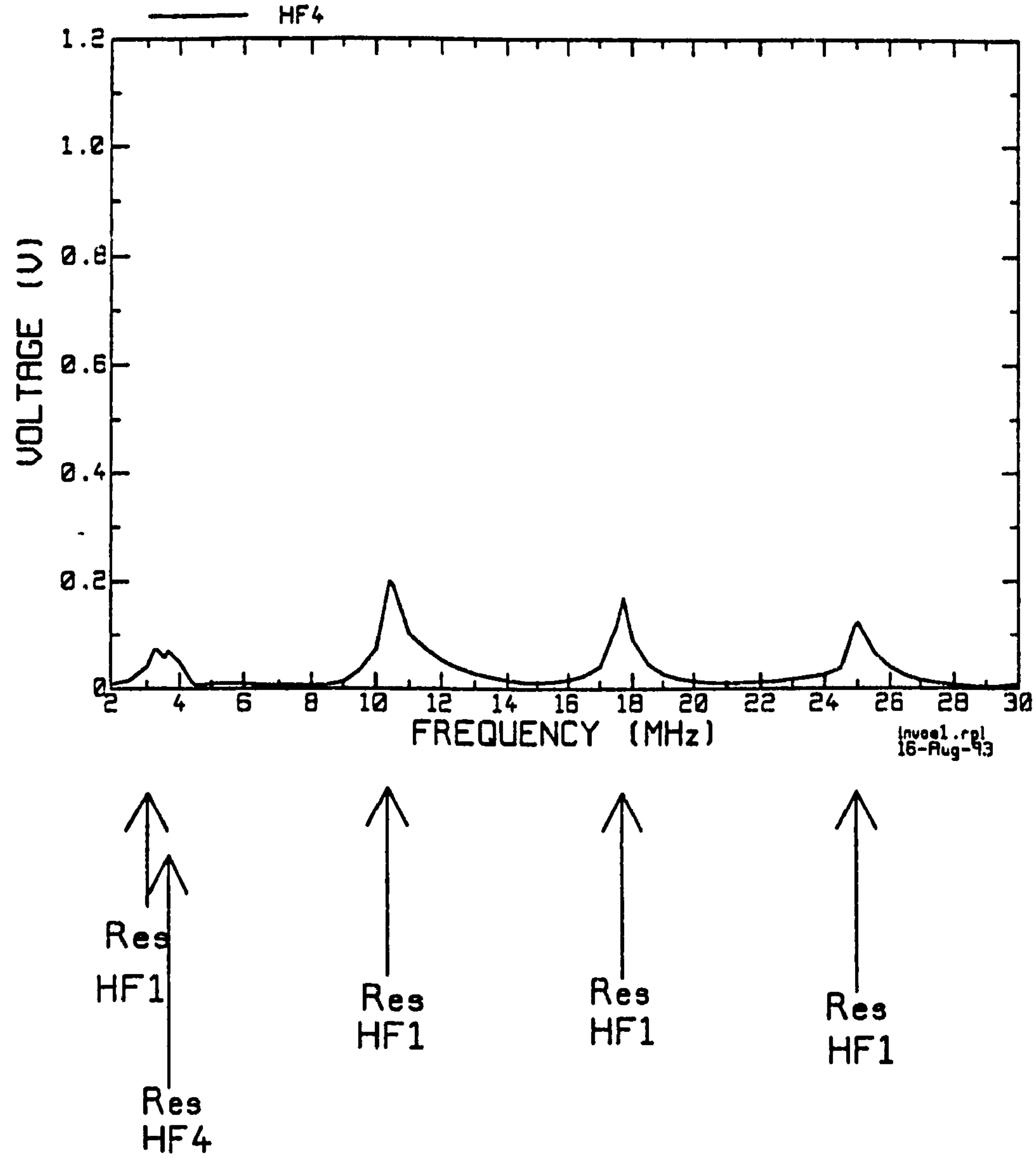

(d) Induced voltage at HF4's terminals when loaded by 50Ω

Fig. 5.19 (Cont'd)

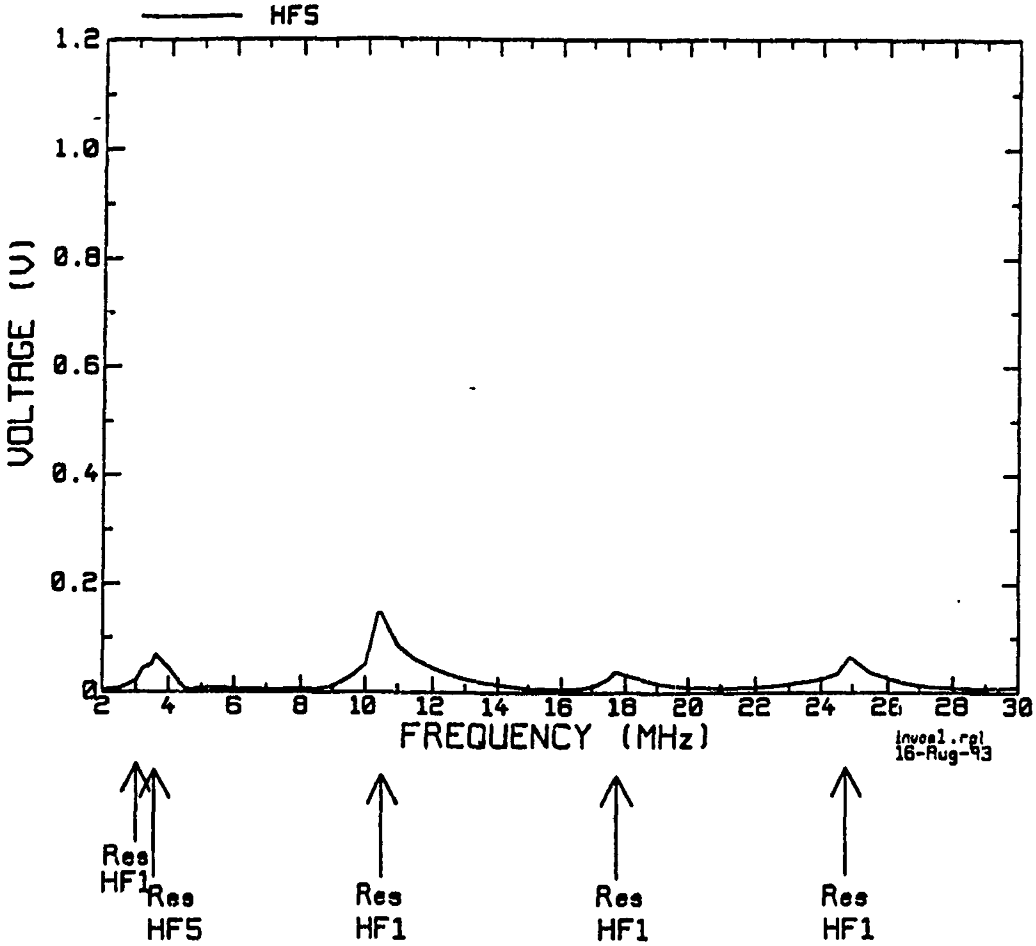

(e) Induced voltage at HF5's terminals when loaded by 50Ω

Fig. 5.19 (Cont'd)

5.19(e).

For HF2, Fig. 5.19(b), four voltage peaks are found near the resonant frequencies of HF1 (and HF2): 3.2, 10.4, 17.6, and 25.0 MHz, with the highest peak (1.1 volts) near 3.2 MHz. The heights of peaks reduce slowly as the frequency is increased. In the case of HF3, Fig. 5.19(c), four peaks are also found near the resonant frequencies of HF1 with much lower magnitudes compared to HF2. In addition, a small "bump" is seen near 14.5 MHz, which is close to the resonant frequency of HF3. As for HF4 and HF5 shown in Fig. 5.19(d) and Fig. 5.19(e), respectively, again four peaks are seen near the resonant frequencies of HF1 with even smaller magnitudes (ranging from 0.05 to 0.25 volts). Another small peak located near the resonant frequency of HF4 (or HF5) (3.6 MHz) is also noticeable. In conclusion, when a passive antenna is terminated in 50 Ω, it experiences strong coupling from the active antenna near the resonant frequencies of the active antenna.

5.2.2 HF4 as the Active Antenna

The induced voltages at the terminals of the passive antennas due to HF4 for open-circuit loading are plotted in Fig. 5.20(a). The highest induced voltage is about 1.2 v, which is much lower than the highest induced voltage observed when HF1 is excited. Indeed, the overall magnitude of the induced voltages at the terminals of all the passive antennas shown in Fig. 5.20(a) is much lower than the one shown in Fig. 5.19(a). For clarity, the induced voltages in Fig. 5.20(a) are plotted separately in Figures 5.20(b) through 5.20(e).

For HF1, Fig. 5.20(b), induced voltage peaks are located near 3.7, 6.5, 9.0, 10.8, 14.0, 18.0, 21.0, 25.0, 28.5, and 29.5 MHz with the highest peak (1.2 volts) near 3.7 MHz. These frequencies can be associated with the resonances of the active antenna HF4 or the anti-resonances of the passive antennas. The resonant frequencies of HF4 include 3.7, 10.8, 18.0, and 25.0 MHz. The magnitude of the induced voltage peak associated with the resonance of HF4 decreases as the frequency is increased. The peaks associated with the anti-resonances of HF1 are located at 6.5, 14.0, 21.0, and 28.5 MHz. These peak values are high except for the one at 28.5 MHz. The remaining two peaks near 9.0, and 29.5 MHz are associated with anti-resonances of HF3 and are relatively low in magnitude.

The induced voltage at the terminals of HF2 shown in Fig. 5.20(c) is very similar to that of HF1, except that the peak at 3.7 MHz is a little lower than the one for HF1. This is sensible because HF1 and HF2 are of the same length but HF2 is a little farther away from the active antenna HF4 than HF1.

For HF3, Fig. 5.20(d), high induced voltages are observed near 3.7, 6.5, 9.0, 10.8,

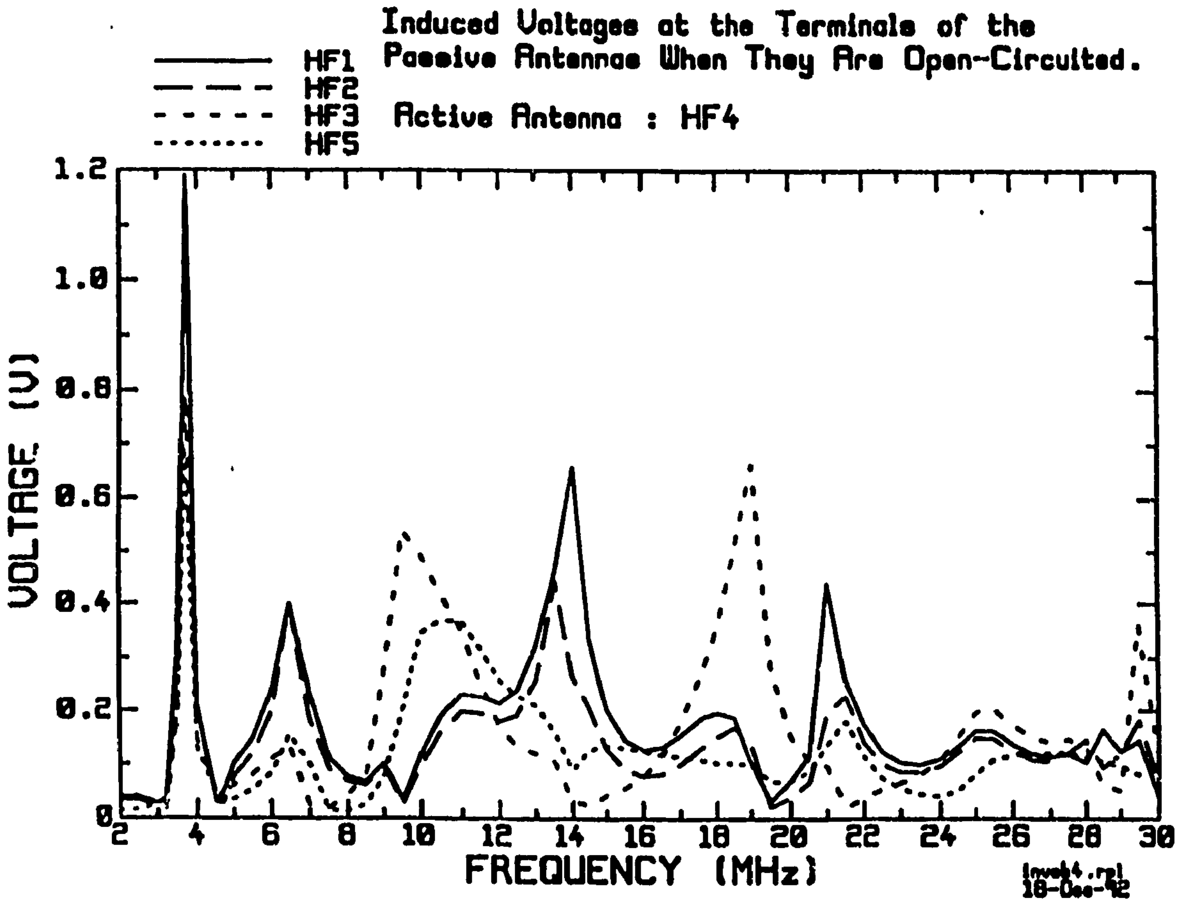

(a) Comparison of induced voltages at the terminals of the open-circuited passive antennas with HF4 active

Fig. 5.20 Induced voltages at the terminals of the open-circuited passive antennas with HF4 active.

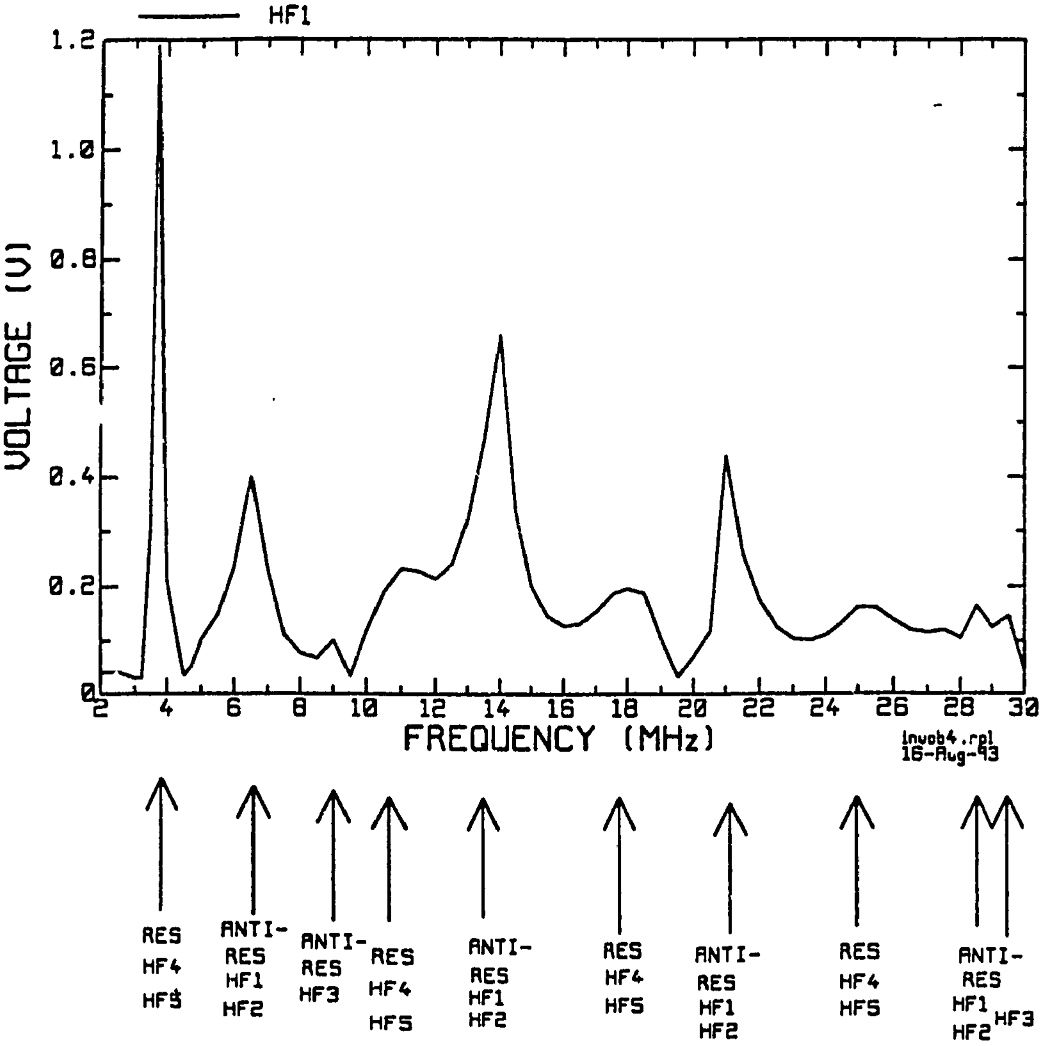

(b) Induced voltage at HF1's terminals when open-circuited

Fig. 5.20 (Cont'd)

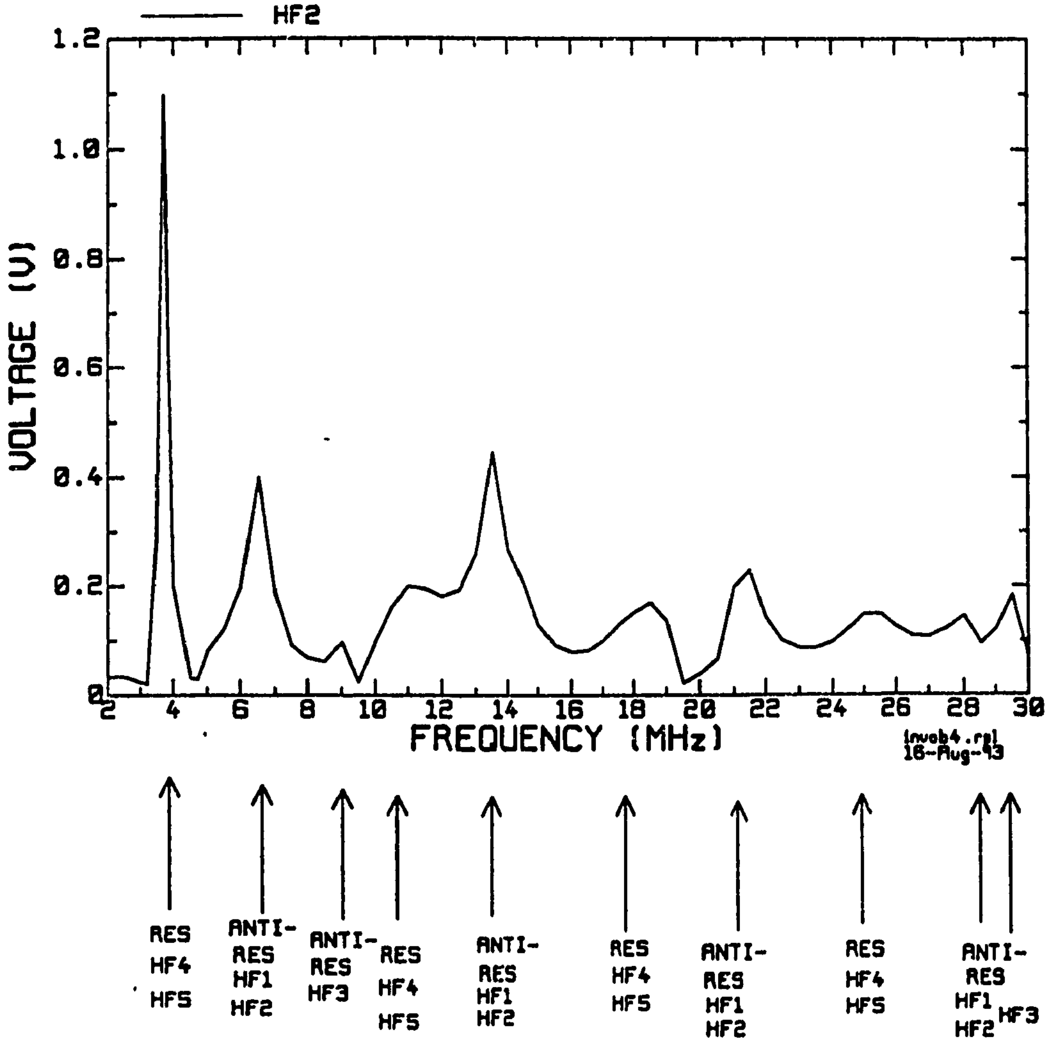

(c) Induced voltage at HF2's terminals when open-circuited

Fig. 5.20 (Cont'd)

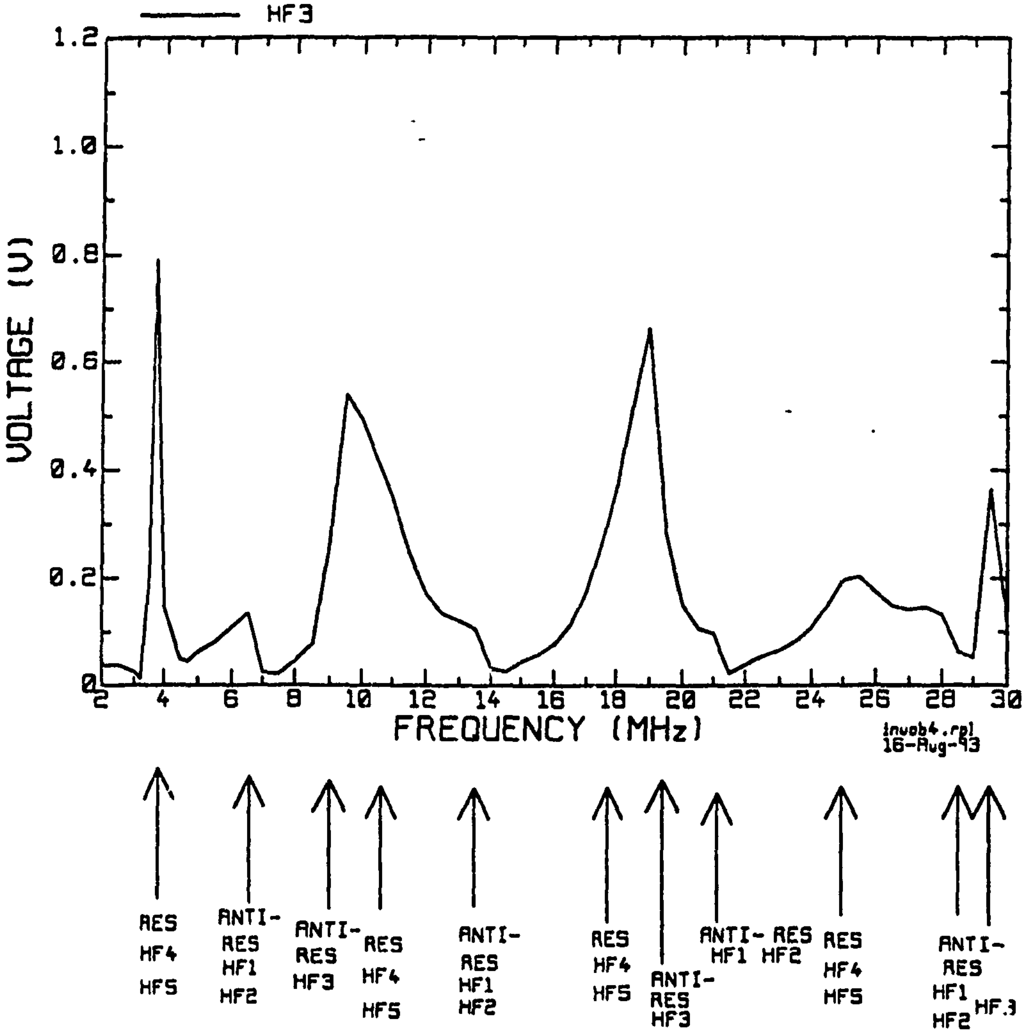

(d) Induced voltage at HF3's terminals when open-circuited

Fig. 5.20 (cont'd)

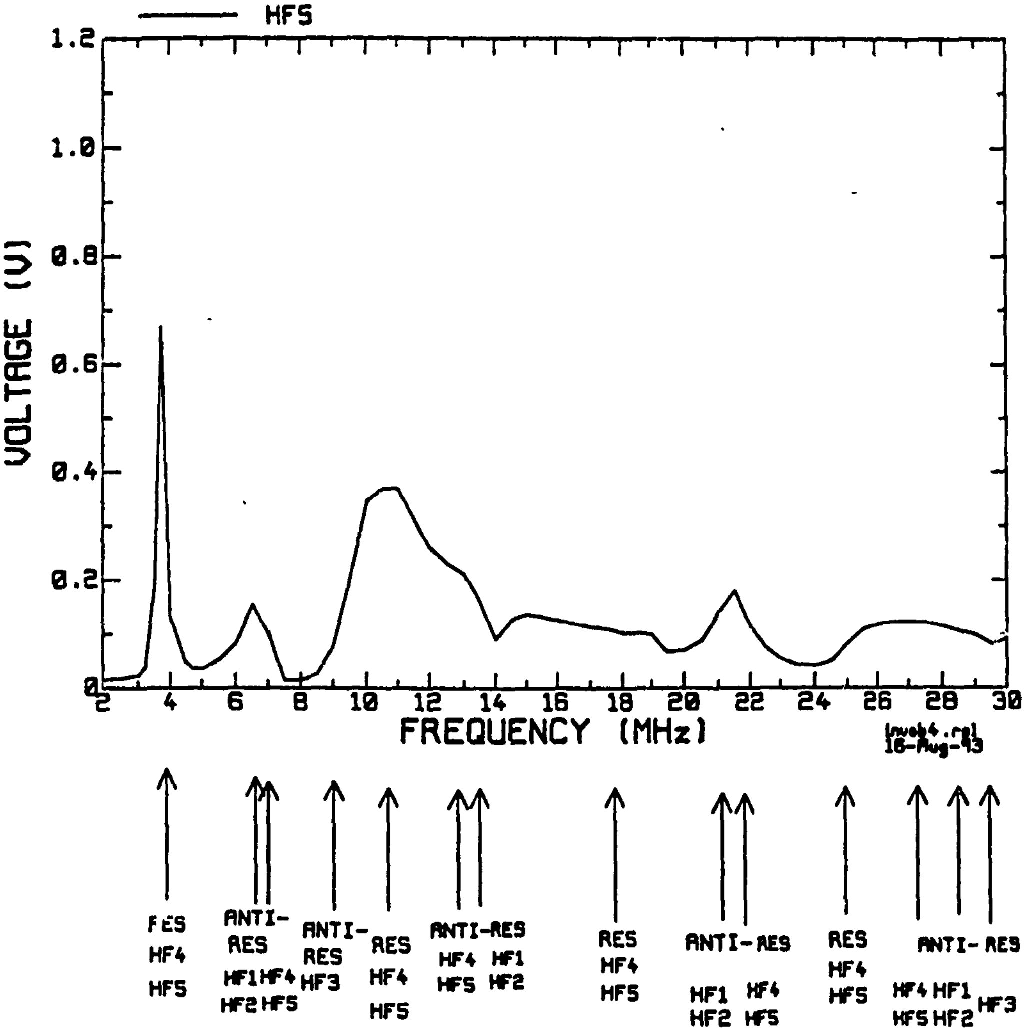

(e) Induced voltage at HF5's terminals when open-circuited

Fig. 5.20 (Cont'd)

13.5, 18.0, 19.0, 21.0, 25.0, 27.0, and 29.5 MHz. Again, these frequencies can be associated with the resonances of the active antenna HF4 and the anti-resonances of passive antennas. Since some of these frequencies are closely spaced, they merge to form several "wide" peaks. Peaks associated with the resonances of HF4 are located at 3.7, 10.8, 18.0 and 25.0 MHz. The remaining peaks are associated with the anti-resonance of HF3: 9.0, 19.0, and 29.5 MHz; HF1 (and HF2): 6.5, 13.5, and 21.0 MHz; and HF4 (and HF5): 27.0 MHz. The three highest peaks are associated with a resonance of HF4 (3.7 MHz) and two anti-resonances of HF3 (9.0, 19.0 MHz), respectively.

As for HF5 in Fig. 5.20(e), high voltages are seen near 3.7, 6.5, 11.0, and 21.5 MHz. Two of the peaks (3.7 and 11.0 MHz) are associated with the resonances of HF4 (or HF5). The peaks near 6.5, 13.0 and 21.5 MHz are believed to be associated with the anti-resonances of both HF1 (or HF2) and HF5 (or HF4).

Fig. 5.21(a) is a comparison of induced voltages at four passive antenna's terminals for 50Ω terminations with HF4 active. The most intriguing thing in this figure is that relatively high induced voltages are observed at all four passive antennas's terminals near 3.6 MHz (resonance of HF4), and the induced voltages reduce considerably as the frequency is increased. These voltage curves are plotted separately in Figures 5.21(b) through 5.21(e).

The induced voltages at HF1 shown in Fig. 5.21(b) and HF2 in Fig. 5.21(c) are very similar. For each antenna, besides the high peaks near the lowest resonant frequency of HF4 3.6 MHz, there are three much lower and wider peaks located near 10.8, 18.0, and 25.0 MHz, which are the higher resonant frequencies of HF4. The voltage peaks at HF1 are a little higher than those at HF2. This is reasonable because HF1 is closer to the active antenna HF4 than HF2.

For HF3, Fig. 5.21(d), the induced voltage curve looks more complicated. In addition to the high peak near 3.6 MHz, five lower and wider peaks are found near 4.7, 10.8, 14.0 ,17.8, and 25.0 MHz. Three of these frequencies, namely, 10.8, 17.8, and 25.0 MHz, are associated with the resonances of HF4, and the remaining two, which arc 4.7, 14.0 MHz, are associated with the resonances of HF3.

Finally, the curve for HF5 shown in Fig. 5.21(e) is similar to the ones for HF1 and HF2. All the four peaks in the curve can be associated with the resonances of HF4 or HF5, with the highest one near 3.6 MHz and three lower and wider ones near 10.8, 17.8, and 25.2 MHz.

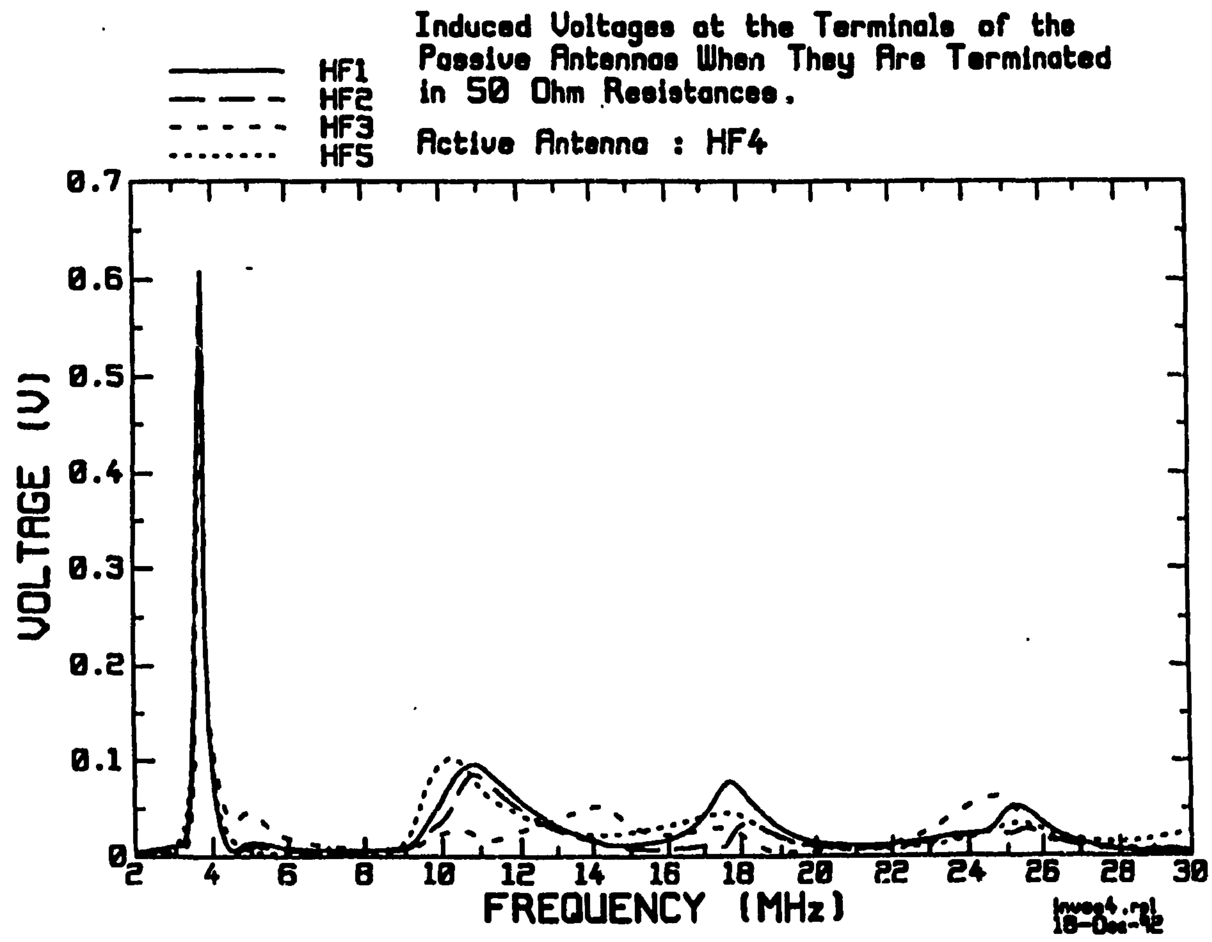

(a) Comparison of induced voltages at the terminals of the 50Ω terminated passive antennas with HF4 active

Fig. 5.21 Induced voltages at the terminals of the 50Ω terminated passive antennas with HF4 active.

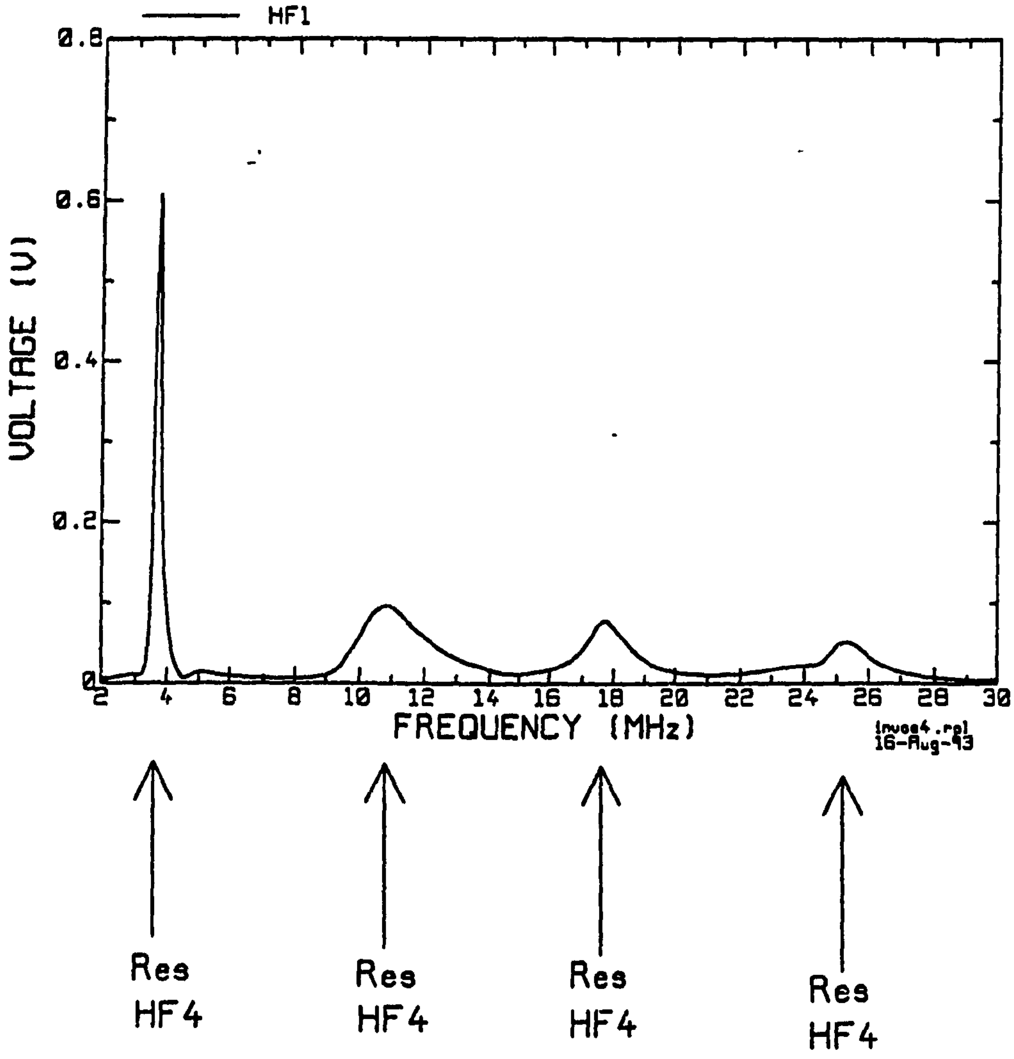

(b) Induced voltage at HF1's terminals when loaded by 50Ω

Fig. 5.21 (Cont'd)

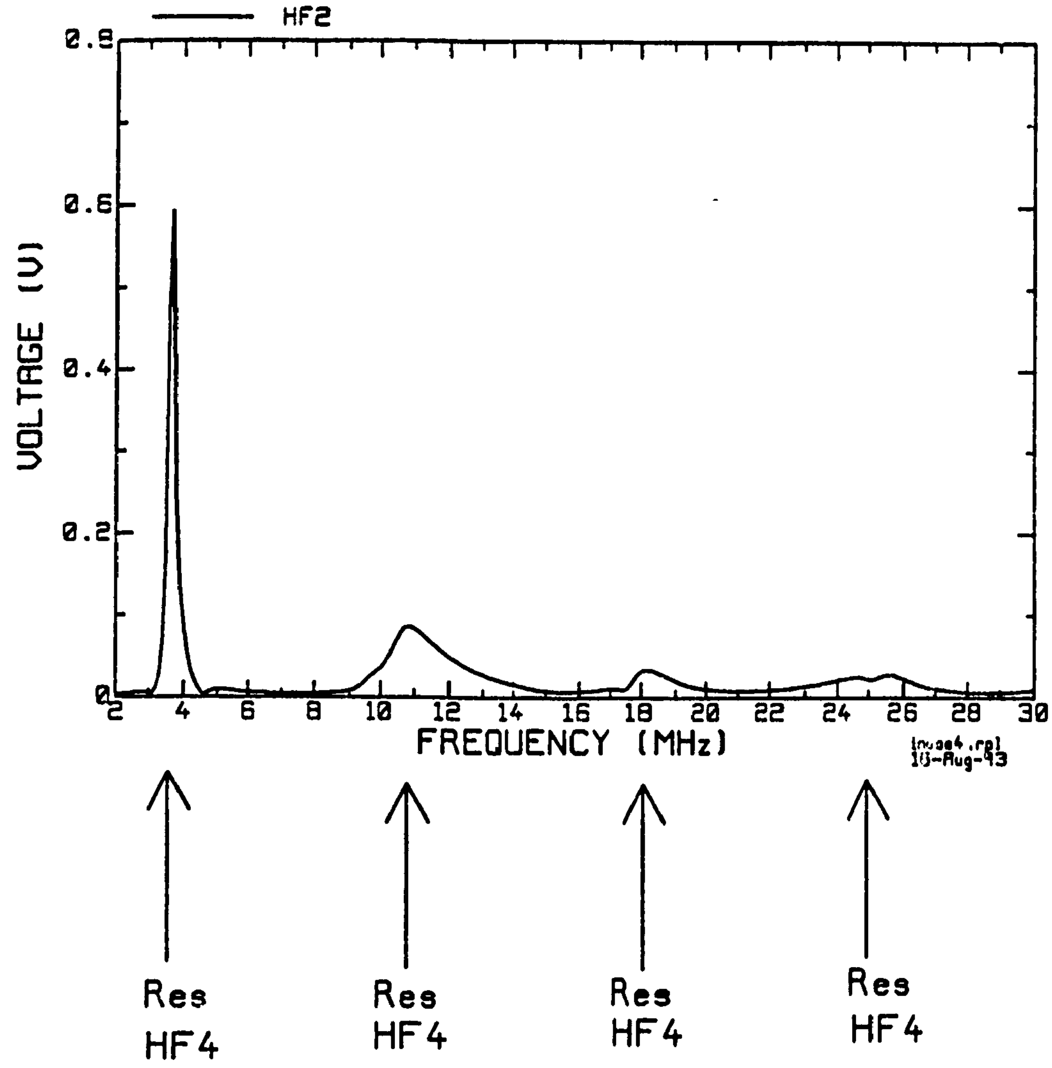

(c) Induced voltage at HF2's terminals when loaded by 50Ω

Fig. 5.21 (Cont'd)

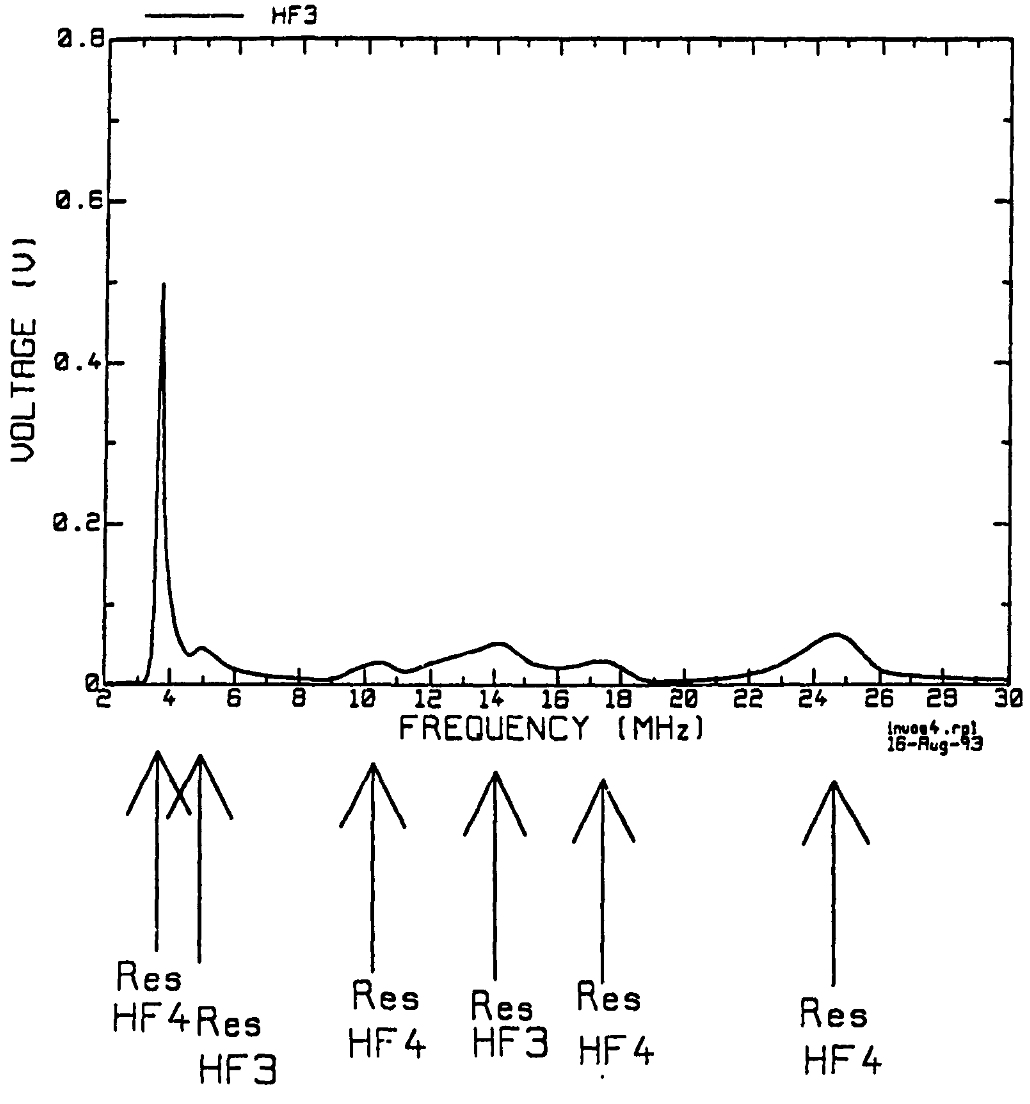

(d) Induced voltage at HF3's terminals when loaded by 50Ω

Fig. 5.21 (Cont'd)

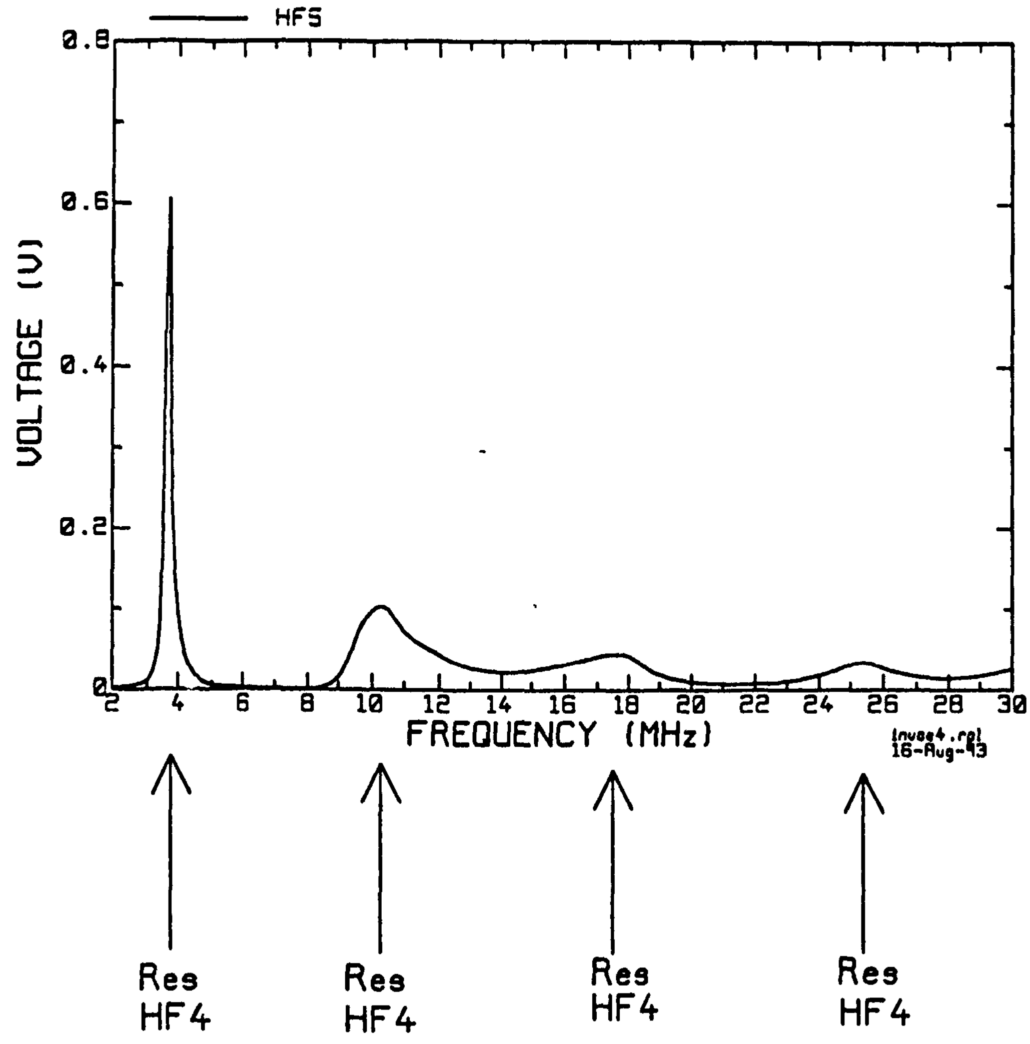

(e) Induced voltage at HF5's terminals when loaded by 50Ω

Fig. 5.21 (Cont'd)

5.3 Detailed Diagnosis of Coupling Modes on the EC-130

From the discussions presented in Sections 5.1 and 5.2, coupling modes on the EC-130 can be deduced as follows. There are three physical quantities that affect the inter-antenna coupling, namely, the resonant length of the antenna; the loading conditions of the passive antennas; and the relative distance between and relative configuration of the active and passive antennas. These factors determine the coupling modes in the following manners.

5.3.1 Inter-Antenna Coupling

The inter-antenna coupling modes are related to the antenna resonant length, the passive antenna loading conditions as well as the relative distance between and relative configuration of the active and passive antennas.

5.3.1.1 Short-Circuit Loading

Tables 5.4 and 5.7 enumerates the inter-antennas coupling modes with the passive antennas short-circuited, and list the effects on the radiation pattern for HF1 active and HF4 active, respectively. When passive antennas are short-circuited to the airframe, high induced currents are present near the resonant frequencies of the passive antennas. For example, in Fig. 5.6(a), the impedance curve for HF1 active indicates that there is strong coupling near 3.5, 10.5, 17.6, and 24.9 MHz. These frequencies are close to the resonant frequencies of passive antennas HF2, HF4, and HF5. Indeed, high induced currents are observed on these three passive antennas at the frequencies mentioned above. In addition, strong coupling is also indicated near 4.7, 14.2, and 25.0 MHz, which correspond to the passive antenna HF3. Examinations of current distributions at these frequencies also show that high current is present on HF3. Similar phenomena are observed in the case of HF4 active.

In short, when passive antennas are short-circuited to the airframe, strong coupling between a passive antenna and the active antenna is expected when the frequency is close to the resonant frequency of this passive antenna.

5.3.1.2 Open-Circuit Loading

Tables 5.5 and 5.8 enumerate the inter-antenna coupling modes with the passive antennas open-circuited to the airframe, and list the effects on the radiation pattern for HF1 active, and HF4 active, respectively. In this open-circuit case the coupling modes are quite different from those in the short-circuit case. Instead of occurring near the resonant frequencies of the passive antennas, high induced voltages are present near the anti-resonant frequencies of the passive antennas. Moreover, high coupled voltage are also observed near the resonant frequencies of the active antenna.

It should be noted that for a passive antenna, high terminal voltage is induced not only near its own anti-resonant frequencies, but could also be induced near the anti-resonant frequencies of other passive antennas. For instance, in Fig. 5.18(a), 9.0 and 19.0 MHz are anti-resonant frequencies of passive antenna HF3, and high voltage peaks are found near these two frequencies. However, the induced voltage is also high at the terminals of HF2 at the two frequencies mentioned above.

The conclusion for the inter-antenna coupling modes when passive antennas are open-circuited to the airframe can be stated as follows. A high induced voltage (strong coupling) at the terminals of a passive antenna is expected: when the frequency the close to the anti-resonant frequency of this passive antenna; or when the frequency is close to the anti-resonant frequency of a "nearby" passive antenna in some cases; or when the frequency is close to the resonant frequency of the active antenna.

5.3.1.3 50 Ω Loading

Tables 5.6 and 5.9 enumerate the inter-antenna coupling modes with the passive antennas terminated in 50 Ω loads. When the passive antennas are loaded by 50 Ω resistances, the magnitude of coupling is reduced substantially. The coupling modes are simpler, that is, high induced voltages at the terminals of the passive antennas are found near the resonant frequencies of the active antenna only.

5.3.1.4 Relative Distance between and relative configuration of the Active and Passive Antennas

Another important factor that affects the magnitude of coupling is the distance between and the relative configuration of the active antenna and the passive antenna. It is expected that the closer the active and the passive antennas are, the stronger the coupling will be. Also, the coupling is expected to be stronger if the two antennas are nearly parallel and of similar geometry than if they are oriented in very different directions and of different shapes.

Indeed from the observations of the induced current and voltage shown in the preceding sections, it is obvious that the coupling magnitude decreases as the relative distance is increased. For example, when HF1 is excited, its closest passive antenna HF2 gets the highest induced voltage and current. The second closest passive antenna HF3 has less intense induced current and voltage. Being the farthest passive antennas and making an horizontal angle of 45° with HF1, the "dog-leg" antennas HF4 and HF5 have weakest coupled current and voltage as expected.

5.3.2 Antenna-to-Airframe Coupling

In the case of HF1 excitation, the antenna-to-airframe coupling is too weak to be noticeable in contrast to the prominent inter-antenna coupling. The effects due to antenna-to-airframe coupling are relatively small and can be ignored.

Nevertheless, in the case of HF4 excitation, the antenna-to-airframe coupling is stronger and induced current paths can be visualized easily in current distribution plots. Two of the current paths on the airframe have lengths approximately equal to half wavelength at 4 MHz. The length of the third path is close to half wavelength at 9 MHz. Compared to the inter-antenna coupling, the antenna-to-airframe coupling has a broader "bandwidth", that is, this kind of coupling exists over a larger frequency range.

5.3.3 Impact of Antenna Coupling on the Radiated Fields

The impact of strong antenna-to-antenna coupling on this aircraft can be seen from the profound changes in radiation pattern and the values of the aircraft HF antenna assessment parameters, which will be presented in this section.

5.3.3.1 Effects on the Radiation Pattern

Due to the high induced current resulting from strong inter-antenna coupling, the radiation pattern of an active antenna is profoundly altered at frequencies where the strong coupling occurs. These drastic changes in radiation patterns can have a positive or negative impact on communication depending on the way the pattern is changed.

Table 5.4 summarizes the antenna-to-antenna coupling effects that have been found when HF1 is active and the passive antennas are short-circuited to the airframe. Fig. 5.22

illustrates examples of the changes in radiation pattern that Table 5.4 refers to. The three dimensional patterns for E_θ and E_ϕ polarizations at 2.0, 3.15, 3.65, 4.0, and 4.7 MHz are shown in Fig. 5.22. The graph shows a three-dimensional polar plots in which the field strength is depicted as the radial distance from the origin in the coordinate system of Fig. 5.22. One can see immediately that the pattern at 3.15 MHz in Fig. 5.22(b) where the strong coupling between HF1 and HF2 shown in Fig. 5.7(a) is very different from the pattern at the adjacent frequency 2.0 MHz in Fig. 5.22(a), where very weak coupling between HF1 and HF2 was observed. The E_θ field is greatly reduced in the θ=90° plane at 3.15 MHz compared to the near isotropic E_θ pattern at 2 MHz. The E_ϕ field is considerably enhanced in the aft direction at 3.15 MHz compared to 2.0 MHz. Similarly, a comparison between the patterns at 3.65 MHz in Fig. 5.22(c) and 3.15 MHz in Fig. 5.22(b) also shows remarkable differences. Frequency 3.65 MHz corresponds to coupling between HF1, HF2, HF3 and the two "dog-leg" antennas HF4 and HF5, as illustrated in Fig. 5.7(f). The side lobes in the E_θ pattern seen at 3.15 MHz disappear at 3.65 MHz; the forward and aft lobes of the E_ϕ pattern observed at 3.15 MHz also disappear at 3.65 MHz. Finally, the patterns at 4.7 MHz in Fig. 5.22(e), where strong coupling between HF1 and HF3 was found in Fig. 5.7(e), are considerably different from those at the vicinity frequency 4.0 MHz in Fig. 5.22(d) as well. Compared to the patterns at 4 MHz, the aft lobe of E_θ is reduced at 4.7 MHz; the side lobes of E_ϕ are rotated forward by 45° and a major lobe is added in the port-aft direction. These examples demonstrate that the radiation pattern can change dramatically over a very narrow frequency band. Major changes in radiation pattern are also observed for the coupling at other frequencies and for other loading conditions.

Table 5.4 Major Changes in Radiation Patterns due to Strong Inter-Antenna Coupling for HF1 Active and Passive Antennas Short-Circuited to the Airframe

Active Antenna: HF1		Loading Condition for Passive Antenna: Short-Circuit	
Frequency (MHz)	Coupling	E_θ Field	E_ϕ Field
3.15	HF1 to HF2	Greatly reduced in the $\theta=90^\circ$ plane, especially in the forward direction.	Considerably enhanced in the aft direction.
3.65	HF1 to HF2, HF3, HF4, HF5	Side lobes disappeared.	Forward and aft lobes disappeared.
4.7	HF1 to HF3	Aft lobe reduced.	Side lobes rotated forward by 45°. One large lobe added in the port-aft direction.
10.6	HF1 to HF2	Reduced in the sector $60^\circ<\theta<120^\circ$.	Enhanced in the forward direction in the top sector.
14.2	HF1 to HF3	Reduced in the bottom sector.	Port-aft lobe reduced.
17.6	HF1 to HF2	Reduced in the forward direction for the sector $45^\circ<\theta<90^\circ$.	Increased in the forward-port and forward-starboard direction in the bottom sector.
24.9	HF1 to HF2	Enhanced in the port-direction.	Enhanced in the port direction.

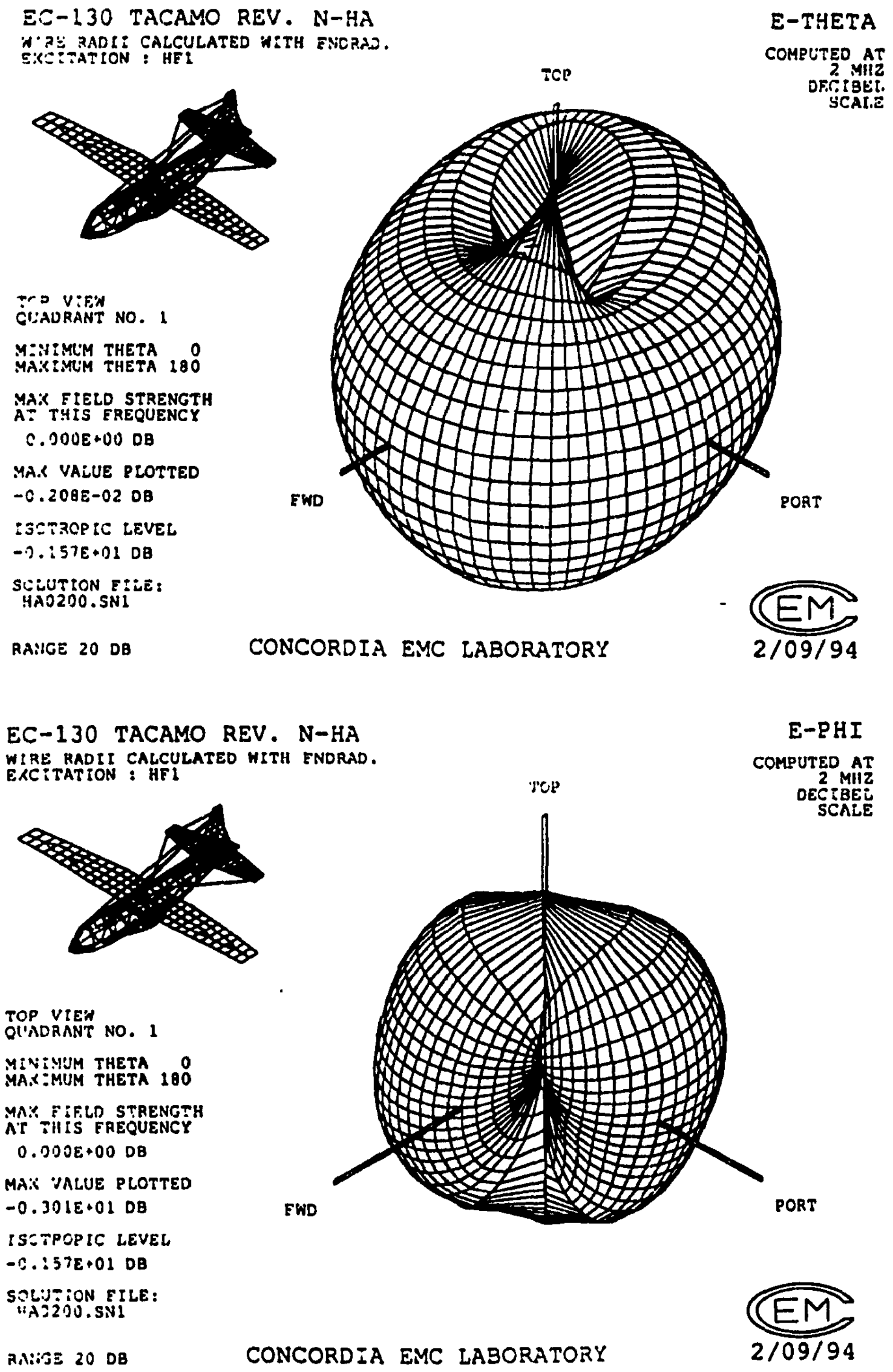

(a) 2.0 MHz

Fig. 5.22 Three-dimensional radiation patterns at selected frequencies for HF1 excited, passive antennas short-circuited.

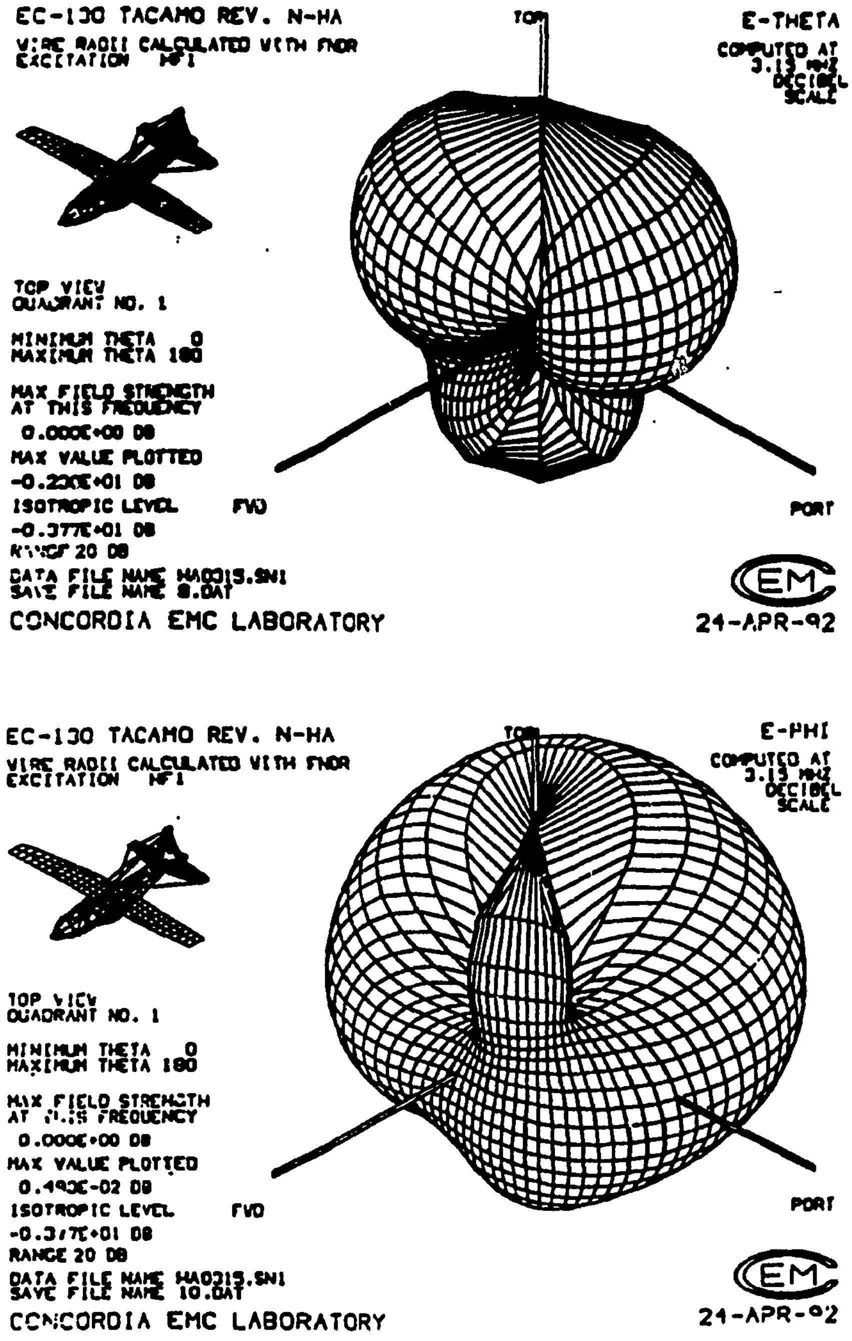

(b) 3.15 MHz

Fig. 5.22 (Cont'd)

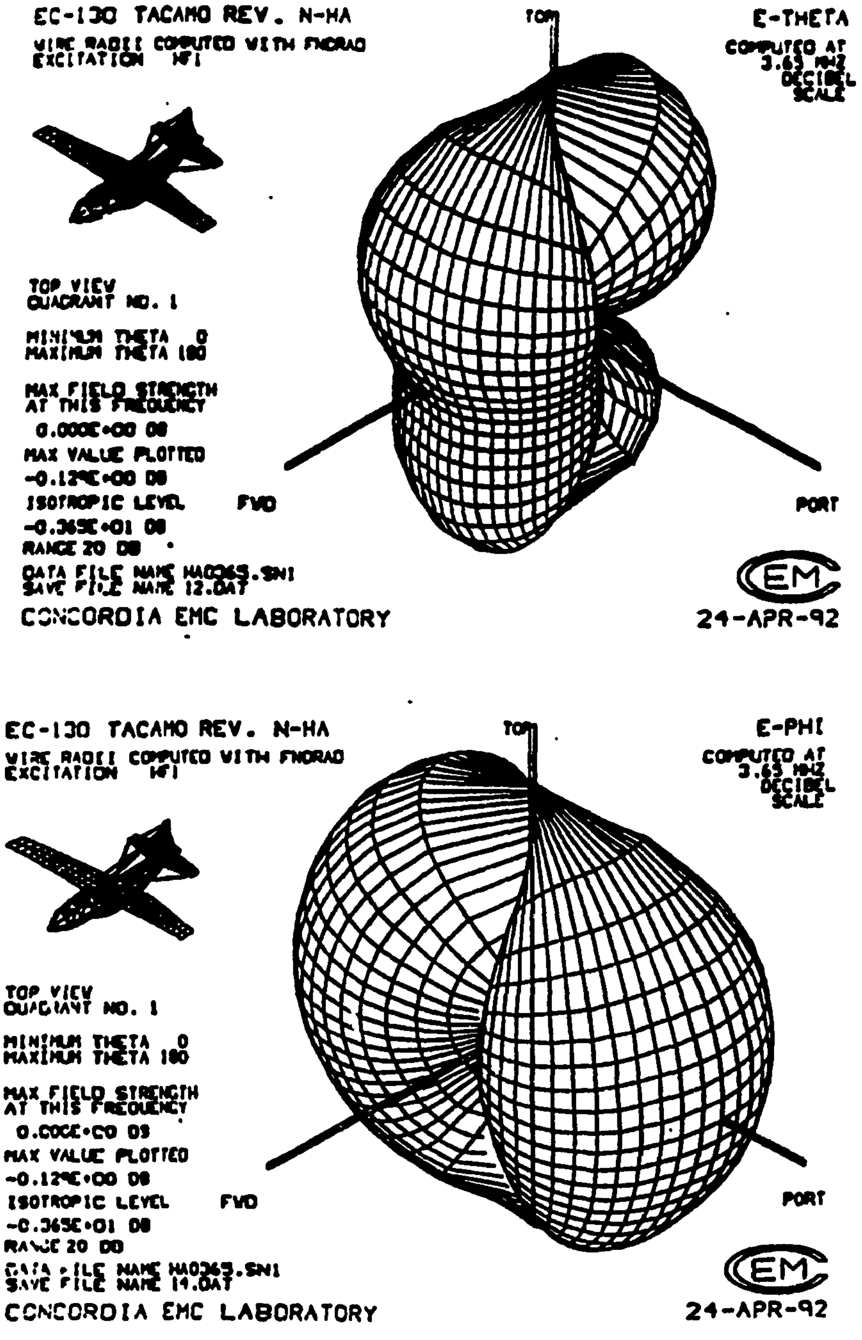

(c) 3.65 MHz

Fig. 5.22 (Cont'd)

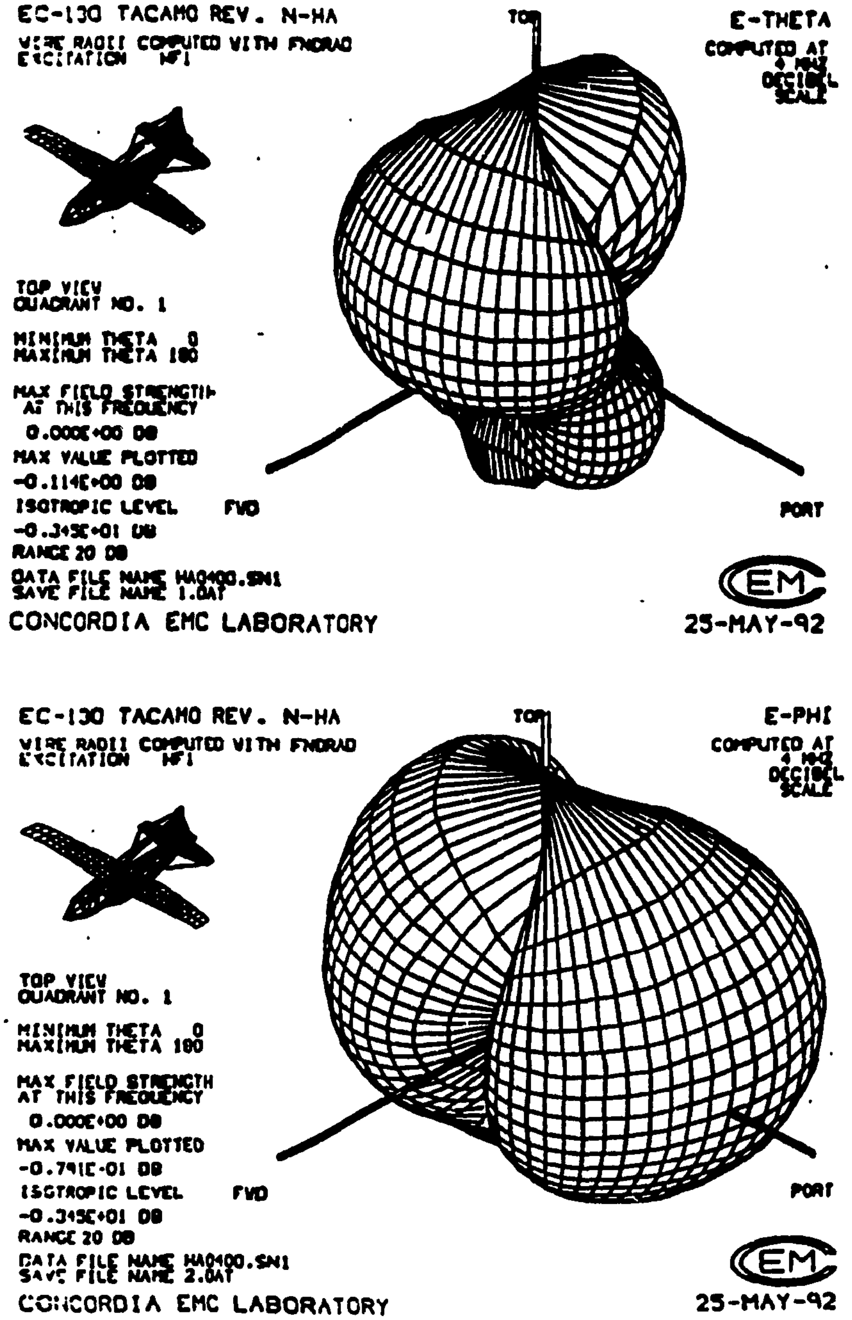

(d) 4.0 MHz

Fig. 5.22 (Cont'd)

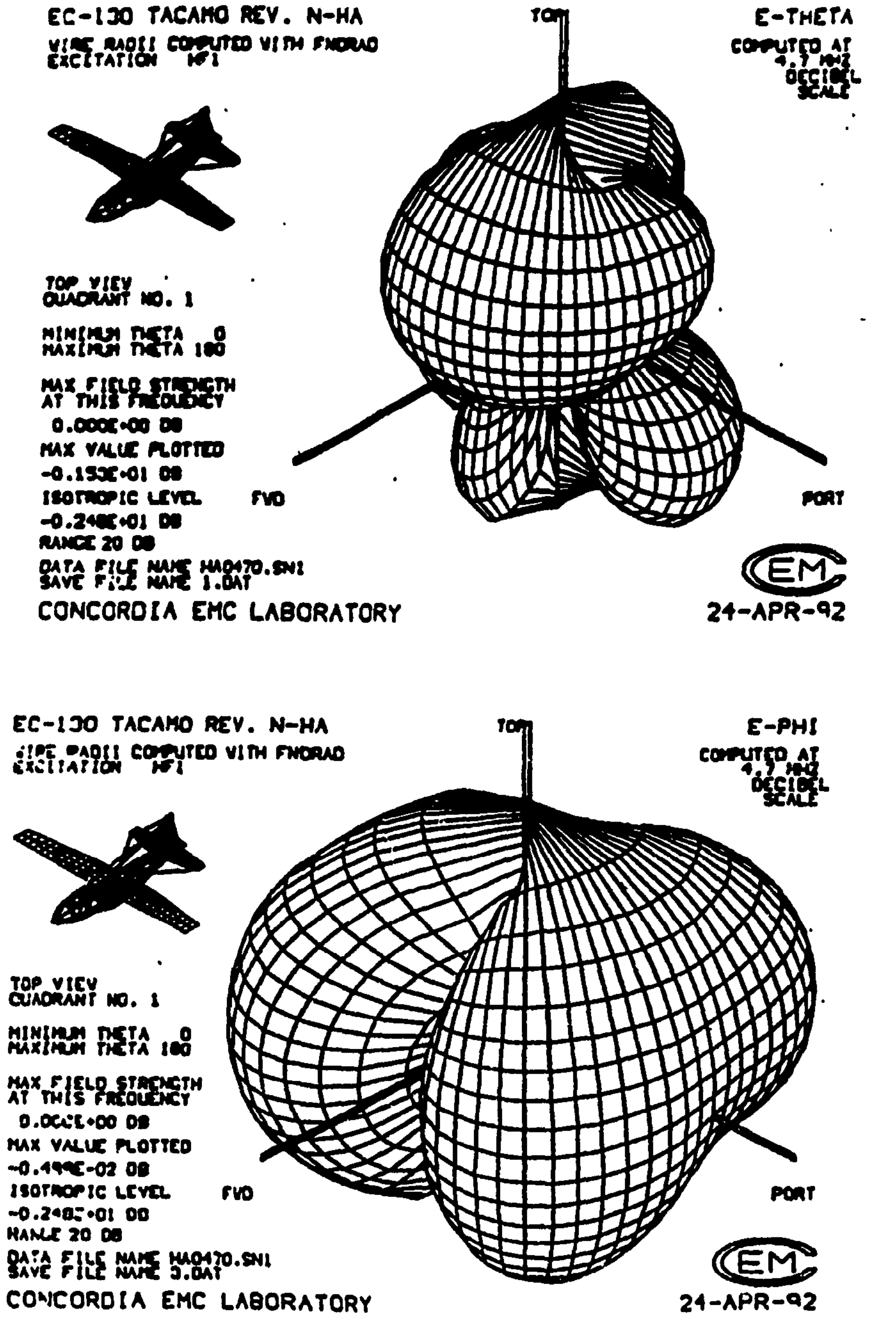

(e) 4.7 MHz

Fig. 5.22 (Cont'd)

Table 5.5 summarizes the effects of inter-antenna coupling on radiation pattern when HF1 is active and passive antennas are open-circuited to the airframe. These changes in radiation pattern are observed from three-dimensional radiation pattern plots at corresponding frequencies. Most profound changes are seen in the E_θ pattern, especially at 9.0, 10.4, and 19.0 MHz.

Similarly, based on the three-dimensional pattern plots at frequencies corresponding to strong coupling and their adjacent frequencies, the effects of inter-antenna coupling on radiation pattern for HF1 active and passive antennas terminated in 50 Ω loads are summarized in Table 5.6. No major changes are seen in the E_ϕ pattern at 10.4, 17.6, and 24.9 MHz, but there is a pattern rotation near 3.2 MHz. The most significant change in E_θ is found near 3.2 MHz where the field is reduced in the forward and aft directions in the sector $60° < \theta < 120°$.

Table 5.5 **Major Changes in Radiation Patterns due to Strong Inter-Antenna Coupling for HF1 Active and Passive Antennas Open-Circuited to the Airframe**

Active Antenna: HF1		Loading Condition for Passive Antenna: Open-Circuit.	
Frequency (MHz)	Coupling	E_θ Field	E_ϕ Field
3.5	HF1 to HF2, HF3	Reduced in the forward direction in the bottom sector.	Two side lobes broadened.
6.5	HF1 to HF2	No major changes.	Enhanced in the starboard direction.
9.0	HF1 to HF2, HF3	Greatly increased in the forward direction.	Each side lobe deformed into two smaller lobes.
10.4	HF1 to HF2, HF3, HF4, HF5	Reduced in the port direction but enhanced in the forward direction.	No major changes.
13.8	HF1 to HF2	No major changes.	Enhanced in the port-aft direction in the top sector.
17.6	HF1 to HF2, HF3	No major changes.	No major changes.
19.0	HF1 to HF2, HF3	Changed from two lobes to four lobes.	No major changes.
21.0	HF1 to HF2	No major changes.	No major changes.
25.0	HF1 to HF2, HF3, HF4, HF5	No major changes.	No major changes.
29.2	HF1 to HF2, HF3	Enhanced in the port-forward, port-aft, and starboard-forward direction.	Reduced in the upward direction.

Table 5.6 Major Changes in Radiation Patterns due to Inter-Antenna Strong Coupling for HF1 Active and Passive Antennas Terminated in 50 Ω

Active Antenna: HF1		Loading Condition for Passive Antennas: 50 Ω Termination.	
Frequency (MHz)	Coupling	E_θ Field	E_ϕ Field
3.2	HF1 to HF2, HF3, HF4, HF5	Reduced in the forward and aft directions in the sector $60° < \theta < 120°$.	Pattern rotated by an azimuth angle, resulting in two lobes oriented in the port and starboard directions.
10.4	HF1 to HF2, HF3, HF4, HF5	No major changes.	No major changes.
17.6	HF1 to HF2, HF3, HF4, HF5	Enhanced in the forward-port direction in the bottom sector.	No major changes.
24.9	HF1 to HF2, HF3, HF4, HF5	No major changes.	No major changes.

The effects of inter-antenna coupling on radiation pattern observed from the three-dimensional plots when HF4 is active and passive antennas are short-circuited to the airframe are summarized in Table 5.7. The coupling near 3.6 MHz results in a rotation of radiation pattern for both E_θ and E_ϕ. No major radiation pattern changes are seen for the coupling near 14.0, 17.7, and 25.0 MHz.

Table 5.7 Major Changes in Radiation Patterns due to Strong Inter-Antenna Coupling for HF4 Active and Passive Antennas Short-Circuited to the Airframe

Active Antenna: HF4		Loading Condition for Passive Antennas: Short-Circuit.	
Frequency (MHz)	Coupling	E_θ Field	E_ϕ Filed
3.6	HF4 to HF1, HF2, HF3, HF5	Pattern Rotated by an azimuth angle of 90° clockwise (viewed from the top).	The starboard lobe rotated by an azimuth angle of 90° clockwise and the forward-port lobe rotated by 30° clockwise (viewed from the top).
4.7	HF4 to HF3	The forward-port lobe rotated by an azimuth angle of 45° counter-clockwise (viewed from the top).	A small lobe added in the forward-port direction.
10.8	HF4 to HF1, HF2, HF3, HF5	Enhanced in the starboard direction.	Enhanced in the port-aft and port-forward direction.
14.0	HF4 to HF3	No major changes.	No major changes.
17.7	HF4 to HF1, HF2, HF3, HF5	No major changes.	No major changes.
25.0	HF4 to HF1, HF2, HF3, HF5	No major changes.	No major changes.

Table 5.8 lists the effects of inter-coupling on radiation pattern for HF4 active and passive antennas open-circuited to the airframe. As in the case of short-circuit, a pattern rotation due to coupling near 3.7 MHz is observed. No significant pattern changes are

seen for the coupling near 21.0, 25.0, and 29.2 MHz.

Table 5.8 Major Changes in Radiation Patterns due to Strong Inter-Antenna Coupling for HF4 Active and Passive Antennas Open-Circuited to the Airframe

Active Antenna: HF4		Loading Condition for Passive Antennas: Open-Circuit.	
Frequency (MHz)	Coupling	E_θ Field	E_ϕ Field
3.7	HF4 to HF1, HF2 HF3, HF5	Pattern rotated by an azimuth angle of 45° clockwise (viewed from the top).	Pattern rotated by an azimuth angle of 45° clockwise (viewed from the top).
6.5	HF4 to HF1, HF2 HF3, HF5	The main lobe in top sector rotated by 90° from port to forward.	The main lobe rotated from port to starboard.
9.0	HF4 to HF3	Pattern changed from irregular shape to two side lobes.	No major changes.
14.0	HF4 to HF1, HF2	No major changes.	No major changes.
19.0	HF4 to HF3	No major changes.	Enhanced in the aft direction.
21.0	HF4 to HF1, HF2, HF3, HF5	No major changes.	No major changes.
25.0	HF4 to HF1, HF2, HF3, HF5	No major changes.	No major changes.
29.2	HF4 to HF1, HF2, HF3	No major changes.	No major changes.

Finally, for HF4 active and passive antennas terminated in 50 Ω loads, the effects of inter-antenna coupling on radiation pattern are summarized in Table 5.9. Again, there is a pattern rotation due to the coupling near 3.7 MHz as in the cases of short-circuit and open-circuit.

Table 5.9 Major Changes in Radiation Patterns due to Strong Inter-Antenna Coupling for HF4 Active and Passive Antennas Terminated in 50 Ω

Active Antenna: HF4		Loading Condition for Passive Antennas: 50 Ω Termination.	
Frequency (MHz)	Coupling	E_θ Field	E_ϕ Field
3.7	HF4 to HF1, HF2 HF3, HF5.	Pattern rotated by an azimuth angle of 45° clockwise (viewed from the top).	Pattern rotated by an azimuth angle of 45° clockwise (viewed from the top).
10.5	HF4 to HF1, HF2 HF3, HF5.	Pattern changed from two side lobes to an irregular shape with minimum in the forward-starboard direction in the sector $60° < \theta < 90°$.	Pattern changed from two lobes to an irregular shape with minimum in the port direction.
17.6	HF4 to HF1, HF2 HF3, HF5	No major changes.	No major changes.
25.0	HF4 to HF1, HF2, HF3, HF5	No major changes.	Enhanced in the forward direction in the bottom sector.

5.3.3.2 Effects on the Aircraft HF Antenna Assessment Parameters

The impact of strong inter-antenna coupling on the aircraft HF antenna assessment parameters is presented in this section. Section 3.5.1 defines the HF assessment parameters. Figure 5.23 shows the aircraft HF antenna assessment parameters for HF1 excited and for three passive antenna loading conditions; Fig. 5.24 shows the parameters when HF4 is excited. Like the input impedance curves, the "peaks" and "notches" on these curves fall at frequencies where there is significant antenna-to-antenna coupling.

5.3.3.2.1 HF1 Excited

In Figures 5.23(a) and 5.23(b), rapid fluctuations of the parameter values occur at lower frequencies, between 2 and 15 MHz. The changes can be as large as 45%. The curves for *Sub-%-*E_θ have the same pattern as the curves for %E_θ, but there is a difference of about 20% in value between the two parameters. Variations in R. P. Efficiency are much smaller compared to %E_θ and *Sub-*%E_θ. In the short-circuit case shown in Fig. 5.23(a), the reduction in %E_θ power due to the coupling between HF1 and HF2 near 10.6 MHz is approximately 35%. Note that when strong coupling between HF1 and HF2 occurs, the currents on the two antennas are always 180° apart in phase, for the short-circuit case. This leads to a cancellation of the far field due to these two antennas since they are closely spaced and nearly parallel. This explains well the reductions in power radiated into the E_θ component at 3.15, 10.6, 17.6, and 24.9 MHz, where strong coupling between HF1 and HF2 is present. We can see in Fig. 5.23(a) that at two frequencies, 3.6, and 4.7 MHz, %E_θ is increased due to coupling. The coupling at 3.6 MHz is between HF1 and all the passive antennas, and the coupling at 4.7 MHz is

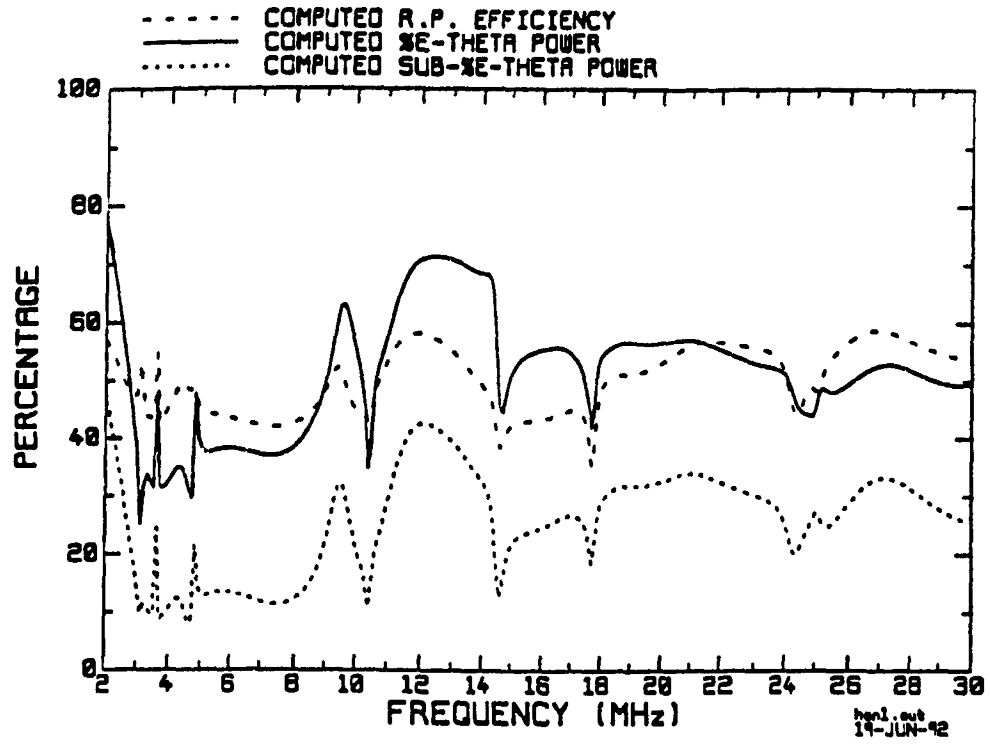

(a) Passive antennas short-circuited

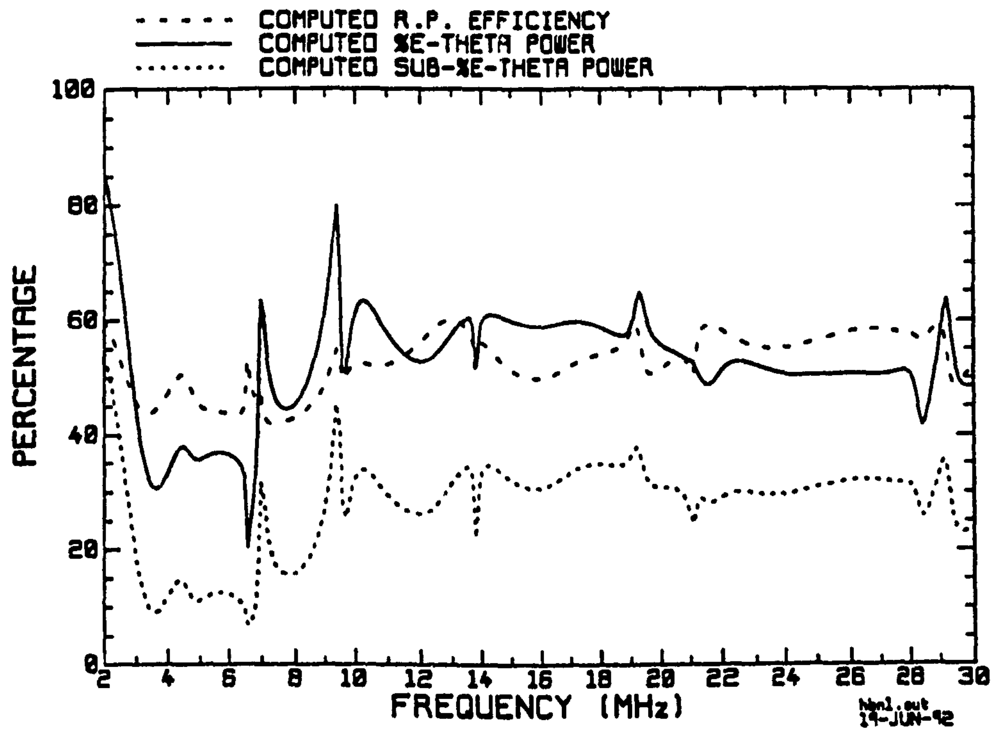

(b) Passive antennas open-circuited

Fig. 5.23 Aircraft HF antenna assessment parameters for HF1 active.

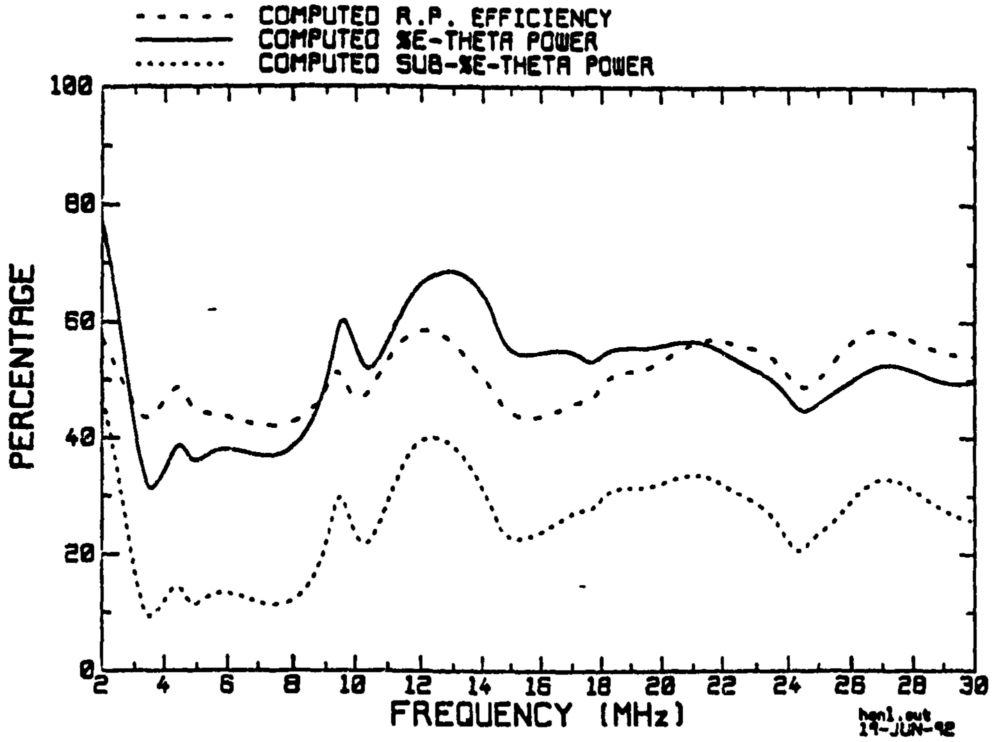

(c) Passive antennas loaded by 50Ω

Fig. 5.23 (Cont'd)

Table 5.10 Impact Due to Major Coupling on the Aircraft HF Antenna Assessment Parameters for HF1 Active and Passive Antennas Short-Circuited to the Airframe

Active Antenna: HF1		Loading Condition for Passive Antennas: Short-Circuited.		
Frequency (MHz)	Coupling	R.P. Efficiency	$\%E_\theta$ Power	Sub-E_θ Power
3.2	HF1 to HF2	+5%	-5%	-
3.6	HF1 to HF2, HF3, HF4, HF5	+10%	+18%	+15%
4.7	HF1 to HF3	+5%	+18%	+12%
10.4	HF1 to HF2	-10%	-35%	-25%
14.1	HF1 to HF3	-5%	-25%	-20%
17.6	HF1 to HF2	-12%	-18%	-10%
25.0	HF1 to HF2	+2%	+3%	+5%

Table 5.11 Impact due to Major Coupling on Aircraft HF Antenna Assessment Parameters for HF1 Excited and Passive Antennas Open-Circuited to the Airframe

Active Antenna: HF1		Loading Condition for Passive Antennas: Open-Circuit.		
Frequency (MHz)	Coupling	R. P. Efficiency	%E_θ Power	*Sub*-%E_θ Power
3.5	HF1 to HF2, HF3	-5%	-8%	-5%
6.4	HF1 to HF2	+8%	-15%	-3%
7.0	HF1 to HF4, HF5	-	+45%	+25%
9.0	HF1 to HF2, HF3	+3%	+35%	+20%
10.4	HF1 to HF2, HF3, HF4, HF5	-	+15%	+8%
13.8	HF1 to HF2	-8%	-8%	-12%
19.0	HF1 to HF2, HF3	+3%	+5%	+2%
21.0	HF1 to HF2	-	-5%	-3%
29.2	HF1 to HF2, HF3	-	+20%	+10%

Table 5.12 Impact due to Major Coupling on the Aircraft HF Antenna Assessment
Parameters for HF1 Active and Passive Antennas Terminated in 50 Ω

Active Antenna: HF1		Loading Condition for Passive Antennas: 50 Ω Termination.		
Frequency (MHz)	Coupling	R. P. Efficiency	%-E_θ Power	*Sub*-%E_θ Power
3.2	HF1 to HF2, HF3, HF4, HF5	-5%	-8%	-5%
10.4	HF1 to HF2, HF3, HF4, HF5	-5%	-10%	-10%
17.6	HF1 to HF2, HF3, HF4, HF5	-1%	-	-
24.5	HF1 to HF2, HF3, HF4, HF5	-9%	-6%	-12%

between HF1 and HF3. Table 5.10 summarizes the effects of inter-antenna coupling on the assessment parameters for HF1 active and passive antennas short-circuited to the airframe. The largest change in R.P. Efficiency is found near 17.6 MHz with a decrease of 12%. For $\%E_\theta$, the largest decrease is 35% found near 10.4 MHz, and the largest increase is 18% found near 3.6 and 4.7 MHz. The decrease in *Sub-*$\%E_\theta$ is largest near 10.4 MHz with 25%, and the increase is largest near 3.6 MHz with 15%.

In the open-circuit case shown in Fig. 5.23(b), the increase in $\%E_\theta$ power due to coupling between HF1 and HF3 near 9 MHz is about 35%. The largest increase in $\%E_\theta$ (about 45%) is found near 7.0 MHz where strong coupling between HF1, HF4 and HF5 is present. Other noticeable changes in $\%E_\theta$ are found near 13.8 MHz where there is coupling between HF1 and HF2; 19 MHz with coupling between HF1 and HF3; and 29 MHz where there is coupling between HF1, HF2 and HF3. Table 5.11 summarizes the effects of inter-antenna coupling on the assessment parameters for HF1 active and passive antennas open-circuited to the airframe. There no significant changes in R.P. Efficiency for coupling near 7.0, 10.4, 21.0, and 29.2 MHz. The changes in R.P. Efficiency due to coupling at other frequencies are small and less than 8%. The largest increases in $\%E_\theta$ and *Sub-*$\%E_\theta$ are found near 7.0 MHz with 35% $\%E_\theta$ for and 25% for *Sub-*$\%E_\theta$. The coupling near 6.4 MHz results in a largest decrease in $\%E_\theta$ with 15%.

In the case of 50 Ω loading shown in Fig. 5.23(c), the variation in parameter values is less radical. This is consistent with the fact the coupling magnitude is much lower in this case. The most noticeable reductions in $\%E_\theta$ are located near 3.2, 10.4, and 24.5 MHz where relatively strong coupling between HF1 and HF2 is present. The effects of inter-antenna coupling on the assessment parameters are summarized in Table 5.12 for HF1 active and passive antennas terminated in 50 Ω loads. The largest reduction in R.P. Efficiency is 9% found near 24.5 MHz. For $\%E_\theta$, the largest reduction is 10% found near 10.4 MHz. A reduction in *Sub*-$\%E_\theta$ of 12% is seen near 24.5 MHz.

5.3.2.2.2 HF4 Excited

Figure 5.24 shows the aircraft HF antenna assessment parameters plotted versus frequency for HF4 active. Tables 5.13, 5.14, and 5.15 summarize the coupling effects. As in the case of HF1 active, the most significant effects of coupling are seen in the $\%E_\theta$ and *Sub*-$\%E_\theta$ power, whereas the changes in R.P. Efficiency due coupling is relatively small. The most interesting observation about the aircraft HF antenna assessment parameters shown in Fig. 5.24 for HF4 is the unusually high $\%E_\theta$ power near 9 MHz for all three loading conditions for passive antennas. The value of this parameter is as high as 85% at 9.5 MHz. This phenomenon can be explained by the large induced currents found on the vertical stabilizer and the large vertical component of the current on the exciting "dog-leg" antenna HF4 near this frequency.

The effects of major inter-antenna coupling on the $\%E_\theta$ power are quite obvious in the short-circuit and open-circuit cases shown in Fig. 5.24(a) and Fig. 5.24(b), respectively. The most noticeable examples are the two peaks due to coupling near 3.6 between HF4 and all the passive antennas, and 4.7 MHz between HF4 and HF3 in the $\%E_\theta$ power curve. Table 5.13 summarizes the changes due to major inter-antenna coupling and antenna-to-airframe coupling on the three assessment parameters. The largest increase in $\%E_\theta$ is 58% and is due to the coupling from HF4 to the aircraft's tail.

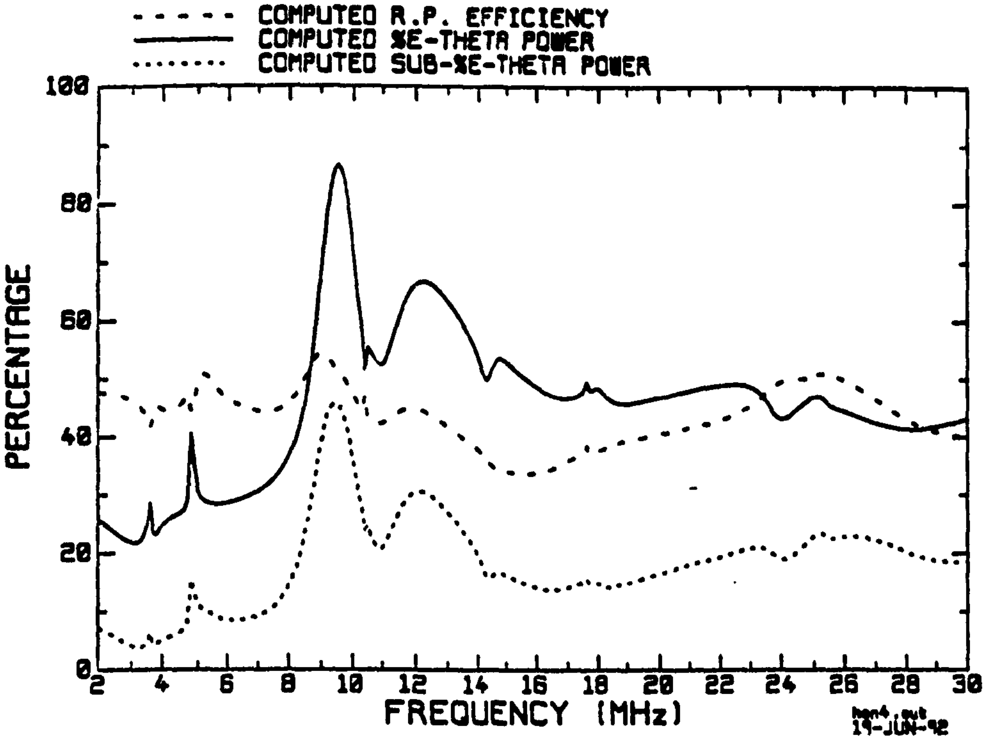

(a) Passive antennas short-circuited

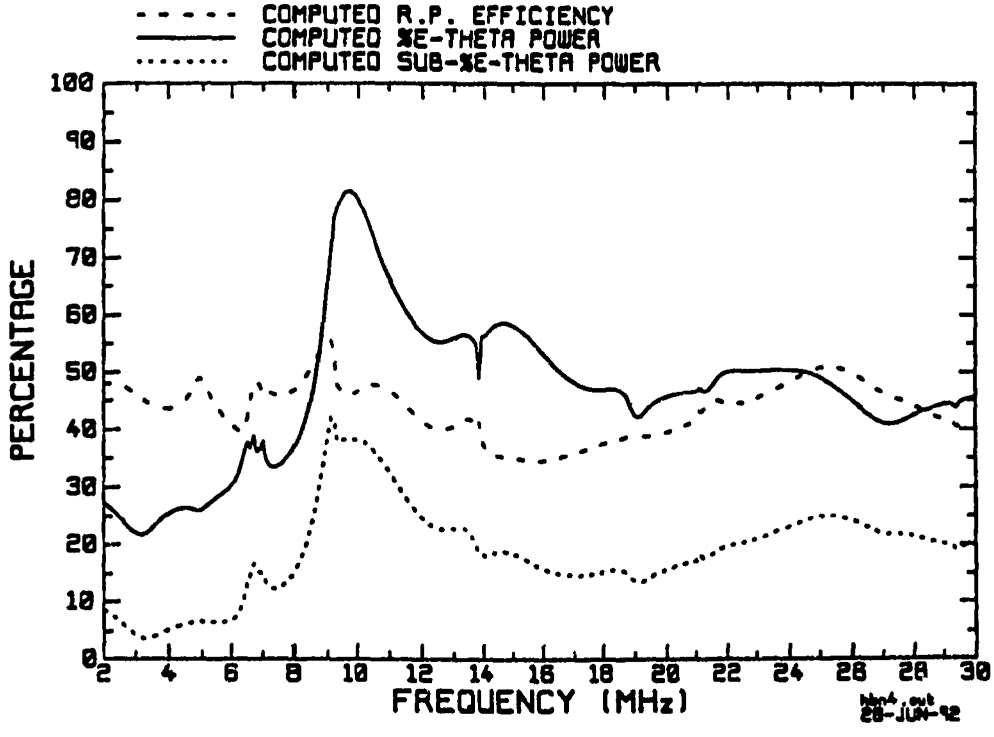

(b) Passive antennas open-circuited

Fig. 5.24 Aircraft HF antenna assessment parameters for HF4 active.

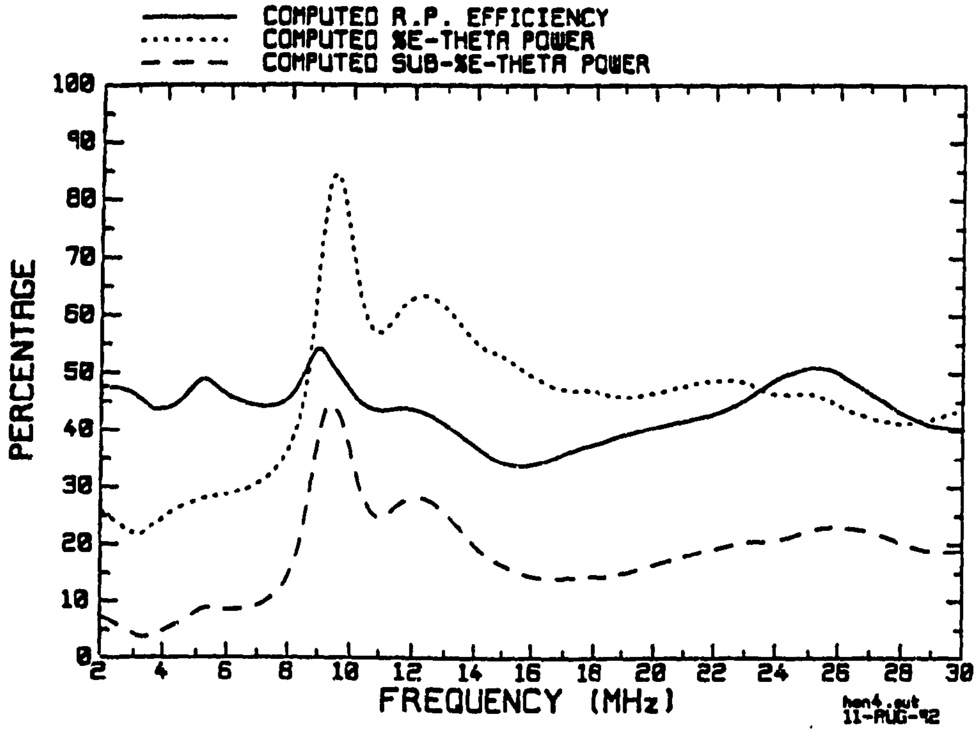

(c) Passive antennas loaded by 50Ω

Fig. 5.24 (Cont'd)

Table 5.13 **Impact due to Major Coupling on Aircraft HF Antenna Assessment Parameters for HF4 Active and Passive Antennas Short-Circuited to the Airframe.**

Active Antenna: HF4		Loading Condition for Passive Antennas: Short-Circuit.		
Frequency (MHz)	Coupling	R. P. Efficiency	%E_θ Power	*Sub*-%E_θ Power
3.6	HF4 to HF1, HF2, HF3, HF5	-2%	+5%	+1%
4.7	HF4 to HF3	-1%	+12%	+5%
9.0	HF4 to Tail	+10%	+58%	+35%
10.8	HF4 to HF5	-2%	+1%	–
14.1	HF4 to HF3	-2%	–	–
17.6	HF4 to HF5	+1%	–	–
25.0	HF4 to HF3	–	+2%	+2%

Table 5.14 Impact due to Major Coupling on Aircraft HF Antenna Assessment Parameters for HF4 Active and Passive Antennas Open-Circuited to the Airframe.

Active Antenna: HF4		Loading Condition for Passive Antennas: Open-Circuit.		
Frequency (MHz)	Coupling	R. P. Efficiency	$\%E_\theta$ Power	$Sub\text{-}\%E_\theta$ Power
6.5	HF4 to HF1, HF2	+8%	±2%	+10%
9.0	HF4 to HF3, Tail	+8%	+45%	+35%
13.8	HF4 to HF1, HF2	+2%	-8%	-5%
19.0	HF4 to HF3	-	-5%	-2%

Table 5.15 Impact due to Major Coupling on Aircraft HF Antenna Assessment Parameters for HF4 Active and Passive Antennas Terminated in 50Ω.

Active Antenna: HF4		Loading Condition for Passive Antennas: 50 Ω.		
Frequency (MHz)	Coupling	R. P. Efficiency	$\%E_\theta$ Power	$Sub\text{-}\%E_\theta$ Power
3.6	HF4 to HF1, HF2, HF3, HF5	-	-4%	-4%
9.0	HF4 to Tail	+10%	+55%	+35%
10.8	HF4 to HF1, HF2, HF3, HF5	-	-6%	-4%

For passive antennas open-circuited, the coupling between HF4, HF5 and HF3 causes the small "ripple" near 6.5 MHz in the $\%E_\theta$ curve. There are also two small "notches" in this curve as a result of the coupling between HF4, HF1 and HF2 near 13.8 MHz and between HF4 and HF3 near 19 MHz. The effects of coupling on the parameters for HF4 active and passive antennas open-circuited to the airframe are summarized in Table 5.14. Except for the HF4-to-tail coupling near 9.0 MHz, the changes in parameter value due to coupling is less than 10%.

The assessment parameter values in Fig. 5.24(c) for passive antennas terminated in 50 Ω resistances show little effects of inter-antenna coupling. All three curves are relatively "smooth" compared to the two other cases. These curves can be viewed as the curves in the two other cases with the "peaks" and "notches" smoothed out. Table 5.15 summarizes the effects of coupling on the parameters for HF4 active and passive antennas terminated in 50 Ω loads. The largest change due to inter-antenna coupling in this case is only 6%, which is the change in $\%E_\theta$ at 10.8 MHz. The increase in $\%E_\theta$ due to the HF4-to-tail coupling is 55%.

5.4 Concluding Comments

Through the application of high resolution spectral analysis, a detailed diagnosis of the HF coupling modes on the EC-130 aircraft has been obtained. Two kinds of coupling are identified: inter-antenna coupling and antenna-to-airframe coupling. The inter-antenna coupling is the most striking kind of coupling on this aircraft. This kind of coupling is much stronger than the antenna-to-airframe coupling. Moreover, its "bandwidth" is narrower in nature. It has been shown that the inter-antenna coupling has a significant impact on the HF communication over a very narrow frequency band.

The resonant frequencies of each of the antennas can be used to sort out the complicated inter-antenna coupling phenomena. The loading conditions for passive antennas are found to have significant influence on the inter-antenna coupling modes. As a result, inter-antenna coupling modes can be described in terms of the resonant and anti-resonant frequencies of the antennas, and the loading conditions for the passive antennas.

The antenna-to-airframe coupling is dominated by the inter-antenna coupling in the case of HF1 excitation and the former has little impact on the radiation characteristics. However, in the case of HF4 excitation, the antenna-to-airframe coupling is stronger and hence plays a more important role in the coupling consequences such as alterations in the radiation pattern and aircraft HF antenna assessment parameter values.

CHAPTER 6

HF ANTENNA PERFORMANCE ON THE CL-600

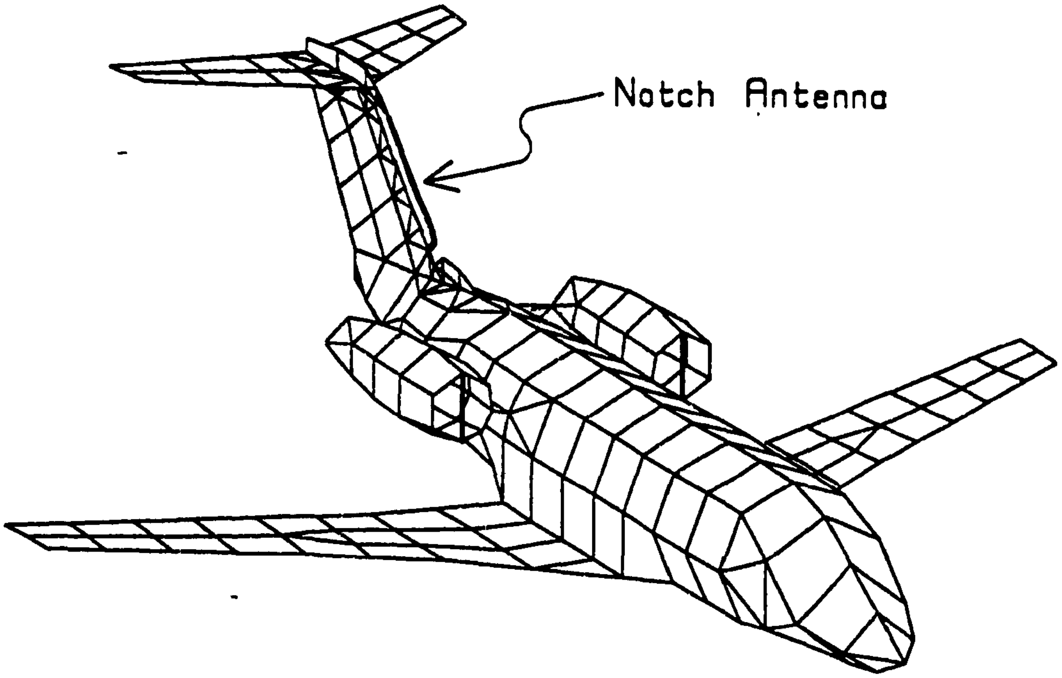

Fig. 6.1 The CL-600 Challenger Aircraft.

This chapter presents the computer modelling results of the CL-600/Challenger aircraft with an emphasis on the coupling from the HF antenna to the airframe.

Unlike the EC-130, the CL-600 shown in Fig. 6.1 has only one HF antenna, which is a "notch" antenna located at the dorsal of the aircraft's tail [30]. Fig. 6.2 shows the construction of the notch antenna. Thus no HF inter-antenna coupling can exist and the study of HF coupling modes on this aircraft is concerned with the coupling between the antenna and the airframe only. The main objectives here are to investigate the radiation

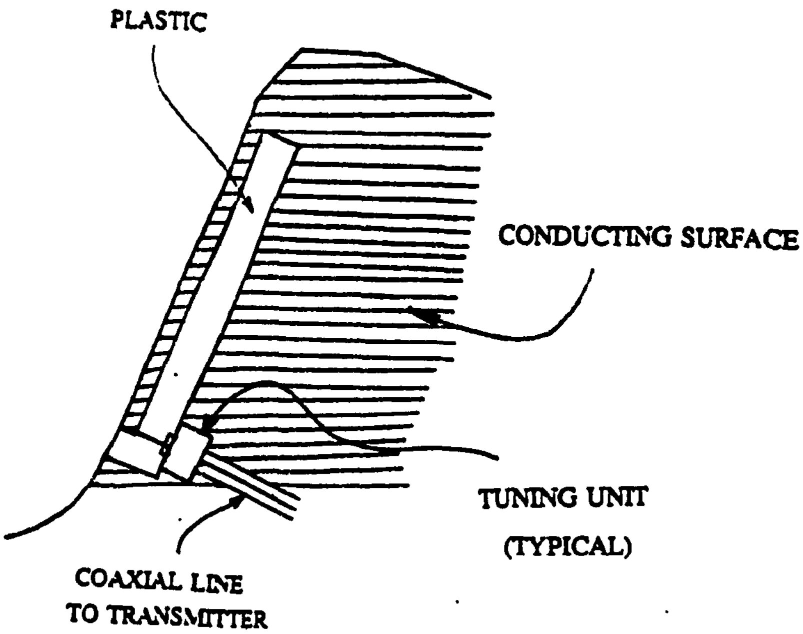

Fig. 6.2 The construction of the notch antenna on the CL-600.

characteristics of this notch antenna and to identify the possible current paths on the airframe and the frequencies at which they occur, as well as their impact on radiated power and the radiated field patterns.

This chapter compares computations with and without the "extended kernel" (EK) described above in Sec. 2.1.2. It was discovered that the EK option of NEC had significant effects on the results because the antenna input impedance curves obtained from running NEC with and without the EK card were considerably different from each other. This chapter shows that the results obtained without the EK option are in better agreement with the impedance characteristics of a notch antenna and the current distributions in the antenna region.

6.1 Notch Antenna Input Impedance

As in the previous chapter, the input impedance of the antenna is used as an indicator to reveal the frequencies where coupling to the aircraft occurs. A curve that represents the impedance of a coupling-free notch antenna must be obtained for reference. Moreover, the theoretical impedance curve is also used to judge the credibility of the results computed with and without the EK card.

6.1.1 Computed Input Impedance

Fig. 6.3 shows the notch antenna input impedance as a function of frequency computed with and without the EK card. It can be seen that the two curves are quite different for the range from 2 to 24 MHz. In the case of no EK, the input resistance is less than 1 ohm from 2 to 6 MHz. There is a "valley" near 9 MHz and a "bump" near 13 MHz in the resistance curve. The input resistance reaches its highest value near 24 MHz where the input reactance changes from positive to negative. By contrast, the input resistance in the case with EK has a value ranging from 10 to 30 ohms in the band from 2 to 6 MHz. No abrupt changes in resistance value are found except near 13 MHz, where a tiny "bump" is observed in the curve. In addition, the input reactance has lower values in the band from 2 to 6 MHz compared to the case without EK.

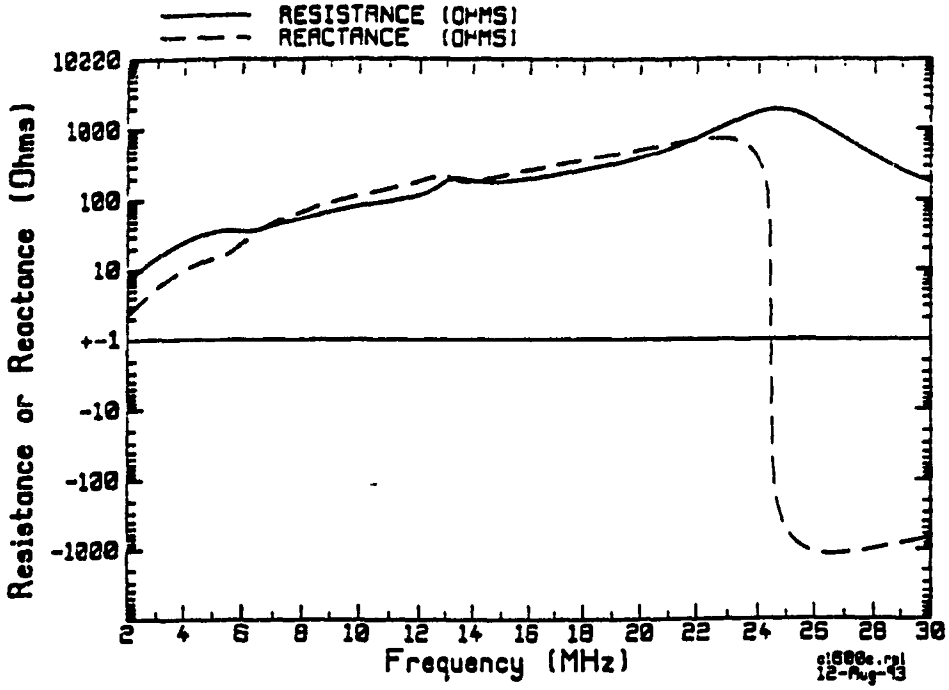

(a) With EK

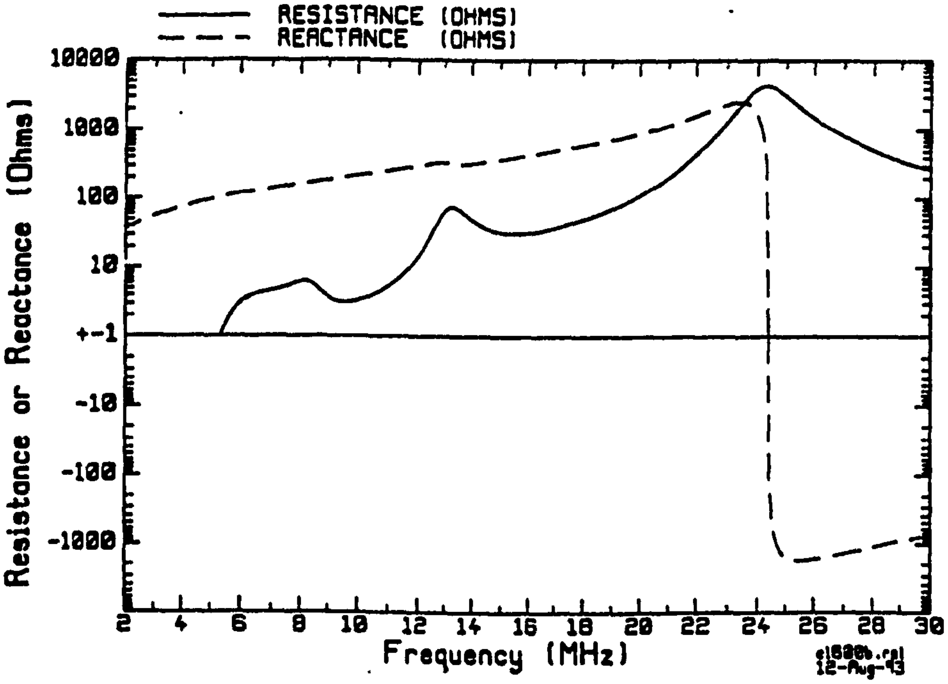

(b) Without EK

Fig. 6.3 Input impedance of the notch computed with and without EK.

6.1.2 Theoretical Input Impedance

It is difficult to determine the theoretical input impedance of the notch antenna on this particular aircraft due to its special geometry and location on the aircraft. A formula for calculating the theoretical input impedance for a notch cut in the edge of a semi-infinite conducting sheet is available [30]

$$Z_{in} = R + jX \tag{6.1}$$

where

$$R = \frac{2\eta}{3[C(\beta l) - \cot(\beta l) S(\beta l)]^2} \tag{6.2}$$

$$X = \frac{Z_l 60\pi^2 \tan(\beta l)}{\ln(\frac{16l}{W}) - 1} \tag{6.3}$$

C(x) and S(x) are even and odd Fresnel integrals, respectively.

$$C(x) = \frac{1}{\sqrt{2\pi}} \int_0^x \frac{\cos t}{\sqrt{t}} dt \tag{6.4}$$

$$S(x) = \frac{1}{\sqrt{2\pi}} \int_0^x \frac{\sin t}{\sqrt{t}} dt \tag{6.5}$$

l is the length and *w* is the width of the notch, and η is the intrinsic impedance of free space which is equal to 377 Ω.

In practice, however, the sheet will always be finite in extent. The conducting sheet may be thought of as the aircraft's dorsal. However, it may also be thought of as the surface of the whole aircraft in a broader sense. Note that on one side of the notch, the conducting sheet is extremely small. The expression for radiation resistance may be expected to be accurate within a few per cent if the sheet extends for a distance of the order of a wavelength from the notch [56]. The reactance expression should be independent of the size of the sheet if it is not extremely small. This is because the reactance is due to the induction field, and it is significant only in the immediate vicinity of the notch [56].

6.1.3 Similarity to the Tranline Antenna

The notch on this particular aircraft has a length $l = 2.64$ m and a width $w = 0.15$ m. This notch antenna of Fig. 6.2 is similar to a short-circuited tranline antenna as shown in Fig. 6.3. A short-circuited tranline antenna is formed by a conducting wire mounted on the airframe which is excited at one end and electrically connected to the airframe at the other end. The input impedance of a short-circuited tranline antenna on a helicopter had been investigated by Esfandiari [8]. Fig. 6.5 shows the measured input impedance of the short-circuited tranline antenna on the BELL-CH135 helicopter [8]. The input impedance in Fig. 6.3 of the notch antenna on the CL-600 is expected to be similar to the tranline antenna input impedance in Fig. 6.5. Comparing Fig. 6.3 and 6.5 shows that the tranline antenna's resistance is like that of the notch computed without using the EK option. Focusing first on the input resistance, the tranline antenna has resistance values close to zero for the frequency range from 2 to 5 MHz, which is similar to the computed resistance without EK. As for the reactance, the tranline antenna's reactance is very much like the computed reactance shown in Fig. 6.3, especially part(b) where the EK option was suppressed.

6.1.4 Comparison between Computed and Theoretical Impedance

The theoretical notch antenna (cut in the edge of a semi-infinite conducting sheet) input impedance of Equations 6.1 to 6.5 is shown in Fig. 6.6 as a function of frequency for the notch dimensions mentioned above. It is desired to determine which of the two computed impedance curves in Fig. 6.3 is more credible. Fig. 6.6 shows that the input resistance for a notch cut in the edge of a semi-infinite sheet is very different from that of the notch on the CL-600. This can be explained by noting that the input resistance strongly depends on the size of the conducting sheet, the resistance for a notch in a semi-infinite sheet is not suitable to be used as a reference for the notch with an extremely narrow conducting strip on this aircraft. This also means that Eq. 6.1 is not suitable for assessing the notch antenna on this aircraft.

The input reactance is less dependent on the size of the conducting sheet. Figures 6.3 and 6.5 show that the tranline reactance and the reactance for a notch in a semi-infinite sheet are very similar. Indeed, they both have the typical reactance pattern of a short-circuited transmission line. When compared to the computed reactance of the notch on the CL-600 in Fig. 6.3, the reactance in Fig. 6.6 or Fig. 6.6 is more like the one in Fig. 6.3(b) where the EK option was suppressed than the one in Fig. 6.3(a) where the EK option was used. We can draw the conclusion that the computed results obtained without using the EK option are more reliable. It is noted that the computed reactance changes from positive to negative near 24.3 MHz. This frequency corresponds to the anti-resonance of a short-circuited transmission line when the length of the line is equal to a quarter wavelength.

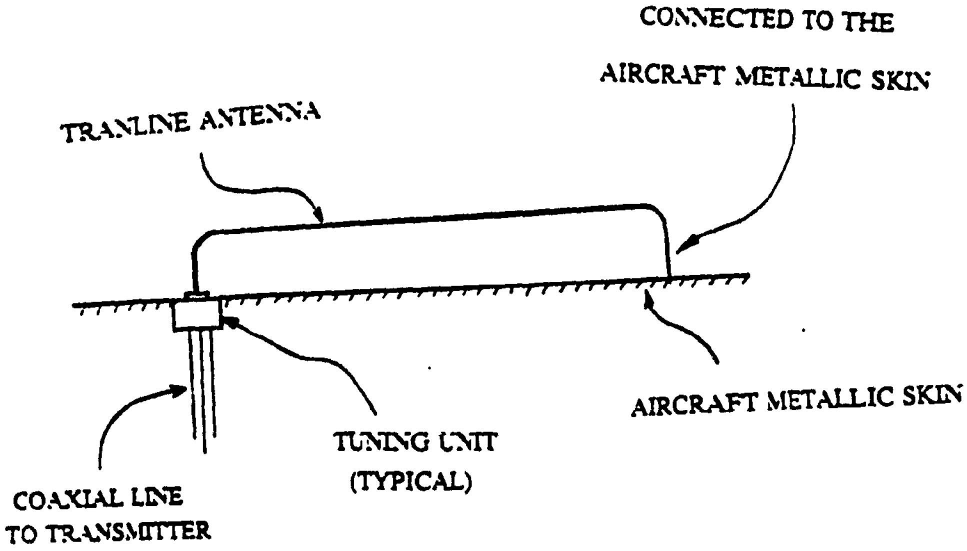

Fig. 6.4 A short-circuited tranline antenna.

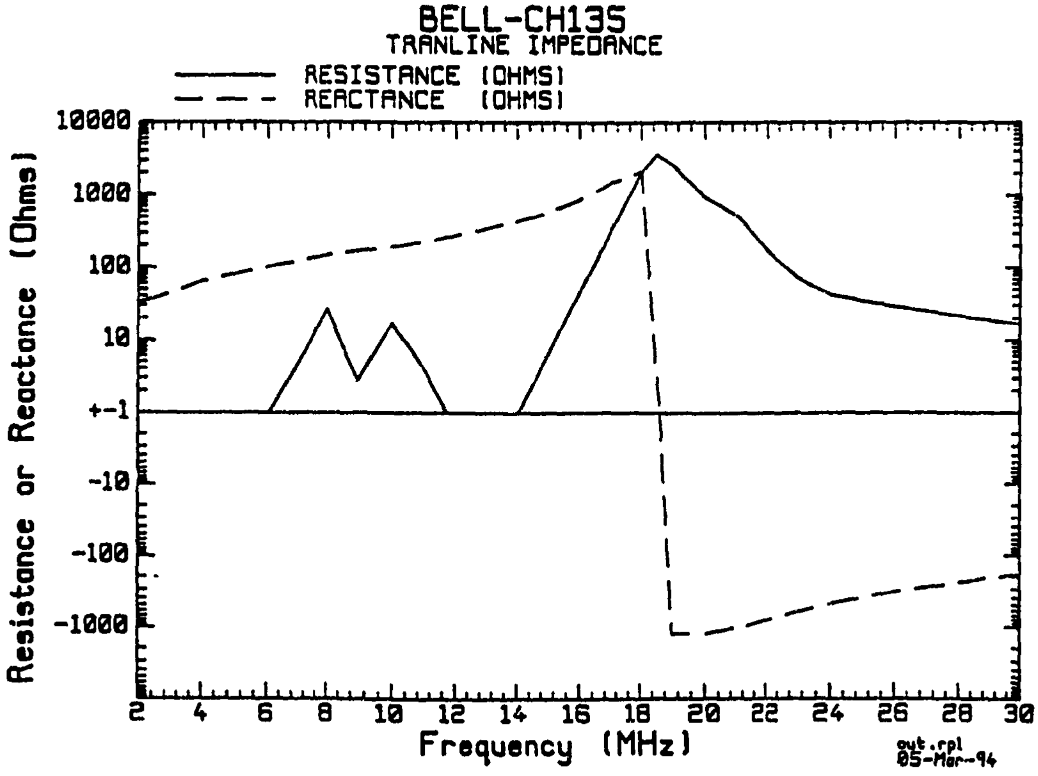

Fig. 6.5 Input impedance of a short-circuited tranline antenna [8].

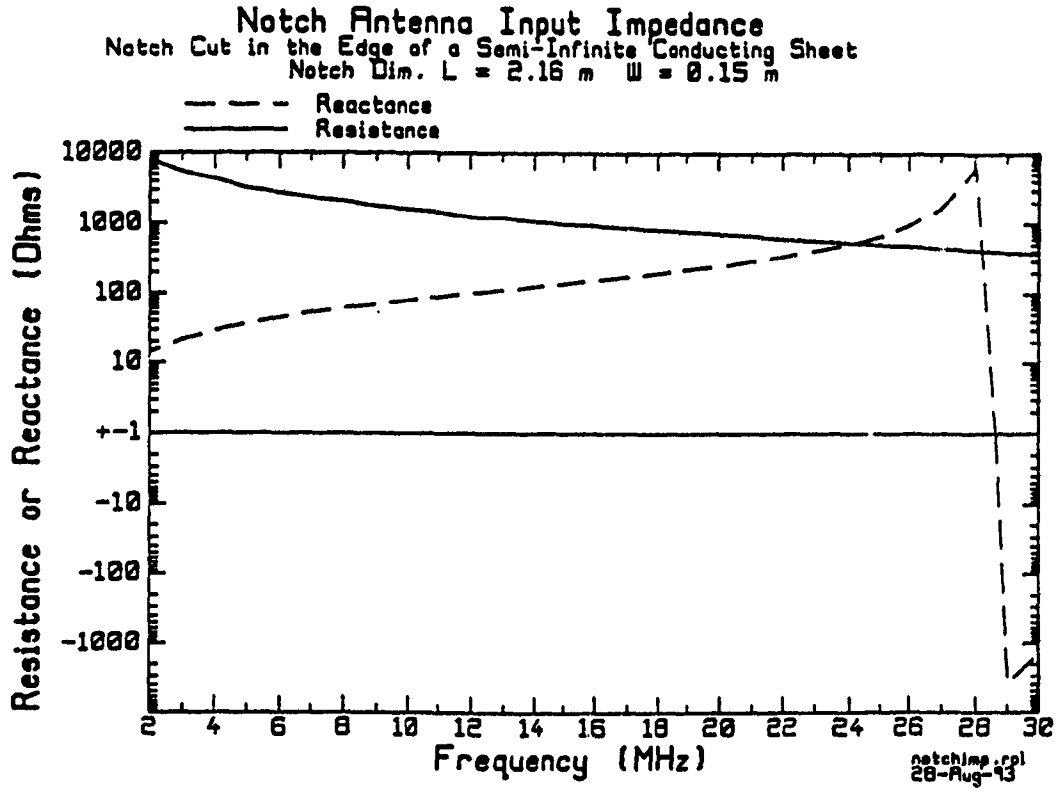

Fig. 6.6 Input impedance of a notch cut in the edge of a semi-infinite conducting sheet.

6.2 Current Paths on the Airframe

Two major pairs of current paths were identified as a result of the coupling of the notch antenna to the airframe. Each pair of current paths is symmetric about the aircraft's axial center-line, because of the symmetry of the aircraft's structure and the location of the exciting notch antenna along the center-line of the aircraft.

Recall that strong coupling usually results in rapid changes in antenna impedance with frequency. It should be possible to associate the coupling paths with the features such as "bumps" and valleys" in the impedance curve. The first symmetric pair of coupling paths are shown in Fig. 6.7(a). Fig 6.8 shows that at 9 MHz, the wires along this pair of paths are plotted in "yellow", indicating that these wires carry larger currents than their neighbours. The frequency of 9 MHz corresponds to the "valley" in the input resistance curve of Fig. 6.2(b). At 9 MHz, the length of the path from the wing-tip to the aft edge of the engine is 15.46 m, corresponding closely to one-half wavelength. An examination of the distribution of current magnitude and phase along the path in a rectangular-graph format shown in Fig. 6.8(b) indicates that the path is indeed at half-wavelength resonance with the peak at the center of the path and a constant phase throughout the path.

The second pair of current paths shown in Fig. 6.7(b) looks a little similar to the first pair, but this path includes the dorsal fin and horizontal stabilizer and is much longer than the first. Fig. 6.9(a) shows that at 13 MHz, large induced currents are present along these paths. A "bump" is seen in the resistance curve of Fig. 6.3(b) near 13 MHz. The length of the path from the wing-tip to the tip of the horizontal stabilizer is 22.87 m, corresponding closely to one wavelength at 13 MHz. The current magnitude and phase along the path shown in Fig. 6.9(b) are similar to the current distribution on a one-wavelength dipole with two magnitude peaks and an abrupt phase shift of 180° at the null in the current magnitude. The following two sections discuss the impact of these couplings from the notch antenna to the airframe on the radiated fields.

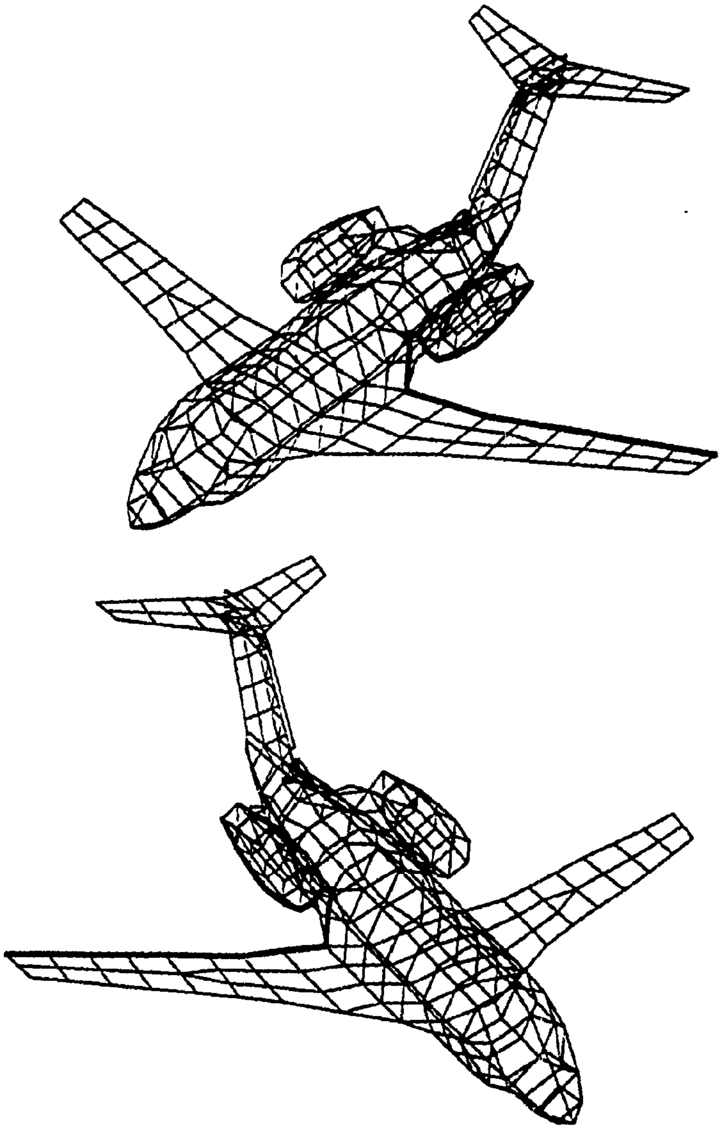

(a) First pair of paths

Fig. 6.7 Current paths on the CL-600.

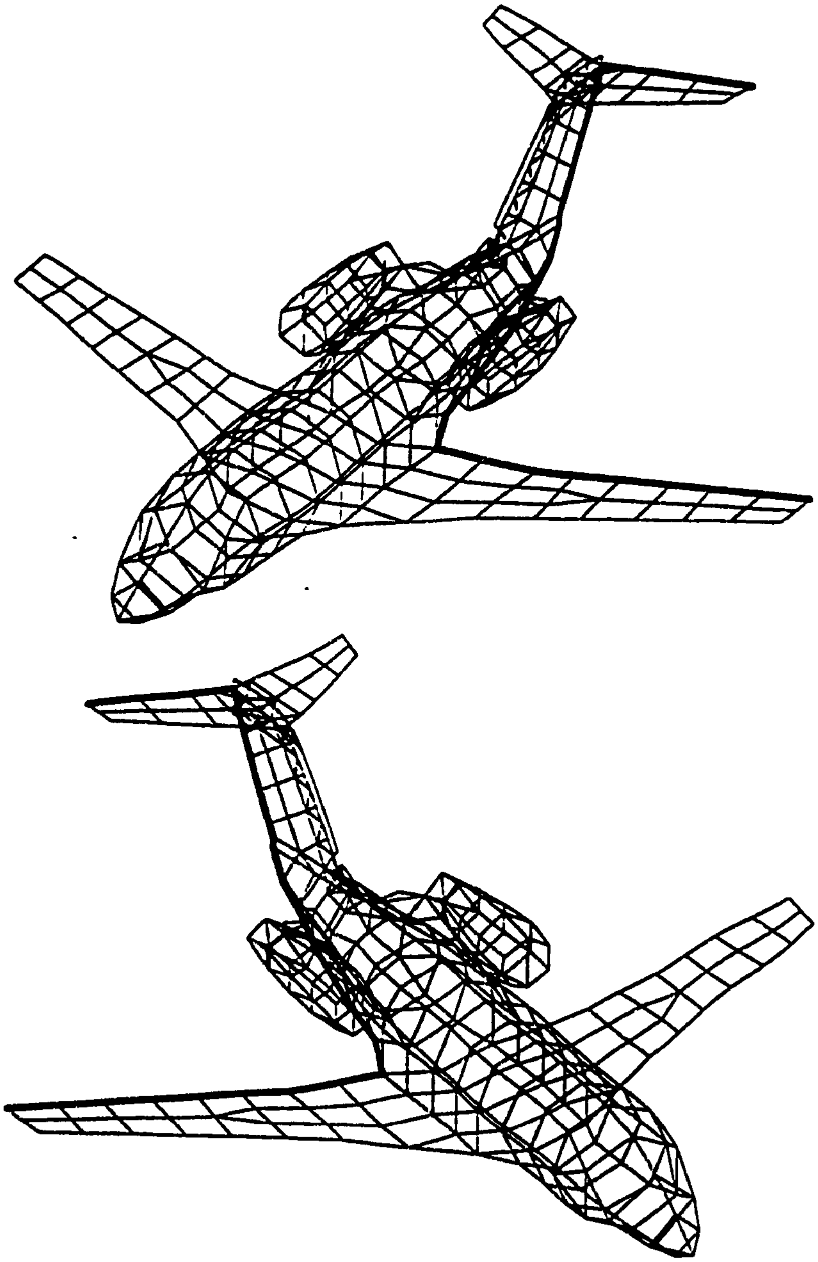

(b) Second pair of paths

Fig. 6.7 (Cont'd)

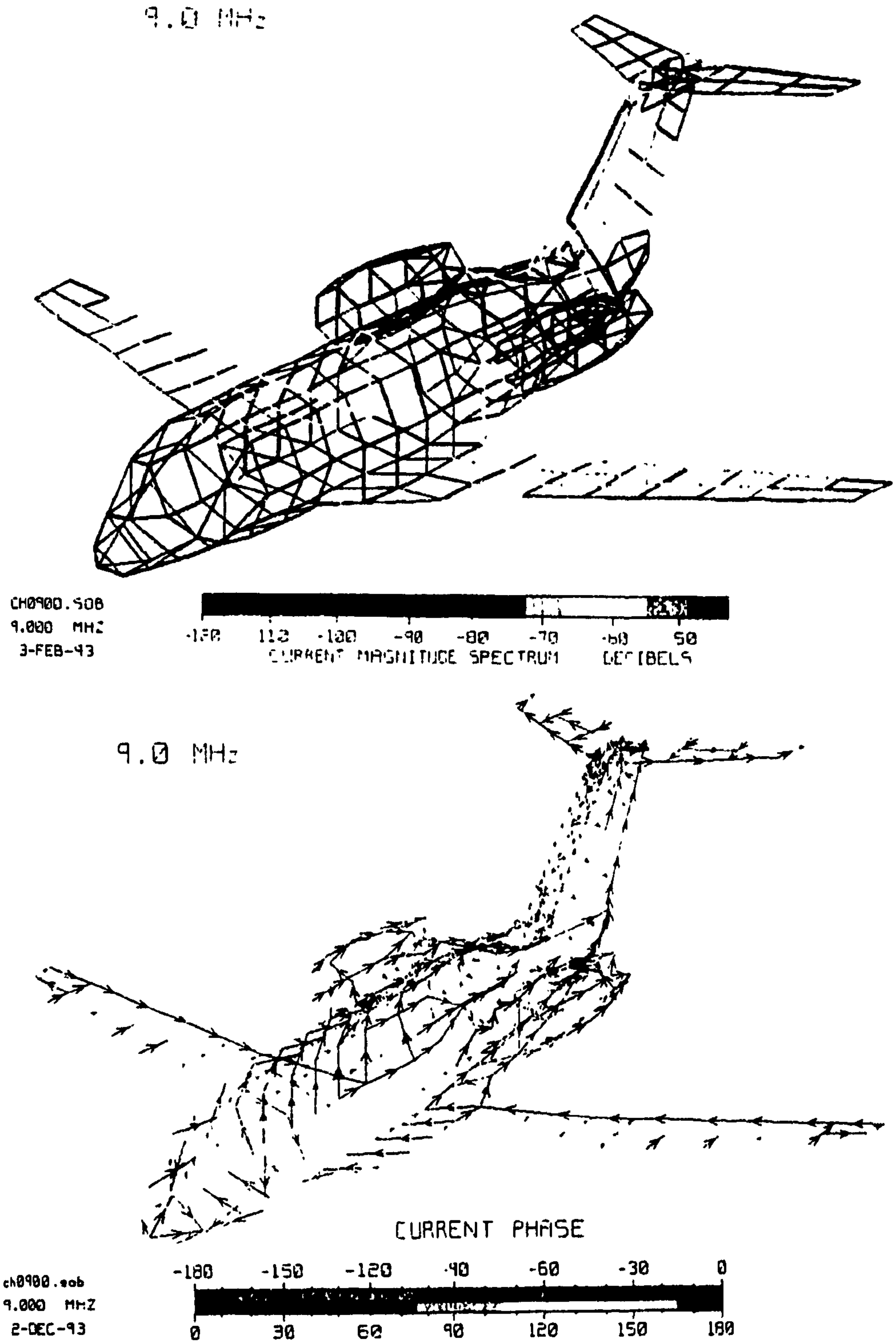

(a) Magnitude and phase shown in color

Fig. 6.8 Current distribution at 9 MHz.

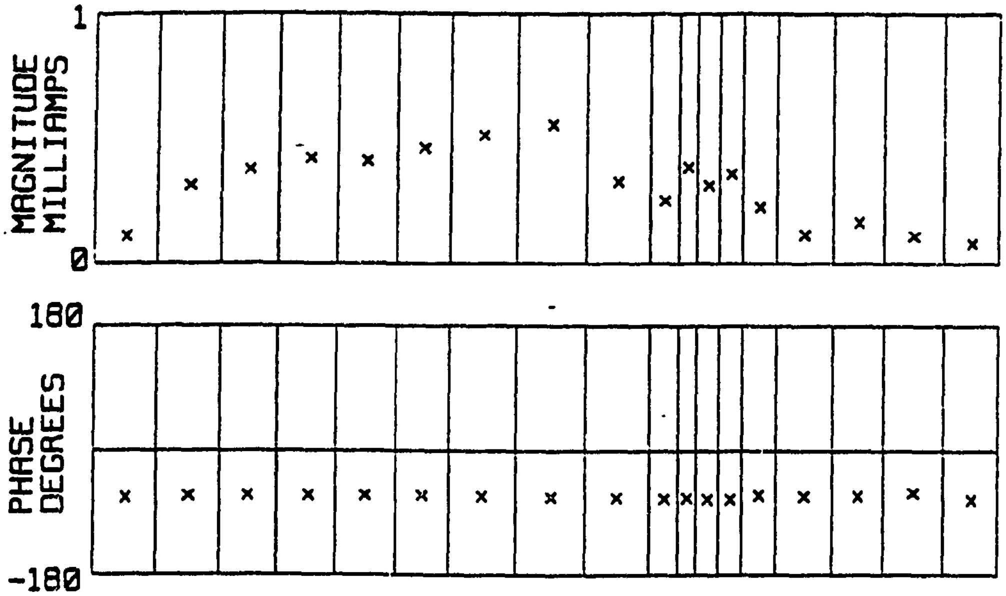

(b) Magnitude and phase along the current path at 9 MHz

Fig. 6.8 (cont'd)

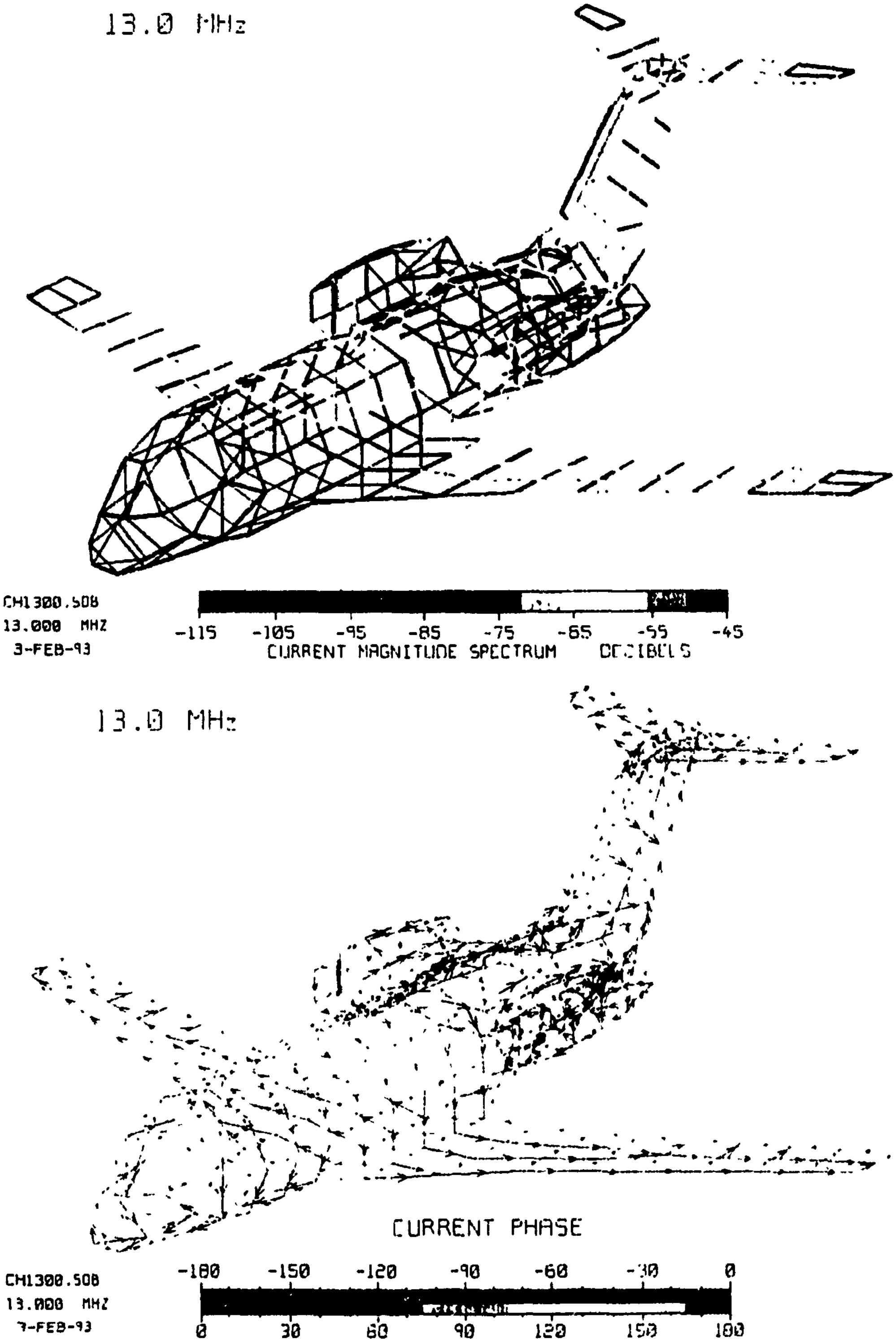

(a) Magnitude and phase shown in color

Fig. 6.9 Current distribution at 13 MHz.

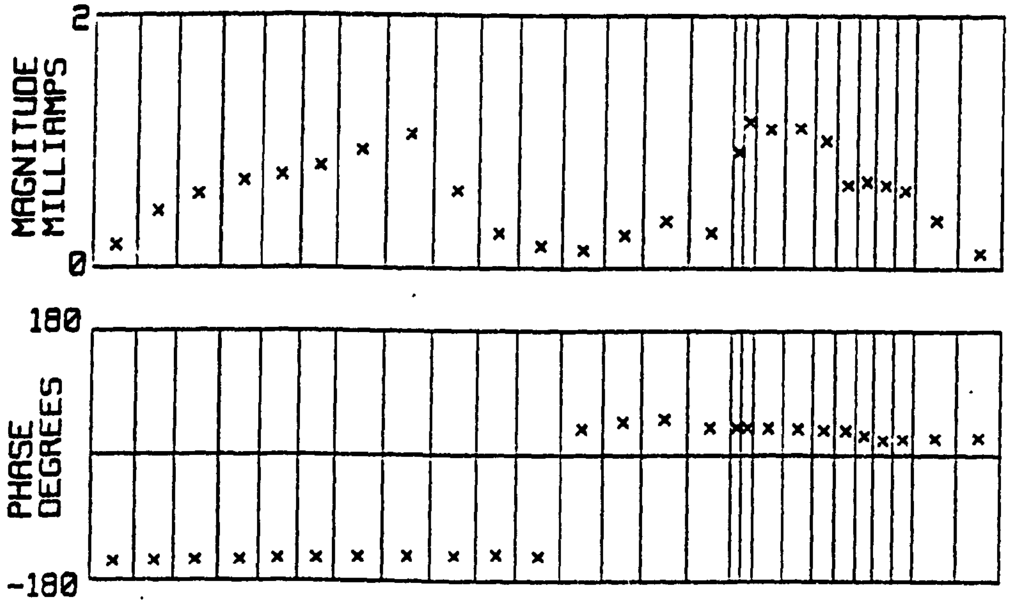

(b) Magnitude and phase along the current path at 13 MHz

Fig. 6.9 (cont'd)

6.3 Effects of Coupling on the Radiation Pattern

In order to observe to the effects of the antenna-to-airframe coupling, radiated patterns in the neighbourhoods of the frequencies where strong coupling occurs are examined in this section. It was shown in the previous section that strong coupling is found near 9 and 13 MHz. The patterns in three principal planes, namely, θ=90°; ϕ=0°; ϕ=90°, as well as the three-dimensional patterns around these two critical frequencies will be presented in the following.

Fig. 6.10 depicts the radiation patterns in the three principal planes at 8, 9, and 10 MHz. In Fig. 6.10(a), E_θ patterns for three frequencies in the θ=90° are compared. The pattern is seen to change from near isotropic at 8 MHz to front-and-back lobes at 10 MHz. For E_ϕ, the comparison of the azimuth pattern is shown in Fig. 6.10(b). It is seen that the E_ϕ pattern changes dramatically from two lobes at 8 MHz to four lobes at 9 MHz, and then it broadens to two lobes in the aft direction. In the elevation plane ϕ=0°, the E_θ pattern, shown in Fig. 6.10(c), changes rapidly from two lobes at 8 MHz to near isotropic at 9 MHz, and then to a heart shape with the minimum in the direction of ϕ=150°. As for E_ϕ, its magnitude is extremely small (near zero) for all directions in this elevation plane and is not shown here. For the elevation plane ϕ=90°, the E_θ pattern, shown in Fig. 6.10(d), undergoes a considerably change from two lobes at 8 MHz to roughly four lobes at 9 MHz, and then to distinctive four lobes at 10 MHz. In contrast, the E_ϕ pattern, shown in Fig. 6.10(e), is unchanged and remains isotropic over this frequency range.

Fig. 6.11 compares the three-dimensional patterns of E_θ and E_ϕ at 8, 9, and 10

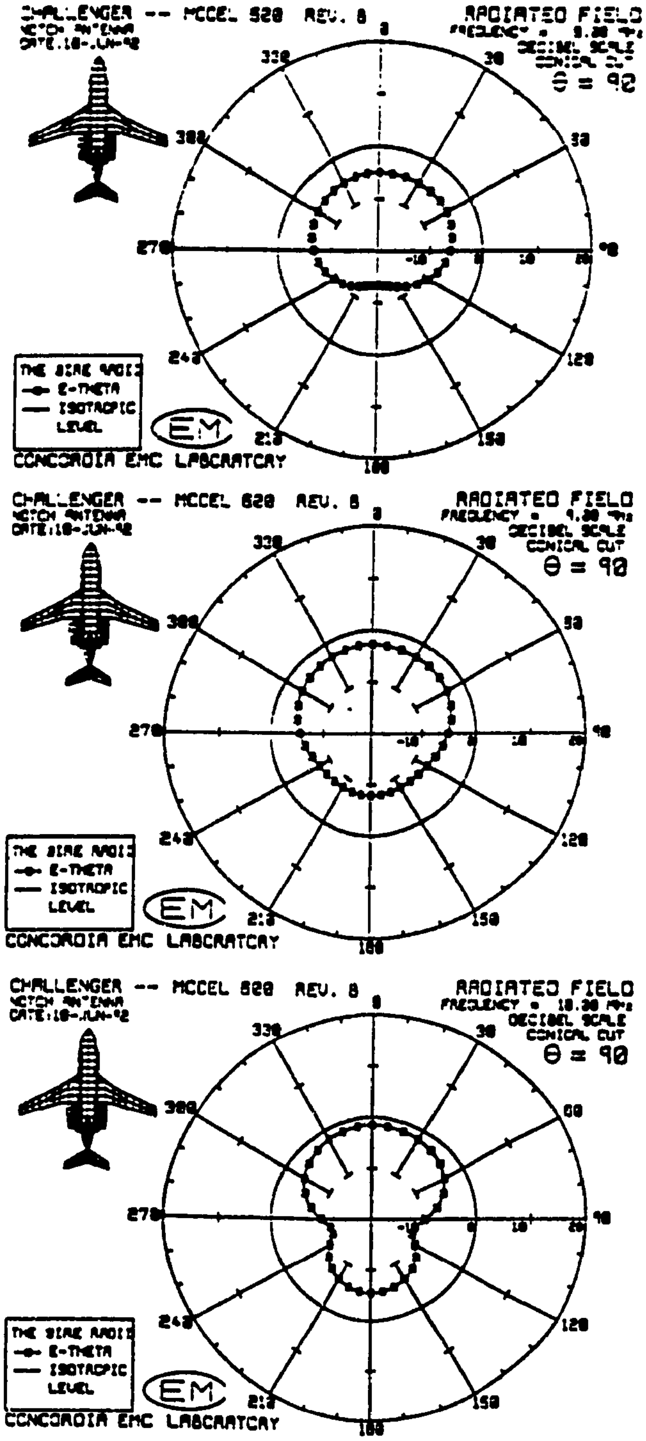

(a) E_θ patterns in the θ = 90° plane at 8, 9, 10 MHz

Fig. 6.10 Radiation patterns in three principal planes in the neighbourhoods of 9 MHz.

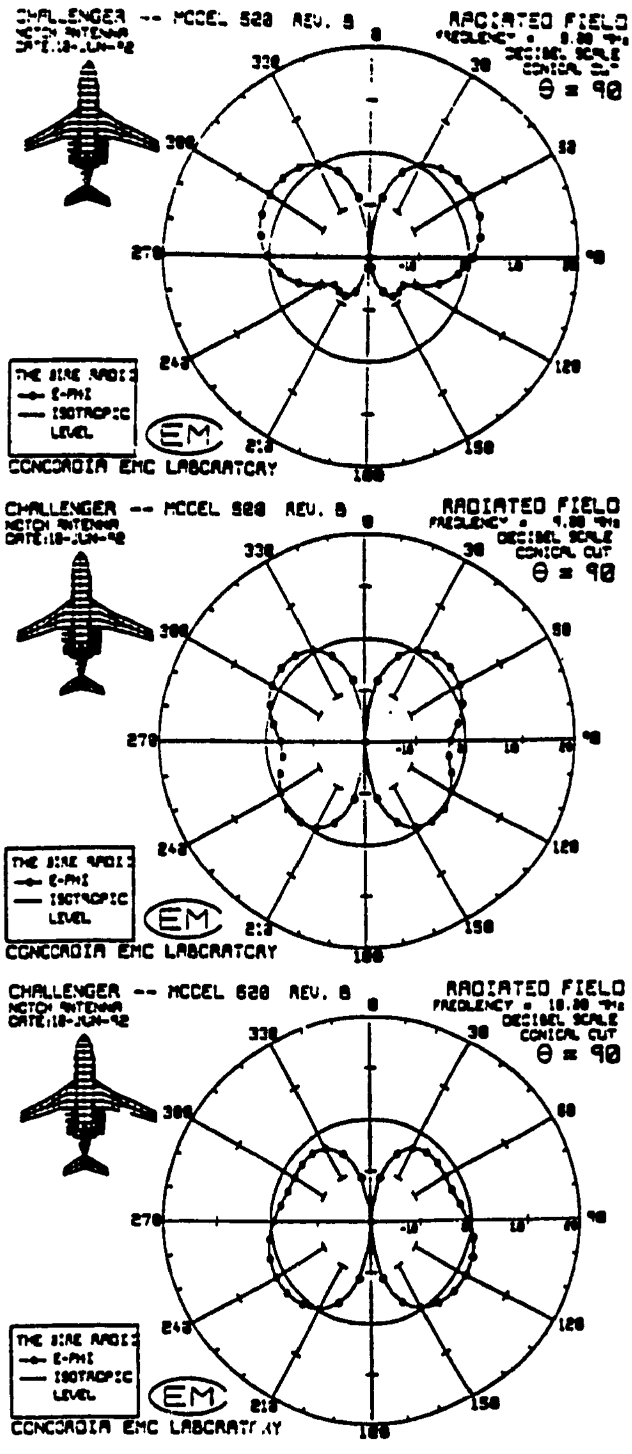

(b) E_ϕ patterns in the $\theta = 90°$ plane at 8, 9, 10 MHz

Fig. 6.10 (Cont'd)

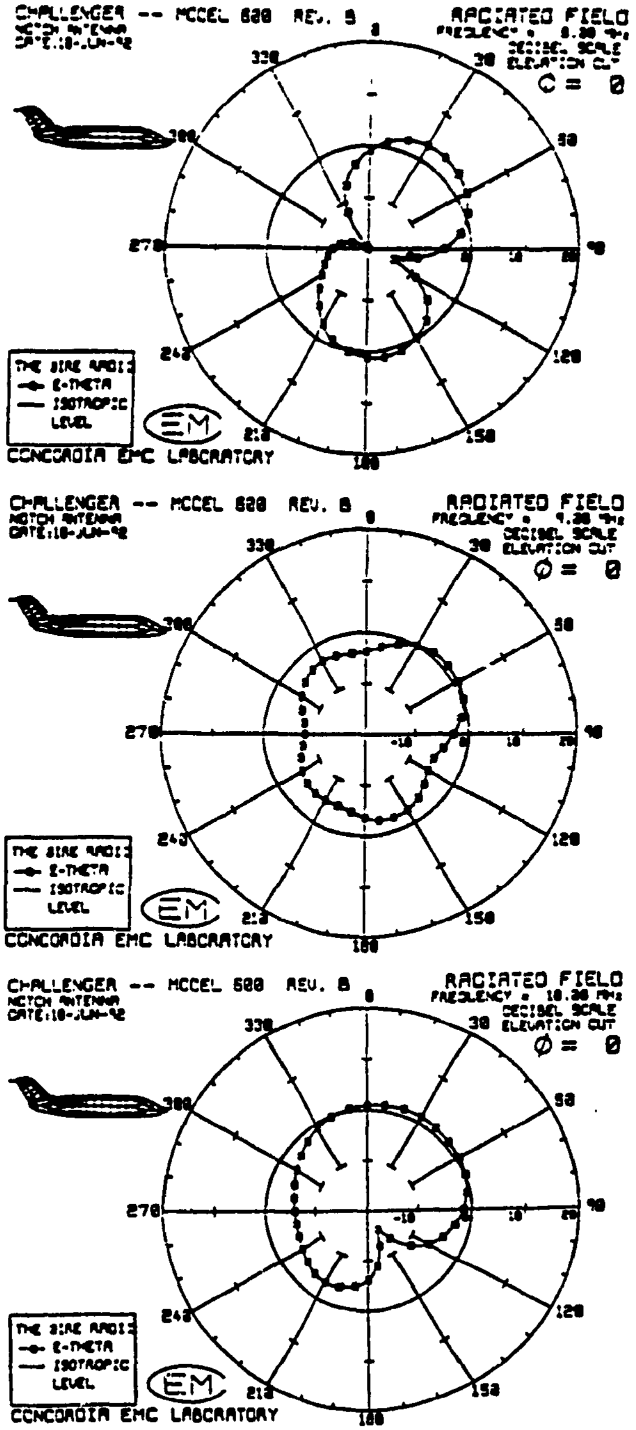

(c) E_θ patterns in the $\phi = 0°$ plane at 8, 9, 10 MHz

Fig. 6.10 (Cont'd)

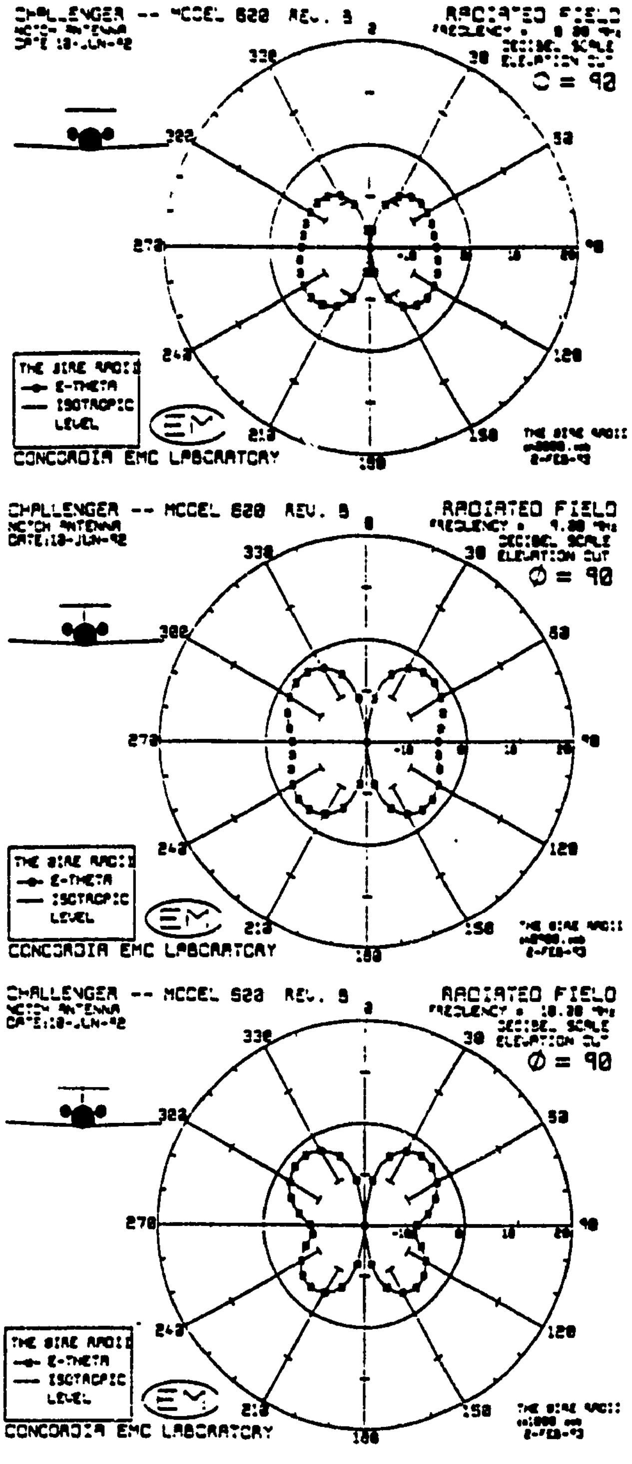

(d) E_θ patterns in the $\phi = 90°$ plane at 8, 9, 10 MHz

Fig. 6.10 (Cont'd)

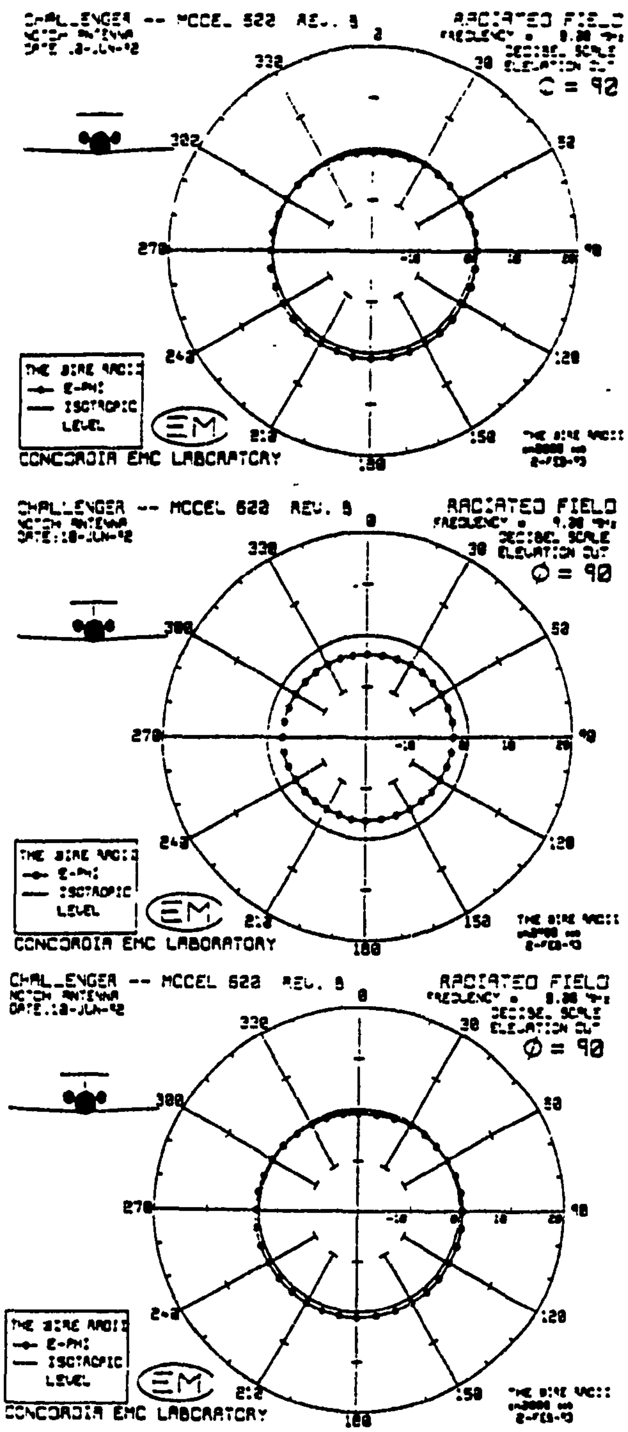

(e) E_ϕ patterns in the $\phi = 90°$ plane at 8, 9, 10 MHz

Fig. 6.10 (Cont'd)

MHz to have an overview of the change due to the coupling near 9 MHz. The E_θ pattern is shown at the top and E_ϕ at the bottom of Fig. 6.10. These three-dimensional plots can be a little misleading. If we did not look at the polar plots for the three principal planes in Fig. 6.9, we would easily conclude that for the coupling near 9 MHz, the most dramatic change in radiation pattern takes place in E_ϕ. As can be seen in Fig. 6.11, the total number of main lobes in the E_ϕ pattern increases from two at 8 MHz to four at 9 MHz and then changes back to two main lobes, with two additional minor lobes at 10 MHz. In contrast to E_ϕ, the change in the pattern of E_θ is less profound, although some minor changes in the bottom part of the E_θ pattern are observed as the frequency is increased from 8 to 10 MHz. However, as discussed in the preceding paragraph, E_θ pattern in fact also undergoes some radical changes, at least in the three principal planes. But these changes are not readily seen in the three-dimensional plots of Fig. 6.11.

For the coupling near 13 MHz, changes in radiation patterns are assessed by examining E_θ and E_ϕ patterns in three principal planes shown in Fig. 6.12, and in a three-dimensional format Fig. 6.13. In Fig. 6.12(a), the E_θ patterns in the $\theta=90°$ plane at 12, 13, and 14 MHz are shown. The changes are not drastic and the pattern remains to be a figure of eight throughout this frequency range, although the field on the two sides of the aircraft increases as the frequency is increased. For E_ϕ, Fig. 6.12(b), the pattern is seen to change rapidly from two lobes at 12 MHz to four lobes at 13 and 14 MHz in this azimuth plane. In the elevation plane $\phi=0°$, the E_θ pattern, shown in Fig. 6.12(c), is seen to change from three lobes at 12 MHz to four lobes at 13 and 14 MHz. As for E_ϕ, its magnitude is extremely small in all directions in this elevation plane and is omitted

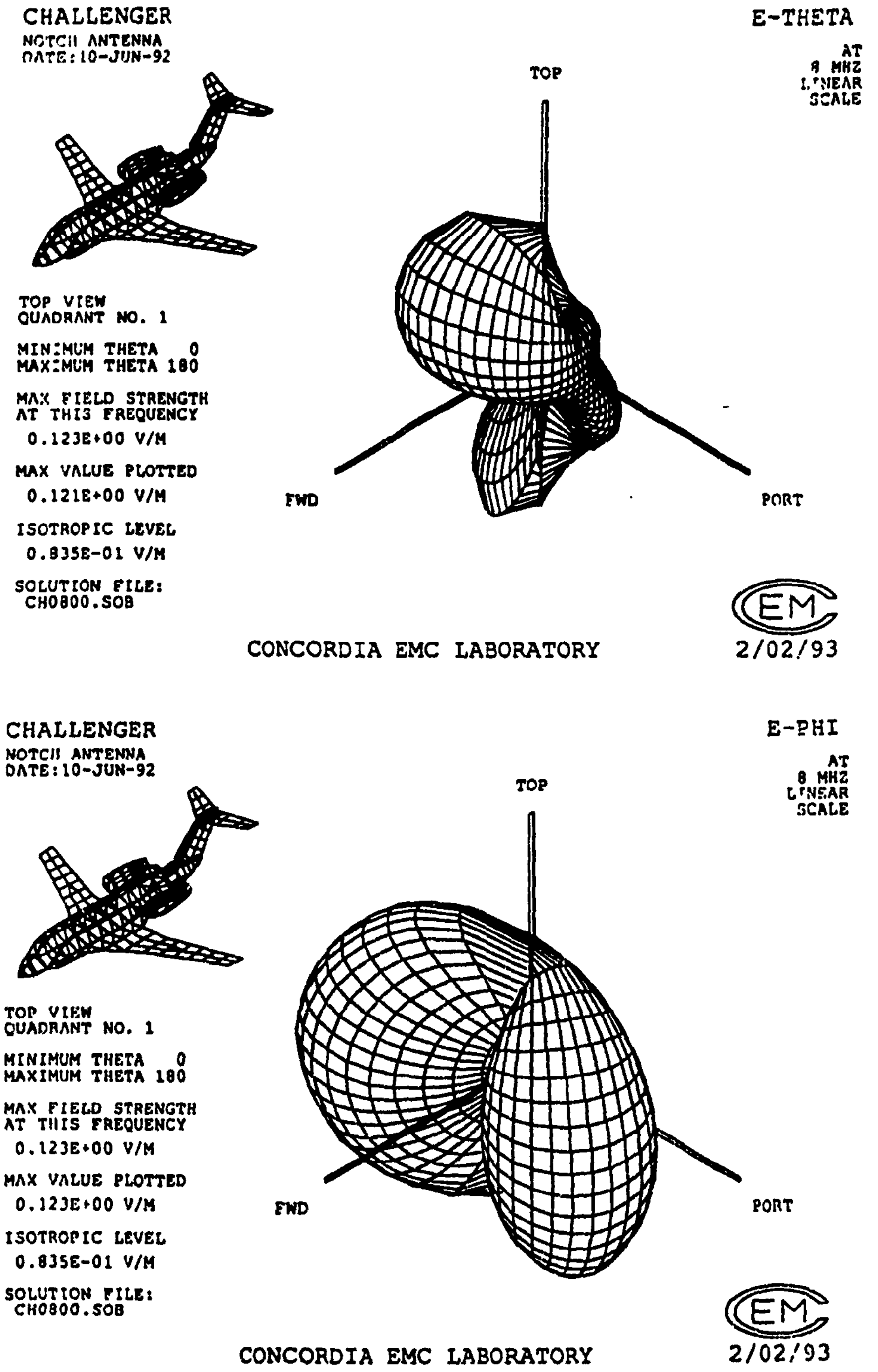

CHALLENGER
NOTCH ANTENNA
DATE:10-JUN-92

E-THETA
AT
8 MHZ
LINEAR
SCALE

TOP VIEW
QUADRANT NO. 1

MINIMUM THETA 0
MAXIMUM THETA 180

MAX FIELD STRENGTH
AT THIS FREQUENCY
0.123E+00 V/M

MAX VALUE PLOTTED
0.121E+00 V/M

ISOTROPIC LEVEL
0.835E-01 V/M

SOLUTION FILE:
CH0800.SOB

CONCORDIA EMC LABORATORY 2/02/93

CHALLENGER
NOTCH ANTENNA
DATE:10-JUN-92

E-PHI
AT
8 MHZ
LINEAR
SCALE

TOP VIEW
QUADRANT NO. 1

MINIMUM THETA 0
MAXIMUM THETA 180

MAX FIELD STRENGTH
AT THIS FREQUENCY
0.123E+00 V/M

MAX VALUE PLOTTED
0.123E+00 V/M

ISOTROPIC LEVEL
0.835E-01 V/M

SOLUTION FILE:
CH0800.SOB

CONCORDIA EMC LABORATORY 2/02/93

(a) 3-D E_θ and E_ϕ patterns at 8 MHz

Fig. 6.11 3-D patterns in the neighbourhoods of 9 MHz.

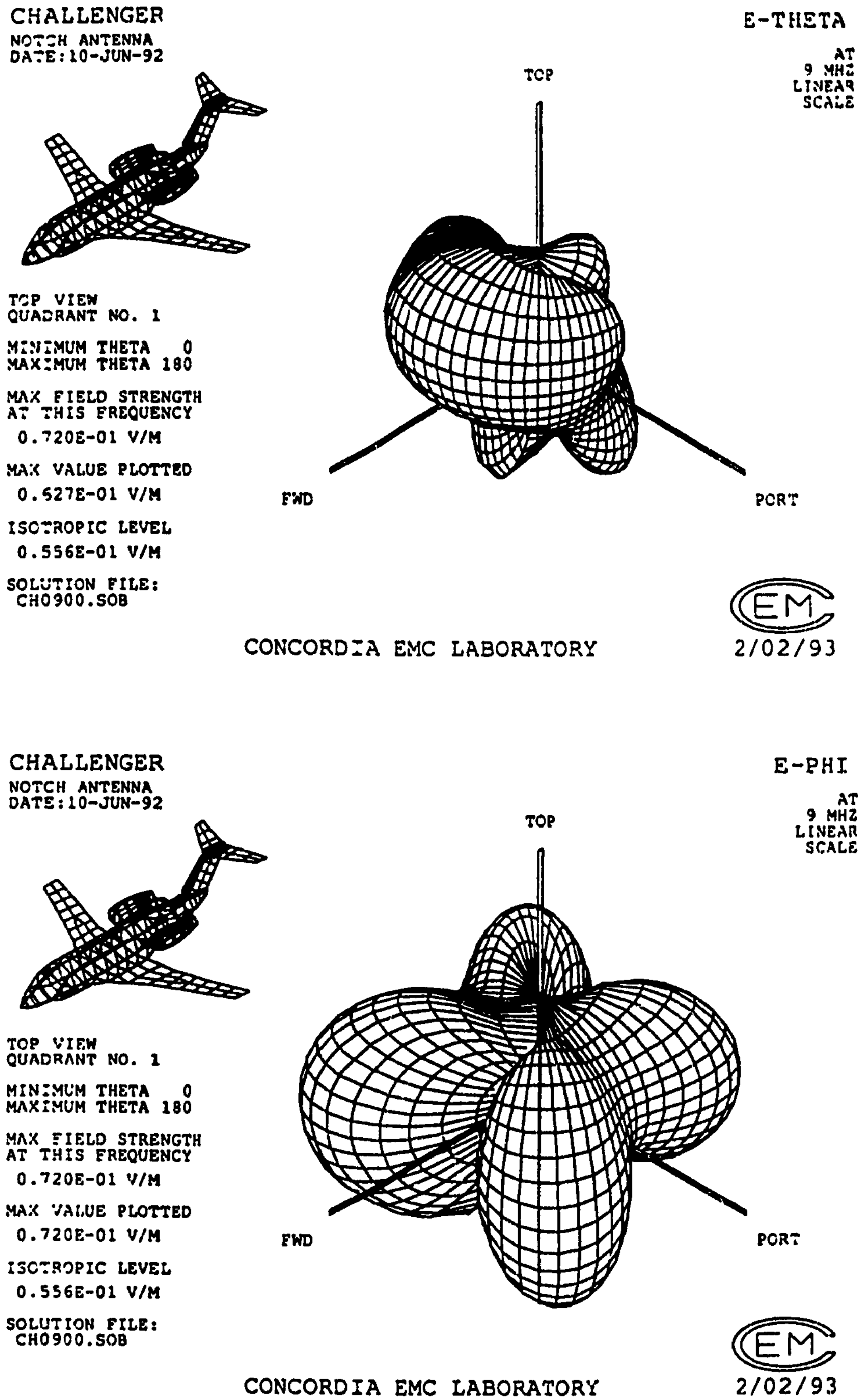

(b) 3-D E_θ and E_ϕ patterns at 9 MHz

Fig. 6.11 (cont'd)

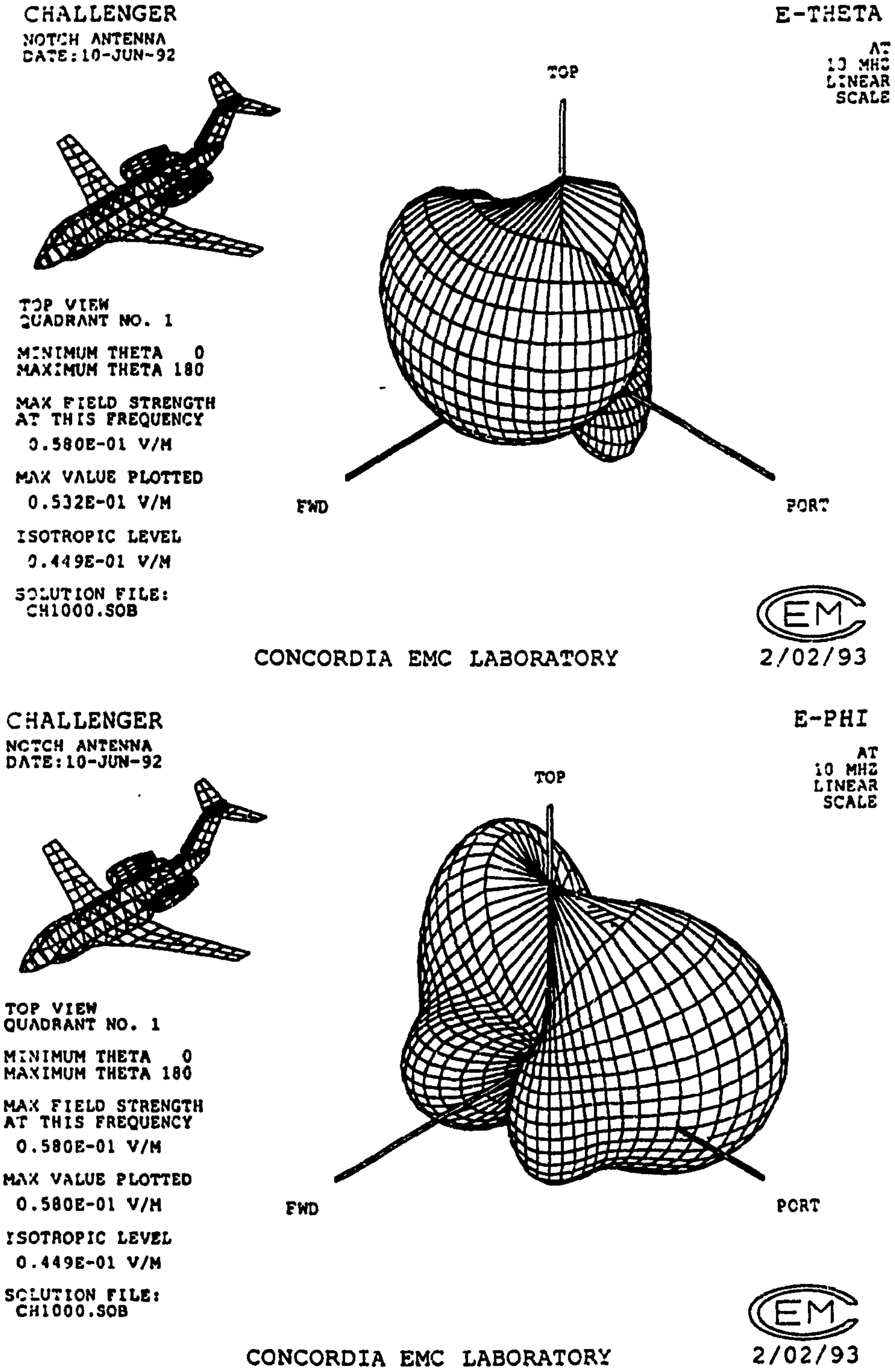

CHALLENGER
NOTCH ANTENNA
DATE: 10-JUN-92

E-THETA
AT
10 MHZ
LINEAR
SCALE

TOP VIEW
QUADRANT NO. 1

MINIMUM THETA 0
MAXIMUM THETA 180

MAX FIELD STRENGTH
AT THIS FREQUENCY
0.580E-01 V/M

MAX VALUE PLOTTED
0.532E-01 V/M

ISOTROPIC LEVEL
0.449E-01 V/M

SOLUTION FILE:
CH1000.SOB

CONCORDIA EMC LABORATORY
2/02/93

CHALLENGER
NOTCH ANTENNA
DATE: 10-JUN-92

E-PHI
AT
10 MHZ
LINEAR
SCALE

TOP VIEW
QUADRANT NO. 1

MINIMUM THETA 0
MAXIMUM THETA 180

MAX FIELD STRENGTH
AT THIS FREQUENCY
0.580E-01 V/M

MAX VALUE PLOTTED
0.580E-01 V/M

ISOTROPIC LEVEL
0.449E-01 V/M

SOLUTION FILE:
CH1000.SOB

CONCORDIA EMC LABORATORY
2/02/93

(c) 3-D E_θ and E_ϕ patterns at 10 MHz

Fig. 6.11 (cont'd)

here. In the plane ϕ=90°, the E_θ pattern, shown in Fig. 6.12(d), changes from distinctive four lobes at 12 MHz to less distinctive four lobes at 13 and 14 MHz. The changes in the E_ϕ pattern, shown in Fig. 6.12(e) are more dramatic. The pattern changes from near isotropic at 12 MHz to one main lobe and one minor lobe at 13 MHz and then to two near equal lobes at 14 MHz.

Fig. 6.13 shows the three-dimensional patterns of E_θ and E_ϕ at 12, 13, and 14 MHz. The changes in E_θ are seen to be less as remarkable as in E_ϕ for this coupling. The most noticeable change in E_θ is the addition of a minor lobe in the aft direction of the top sector as the frequency is increased from 12 to 14 MHz, whereas the E_ϕ pattern is deformed from two aligned side lobes at 12 MHz to three main lobes oriented in the forward-port, forward-starboard, and aft directions at 14 MHz.

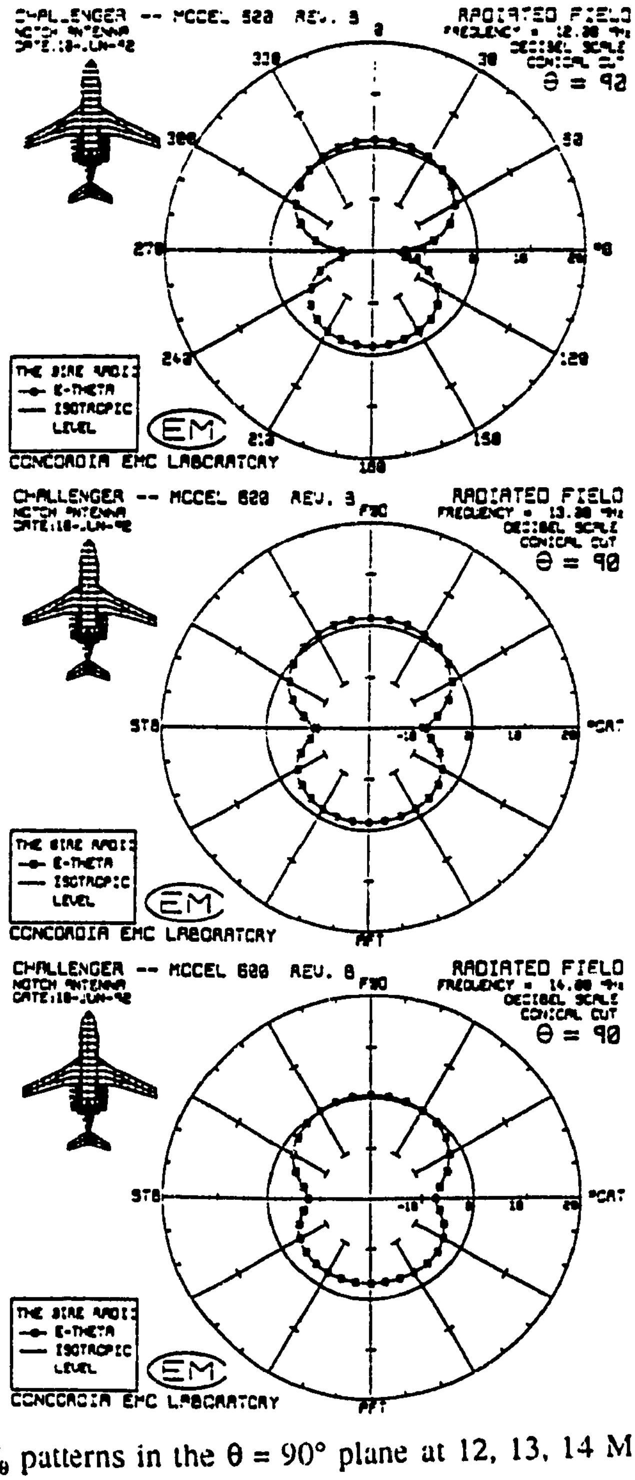

(a) E_θ patterns in the $\theta = 90°$ plane at 12, 13, 14 MHz

Fig. 6.12 Radiation patterns in three principal planes in the neighbourhoods of 13 MHz.

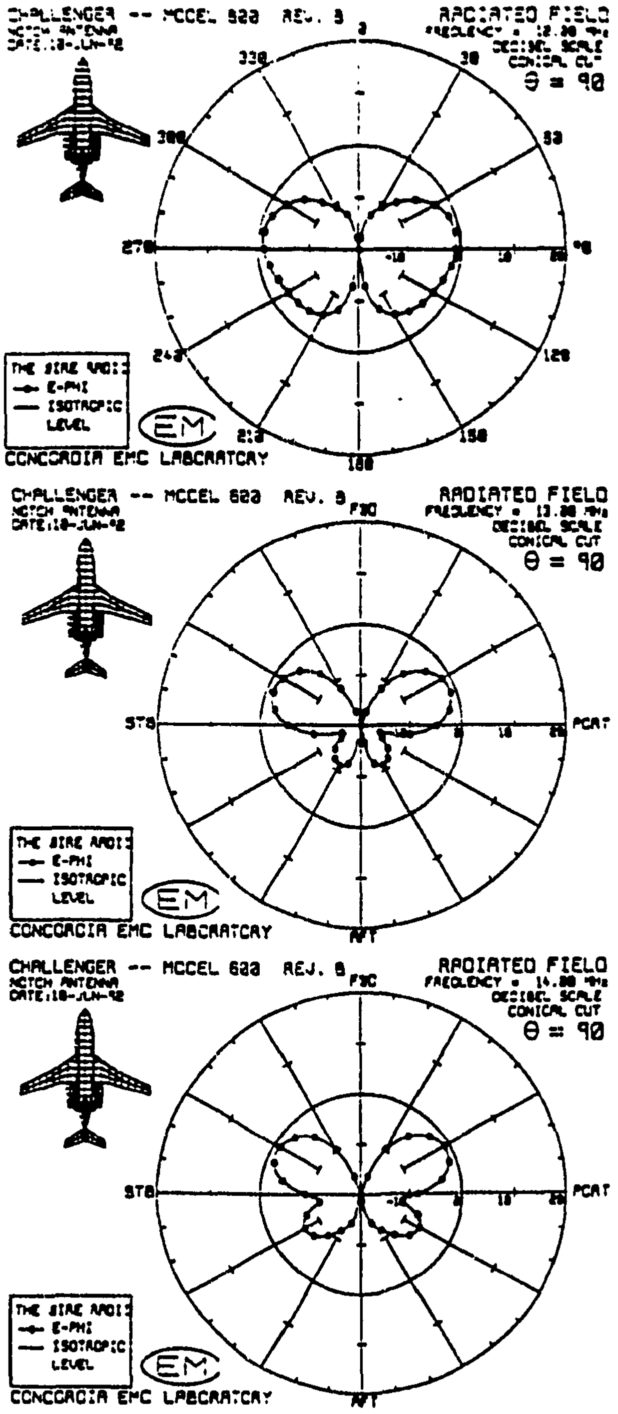

(b) E_ϕ patterns in the $\theta = 90°$ plane at 12, 13, 14 MHz

Fig. 6.12 (Cont'd)

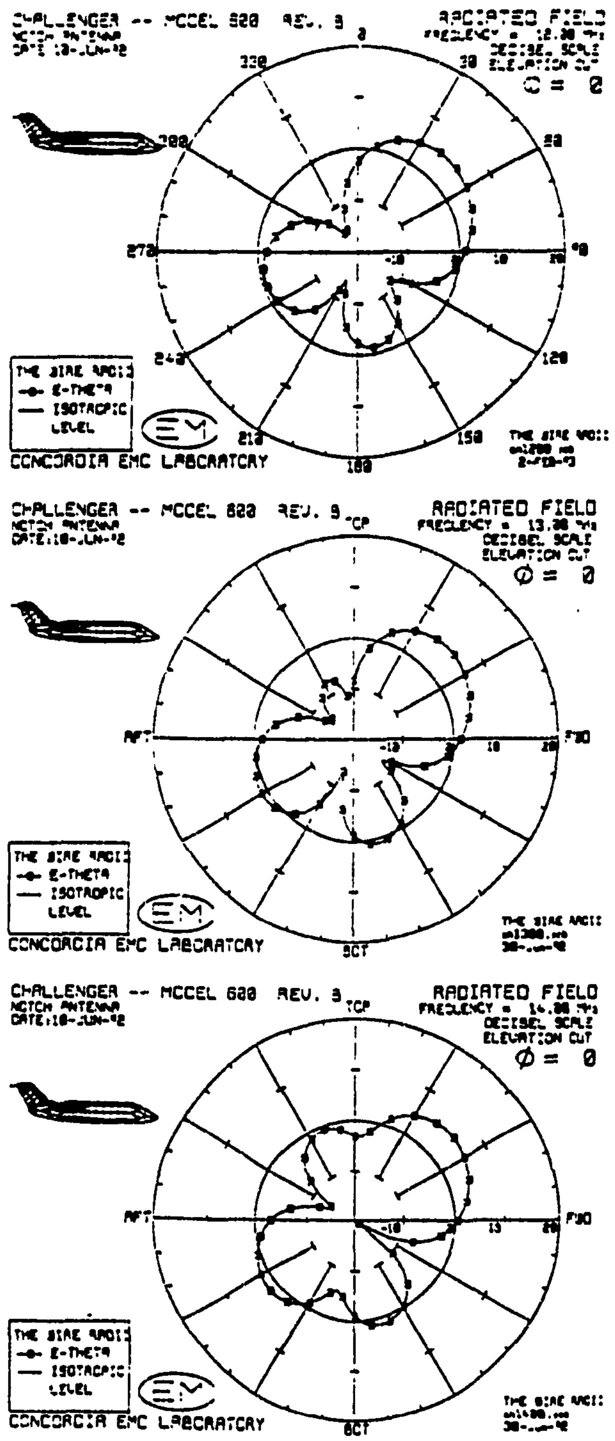

(c) E_θ patterns in the $\phi = 0°$ plane at 12, 13, 14 MHz

Fig. 6.12 (Cont'd)

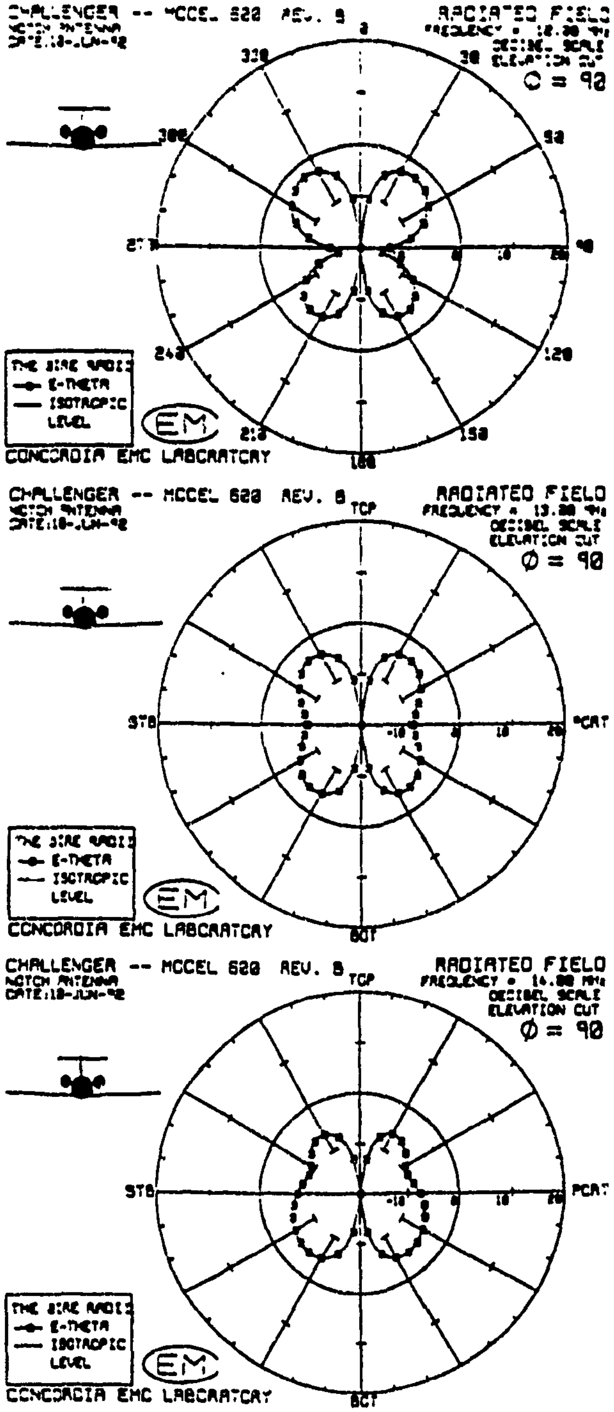

(d) E_θ patterns in the $\phi = 90°$ plane at 12, 13, 14 MHz

Fig. 6.12 (Cont'd)

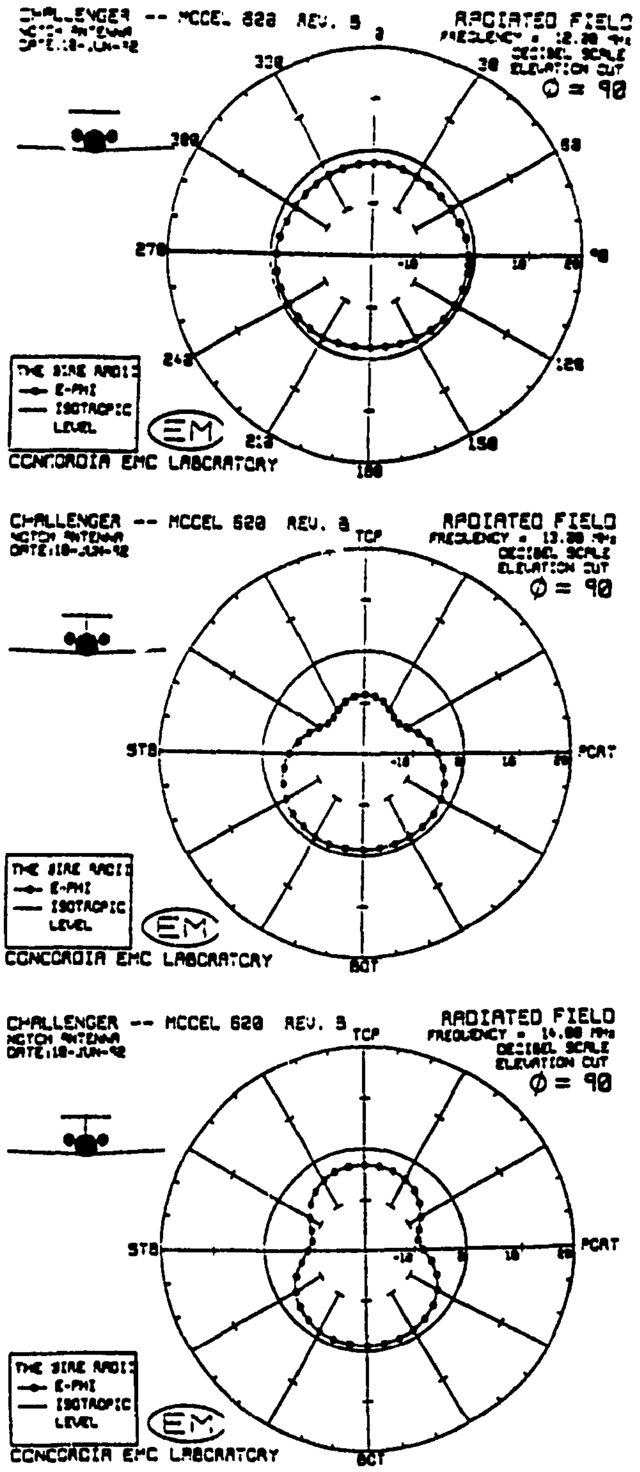

(e) E_ϕ patterns in the $\phi = 90°$ plane at 12, 13, 14 MHz

Fig. 6.12 (cont'd)

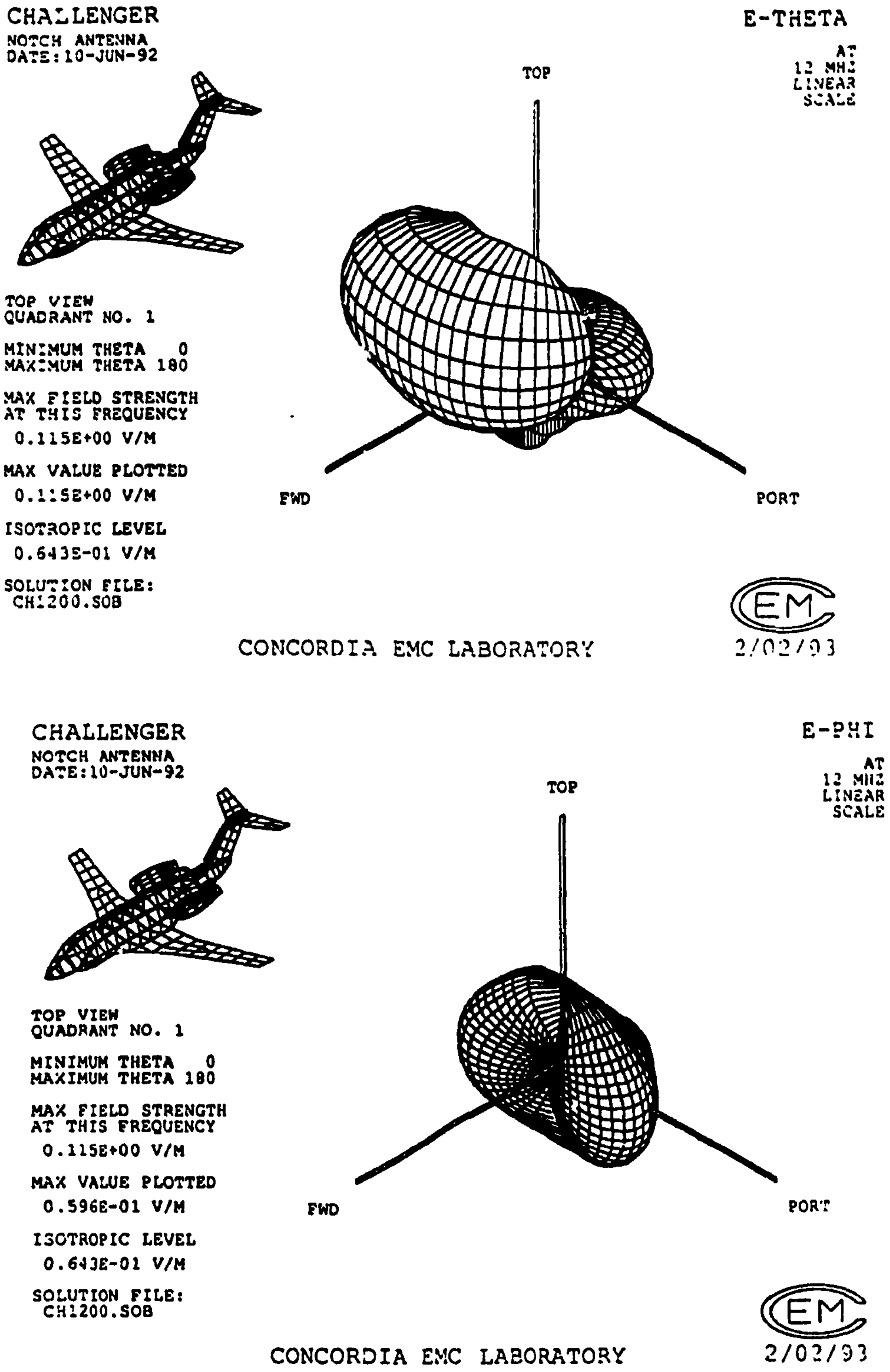

(a) 3-D E_θ and E_ϕ patterns at 12 MHz

Fig. 6.13 3-D radiation pattern in the neighbourhoods of 13 MHz.

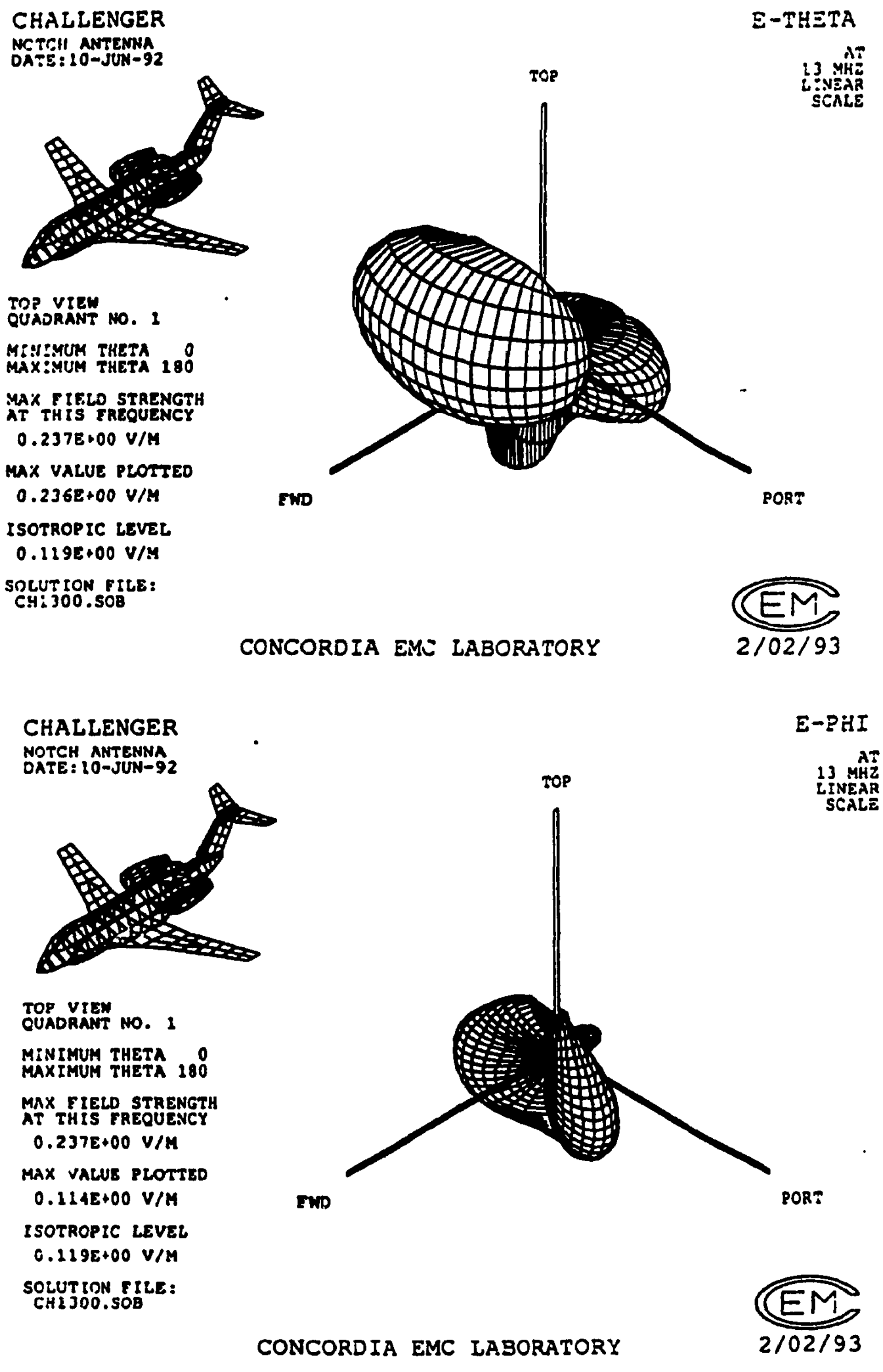

(b) 3-D E_θ and E_ϕ patterns at 13 MHz

Fig. 6.13 (cont'd)

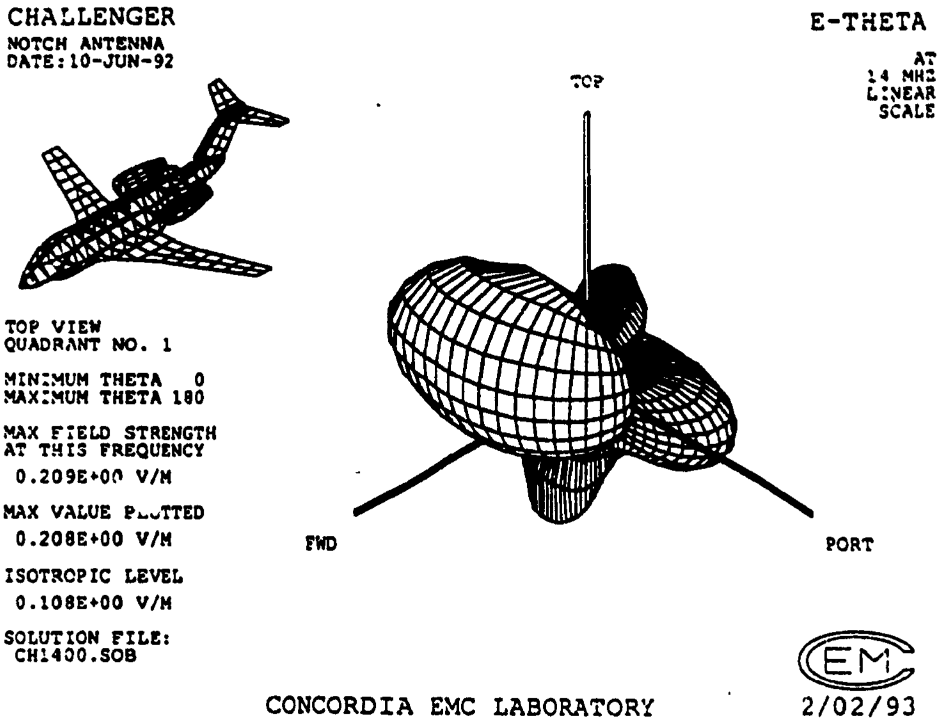

CHALLENGER
NOTCH ANTENNA
DATE:10-JUN-92

E-THETA
AT
14 MHZ
LINEAR
SCALE

TOP VIEW
QUADRANT NO. 1

MINIMUM THETA 0
MAXIMUM THETA 180

MAX FIELD STRENGTH
AT THIS FREQUENCY
0.209E+00 V/M

MAX VALUE PLOTTED
0.208E+00 V/M

ISOTROPIC LEVEL
0.108E+00 V/M

SOLUTION FILE:
CH1400.SOB

CONCORDIA EMC LABORATORY

2/02/93

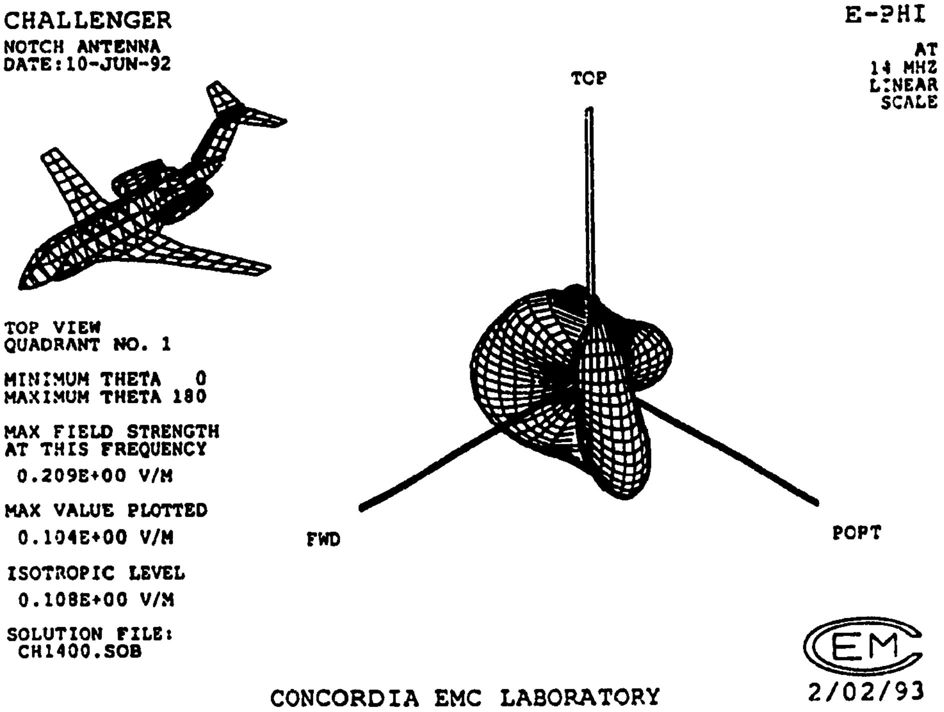

CHALLENGER
NOTCH ANTENNA
DATE:10-JUN-92

E-PHI
AT
14 MHZ
LINEAR
SCALE

TOP VIEW
QUADRANT NO. 1

MINIMUM THETA 0
MAXIMUM THETA 180

MAX FIELD STRENGTH
AT THIS FREQUENCY
0.209E+00 V/M

MAX VALUE PLOTTED
0.104E+00 V/M

ISOTROPIC LEVEL
0.108E+00 V/M

SOLUTION FILE:
CH1400.SOB

CONCORDIA EMC LABORATORY

2/02/93

(c) 3-D E_θ and E_ϕ patterns at 14 MHz

Fig. 6.13 (cont'd)

6.4 Effects of the Coupling on the Aircraft HF Antenna Assessment Parameters

The polarization of the radiated power from a notch-fed dorsal fin antenna can be characterized as having high $\%E_\theta$ power, as demonstrated by Wong [57] through the measurements conducted on a scale-model of the Canadair CL-28 aircraft. Fig. 6.14 shows the three aircraft HF antenna assessment parameters as functions of frequency for the notch antenna on the CL-600. The R.P. Efficiency fluctuates slowly within the range of 35 to 55%, which is something similar to the case of the wire antennas on the EC-130 presented in Chapter 5. Greater variations are seen in the $\%E_\theta$ and *Sub-%-*E_θ. The value changes between 30 and 80% for $\%E_\theta$ and between 5 and 40% for *Sub-%-*E_θ. A substantial increase in $\%E_\theta$ power and *sub-*$\%E_\theta$ power near 13 MHz is observed. This is most likely due to the strong antenna-to-airframe coupling around that frequency because the induced current on the nearly vertical dorsal is quite high as shown in Fig. 6.8, considerably enhancing the vertically-polarized radiated field. Since the short and medium range communication via the ground mode relies on the θ-component of the radiated field [9], this coupling has a positive impact on the HF communication.

The effect of the coupling near 9 MHz can also be seen in the three power parameter curves but is less obvious compared to the previous case. It appears as a small "bump" in the R.P. efficiency curve and a barely noticeable "lump" in the $\%E_\theta$ power and *sub-*$\%E_\theta$ power curves. These changes in radiated power parameter values are too small to be significant.

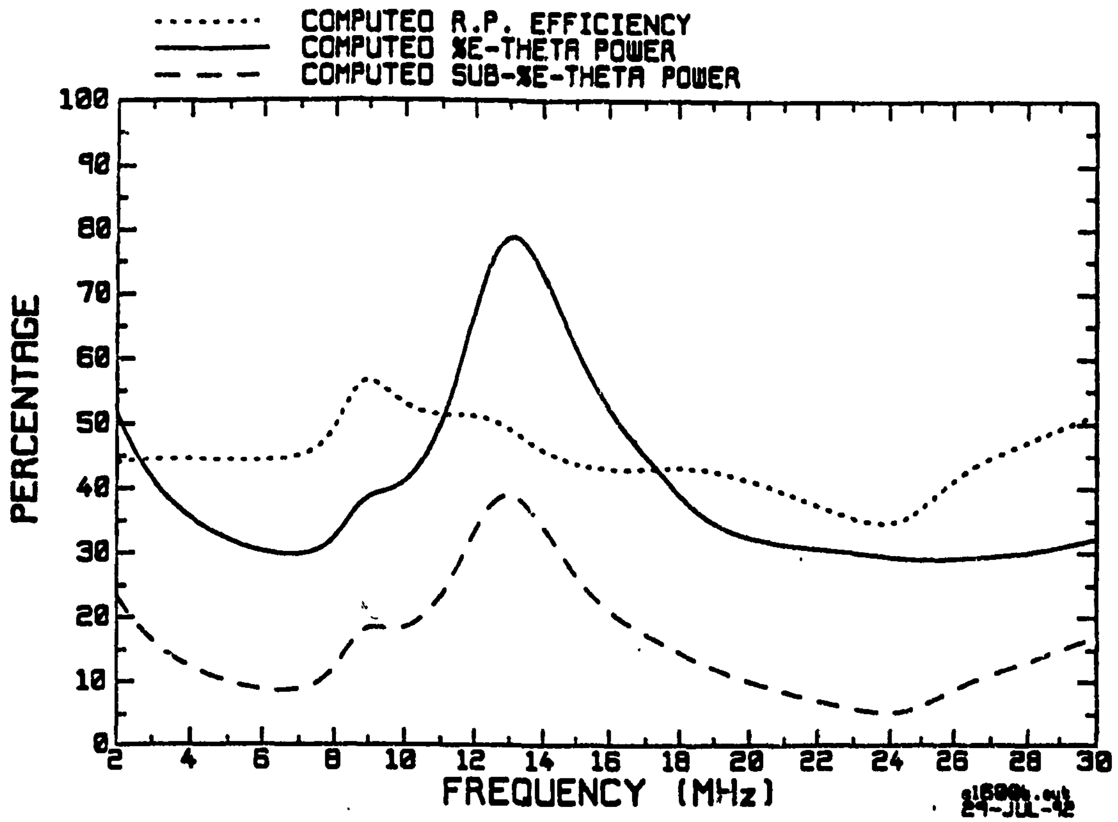

Fig. 6.14 Aircraft HF antenna assessment parameters for the CL-600's notch antenna.

6.5 Concluding Remarks

The HF coupling on this CL-600 aircraft is found to be strongest near 9 and 13 MHz. The induced current paths results from the coupling near 9 MHz are approximately half wavelength long, while the current paths associated with the coupling near 13 MHz are close to one wavelength in length. The coupling near 9 MHz dramatically changes the radiation pattern of both E_θ and E_ϕ but the effect on the aircraft HF antenna assessment parameters is very limited. The coupling near 13 MHz substantially increases the $\%E_\theta$ and *Sub-*$\%E_\theta$ power and changes the E_ϕ pattern considerably.

CHAPTER 7

CONCLUSION

Advances in computer technologies with much higher speed processors and much larger memory capacities have considerably increased our capability for the computer simulation of complicated phenomena. This thesis has taken advantage of these newly available powerful computers in the application of numerical techniques to model complicated electromagnetic interactions on large aircraft. Computer simulation in this thesis was carried out using wire-grid models of aircraft which were carefully designed to comply with wire-grid modelling guidelines. The availability of programs MESHES, FNDRAD, and CHECK facilitates and systematizes the model design and error-checking processes. These programs constitute "expert system" software for the design and error-checking of wire-grid models. Scale-model measured radiation patterns were available for the EC-130 and were used to validate the EC-130 model. Although measured data were not available for the CL-600 model, delicate wire-grid design that fully complies with the modelling guidelines gives confidence in the results. The phenomena associated with strong coupling such as large induced current and rapid changes with frequency of antenna input impedance, induced voltage and radiation pattern were displayed in this thesis with the graphic software modules. This made possible the comprehensive identification, verification and assessment of coupling phenomena.

This thesis has presented an in-depth study of HF coupling modes on two large aircraft. First, in order to take advantage of the availability of the "expert" software, the

EC-130 model used in Rosenzweig thesis was revised to obtain a much better wire-grid design and eliminate modelling errors. Then the revised model was solved with the newly-available powerful DEC 5000 workstations. The high resolution spectral analysis technique was used to exploit the computational power of the new computer systems and the integrated graphic software to study the antenna-to-antenna coupling and antenna-to-airframe coupling on the EC-130. As a means of identifying coupling modes and assessing the impact of coupling, the integrated graphic software was used to correlate the coupling indicators, such as peaks and minima in both the impedance curves and induced voltage curves, with the current distributions and with the radiation patterns. Hence all the antenna-to-antenna coupling frequencies on the EC-130 were identified and were related to aircraft currents and to radiation patterns. This was summarized in Tables 5.4 through 5.9 of Chapter 5. In addition, the high resolution spectral analysis technique was applied to the CL-600 aircraft model. The similarity between its notch antenna and a short-circuited tranline antenna was noted. Couplings to the airframe of the CL-600 aircraft were identified and described. These results represent a new plateau in the applications of computer modelling and analysis to an electromagnetics problem for structures of this complexity. This thesis has demonstrated that numerical modelling can provide complete and detailed analysis with higher degree of flexibility compared to measurements.

This chapter summarizes the achievements that were made in this thesis and proposes further work that is feasible in the future to further explore these fascinating and important electromagnetic compatibility problems.

7.1 HF Coupling Modes on the EC-130/TACAMO Aircraft

The EC-130/TACAMO wire-grid model was carefully refined to ensure that the most accurate numerical results that are possible could be obtained. An effort was made to eliminate the NEC-incompatibility errors that existed in the original model by modifying the wire-grid geometries in the problem regions. In addition, a great number of wires were added to the wings and stabilizers to better model the current flows on the surfaces of those parts. Increased confidence in the resulting 924 wire-segment model was supported by the better agreement between the computed and the scale-model measured radiation patterns.

The study of HF coupling modes was accomplished by analyzing the results obtained from executing NEC with a 0.1 MHz frequency step over the 2 to 30 MHz frequency band. Two representative antennas, HF1 and HF4, on the aircraft were chosen as active antennas and were excited in turn for three different passive antenna loading conditions: short-circuit, open-circuit, and 50 Ω "matched" load.

It was found that the resonant and anti-resonant length of the antenna are useful guides for sorting out complicated inter-antenna coupling behavior. The loading condition of the passive antennas was shown to have a strong influence on the inter-antenna coupling modes. When the passive antennas are short-circuited to the airframe, strong induced currents occur near the resonant frequencies of the passive antennas and the input impedance of the active antenna changes rapidly near these frequencies. If passive antennas are open-circuited to the airframe, strong induced voltages occur near the anti-resonant frequencies of the passive antennas rather than their resonant frequencies.

Accompanied by the high induced voltages at the terminals of the passive antennas are large changes in the active antenna's input impedance. Induced voltages as high as 5 times the voltage of the exciting source were observed at the terminals of the passive antennas. In the case of 50 Ω loading, the magnitude of coupling effects is much lower compared to the two other cases. Induced voltages are relatively low and changes in input impedance due to coupling are small and even unnoticeable at the higher end of the HF band. Coupling frequencies were seen to be close to the resonant frequencies of the passive antennas, as in the short-circuit case. Drastic changes in radiation pattern within a very narrow frequency band due to strong couplings were observed in the short-circuit and open-circuit cases. The three aircraft HF antenna assessment parameters also reflect the impact of coupling with abrupt changes at the frequencies where strong coupling occurs.

Antenna-to-airframe coupling was observed to be more prominent when the HF4 "dog-leg" antenna is excited than when the HF1 straight antenna is excited. This kind of coupling was seen to have a broad-band nature whereas the inter-antenna coupling is highly sensitive to frequency changes. Major induced current paths on the airframe were identified when the excited antenna is HF4. In some cases, the length of the active antenna HF4 is included as part of the current path. The lengths of the paths are comparable to a half wavelength .

The inter-antenna coupling modes and their effects on radiation pattern and on aircraft HF antenna assessment parameters are summarized in Tables 5.4 through 5.15. These information sets of HF antenna performance and EMC interaction analysis are very difficult, if not impossible, to obtain by any scale-model or full-scale measurements.

7.2 HF Coupling Modes on the CL-600/CHALLENGER Aircraft

Unlike the EC-130 model used in this thesis, which was refined from an existing flawed model, the CL-600 model is a new wire-grid built "from the ground up" to comply with the guidelines for wire-grid design. It has been shown that the application of the same analysis techniques used on the EC-130 provides comprehensive information on the radiation characteristics of the notch antenna on this particular aircraft and antenna type for the first time. The similarity between this notch antenna and the short-circuited tranline antenna was recognized. Since there is only one HF antenna on this aircraft, the antenna-to-airframe coupling is the only type of HF coupling present. The variations in input impedance due to coupling were correlated with the current paths on the airframe. The effects of antenna-to-airframe coupling on the performance of the HF communication systems were assessed.

The input impedance of the notch antenna on this particular aircraft was shown to be similar to the impedance of the short-circuited tranline antenna. The behaviour was compared to a notch antenna cut in the edge of a semi-infinite conducting sheet, and significant differences were found.

Major induced current paths on the airframe were found which are associated with two strong coupling modes from the antenna to the airframe. They appear as symmetric pairs due to the geometrical symmetry of the aircraft about the exciting notch antenna. The length of each path in one pair was found to be close to a half wavelength, whereas the paths in another pair were found to be approximately one wavelength long. These two pairs of current paths are associated with the couplings near 9 and 13 MHz, respectively, which give rise to increases in the resistive part of the impedance near these frequencies.

The impact of such coupling to the airframe was seen in the radiation pattern for the E_θ component, where remarkable pattern changes were observed. The effect on the HF performance-assessment parameters is a substantial increase in the $\%E_\theta$ and the *sub-*$\%E_\theta$ values, indicating that the field strength in the E_θ component was increased by these coupling modes, although the R.P. efficiency is not much changed.

These results are critical for understanding the overall performance of the notch antenna in the HF band.

7.3 Future Work

It is natural, at the end of a project, for a researcher to have some reflections on the way his research was conducted. The author would like to give some suggestions for future researchers that may be beneficial in the endeavor for better understanding of such important and fascinating electromagnetic compatibility issues. Although the time required to design a new model is enormous, it may be worthwhile to completely redesign the EC-130 model following the wire-grid guidelines, because the "base line" EC-130 wire-grid violates some fundamental guidelines: many meshes are not squared; and wires meet at shallow angles. Removing these errors is as much labor as rebuilding the grid entirely. It would be useful in the future to calculate the impedance of each wire antenna on the EC-130 individually, that is, to calculate the impedance of each antenna with all the other antennas removed. This will provide a reference curve for comparison with the impedance when the other antennas are present. Differences would be a strong indication of antenna-to-antenna coupling. Further investigations should be made of the limitations of the EK option of NEC. Using EK at lower frequencies, where the meshes in a wire-grid model are "electrically small", tends to give rise to serious problems in which small loops carry large circulating currents which are non-physical. It is known that the basis functions for current used in NEC may give inaccurate results for electrically small meshes. However, how the EK formulation worsens the results is not fully understood or well documented.

One can further study the electromagnetic compatibility issues on these two large aircraft by considering the in-band and out-of-band coupling problems. The investigation of coupling in this thesis was limited to the coupling between HF antennas, and coupling of the HF antennas to the airframe. However, antennas operating in higher frequency bands such as VHF and UHF are also used on the aircraft for various purposes. Thus coupling between antennas operating in different frequency bands can exist and can be categorized into two kinds: in-band coupling and out-of-band coupling.

HF in-band coupling (2-30 MHz) is the coupling at HF frequencies from an HF antenna to another antenna that normally operates in another band, UHF or VHF. The term "in-band coupling" here means that power at HF frequencies couples into, for example, a VHF antenna and receiver. This power is usually rejected by the filter in the receiver; however if the HF power is too high it can leak through the filter and cause electromagnetic interference (EMI). On the CL-600 aircraft, for example, a number of VHF and UHF antennas are installed in various locations on the airframe. It is desired to investigate the HF power that could couple to these antennas from the HF notch antenna. This can be accomplished by adding the VHF and UHF antennas to the corresponding locations in the wire-grid model of the CL-600 and then calculating the coupled voltages at the feed elements of these antennas which are loaded by appropriate impedances. Another way of doing it is to calculate the near fields just above the feed points of the VHF and UHF antennas and then estimate the coupled voltages using the equivalent lengths of these antennas. These two approaches should only be used after modifications to the feed regions of these antennas in the model are carried out to give finer wire-grids that can properly model the current flows there.

Due to frequency harmonics that are generated in the HF transmitter, out-of-band coupling is also possible. "Out-of-band" here means that unwanted power at frequencies other than HF originating from an HF system couples into an antenna and its receiver that are operating in the frequency band of the unwanted power. For instance, the HF notch antenna on the CL-600 could radiate energy at harmonics of the HF frequency that lie in the VHF band. This VHF energy could be received by the VHF antennas, resulting in out-of-band coupling. If the power in the harmonics of the HF system is too large, EMI could result. In order to investigate this kind of coupling, the CL-600 wire-grid model must be upgraded to a "high frequency model" which consists of smaller grid cells with shorter wire segments to make segments shorter than $\lambda/5$ at VHF frequencies. With the presently available computer systems at the EMC Laboratory, wire-grid models with up to 2000 segments are not prohibitively complex for high resolution spectral analysis.

In conclusion, studying electromagnetic coupling on large aircraft with computer modelling can provide complete, detailed and useful information pertaining to the extremely complicated coupling phenomena. The information is valuable for aircraft antenna engineers in assessing the performance of a vital communication system.

REFERENCES

[1] Granger, J.V.N., and Bolljahn, J.T., 'Aircraft Antennas', Proceedings of the I.R.E., Vol. 43, pp. 533-550, May 1955.

[2] Granger, J.V.N., and Morita, T., 'Radio-Frequency Current Distributions on Aircraft Structures,' Proceedings of the I.R.E., pp. 932-938, August 1951.

[3] Forgan, D.H., 'Numerical Prediction of Aircraft Antenna Performance,' International Conference on Antennas for Aircraft and Spacecraft, pp. 239-242, Institution of Electrical Engineers, Savoy Place, London WC2, 3-5 June 1975.

[4] Kubina, S.J., and Pavlasek, T.J.F., 'Evaluation of HF Antennas for Helicopters and Small Aircraft,' International Conference on Antennas for Aircraft and Spacecraft, pp. 165-170, Institution of Electrical Engineers, Savoy Place, London WC2, 3-5 June 1975.

[5] Rao, B.R., 'Modelling and Measurement of High Frequency Antennas for the U.S. Coast Guard HH-60J Helicopter,' IEEE Antennas and Propagation Society International Symposium, URSI Radio Science Meeting, Ann Arbor, Michigan, U.S.A., June 28-July 2, 1993.

[6] Larose,C.L., Advances in Wire-Grid Modelling of Antennas and Auxiliary Computer Graphics Systems with the CP-140 Case Study, M.ENG. Thesis, Department of Electrical Engineering, Concordia University, Montreal, Quebec, Canada.

[7] Rosenzweig, B.R., 'Numerical Modelling of EC-130 Airframe and Antenna Installation for Prediction of Radiation Characteristics over the HF Band', M.ENG. Thesis, Department of Electrical and Computer Engineering, Concordia University,

Montreal, Quebec, Canada.

[8] Esfandiari, S., Analysis of HF Antennas on A Helicopter by Scale-Model Measurements and Computer Modelling, M.A.Sc. Thesis, Department of Electrical and Computer Engineering, Concordia University, March 1992.

[9] Jordan, E.C., and Balmain,.K.G., Electromagnetic waves and Radiating Systems, Second Edition, Prentice-Hall Inc., Englewood Cliffs, N.J., 1968.

[10] Mittra, R., editor, 'Numerical and Asymptotic Techniques in Electromagnetics,' Springer-Verlag, 1975.

[11] Itoh, T., editor, 'Numerical Techniques for Microwave and Millimeter-Wave Passive Structures,' John Wiley & Sons, 1989.

[12] Silvester, P., 'Finite Elements for Electrical Engineers,' Cambridge University Press, New York, 1983.

[13] Yee, K.S., 'Numerical Solution of Initial Boundary Value Problems Involving Maxwell's Equations in Isotropic Media', IEEE Trans. on Antennas and Propagation, Vol. AP-14, No. 3, pp 302-307, May, 1966.

[14] Harrington, R.F., 'Field Computation by Moment Methods,' Reprinted by the Author, R.D.2, West Lake Road, Cazenovia, N.Y. 13035, 1968.

[15] Johns P.B. and Beurle, R.L., Numerical solution of 2-dimensional scattering problems using a transmission-line matrix,' Proc. Inst. Electr. Eng., vol. 118, pp. 1203-1208, Sept. 1971.

[16] Hafner, Ch., The Generalized Multipole Technique for Computational Electromagnetics, Artech House Inc., 1990.

[17] Keller, J.B., 'Geometrical theory of diffraction,' J. Opt. Soc. Amer., vol. 52, no. 2, pp. 116-130, February 1962.

[18] Kouyoumjian, R.G., and Pathak, P.H., 'A uniform geometrical theory of diffraction for an edge in a perfectly conducting surface,' Proc. IEEE, vol. 62, no. 11, pp. 1448-1461, November 1974.

[19] Balanis, C.A., Advanced Engineering Electromagnetics, John Wiley & Sons, 1989.

[20] Mur, G., 'Absorbing Boundary Condition for the Finite-Difference Approximation of the Time Domain Electromagnetic Field Equations,' IEEE Trans. on Electromagnetic Compatibility, Vol. EMC-23, No. 4, Nov. 1981.

[21] Leuchtmann P., and Bomholt, L., 'Thin Wire Feature for the MMP-Code,' Conference Proceedings, 6th Annual Review of Progress in Applied Computational Electromagnetics, pp. 233-240, Monterey CA, March 19-22, 1990.

[22] Burke, G.J., and Poggio, A.J., Numerical Electromagnetics Code (NEC) -- Method of Moments, Naval Ocean System Center, Technical Document 116, July 1977.

[23] Richmond, J.H., 'A Wire Grid Model for Scattering by Conducting Bodies,' IEEE Trans. on Antennas and Propagation, Vol. AP-14, pp. 782-786, Nov. 1966.

[24] Lee, K.S.H., Martin, L., and Castillo, J.P., 'Limitations of Wire Grid Modelling of a Closed Surface,' IEEE Trans. on Electromagnetic Compatibility, Vol. EMC-18, No. 3, pp.123-129, August 1976.

[25] Ludwig, A.C., 'Wire-Grid Modeling of Surfaces,' IEEE Trans. on Antennas and Propagation, Vol. AP-35, pp. 1045-1048, Sept. 1987.

[26] Trueman, C.W., and Kubina S.J., 'Fields of Complex Surfaces Using Wire-Grid

Modelling,' IEEE Trans. on Magnetics, Vol.27, No. 5, pp. 4262-4267, September 1991.

[27] Paknys, R.J., 'The Near Field of a Wire-Grid Model,' IEEE Trans. on Antennas and Propagation, Vol. 39, No. 7, pp. 994-999, July 1991.

[28] Kubina, S.J., Trueman, C.W, Gaudine, D., and Ramos, A., 'Creation,Visualization and Analysis -- The Dynamics of Complex Models', 9th Annual Review of Progress in Applied Computational Electromagnetics Society, Monterey, California, March 22-26, 1993.

[29] Trueman, C.W., and Kubina, S.J., 'Verifying Wire-Grid Model Integrity with Program "CHECK",' Appl. Comput. Electromagnet. Soc. J., Vol. 5, No.2, Winter 1990.

[30] Jasik, H., editor, Antenna Engineering Handbook, McGraw Hill Inc., 1961.

[31] Kubina, S.J., Cerny, E., and Gaudine, D., 'The DIDEC System : A New Interactive Model Building Technique,' Technical Note No. TN-EMC-84-04. Concordia University, EMC Lab, Montreal, Canada.

[32] Autocad Manual, Release 1D C2(10/26/88) IBM PC, Autodesk Inc.

[33] Trueman, C.W., 'Automated Radius Calculation for Wire-Grid Models,' 7th Annual Review of Progress in Applied Computational Electromagnetics Society , Monterey, California, March 18-22, 1991.

[34] Luu, Q.C., Kubina, S.J., Trueman, C.W., De Carlo, D., 'High Resolution Spectral Analysis of HF coupling Modes on the EC-130 Aircraft', 9th Annual Review of Progress in Applied Computational Electromagnetics, Conference Proceedings,

Monterey, California, March 22-26, 1993.

[35] RCS Computer Program BRACT, Log-Periodic Scattering Array Program -- II, MBAssociates Report No. MB-R-69/46, Contract No. F04701-68-C-0188, 1969.

[36] Richmond, J.H., 'Digital computer solutions of the rigorous equations for scattering problems,' Proc. IEEE 53, pp. 796-804, 1965.

[37] Mei, K.K., 'On the integral equation of thin wire antennas,' IEEE Trans. Ant. & Prop. AP-13, pp. 374-378, 1965.

[38] Antenna Modeling Program -- Engineering Manual, MBAssociates Report No. MB-R-74/62, 1974.

[39] Antenna Modeling Program -- Supplementary Computer Program Manual (AMP2), MBAssociates Report No. MB-R-75/4, 1975.

[40] Trueman, C.W., and Kubina, S.J., 'The Radar Cross-Section of Aircraft, Ships and Missiles at HF Frequencies,' EMC Lab Report No. TN-EMC-92-06, Contract No. W7714-9-9216/01-SZ, September 1992.

[41] Pocklington, H.C., 'Electric Oscillations on Thin Wires,' Proceedings of the Cambridge Philosophical Society, vol. 9, pp. 324-332, 1897.

[42] Trueman, C.W., Average Field Matching Wire Antenna Moment Method and Aircraft HF Antenna Application, Ph.D. Thesis, McGill University, April 1979.

[43] Poggio, A.J., and Adams, R.W., 'Approximations for the Terms Related to the Kernel in Thin-Wire Integral Equations,' UCRL-51985, Lawrence Livermore Laboratory, CA, December 19, 1975.

[44] Neureuther, A.R. et al., 'A comparison of Numerical Methods for Thin Wire

Antennas,' Presented at the 1968 Fall URSI Meeting, Dept. of Electrical Engineering and Computer Sciences, University of California, Berkeley, 1968.

[45] Miller, E.K. et al., An Evaluation of Computer Programs Using Integral Equations for the Electromagnetic Analysis of Thin Wire Structures, UCRL-75566, Lawrence Livermore Laboratory, CA,.March 1974.

[46] Poggio, A.J., 'Integral Representations for Fields Due to Sources on Open Surfaces with Applications to End Caps,' UCRL-51723, Lawrence Livermore Laboratory, CA, December 16, 1974.

[47] Wu, T.T., and King, R.W.P., 'The Tapered Antenna and Its Application to the Junction Problem for Thin Wires,' IEEE Trans. Ant. and Prop., AP-24, No. 1, pp. 42-45, January 1976.

[48] Burden, R.L. et al, Numerical Analysis, Prindle, Weber & Schmidt, Boston, Massachusetts, 1981.

[49] Burke, G.J., 'Recent Advances to NEC -- Applications and Validation,' Lawrence Livermore National Laboratory preprint number UCRL-100651, March 3, 1989.

[50] MIL-A-9080 (U.S.A.F.), Military Specification for Antenna Liaison Communication Equipment, Feb. 1954.

[51] Bahsoun, Y., and Kubina, S.J., A Digital Data Base for the Numerical Calculation of Isotropic Level and Radiated Power by An Aircraft Antenna, Technical Note No. TN-EMC-81-06, EMC Laboratory, Loyola Campus, Concordia University, Montreal, Canada,August 1981.

[52] Bahsoun, Y., Evaluation of an HF helicopter antenna measurements and numerical

techniques. Master's thesis, Faculty of Engineering, Concordia University, Montreal, Quebec, Canada, March 1982.

[53] Christiansen H., and Stephenson, M., MOVIE BYU Training Text, 1985 Ed., H.N. Christiansen, Graphics Utah Style, 1980 North 1450 East, Provo, Utah, 84604.

[54] Paul, C.A., and Nasar, S.A., 'Introduction to Electromagnetic Fields', McGraw-Hill Book Company, 1982.

[55] Stutzman, W.L., and Thiele, G.A., Antenna Theory and Design, John Wiley and Sons, 1981.

[56] Johnson, W.A., 'The Notch Aerial and Some Applications to Aircraft Radio Installations.' Proc. IEE (London), pt. B, vol. 102, pp. 211-218, March, 1955.

[57] Wong, J.Y., 'Radiation Pattern Efficiencies of Some Suppressed HF Aircraft Antennas', IRE Transactions on Aeronautical and Navigational Electronics, March, 1958.

[58] Kubina, S.J., Radiation Characteristics of Vehicle Mounted Antennas and Their Application to Comprehensive System Design," Ph.D. Thesis, Department of Electrical Engineering , McGill University, Montreal, Aug. 1972.